MULTICOMPONENT SEISMIC ANALYSIS FOR VELOCITY VARIATIONS WITH AZIMUTH RELATED TO HORIZONTAL TRANSVERSE ISOTROPY

by

Samara Omar

A thesis submitted to the Faculty and the Board of Trustees of the Colorado School of Mines in partial fulfillment of the requirements for the degree of Master of Science (Geophysics).

Golden, Colorado

Date _____

Signed: _____
Samara Omar

Signed: _____
Dr. Jim Simmons
Thesis Advisor

Golden, Colorado

Date _____

Signed: _____
Dr. John Bradford
Professor and Head
Department of Geophysics

ABSTRACT

Hydrocarbon recovery from unconventional reservoirs is driven by the presence of natural and induced fractures in the reservoir. While estimation of these fractures using single component seismic data is well practiced, the process may be ambiguous. Nine-component (9-C), 3-D seismic acquisition was developed with an interpretive emphasis on improving fracture network mapping in these unconventional plays. This research explores the application of pre-stack multicomponent interpretation for fracture identification.

Prior to interpretation, multicomponent acquisition requires rotation of the horizontal components such that the wave modes are separated into meaningful data sets. I discuss the implications of processing 9-C data in different coordinate systems and demonstrate the effectiveness of the radial-transverse system regardless of anisotropic conditions.

A technique of 9-C fracture interpretation takes advantage of the idea that in the presence of horizontal traverse isotropy (HTI), waves show variation in velocity depending on the source-receiver azimuth (VVAz). HTI is assumed for modeling presented in this research as it best describes a reservoir with a single, dominant vertical fracture set.

Conventional post-stack techniques attempt to map these velocity variations using shear wave splitting (SWS) calculations, however, the most insightful observations are in the details of pre-stack multicomponent data. I show the advantages of common-offset, common-azimuth (COCA) gathers and limited azimuth stacks (LAS) for shear wave splitting analysis on pre-stack 9-C data.

All nine components uniquely expose HTI conditions in the reservoir. VVAz is observed at reflectors below the HTI interval since waves must traverse the fractures in order to polarize, and accumulate a travel time delay. While the VVAz signature is unique to each component, the observations are complementary due to the orthogonality of particle motion of all wave modes. Assuming an HTI medium, along fracture strike, the P-wave and SV-wave

velocities are fast and the SH-wave velocity is slow. The cross-term components show no energy parallel or perpendicular to fracture strike.

This research demonstrates the added value of shear wave components based on the increased sensitivity of their VVAz response at all offsets and for thinner HTI layers. For this anisotropic feasibility study, the Niobrara stratigraphy of the Wattenberg field is modeled with varying extents of the fractured reservoir. The largest VVAz exposed on the noise-free model with the entire reservoir fractured shows 2.5s of splitting on the pure shear wave components and 1.8s on the converted wave components. Where the fractured interval thins to less than 25m, the P-wave velocity anisotropy is visually indistinguishable on COCA gathers. Based on modeling, field data is expected to show little HTI-related VVAz response on all components.

The Reservoir Characterization Project (RCP), Colorado School of Mines has explored the added interpretive value of 9-C data on unconventional reservoir development. Often, the nine data sets are interpreted separately even though all components are responding to the same subsurface conditions. This research evaluates the converted wave and shear wave inversion techniques used to solve for fracture azimuth and shear wave splitting and introduces a joint converted-shear wave inversion for improved fracture azimuth detection.

In recent years, the RCP has focused on the unconventional Niobrara-Codell reservoir within a 1-square mile section of the Wattenberg Field (Wishbone Section). The Niobrara-Codell formations are a typical unconventional petroleum system in which the efficiency of natural and induced fracture networks critically influence production in the low permeability, low porosity reservoir. The hypotheses and conclusions of this research are evidenced by both synthetic data and field data. Synthetic examples are based on simple HTI and Niobrara models and the simultaneous interpretation of the RCP multicomponent field survey over the Wishbone Section emphasizes the implications of noise, acquisition and processing on multicomponent data.

TABLE OF CONTENTS

LIST OF FIGURES

LIST OF TABLES

LIST OF SYMBOLS

Azimuth of fast velocity . . . . . θ_{fast}

Change in P-wave velocity with phase angle . . . . . $\delta^{(V)}$

Fractional difference between the vertical and horizontal P-wave velocity . . . . . $\epsilon^{(V)}$

Fractional difference between the vertical and horizontal S-wave velocity . . . . . $\gamma^{(V)}$

P-wave velocity . . . . . α

Reflectivity along isotropic plane . . . . . $R^{isotropy}$

Reflectivity along symmetry plane . . . . . R^{sym}

Reflectivity in an isotropic medium . . . . . R^{iso}

S-wave velocity . . . . . β

Travel time difference associated with shear wave splitting . . . . . $\Delta_{t_{split}}$

LIST OF ABBREVIATIONS

Amplitude Variation with Angle	AVA
Amplitude Variation with Azimuth	AVAz
Amplitude Variation with Offset	AVO
Common Offset, Common Azimuth	COCA
Compensated radial component with shear wave splitting removed	Rc
Converted shear SV-wave generated by a vertical source	C-wave
Crossline	XL
Fast-slow coordinate system	F-S
Field coordinate system	X-Y
Horizontal Transverse Isotropy	HTI
Inline	IL
Limited Azimuth Stack	LAS
Multicomponent seismic data	9-C
Primary or compressional wave generated by a vertical source	P-wave
Pseudo fast-slow shear wave components	FF',FS',SF',SS'
P-wave velocity	Vp
Radial-Transverse coordinate system	R-T
Receiver component oriented in the X direction	Rx
Receiver component oriented in the Y direction	Ry
Receiver component oriented in the Z direction	Rz

Splitting Estimation and Compensation . . . . . SEAC

Shear waves (pure) generated by a horizontal source . . . . . S-wave

Shear waves with particle motion perpendicular to direction of wave propagation SV-wave

Shear waves with particle motion perpendicular to plane of wave propagation . SH-wave

Shear wave splitting . . . . . SWS

Source generating particle motion in the X direction . . . . . Sx

Source generating particle motion in the Y direction . . . . . Sy

Source generating particle motion in the Z direction . . . . . Sz

S-wave velocity . . . . . Vs

Time-Lapse seismic surveys 4-D

Velocity Variation with Azimuth . . . . . VVAz

Vertical Transverse Isotropy . . . . . VTI

ACKNOWLEDGMENTS

What a long strange trip it's been. I cannot end my research without first thanking my advisor, Dr. Jim Simmons a.k.a J. The motivation for this work, the passion that kept it challenging, and the jokes that kept it fun, all stemmed from his brilliance and charisma. Thank you for the patience and perseverance.

Not only was I fortunate to have a great teacher and mentor, but I acknowledge that without love in the dream, it will never come true. Words cannot express my gratitude to my family - my parents, Deryck and Karen Omar, brothers, Michael and Paul and boyfriend, Richie. Thank you for the endless support, the shoulders to lean on, the needed distractions and the motivation to just keep truckin' on.

Not only do I owe gratitude to my family, but my RCP 'Fam' and colleagues I met along the way. I feel incredibly fortunate to have been part of the Reservoir Characterization Project and thank RCP Director, Dr. Ali Tura for the constructive feedback and leadership. I am also blessed to have met the incredibly understanding, dedicated and hardworking, Sue Jackson. Sue has been instrumental in making the journey, very much, stress-free.

I would like to say a particular thank you to Dr. Tom Davis. Tom not only recommended me to the RCP but has been an inspiration to my own professional and personal character. I hope to impact lives while doing what I love, as I have seen him do with so many of his own students. Thank you for the continued support and advice Tom. I really do appreciate it.

Finally, thank you to my committee and the RCP sponsors and mentors who have challenged me and elevated my excitement to step into the E&P industry. I look forward to our next encounter but for now, there is nothing much left to do but smile, smile, smile.

Dedicated to Mommy and Daddy Omar.

CHAPTER 1

INTRODUCTION

In 2013, the Reservoir Characterization Project (RCP) at the Colorado School of Mines launched Phase XV: an exploration and development project of the Wattenberg Field, Colorado with field sponsor Anadarko Petroleum Company (APC). The focus of the project is to understand the factors controlling commercial production of eleven horizontal wells in the Wishbone Section using data sets which include a time-lapse (4D), multicomponent (9-C) seismic survey. The Wishbone Section, is a 1 square-mile area owned and operated by APC, and the 11 wells target either the Niobrara formation or the Codell Member of the Carlile formation. The ultimate objective of the collaborative study is to maximize hydrocarbon recovery through the integrated analysis of geophysical, geological and engineering data.

1.1 Motivation

A few of the factors contributing to a reservoirs success include quality of the reserves, recovery factor and efficiency of completions. Previous research completed in the RCP Wattenberg Team has been geared towards understanding these individual components as they affect the production of the Wishbone Section. In particular, geomechanical models and reservoir simulations have exposed a strong correlation between fracture conductivity and increased production of the 11 horizontal wells (Alfataierge, 2017). As such, the mapping of fracture network orientation and density in the Niobrara/Codell reservoirs may significantly improve well positioning and hydrocarbon recovery.

Conventional techniques of seismic interpretation have focused on the application of P-wave seismic data in resolving fractures in shale reservoirs. P-wave velocity variation with azimuth (VVAz) becomes ambiguous when the maximum incidence angle is limited and/or the fractured layer is thin. P-wave interpretations can therefore be insufficient and uncertain in evaluating reservoir fracturing.

Shear waves are sensitive to horizontal transverse isotropy (HTI) at small incidence angles because of their horizontal particle motion. In addition to having more than one component to interpret (unlike the single P-wave component), shear waves can reduce uncertainty of fracture interpretation using VVAz techniques. This research examines the added value of the pure shear components in the radial-transverse domain for improved fracture characterization in the Niobrara/Codell reservoirs.

1.2 Scope of Work Presented

To set the stage for the studies presented in this manuscript, Chapter 2 elaborates on the motivation for mapping fracture networks in the Niobrara-Codell reservoir of the Wattenberg Field. The regional geology of the Rocky Mountain Region is well documented in literature (Sonnenberg, 2011, 2012; Sonnenberg and Weimer, 1993, 2003; Weimer et al., 1986; Weimer, 1996) and understanding this background is the first step to understanding the petroleum system of the Wishbone section study area. The production of eleven horizontal wells in the study area is described in this chapter as well as the data sets available for analysis. Previous research completed by students of the Reservoir Characterization Project (Alfataierge, 2017; Davis, 1985; Dudley, 2015; Grechishnikova, 2017; Ning, 2017; White, 2015) are presented and prove that there exists a direct correlation between fracturing (induced and natural) and productivity of the horizontal wells. Mapping fracture networks in the Niobrara-Codell reservoir is thus prioritized using a 3-D multicomponent, time-lapse seismic survey which acquires all wave modes and cross-component data sets.

Chapter 3 provides an overview of body waves and their propagation in isotropic media. Basic principles regarding the wave propagation kinematics and amplitudes are described and explained using reflectivity modeling. The modeling which is detailed in this chapter is used throughout the thesis and is developed and applied by Simmons (2004, 2009) which uses formulations established in Fryer and Frazer (1984); Kennett (1983). Due to the complexity of wave mode propagation in 3-D acquisition, it is difficult to process the horizontal components in the acquisition coordinate system (Gaiser, 1999; Garotta and Granger, 1988; Martin

and Davis, 1987; Simmons and Backus, 2001). The radial-transverse coordinate system for separation of wave modes is described in Chapter 3 for isotropic media and in Chapter 4, wave propagation and coordinate systems for anisotropic media is discussed.

An HTI medium is used as a simple model to describe a reservoir with a single set of vertical fractures imposed on an isotropic background. Shear wave propagation along the symmetry planes of an HTI medium is well documented (Ruger, 2002; Thomsen, 1988; Tsvankin, 2012) and reviewed in Chapter 4. Waves polarize into orthogonal directions of particle motion associated with fast and slow velocities. With the goal of separating the fast and slow waves, a fast-slow coordinate system was developed. As demonstrated in this chapter, this coordinate system inappropriately mixes the shear wave modes and is not suitable for processing. The radial-transverse system is preferable regardless of anisotropic conditions in the reservoir or overburden and these observations are evidenced by complex reflectivity modeling.

In Chapter 5, modeling specific to the Niobrara stratigraphy is explored. Azimuthal information of seismic data can suggest a dominant fracture orientation in an HTI medium and the travel time difference between the fast and slow arrivals can indicate fracture density. Limited azimuth stacks (LAS) and common offset, common azimuth (COCA) gathers are built for all nine synthetic components generated from the Niobrara modeling. The complementary interpretation of all wave modes stem from the orthogonality of their particle motion as described in Chapters 3 and 4. In this chapter, the added value of interpretation using all components is demonstrated and emphasized in a resolution feasibility study. When the fractured interval thins, the far offset data on all components and in particular the horizontal components, maintain the best resolution of VVAz effects.

Although the expected VVAz response is small based on Niobrara modeling, the complementary interpretation of all nine components holds true, with the pure shear wave components having the strongest response to velocity anisotropy. In Chapter 6, the multicomponent, time-lapse survey over the Wishbone study area is analyzed for HTI-related VVAz

effects using LAS and COCA displays. Comparison of all components across the survey area, as well as between the time-lapse acquisitions, do not show HTI-related VVAz effects or intuitive interpretations with respect to the spatial locations or time-lapse changes.

Chapters 5 and 6 elaborate on the constrained and derisked interpretation using all nine components as opposed to a single component analysis. In Chapter 7, a review of inversion techniques for fast azimuth and shear wave splitting estimations (Gaiser, 1999; Simmons, 2009) is presented and discussion is focused around the joint interpretation and inversion of the multicomponent data sets for a single solution. All wave modes demonstrate unique VVAz responses to the same earth conditions and should thus be telling the same story in interpretation.

Chapter 8 summarizes key findings and contribution of the research to both academic and exploration geophysicists. While complex modeling with overburden anisotropy and faulting can provide insight into field observations presented in Chapter 5, a supplementary study would include how best to interpret this data or layer strip to expose reservoir conditions. Additionally, amplitude variation with azimuth (AVAz) responses can provide higher resolution interpretation and the reflectivity method and feasibility studies presented in this research can be extrapolated to amplitude studies.

CHAPTER 2

WATTENBERG FIELD AND NIOBRARA RESERVOIR GEOLOGIC BACKGROUND

The Wattenberg Field spans 3,200 square-miles (Matuszczak, 1973) and is located approximately 35 miles north-east of Denver, Colorado in the Denver Basin. The field was discovered in 1970 and covers 1.9 million acres in northeast Colorado. The Denver Basin is an asymmetric basin with a steeply dipping west flank bounded by the Front Range and a gently dipping east flank (Philip and Santus, 2011). The basin spans Eastern Colorado, Southeastern Wyoming and southwestern Nebraska (Higley and Cox, 2007) as shown in Figure 2.1. The field contains approximately 13,000 ft of stratigraphic section with its thickest deposits trending along the north-south axis of the basin (Weimer, 1996). The Wattenberg Field straddles the basin axis as shown in Figure 2.2 (Matuszczak, 1973) and hosts the more productive areas of the Niobrara and Codell reservoirs in the Denver Basin. The Codell and Niobrara are Upper Cretaceous aged formations deposited in the Western Interior Seaway during a time of major marine transgression.

2.1 Origin of the Codell Formation

The Lower Codell sandstone was deposited as marine-shelf shaly-sands and marine sand bars during a sea-level rise. Following subsequent deposition events of the Sage Break Shales and Upper Codell, a sea level fall triggered an erosional event along the north-east trending Transcontinental arch. This left the Lower Codell unconformably overlain by the Fort Hayes member of the Niobrara Formation as shown in the stratigraphic column in Figure 2.3 (Weimer et al., 1986). According to Weimer et al. (1986), while the erosion primarily removed the porous and permeable sands of the marine bars, remnants of this facies remain the best exploration targets in the Codell in present day exploration. The Codell Formation varies in thickness from 10 to 20 feet (Weimer, 1996).

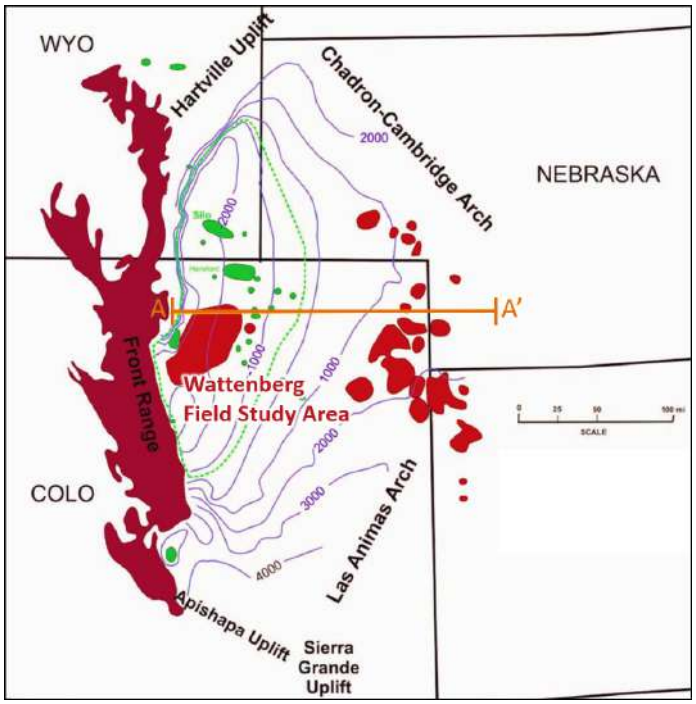

Figure 2.1: Structure map at the top of the Niobrara formation, Denver Basin with 1000 feet depth contour interval. The Denver Basin spans north-eastern Colorado, south-western Wyoming and south-western Nebraska. The black lines highlight the state boundaries. Gas fields are colored red with the Wattenberg Field (study area) being the largest. Oil fields are colored green. The dashed green perimeter indicates the extent of mature source rock (Modified from Sonnenberg (2011))

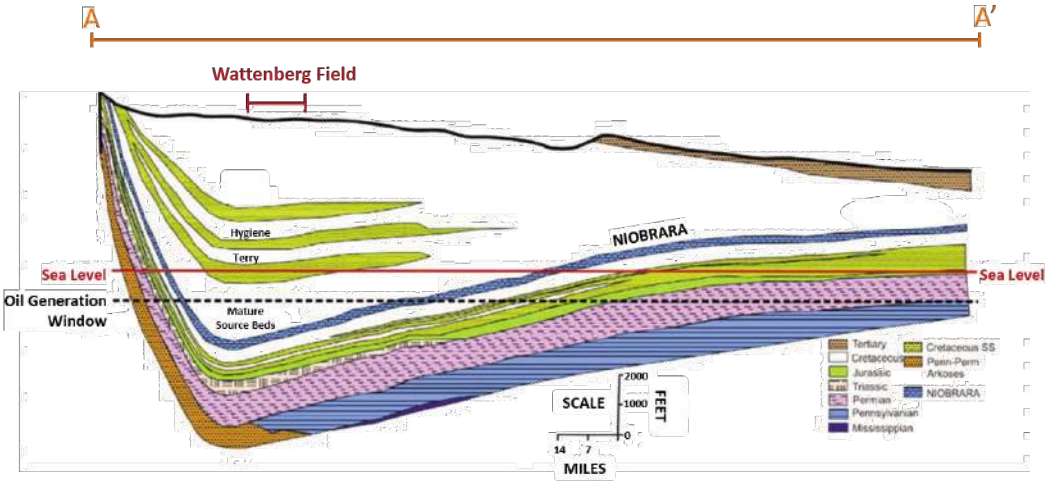

Figure 2.2: Cross section of the Denver Basin from West to East (A to A' on Figure 2.1). (Modified from Sonnenberg (2011))

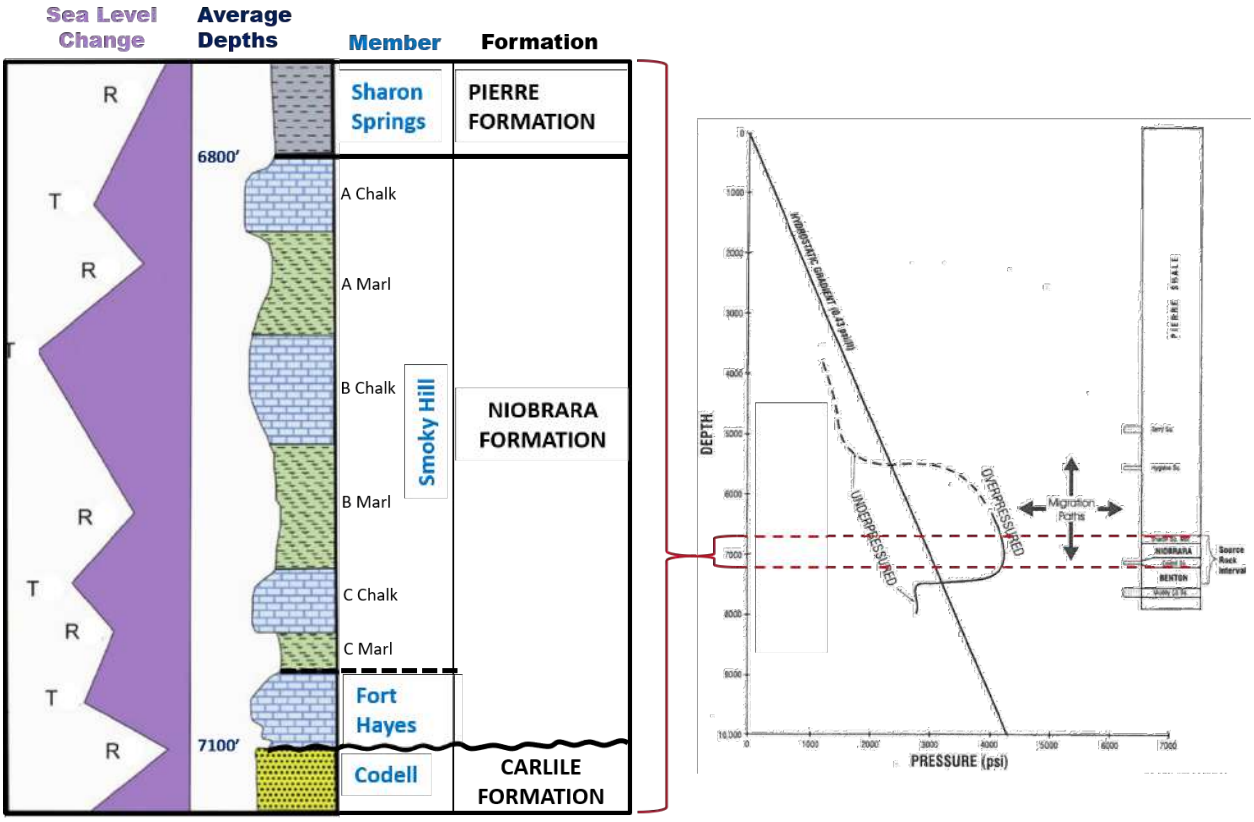

Figure 2.3: The left schematic shows the average stratigraphy of the Niobrara-Codell interval in the Wattenberg Field relative to the purple chart which shows sea level changes associated with the lithofacies deposits in the right column over. The right graph is a formation pressure plot based on measurements from 28 wells in the Wattenberg Field showing the overpressuring in the Niobrara-Codell interval. (Modified from Sonnenberg (2011) and Weimer (1996))

2.2 Origin of the Niobrara Formation

The Niobrara formation is comprised of the Fort Hayes and Smoky Hill members. The Fort Hayes Limestone member was deposited during a third order transgression and smaller cycles of sea level changes resulted in the interbedded deposition of chalks and marls of the Smoky Hill member. The carbonate-rich chalk intervals were deposited during fourth-order transgressions in the presence of well oxygenated deep waters with warm Gulf currents (Lachance and Robinson, 2012). The organic rich marls were deposited during fourth order marine regressions with anoxic shallow water conditions and colder currents. These chalk-

marl sequences are described as A, B and C Niobrara benches (Figure 2.3). In some areas there is a D bench, but in areas such as the Wattenberg Field, the D bench is absent. The Niobrara formation, in the Wattenberg Field, varies in thickness from 200 to 400 feet with each bench ranging between 30 to 50 feet. On the western edge of the Niobrara deposition, outside of the Denver basin, the formation can thicken to as much as 1,500 feet (Lachance and Robinson, 2012). A major marine regression ended the Niobrara formation with the deposition of the Sharon Springs Member of the Pierre Formation.

2.3 Niobrara-Codell Petroleum System

High productivity in the Wattenberg field is generally associated with its location above a high temperature anomaly in the subsurface. This geothermal hot spot sits at the intersection of the Colorado mineral belt and the Denver Basin. The major wrench faults in the basin trending north-east are zones of weakness facilitating heat flow through the productive formations (Weimer, 1996). As such, although hydrocarbon generation in the Denver Basin began in the late Cretaceous at the deposition of the Mowry, Huntsman, Graneros and Carlile formations, the heat anomaly allowed for the shallow maturation of the Niobrara-Codell source rocks and the Sharon Springs.

According to Weimer (1996), this hot spot caused overpressuring in the Niobrara Formation and in the base of the overlying Pierre Formation (shown in the pressure plot of Figure 2.3). The overpressured Niobrara-Codell interval is capped by the underpressured Terry-Hygiene of the Pierre Formation and bounded below by the underpressured J Sand. Oil and gas is generated in the high pressured cells and migrates outward to lower pressured formations. However, in productive Niobrara-Codell areas, there are observed vertical seals which contain the pressured unit and thus trap hydrocarbons within the source bed. Although the exact nature of the seals are still uncertain Weimer (1996) suggests it may be an artifact of source rock diagenesis or bentonites in the shales. Lateral seals may also be caused by diagenesis however, in the Wattenberg Field, complex faulting and fracture systems are key players in the entrapment of the Niobrara-Codell source rock plays.

The diagenetic process also acted to reduce the porosities in the Niobrara to less than 10% in areas where the rock is both thermally mature and productive. Kerogen in the Niobrara is Type II (oil-prone) with total organic content ranging from 0.5 to 8 wt % and low permeability of .1 mD (Sonnenberg, 2011). Sonnenberg further emphasizes the importance of fracture efficiency for reservoir performance given the low matrix permeability and small pore throat sizes (less than a few tenths of a micron). In general, the Niobrara chalks have higher permeability than the marls, with the B and C chalks in the Wattenberg Field being the best targets due to the higher permeabilities (White, 2015).

The Codell sandstone is a low porosity (4-12%) and low permeability ($<$ .1 mD) tight oil reservoir, similar to the Niobrara chalks (Stamer, 2016). Higher clay content in the Codell may be a contributing factor to the low permeability but it also causes the low resistivity response. Similar to the Niobrara, the Codell is a combination play with structural and stratigraphic compartmentalization and pressure anomalies all contributing to productivity. In particular, structural compartmentalization caused by faulting and fracturing is key to well success in the RCP study area. The next section introduces this area and discusses some key conclusions, based on previous research, regarding the factors driving production.

2.4 Wishbone Section Study Area and Project Data

The RCP study area is a 1 square-mile section called Wishbone located in the south western area of the Wattenberg Field (Figure 2.4). Eleven horizontal wells were drilled into the Wishbone section with 7 wells targeting the Niobrara and 4 targeting the Codell. Data sets available for the evaluation of these 11 wells include core from five vertical wells around the Wishbone section, FMI logs for some vertical and lateral wells, electric logs including gamma ray, resistivity, neutron porosity, and density logs, synthetic sonic logs and seismic surveys. The surveys include a 50 square-mile merged 3D P-wave, an 11 square-mile 3-C, 3-D survey and a 4 square-mile 9-C time-lapse survey called Turkey Shoot (Figure 2.4).

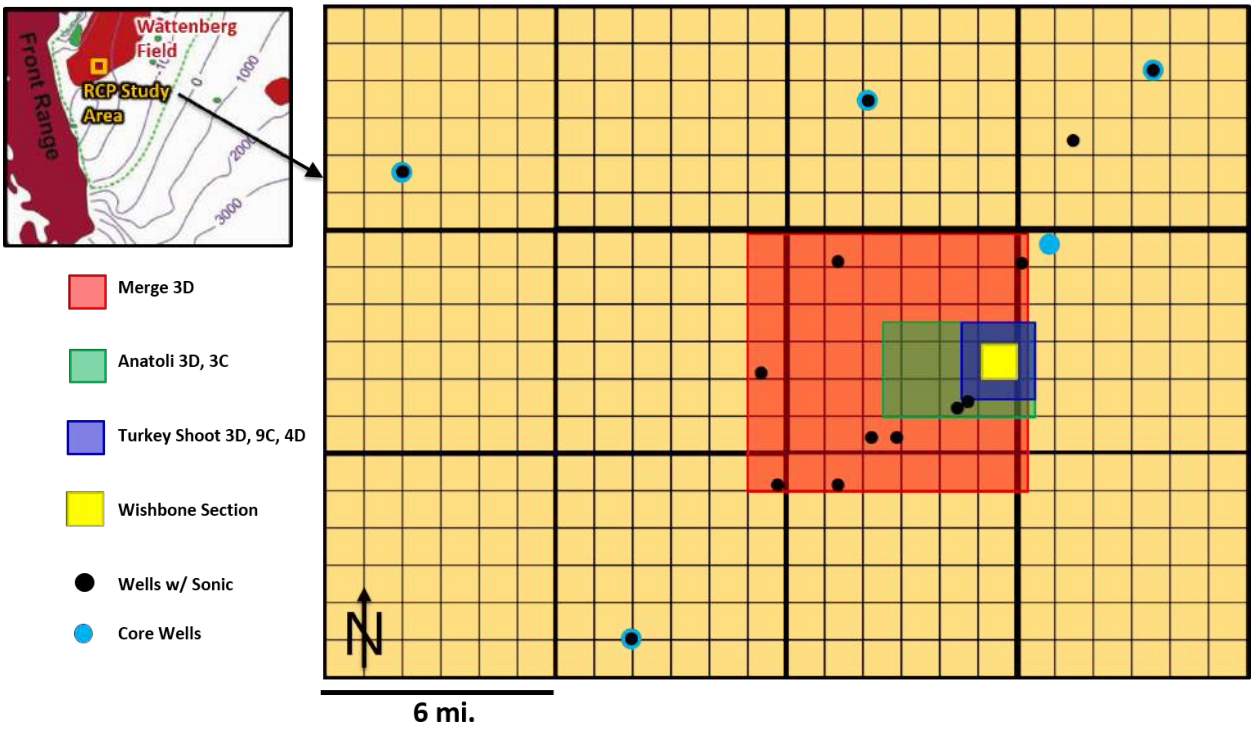

Figure 2.4: RCP study area relative to available seismic surveys and neighboring wells.

The 9C Turkey Shoot was designed so that the Wishbone section has maximum fold for the P-wave data and that acquisition was repeatable for 4D interpretation. Figure 2.5 shows the location of the 11 horizontal wells with respect to the Turkey Shoot survey. While the Niobrara wells (except 11N) primarily target the C chalk, the 4,000 foot laterals are tortuous and vary in and out of the target bench according to geosteering reports.

The wells were drilled in June 2013 and completed in August 2013 starting from the east and moving west. The first Turkey Shoot Monitor survey was shot after completion of the 11 wells and the second was shot after two years of production. Table 2.1 describes the acquisition of the Turkey Shoot multicomponent surveys and surface microseismic with respect to the drilling, completion and production of the 11 horizontal wells.

The Wishbone section was initially developed to test and evaluate optimal well spacing and completion techniques for improved production. As a result, three wells to the west (7N, 8C and 9N) were zipper fracked (fracked in sequence such that while one well is holding

fracutre pressure, the other is being fracked), the well spacing ranges from 1200 feet for the eastern wells to tighter spacing of 600 feet for the western wells and the number of stages per wells also varied from 32 to 20 stages from the east wells to the west wells. Fluid and proppant volume were also varied with the completion of the 11 wells as shown in Table 2.2.

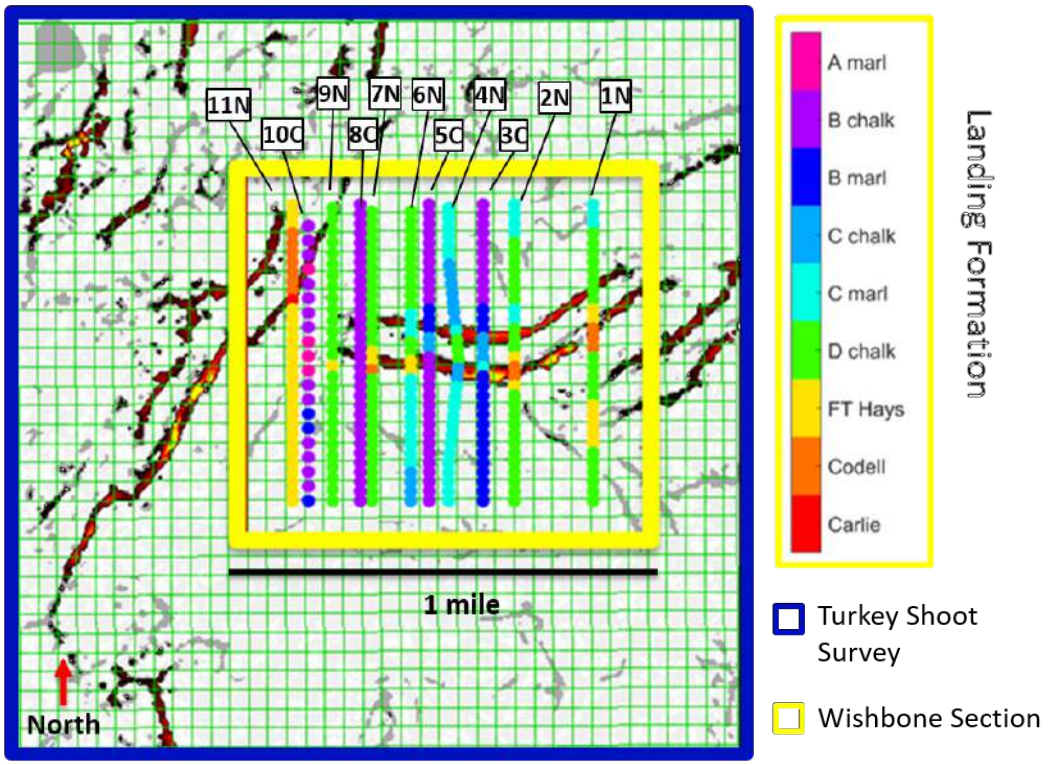

Figure 2.5: The Wishbone section centered in the 4D, 9C Turkey Shoot survey area. The wells are labeled 11 to 1 from West to East with the N and C indicating whether the target formation for that well was Niobrara or Codell. Each stage of the 11 wells shown are colored by the landing formation and the background fault map is interpreted at the top of the Niobrara from P-wave data.

Table 2.1: Timeline for the Phase XVI Wattenberg Project

Wishbone Section Drilled	May 2013	11 Horizontal Wells
Turkey Shoot 9C Baseline	June 2013	4 sq. mi. coverage
Wishbone Well Completion	August 2013	Fracked East to West
FracStar Surface Microseismic	August 2013	12.25 sq. mi. coverage
Turkey Shoot 9C Monitor 1 Recorded	October 2013	4 sq. mi. coverage
Turkey Shoot 9C Monitor 2 Recorded	January 2016	4 sq. mi. coverage

Table 2.2: Summary of Well Completions for the Wishbone section

Well	Stimulation	Flowback	Stages	Fluid Injected (Ratio of Well to Average)	Proppant Injected (Ratio of Well to Average)
1N	Day 1	Day 12	32	0.87	0.88
2N	Day 3	Day 15	32	0.87	0.88
3C	Day 5	Day 15	32	0.98	0.88
4N	Day 8	Day 21	32	0.91	0.88
5C	Day 10	Day 22	32	0.93	0.92
6N	Day 13	Day 21	32	0.92	0.97
7N	Day 14	Day 33	32	0.96	0.92
8C	Day 14	Day 34	32	0.97	0.92
9N	Day 14	Day 30	27	1.03	0.85
10C	Day 22	Day 45	20	0.81	0.92
11N	Day 23	Day 45	32	1.75	2.01

Wishbone production data has been acquired for 1450 days. Normalizing completion data (study by RCP Student, Erdinc Eker), we observe a 37% difference in BOE production between the lowest (4N) and highest producer (9N) in the Niobrara, and a 26% difference in BOE (barrels of oil equivalent) production between the lowest (8C) and highest (10C) Codell producer (Figure 2.6).

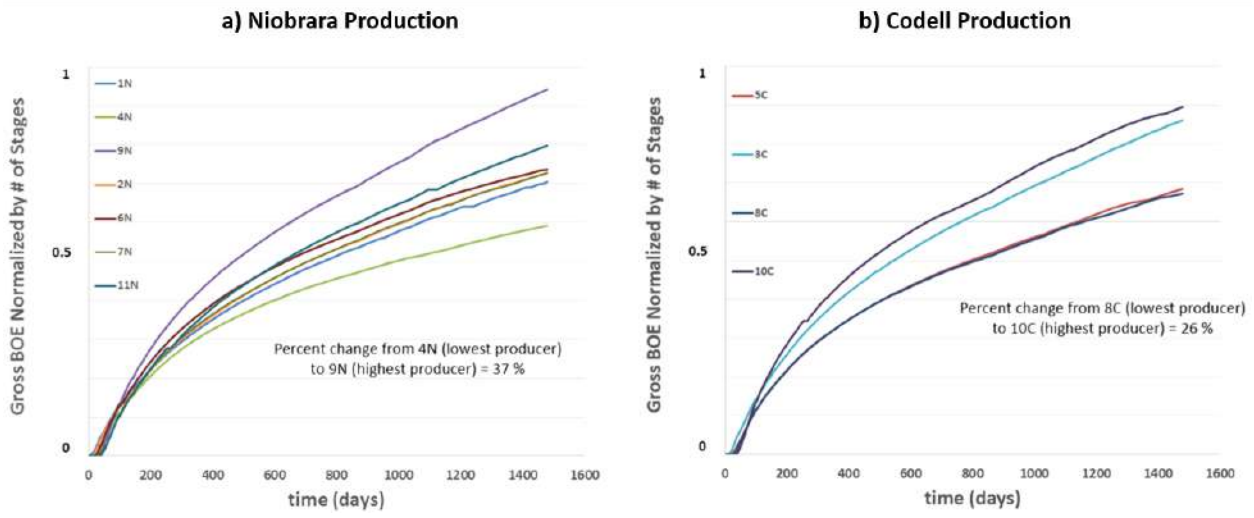

Figure 2.6: Gross BOE produced from a) Niobrara wells and b) Codell wells after normalizing by number of stages (study by RCP Student, Erdinc Eker).

The Wattenberg team has built a comprehensive geologic model with structure and stratigraphy following that of the Wishbone section. History matching reservoir simulations to early production numbers has validated our understanding of the baseline state of the reservoir, however, in these later years of production, it becomes increasingly important to understand the changing role of fracturing and faulting on production.

2.4.1 The role of Fracturing and Faulting on Production in the Wishbone section

Resistivity anomalies in the Niobrara chalks of the analogous Silo Field of the Denver Basin map to highly fractured intervals (Sonnenberg and Weimer, 1993). This correlation is possibly due to fractures being filled with oil, or partially cemented with calcite, and also mentions the correlation of these anomalies to more productive areas of Silo Field. While resistivity logs may aid in mapping hydrocarbon filled fractures, mapping the density and orientation of these fractures are equally as important in understanding the economic potential of a well.

Listric normal faults are prevalent in the Cretaceous aged interval of the Wattenberg Field. Davis (1985) identifies three major stratigraphic intervals where such faulting is observed - the Upper Pierre, Terry/Hygiene formation of the Lower Pierre and the Niobrara-Carlile-Greenhorn interval. He suggests that this Cretaceous faulting is associated with the recurrent movement of near-vertical deep seated wrench faults. The axis of the wrench fault zones trend along the paleo, maximum horizontal stress orientation (NE-SW) with secondary synthetic and antithetic faults occurring between the zones and facilitating the compartmentalization of the Cretaceous aged reservoirs (Weimer, 1996).

At the Niobrara interval in the Wishbone section, the horizontal wells, drilled north-south, cross an east-west trending graben (Figure 2.5) with a 150 foot throw. A second fault trends north-east to south-west on the north-western side of the Wishbone section and follows the paleo, maximum horizontal stress orientation. Similar to analogous fields as discussed by Davis (1985), faulting orientation and patterns in the Wishbone section strongly differ

between the major stratigraphic intervals. Figure 2.7 highlights a few faults on a seismic section extracted from the Turkey Shoot Baseline survey. At the bottom of this section on Figure 2.7, horizon maps extracted at the Terry/Hygiene and Niobrara intervals show the changing fault orientations and densities throughout the vertical section.

Reactivation of the basement faults and subsequent listric normal faults over time has led to the formation of the extensive fracture networks observed in the Niobrara-Codell interval. Dudley (2015) suggests that the present day maximum stress direction is averaging NW-SE (N70W or 110 degrees clockwise from North) based on image log interpretations of three horizontal wells in the Wishbone section (Figure 2.8).

The interpretation made by Grechishnikova (2017) based on outcrop and image logs suggests four fracture orientations in the Wishbone Section of the Wattenberg Field. Figure 2.9 shows the two stereonets describing the observed four fracture sets. The position of the dots indicate the dip orientation and their proximity to the center indicates the dip angle (horizontal at the center or vertical at the outer edge of the stereonet). The bars represent the strike of the same dotted events. These plots have not been normalized and as a result, the size of the bars simply represents the number of measurements taken for that fracture set.

The first two sets are joint fracture sets with the J1 set orientation having an average strike of 269° (red cluster) and dip of 83° and the J2 set (green cluster) having an average strike of 180° (almost parallel to the well bore orientations) and dip of 81°. Due to the parallel orientation of the J2 fracture set to the wellbores, this fracture set is not commonly observed in the image logs, but very prevalent in the outcrops.

Grechishnikova (2017) interprets small faults with little to no displacement or lithological change across the faults as shear fractures. The S3 trend varies between 125° and 155° in strike orientation with an average dip of 50°. The S4 trend varies between 216° to 240° strike and varies between 56° to 78° in dip.

Microseismic data show two major fracture trends post-completion. The first fracture set is oriented N70W and is aligned to the present day maximum horizontal stress direction. This orientation correlates to the image log interpretations of the three Wishbone wells (Dudley, 2015). The second fracture set mapped from mircoseismic is oriented N50E and roughly correlates to the S4 set observed in outcrop and seismic studies (Grechishnikova, 2017).

Work done by Grechishnikova (2017) also identifies throughgoing and lithofacies-bound fractures in the Niobrara based on image logs of two horizontal wells penetrating the chalk and marl beds. The lithologically-bound fractures are more common in the chalk intervals making up over half (54%) of the identified fractures which, based on the classification by Dudley (2015), means that most fractures in the Niobrara are partially sealed to sealed. In marls lithologically-bound fractures occur in 25% of the sampled fracture population (Grechishnikova, 2017). Most other fractures identified were throughgoing fractures which interconnect the benches of the Niobrara Formation (Figure 2.10) and potentially contribute to vertical hydraulic connectivity within the formation. In both chalks and marls, fracture density increases with proximity to faults as shown in Figure 2.10. This potentially means that the best 'sweet spots' are within the chalk benches around the fault zones.

The Anadarko Petroleum Company has tasked the RCP with better understanding the main drivers of Wishbone well production in order to improve well placement, field development and overall play success. The complex faulting and fracturing in the Wishbone section are proven drivers of production as such the question posed is: Can seismic data be used to predict the influence of fracturing and faulting on production so as to reduce risk in field development?

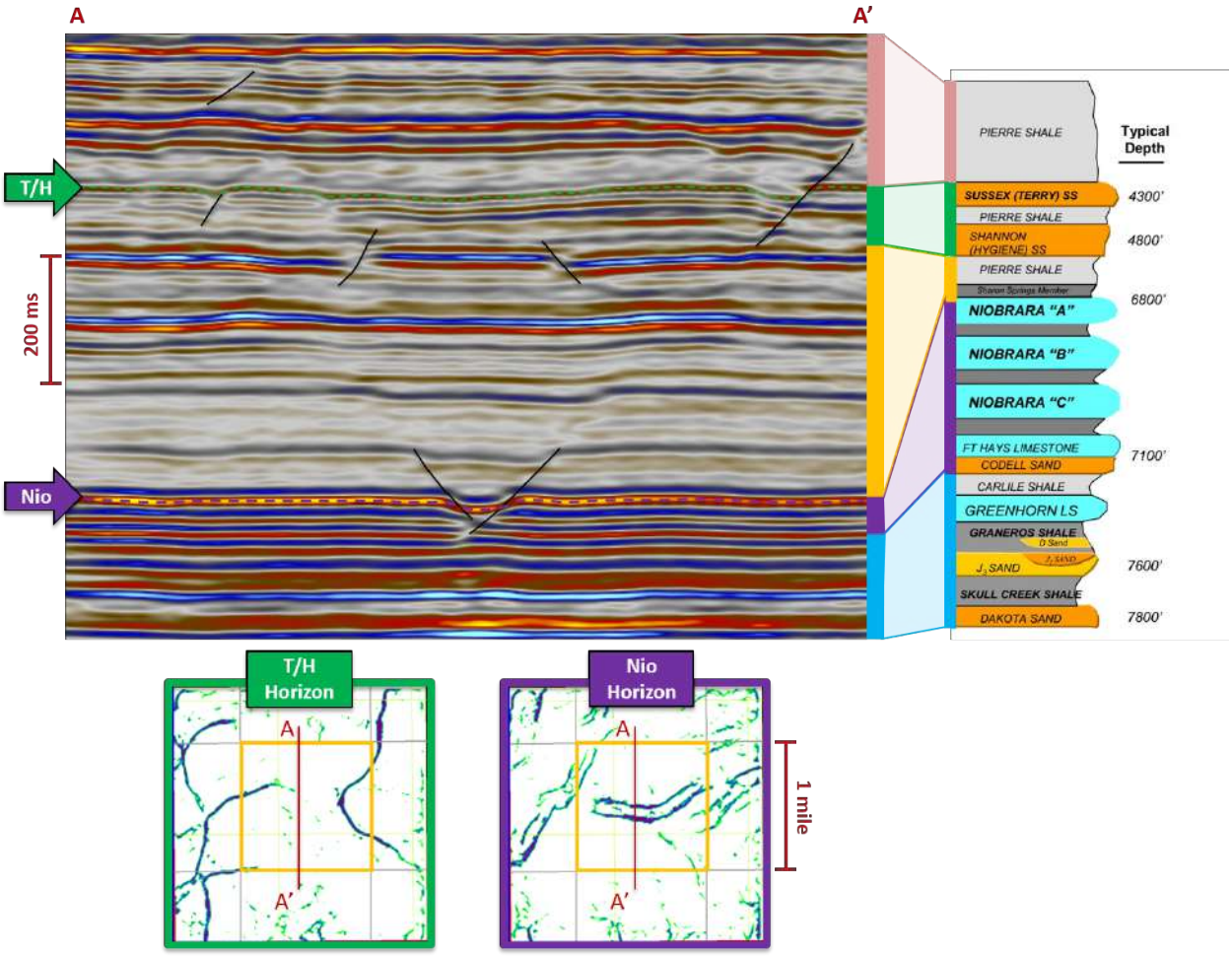

Figure 2.7: A 1 mile seismic profile across the Wishbone section highlighting the unique faulting and fracturing throughout the stratigraphic section as documented by Sonnenberg (2011). The section is extracted from the migrated P-wave stack of the Turkey Shoot Baseline Survey. The colored bars on the right of the seismic section correlate to the colored bars on the stratigraphic column for ease of identifying the formations on the seismic profile. Two time horizon maps at the base of the section show the changing fault azimuths at different depths in the Wishbone section.

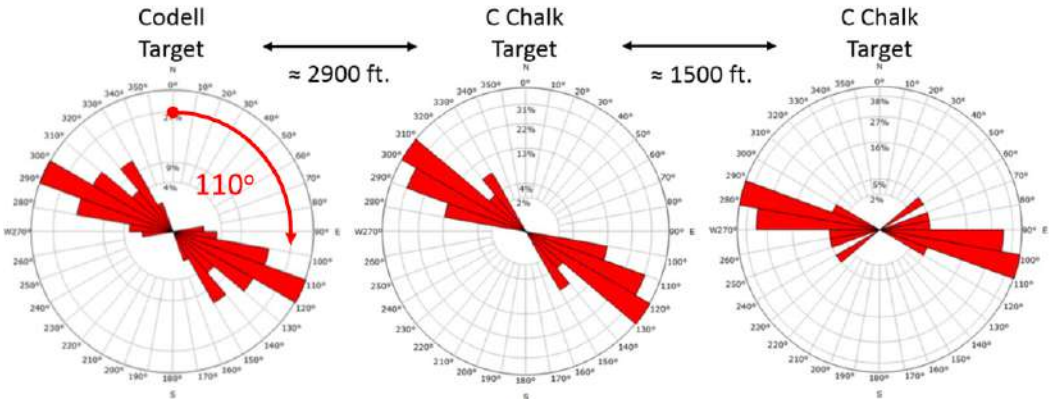

Figure 2.8: Maximum horizontal stress direction approximating N70W based on image log interpretation of three N-S oriented wells. The wells from right to left are the 2N, 6N and 101C. Wells 2N and 6N are located in the Wishbone section and separated by 1500ft as shown in Figure 2.5. Well 101C is located just outside the Wishbone section, 2900ft to the west of well 6N. (Modified from Dudley (2015))

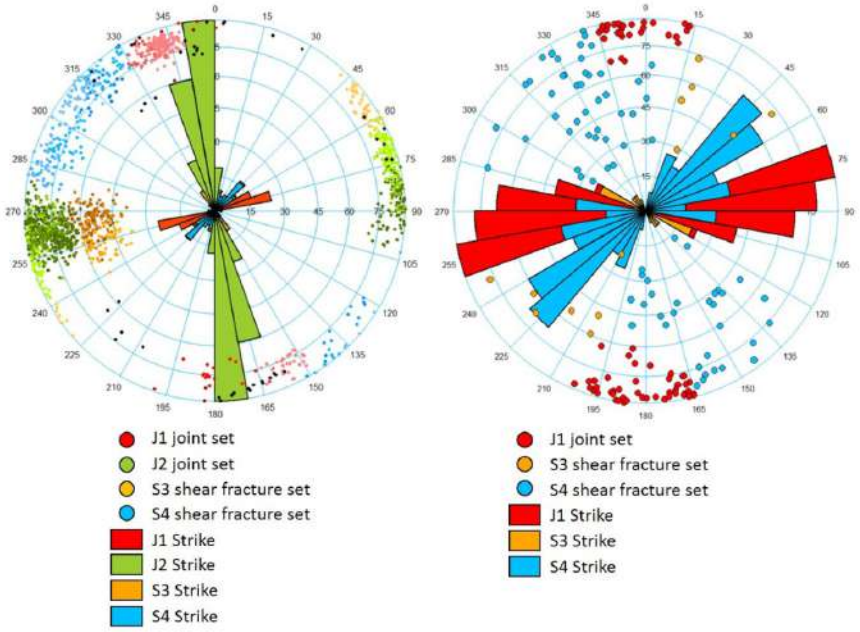

Figure 2.9: Stereonets showing outcrop fracture data (left) and subsurface fracture data (right) (Grechishnikova, 2017). Strike orientations for four fracture sets are represented by colored bars and the dips of the fracture sets are represented by the dots. Note that the outcrop stereoenet is biased by the number of measurements made for each fracture set and the subsurface stereonet is biased against the J2 set due to the N-S orientation of the wellbore.

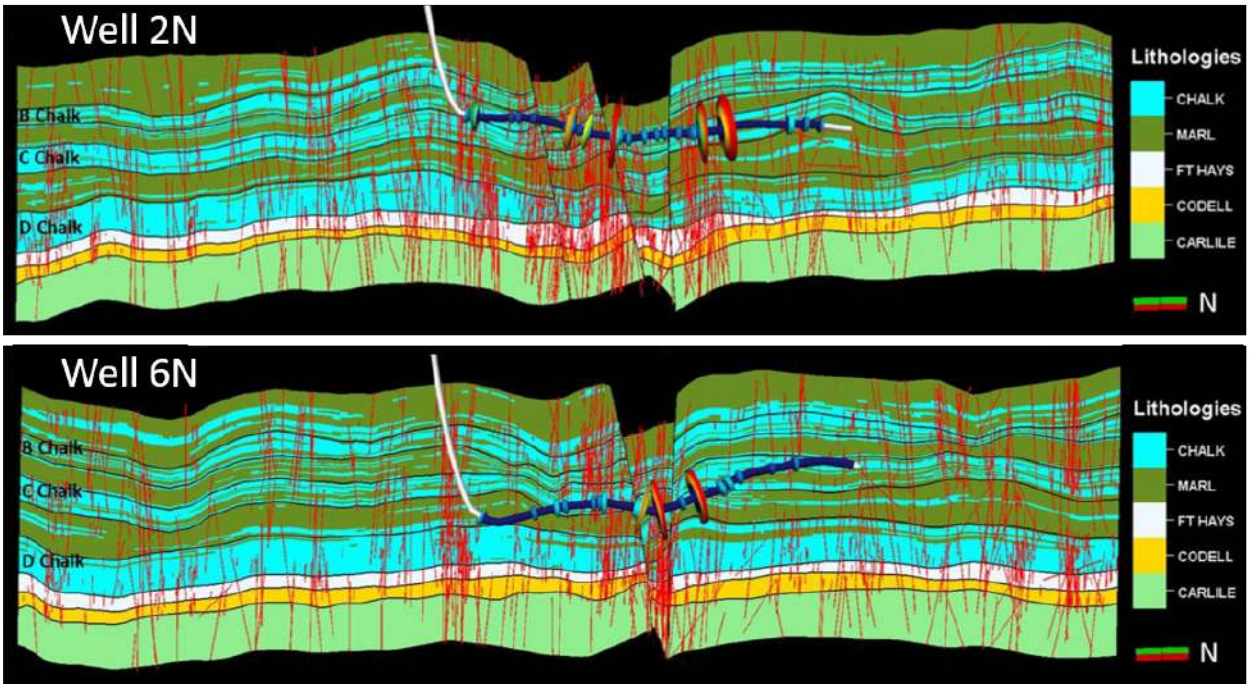

Figure 2.10: Cross-sections of the discrete fracture model for the Wishbone section showing the increased fracture intensities nearer faulted zones (Grechishnikova, 2017) for two well trajectories.

CHAPTER 3

SHEAR-WAVES IN ISOTROPIC MEDIA: PARTICLE MOTION AND COORDINATE SYSTEMS

3.1 Introduction and Motivation

Three-dimensional (3-D) nine-component (9-C) seismic surveys record data on three-component (3-C) geophones (Rz, Rx, and Ry) generated by vertical (Sz), and orthogonal horizontal (Sx and Sy), point-force sources (a vertical vibrator and orthogonal horizontal vibrators). The shear-wave (S-wave) data are taken from the horizontal sources and horizontal receivers as SxRx, SxRy, SyRx and SyRy. The compressional-wave (P-wave) data are taken from SzRz, and the converted wave (C-wave) taken from SzRx and SzRy. A main goal of 3-D 9-C surveys is to detect, expose, and characterize subsurface fractures (either natural or induced by hydraulic fracturing).

Early 3-D 9-C projects processed the shear wave components in field X-Y (or acquisition) coordinates (Garotta and Granger, 1988; Lewis et al., 1991; Martin and Davis, 1987), or fast-slow (F-S) coordinates (DeVault et al., 2002; Grechka and Vasconcelos, 2007; Shuck, 1993; Terrell, 2004). An assumed regional stress direction would be used to transform (rotate) the four shear-wave components from X-Y into F-S coordinates and preprocessing and imaging occurred in F-S coordinates. Post-stack analysis/interpretation generally used Alford Rotation (Alford, 1986), with the implicit assumption of HTI media, to attempt to estimate variations in fracturing (lateral and vertical). Interpretive products would include maps of the azimuthal orientation of the fast shear wave, and the amount of shear wave splitting.

Note that the Alford Rotation is strictly based on normal-incidence shear wave data. At normal incidence, the orthogonally polarized shear waves are simply SH-waves polarized in orthogonal directions. A classic example of SH-waves in 2-D and shear-wave splitting is that of Lynn and Thomsen (1990).

At non-normal incidence, the distinctions between SH-waves and SV-waves become important, even in a 1-D (varies in depth) flat layered, homogeneous, isotropic media. SV-waves and P-waves are coupled, whereas SH-waves behave similarly to P-waves in acoustic media.

In 3-D, the effect of variable source-receiver azimuth, and the fact that the horizontal-force sources are polarized (azimuthally dependent) complicates shear-wave processing and analysis in field, and/or F-S coordinates. P-waves, SV-waves, and SH-waves become mixed on all four of the prestack shear wave components. Converted waves produced by the vertical-force source are similarly mixed in 3-D due to the variable source-receiver azimuth. The vertical-force source is azimuthally independent (the same for all source-receiver azimuths).

Converted-waves are commonly treated in radial-transverse (R-T) coordinates as shown by Gaiser (1999). R-T coordinates remove the effect of source-receiver azimuth, and focus converted wave reflections onto the radial component in flat-layered, homogeneous, isotropic and/or VTI media with the transverse component equal to zero. In the presence of HTI media which polarize the upgoing shear waves, the transverse component is non-zero, and is commonly used as the indicator of shear wave splitting.

The use of R-T coordinates for shear waves in 3-D was demonstrated on two field datasets by Simmons and Backus (2001). R-T coordinates, to first order, separates SV (and P) waves from SH-waves, and greatly simplifies data processing and analysis. The cross-terms, similar to that of the transverse component for converted waves, are now a direct indicator of shear wave splitting. A virtue of Simmons and Backus (2001) is that they used field data, but they lacked suitable prestack modeling capability at the time to clearly, and convincingly, demonstrate the concepts/implications involved in treating prestack shear wave data in field, fast-slow, and radial-transverse coordinates.

I begin by showing 9-C prestack synthetic data in 2-D and illustrate the concepts of particle motion versus propagation direction for P-waves, SV-waves, and SH-waves in flat layered, homogeneous, isotropic media. The 2-D synthetics show the differences between SV-waves and SH-waves, along with the azimuthal dependence of the horizontal point-force

source radiation patterns. In 3-D, the wave-mode mixing attributed to variable source-receiver azimuth and the horizontal-force source directivity is clearly illustrated in field coordinates. Rotation from field to R-T coordinates separates the shear waves into SV-waves and SH-waves, produces cross-terms that are equal to zero (since the model is flat layered and isotropic), and supports the arguments of Simmons and Backus (2001).

Note that I compare F-S and R-T coordinates using prestack synthetics generated with simple and complex HTI models in Chapter 4.

3.2 Prestack Multicomponent Reflectivity Modeling

The earth model consists of horizontal, homogeneous layers, where any or all layers may be generally anisotropic. In this thesis, a single set of vertical fractures is used as the source of anisotropy. Three-component geophones are equally spaced in X and Y at a constant depth over a square grid. Vertical and orthogonal horizontal point-force sources are located at the center of the grid (Figure 3.1). The horizontal point-force sources are directed in the X and Y directions (Sx and Sy), as are the horizontal geophones (Rx and Ry), with the vertical source and vertical receiver denoted as Sz and Rz, respectively.

Plane waves are propagated through the layered model for all temporal frequencies, and horizontal wavenumbers in the X and Y directions. Negative wavenumbers are needed to properly model source-receiver azimuthal effects, the point-force source directivity, and to generate the seismic response in anisotropic media (Fryer and Frazer, 1984, 1987). Kennett's recursion relations (Kennett, 1983) propagate the reflection-transmission coefficients downward through the layered stack, and calculate the complete plane-wave response. An inverse 3-D Fourier Transform produces 3-C prestack cubes of traces for each source that are equally sampled in time and space.

All wave modes are generated by the reflectivity modeling; primary reflections (P-P, SV-SV, SH-SH), converted waves (P-SV, SV-P), head waves (refractions), interbed multiples, as well as surface multiples and surface waves depending on whether free-surface effects are included. Free-surface effects are not included in any of the model simulations shown in this

thesis.

The prestack cubes show the data recorded using a 3-D acquisition geometry although the earth model itself is 1-D (layer properties vary only with depth). Applications of this particular code can be found in Simmons (2004, 2009).

3.3 Prestack 9-C Modeling for 2-D Acquisition in Isotropic Media

There are three body waves that propagate through a flat-layered, homogeneous, isotropic earth. The compressional wave (P-wave) has particle motion parallel to the direction of propagation. The shear waves (SV and SH) travel slower, and have particle motion perpendicular to the direction of propagation. SV-waves have particle motion in the horizontal and vertical plane (as do P-waves, in general), while SH-wave particle motion is only in the horizontal plane. P-wave and SV-wave propagation are coupled, whereas SH-waves are independent and propagate as do acoustic P-waves (only SH-waves are produced upon reflection/transmission from an incident SH-wave).

Nine-component seismic data uses 3-C receivers (Rx, Ry and Rz) and 3-C sources (Sx, Sy, and Sz) (Figure 3.1). In this section, I focus on receiver lines A and B as they represent the set up for a 2-D 9-C seismic acquisition. As mentioned earlier, the conventional P-wave dataset is taken as SzRz, converted wave data are taken from SzRx and SzRy, with the shear wave data taken from SxRx, SxRy, SyRx and SyRy. Note that only seven of the nine components are usually analyzed; SxRz, and SyRx are generally discarded.

Prestack synthetics obtained along receiver line A from the isotropic earth model shown in Figure 3.1 are shown in Figure 3.2. The upper row of seismograms in Figure 3.2 show the waves recorded on the three receiver components from a vertical point source (Sz). The SzRz component is considered the P-wave component, although P-waves can also be seen on SzRy component since P-wave particle motion is in the Z-Y plane for receiver line A. Converted wave reflections are predominantly on SzRy, but are also found on SzRz because the SV particle motion is in the Z-Y plane. SV-waves (the direct wave and SV-SV reflections) are also seen on SzRz and SzRy because a vertical-force source generates P-waves and SV-waves.

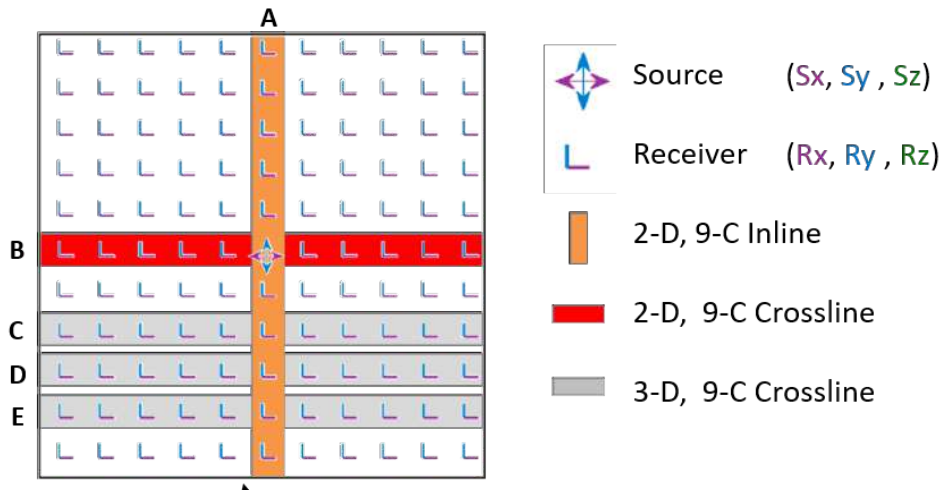

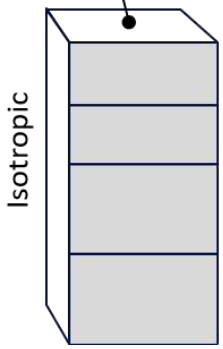

Depth (m)	Vp (m/s)	Vs (m/s)	Density (g/cc)
0	2400	1200	2.37
200	2800	1400	2.51
400	3600	1800	2.58
700	4000	2000	2.54

Figure 3.1: Top: Acquisition geometry for reflectivity modeling. Point-force sources are located at the center of the grid and are oriented in the X, Y, Z directions (Sx, Sy, Sz), with 3-C receivers equally spaced in X and Y (Rx, Ry, Rz). Receiver lines are labeled A - E. Receiver lines A and B are the set up for a 2-D 9-C seismic acquisition where for receiver line A: SyRy = SV, SxRx = SH and for receiver line B: SyRy = SH and SxRx = SV. Bottom: Description of the 1-D isotropic earth model.

Along receiver line A, the Sx source generates an SH-wave. Horizontal particle motion is in the X direction which is orthogonal to the direction of wave propagation. The SH-wave causes displacement in the X direction and is registered on the Rx component. The Sy source generates the SV-wave along receiver line A. The particle motion of this wave is along the direction of wave propagation (Y direction) and is recorded on the Ry component. The converted P-wave from the Sy source (or SV source) is registered on the Rz component.

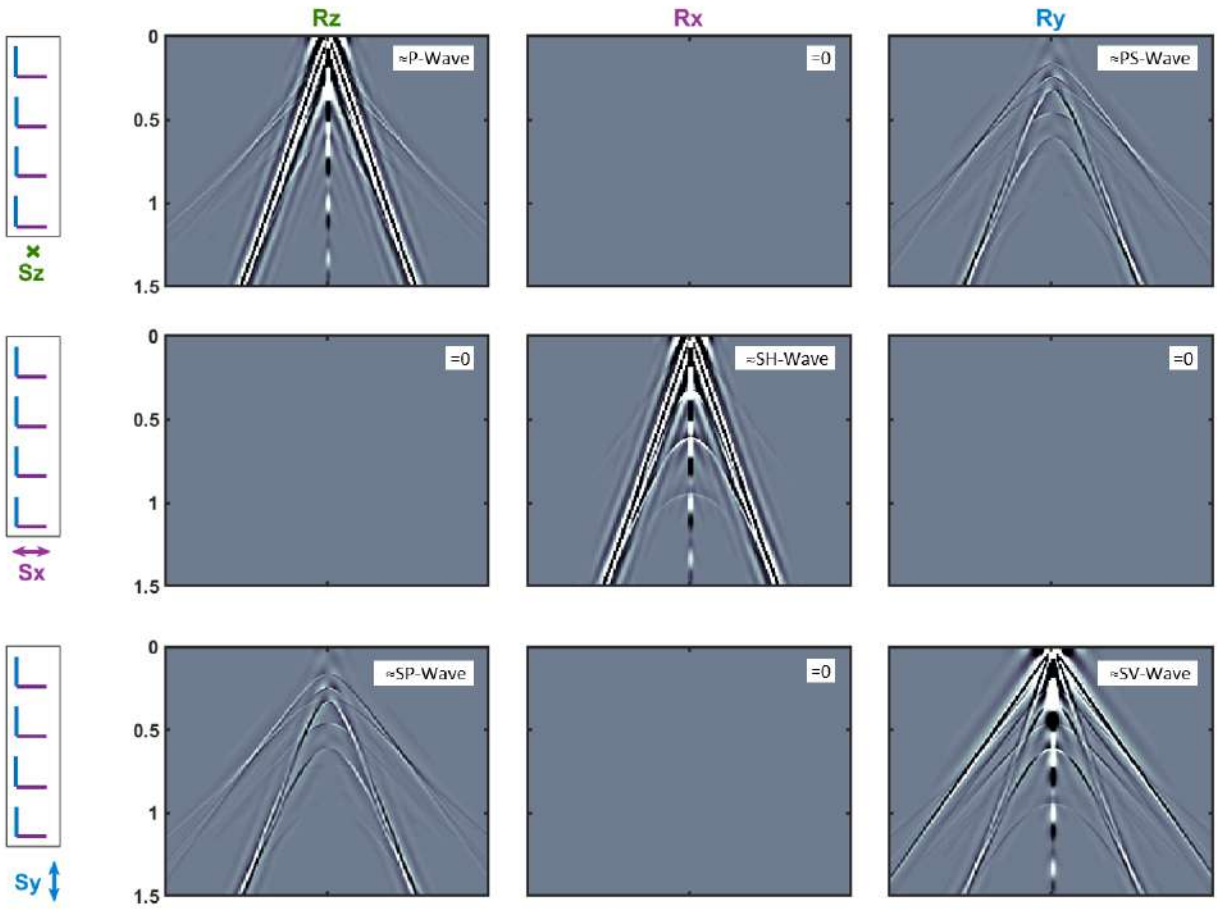

Figure 3.2: Synthetic seismograms along receiver line A. The icons at the left refer to the northern half of receiver line A, with the horizontal receivers and source polarization directions shown. For the receiver line, SzRz = P-wave, SzRy = converted wave, SxRx = SH-wave, and SyRy = SV-wave. As expected, SzRx = SxRz = SxRy = SyRx = 0 for this isotropic model.

The cross-term shear components (SxRy and SyRx) are key data sets used for interpretation of shear wave splitting and fracture analysis as they register split shear waves polarized into the orthogonal plane. The SxRy component (Figure 3.2) for example registers particle motion in the Y direction from a source generating displacement in the X direction. In a flat-layered, isotropic model, the cross-terms are zero.

Data recorded along receiver line B are shown in Figure 3.3. A simple change in the source-receiver azimuth demonstrates the mixing of wave modes amongst the various source-receiver components.

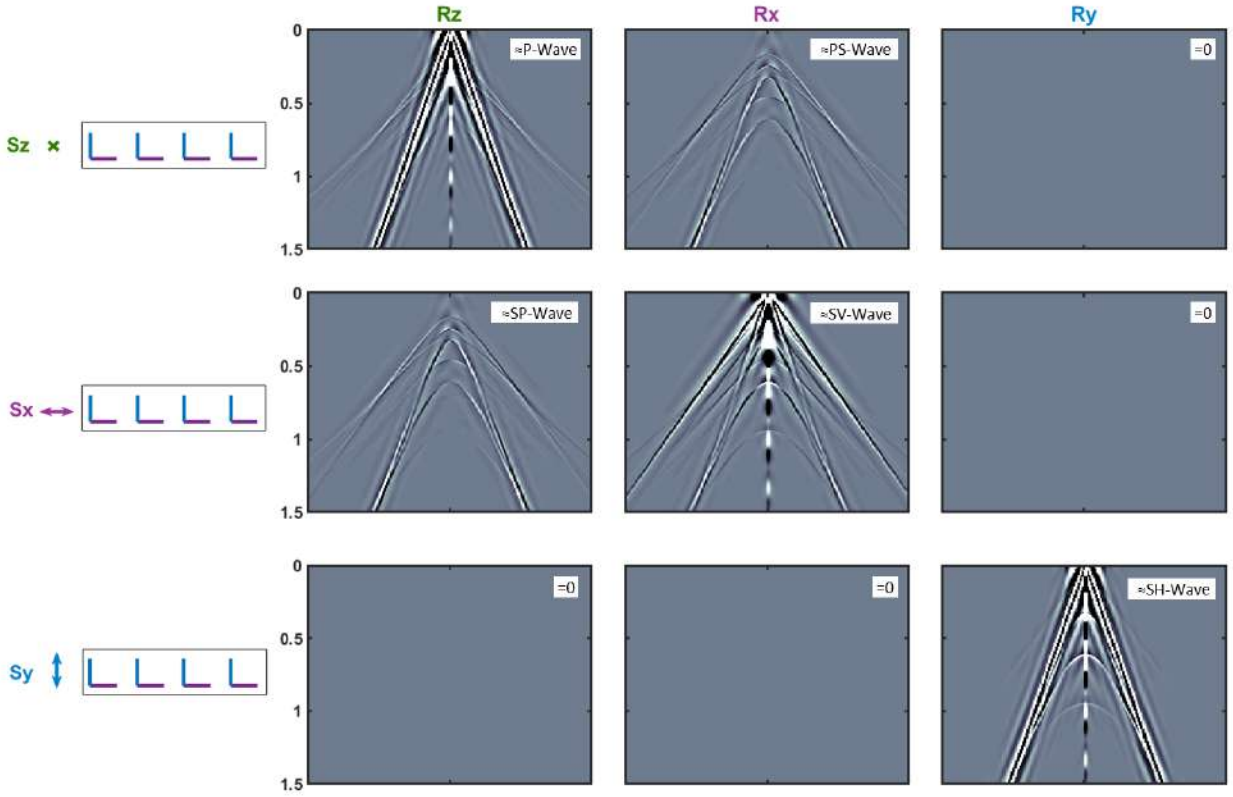

Figure 3.3: Synthetic seismograms obtained for receiver line B; SzRz=PP, SxRx=SV and SyRy=SH along this receiver line as opposed to receiver line A where SxRx=SH and SyRy=SV. As expected, cross-terms (SzRx, SxRy and SyRx) contain no signal for this isotropic model

The P-wave data SzRz is azimuthally independent and contains the same data as for the receiver line A (since the source-receiver offsets are the same). The horizontal components are azimuthally dependent i.e. the wave mode observed depends on the azimuth of the receiver line. The converted wave from an Sz source is recorded on the Rx component in Figure 3.3 and on the Ry component in Figure 3.2. This observation is in accordance with that of Gaiser (1999) where, in XY space, the converted wave data has inconsistent amplitudes and polarization directions at different receivers. The same is true for pure shear wave data. For receiver line A, SxRx = SH-waves (Figure 3.2) and for receiver line B, SxRx = SV-waves (Figure 3.3) .

The 2-D subsets from the full 3-D acquisition geometry illustrate the 'wave-mode mixing' that occurs simply by changing the source-receiver azimuth. Zooming onto the SzRz, SxRx and SyRy components of receiver line A (Figure 3.4) which are predominantly associated with the P-wave, SH-wave and SV-wave data sets, respectively, we observe other wave modes mapped onto these components. On the P-wave component there are obvious shear wave reflections of slower move out velocity and on the SV-wave component there are P-wave reflections observed. As previously mentioned, the P-waves and SV-waves are coupled since they both exhibit particle motion in the same vertical plane. The polarity reversal observed on the SV-wave data is also due to this coupling. The SH-waves are independent from P-waves and show different amplitude character to the SV-wave however there is some faint P-wave reflectivity observed on the SH-wave synthetic. This is due to the elliptical-like radiation patterns of the vertical and horizontal point-force sources.

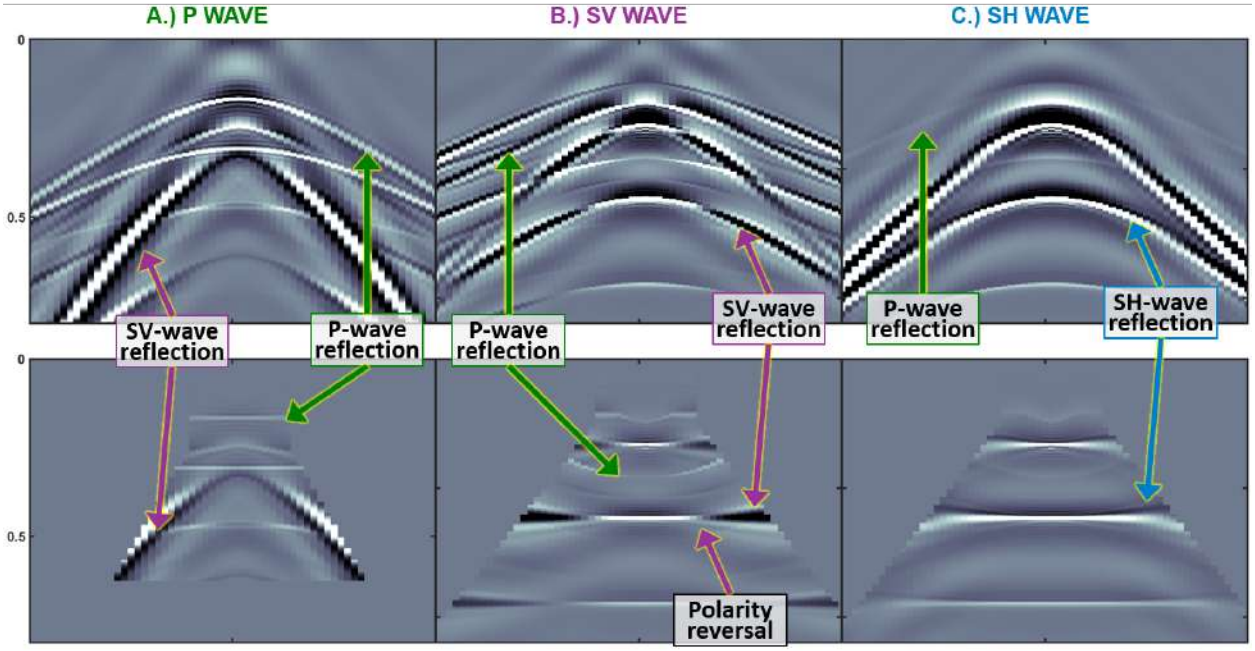

Figure 3.4: Zoom of the PP, SV and SH-waves produced in Figure 3.2. The lower panel contains NMO corrected versions of the upper panel. The vertical axis is time, and the horizontal axis is offset with the near offset at the center of each panel.

A vertical point source on a free surface generates both P- and SV-waves in an elastic subsurface (Gaiser, 2016; Miller and Pursey, 1954). Figure 3.5 shows the far field radiation pattern from a vertical point source. The strongest P-wave energy is emitted downward (θ=0^o); but the P-wave energy decreases to zero for horizontal propagation (θ=90^o) (Gaiser, 2016). This occurs at all azimuths (ϕ), hence the azimuthal independence of the vertical point source. This horizontally propagating energy however, is dominated by SV-wave energy which in this case exhibits particle motion in the vertical direction. This high-angle SV-wave is generated from an Sz source and records displacement on the Rz receiver.

A horizontal point source on a free surface generates P-, SV- and SH-waves in an elastic subsurface (Gaiser, 2016; Miller and Pursey, 1954). Figure 3.6 shows the far field radiation pattern of all wave modes from a horizontal point source.

The SH-wave radiation pattern is simplest. Along the direction of the force (X axis), there is little SH-wave radiation as SH-waves are polarized perpendicular to the source direction. The SH-wave field strength is constant for all angles (θ) from vertical to near horizontal in the direction perpendicular to the source (Y direction) (Gaiser, 2016).

The SV- and P-waves are polarized in the plane parallel to the direction of the source (X axis). The SV-wave is strongest vertically, similar to the SH-wave. There is an absence of P-wave energy transmitted vertically from a horizontal source. As the angle (θ) increases, the P-wave becomes evanescent and the radiation amplitude of the SV-wave spikes and then drops to zero. Beyond this angle, the SV-wave field strength is small. The P-wave field strength remains small at all angles and drops to zero for horizontal propagation.

There is a faint P- and SV-wave energy observed on the SH-wave seismogram (Figure 3.4. Although, the horizontal point force is oriented along the X axis, the SV-waves do propagate at azimuths offset to the X-direction. At these azimuths, SV-wave exhibit particle motion along the ray paths which are obliquely angled to the X and Y oriented receivers. Some SV-wave energy is thus registered on the SH-wave seismogram. Similarly, P-waves are observed on the SH-wave component and SH-waves are observed on the SV-wave component.

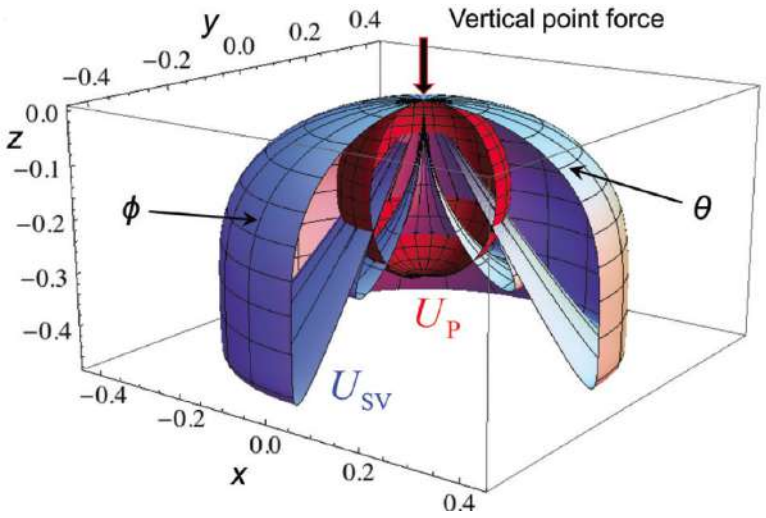

Figure 3.5: Radiation pattern of seismic waves from a vertical point source at a free surface. θ = angle of wave propagation, ϕ = azimuth of wave propagation, U_P = P-wave displacement field and U_{SV} = SV-wave displacement field (Modified from Gaiser (2016))

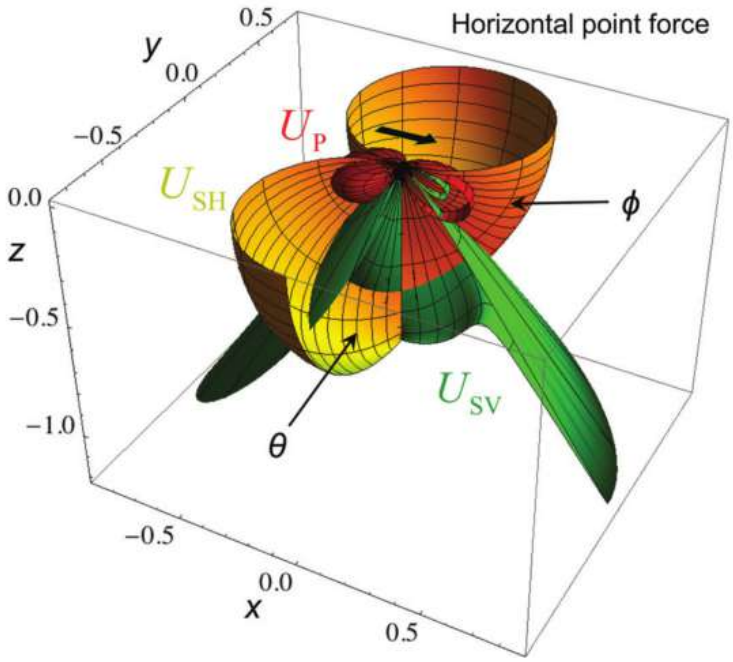

Figure 3.6: Radiation pattern of seismic waves from a horizontal point source oriented in the X direction at a free surface. U_P = P-wave displacement field, U_{SV} = SV-wave displacement field and U_{SH} = SH-wave displacement field (Modified from Gaiser (2016))

Also observed on the SV and SH prestack seismograms in Figure 3.4 are the different amplitude-versus-offset (AVO) responses. On the SV-wave data, there is a polarity reversal around 20-degrees angle of incidence. This SV-wave polarity reversal is caused by the coupling of SV- and P-waves, the first critical angle of an incident SV-wave, and the principle of total internal reflection in optics. Amplitude-versus-angle curves for the reflection between layers 3 and 4 of the model in Figure 2.1, are shown in Figure 3.7. These curves are produced from the full Zoeppritz equations given in Aki and Richards (1980).

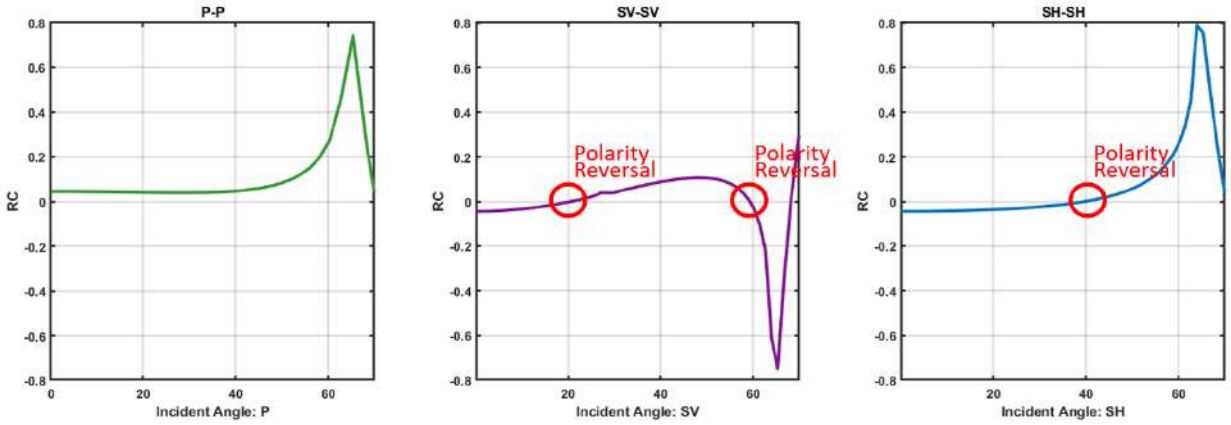

Figure 3.7: P-P, SV-SV and SH-SH body wave reflectivities for the boundary between the third and fourth layers of the isotropic model described in Figure 3.1. Third layer properties: Vp =3600, Vs=1800 and Density=2.58. Fourth layer properties: Vp =4000, Vs=2000 and Density=2.54. Reflection magnitudes are calculated using Zoeppritz equations.

An incident P- or SV-wave generates the other upon reflection at a boundary in the subsurface. Snell's law states that wave mode reflection at a horizontal interface conserves the ray parameter, p. For an incident wave this means:

$$\begin{aligned} p &= \frac{sin(\theta_i)}{v_1} \qquad \text{(Incident ray parameter)} \\ &= \frac{sin(\theta_R)}{v_2} \qquad \text{(Refracted ray parameter)} \end{aligned} \tag{3.1}$$

where v represents the velocity of the associated waves and the indices 1 and 2 represent the properties above and below the horizontal interface, respectively.

Refraction occurs only when $V_1 < V_2$. Internal reflection, where the refracted wave travels along the horizontal interface occurs at the critical angle of the incident wave. The SV-wave has two critical angles, the first of which is associated with total internal reflection of the P-wave energy at mid offsets and the second is associated with the total internal reflection of the SV-wave at farther offsets.

Following Equation 3.1, the total reflection of the P-wave occurs when, $\theta_{P_R} = 90$ degrees (Equation 3.2) and the total reflection of the SV-wave occurs when, $\theta_{SV_R} = 90$ degrees (Equation 3.3).

$$\begin{aligned} \frac{sin(\theta_i)}{v_{S1}} &= \frac{sin(90)}{v_{P2}} \\ sin(\theta_i) &= \frac{v_{S1}}{v_{P2}} \\ \theta_i &= asin\left(\frac{v_{S1}}{v_{P2}}\right) \end{aligned} \tag{3.2}$$

$$\begin{aligned} \frac{sin(\theta_{i1})}{v_{S1}} &= \frac{sin(90)}{v_{S2}} \\ sin(\theta_i) &= \frac{v_{S1}}{v_{S2}} \\ \theta_i &= asin\left(\frac{v_{S1}}{v_{S2}}\right) \end{aligned} \tag{3.3}$$

The model used to generate the plots in Figure 3.7 is based on an upper layer with $Vp = 3600\ m/s$, $Vs = 1800\ m/s$ and $Density = 2.58\ g/cc$ and lower layer with $Vp = 4000\ m/s$, $Vs = 2000\ m/s$ and $Density = 2.54\ g/cc$. The calculated critical angle associated with total P-wave reflection is 26.7 degrees and 64.2 degrees for total SV-wave reflection.

The polarity reversals observed on the SV reflection in Figure 3.7 occur near these critical angles. Zoeprittz equations define how reflection amplitudes change with incident angles for different velocities and Snell's law controls the relationship between incident angles and velocities. The relationship between these three elements, relfectivity, incidence angle and velocity is the basis on which the polarity reversal of SV-waves occur.

Beyond the critical angle of any wave, the reflection coefficient becomes complex (Castagna and Backus, 1993) and this has made the shear wave prestack data particularly difficult to process and interpret. Additionally, the differences in amplitude and velocity character of the SV- and SH-waves have added complications to these processes. The shear wave data however, contain relevant direction-dependent information that respond to azimuthal anisotropy and lateral variations in rock and fluid types (Hardage et al., 2011) and should not be discounted. In the next section, I examine the systematic, azimuthal dependence of the shear wave data at all offsets (inclusive of post-critical angles).

3.4 Wave Propagation in Isotropic Media in 3-D: Azimuthal Dependence in X-Y Coordinates

The orientation of a source with respect to the receiver line (source-receiver azimuth) will change the shear wave mode registered on the horizontal receiver components. The azimuthal independence of the P-wave data allows for valid processing in the X-Y acquisition coordinate system. However, shear wave data (converted or pure) cannot be processed in this system due to the changing wave mode response on receiver components.

The two receiver lines A and B shown in Figure 3.2 and 3.3 are 2-D subsets of a 3-D 9-C survey. In 3-D, these are the only azimuths for which pure shear wave, SV and SH-waves are naturally recorded. Variation of the source-receiver azimuth is introduced when considering a receiver line offset from the source location.

Figure 3.8 shows the P-wave and converted waves generated from an Sz source and recorded on the three receiver components for receiver lines offset from the source in the Y direction. The P-wave is consistently recorded on the SzRz component, and inconsistent converted wave signal is observed on the SzRx and SzRy components. For receiver line B (top panels), the SzRx component records the true converted wave signal.

Figure 3.9 shows the shear wave response at receiver lines offset to the source location. The separated wave modes that are identifiable in the first row (receiver line B which is over the source location) are indistinguishable on all other rows where the receiver line is offset to

the source location (Receiver lines C, D and E). At these offset receiver lines, all components register some signal for this isotropic model and the wave modes are mixed.

Figures 3.10 and 3.11 are 3-D visuals showing the mixing of shear wave modes at different azimuths for the field coordinate system. These 3-D prestack cubes show the energy recorded on orthogonal receiver lines (A and B) for the SxRx component. Along receiver line B, the Rx components register the SV-wave energy (equivalent to SxRx response on Figure 3.3). Along receiver line A, SH-wave energy is recorded (equivalent to SxRx response on Figure 3.2). The time slice through the prestack cube demonstrates the mixing of shear wave modes between these azimuths parallel (red) and perpendicular (orange) to the source direction (Sx). In Figure 3.11, the mixed shear wave signal along receiver line D is shown which is equivalent to the third SxRx panel in Figure 3.9.

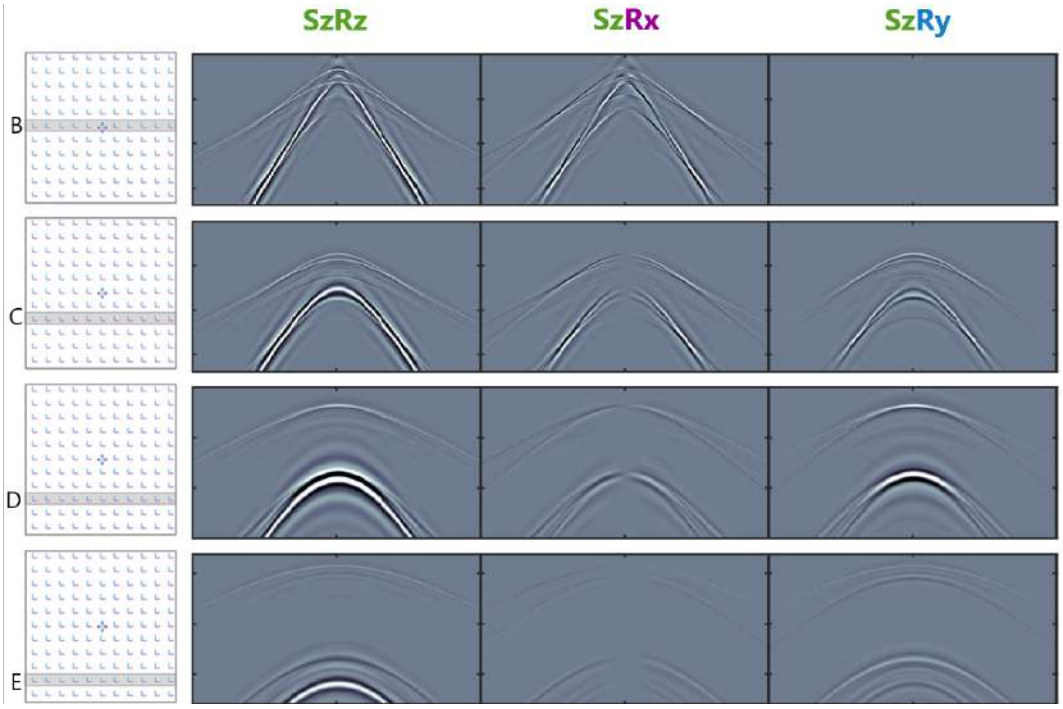

Figure 3.8: P and converted waves in X-Y space generated from the Sz source and recorded on receiver lines oriented E-W and offset from the source location. Peaks are white, troughs are black and time scales are the same for all displays. At receiver line B over the source location, the converted shear (and coupled P) is registered only on the SzRx component. At receiver lines C, D and E, converted waves (and coupled P) are registered on SzRx and SzRy in various proportions.

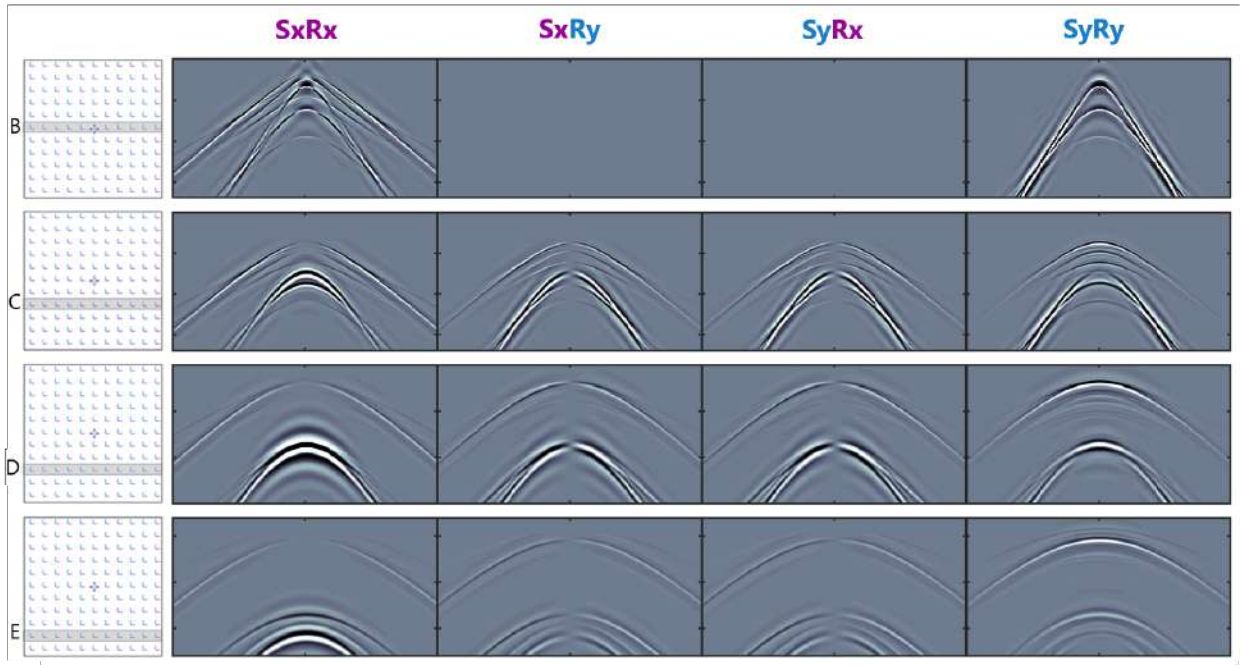

Figure 3.9: Shear components (generated from horizontal sources) in X-Y space for receiver lines oriented E-W and offset from the source location. Peaks are white, troughs are black and time scales are the same for all displays. At receiver line B over the source location, the cross-terms (SxRy and SyRx) are zero for the isotropic model. At offset receiver lines (C, D and E) all components contain a mix of shear wave and P-wave energy. Cross-terms are not minimized in acquisition coordinates due to the variable source-receiver azimuth.

As mentioned, the cross-term components (SxRy and SyRx) are the main indicators of subsurface anisotropy and are equally as important to analyze. Recall, that the cross-term components in the isotropic model should not contain coherent signal. However, in Figure 3.12, the SxRy cross-term data is shown at all azimuths, and at azimuths oblique to the source direction significant energy is observed.

This energy is purely due to the source-receiver azimuth. Figure 3.13 shows the cross-term energy at all azimuths. In each quadrant, there is a polarity reversal due to the varying source-receiver azimuth.

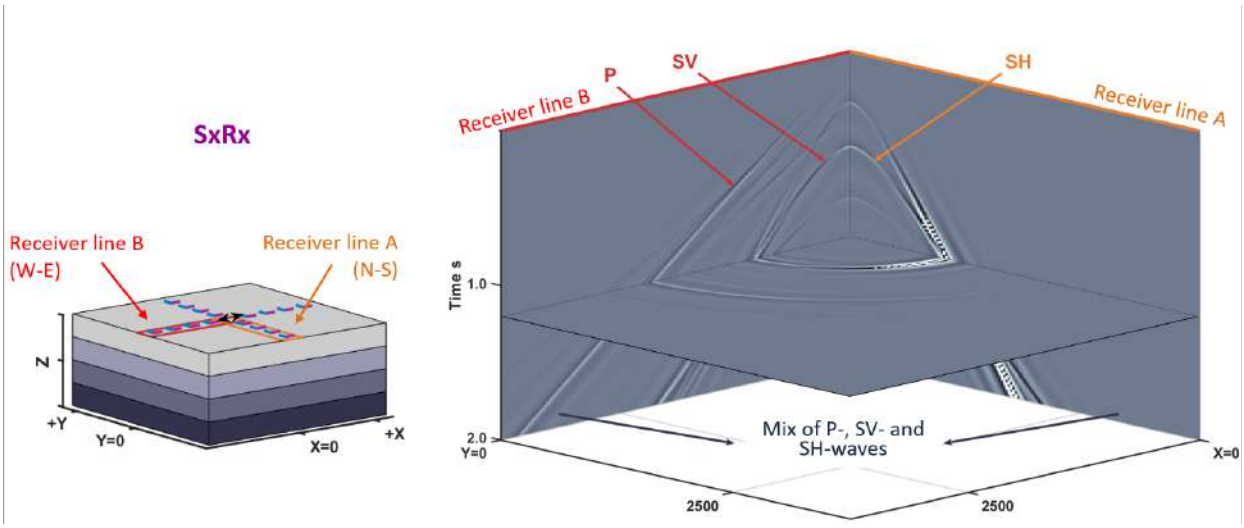

Figure 3.10: 3D view of shear wave mode projection at varying receiver azimuths for the SxRx component. Receiver line A is colored orange and registers the converted wave and coupled P-wave. Receiver line B is colored red and registers the SH-wave. Between these azimuths, the SxRx data component contains a weighted mix of the SH- and SV-wave modes.

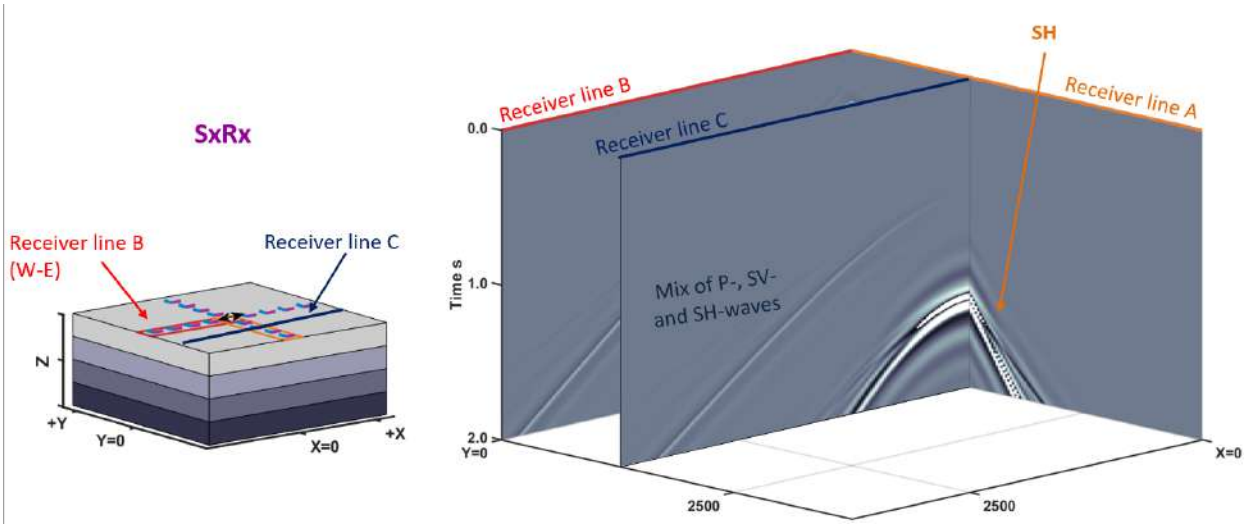

Figure 3.11: 3D view of shear wave mode projection at receiver line C (Figure 3.10) for the SxRx component. The SxRx component along receiver line C contains a mix of P-, SV- and SH-wave modes in X-Y space due to variable source-receiver azimuth.

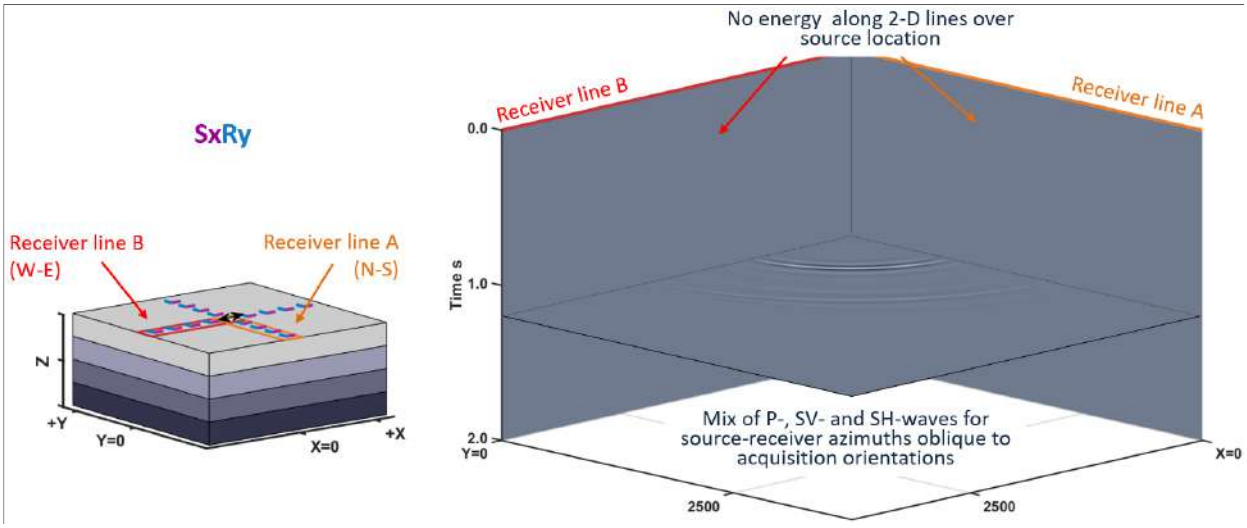

Figure 3.12: 3D view of shear wave mode projection at varying receiver azimuths for the SxRy, component. Parallel (receiver line B in red) or perpendicular (receiver line A in orange) to the source direction (Sx), the crosterm contains no signal. For azimuths oblique to the source direction the cross-term registers a mix of SV and SH-waves. Energy on this cross-term component (SxRy) is often interpreted as shear wave splitting, which in this coordinate system, is not accurate.

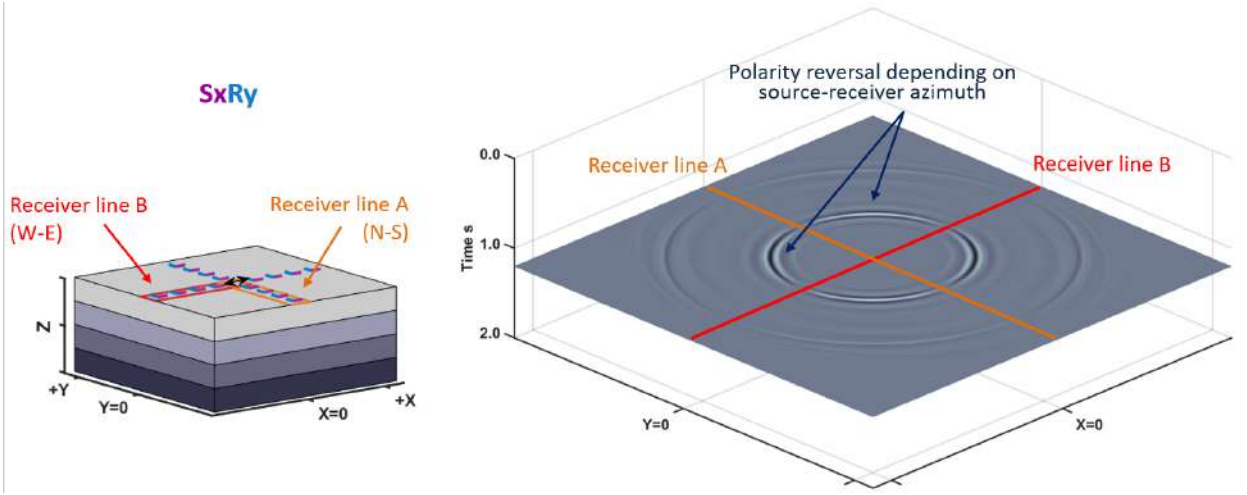

Figure 3.13: 3D view of shear wave mode projection at all receiver azimuths for the cross-term, SxRy, component. Note the polarity reversal between quadrants due to the changing source-receiver azimuth relative to source propagation.

3.5 Shear Wave Propagation in Isotropic Media in 3-D: Azimuthal Independence in R-T Coordinates

An analysis of converted wave data recognized that in field coordinates, different source-receiver azimuths contain varying amounts of converted wave energy (Gaiser, 1999). In Figure 3.3, the converted wave component was observed on the Rx component whilst in Figure 3.2 it is registered on the Ry component. To obtain consistency from one receiver station to the next, Gaiser (1999) suggests rotation into a source-centered coordinate system.

Simmons and Backus (2001) introduce a similar solution with respect to pure shear wave data (SH and SV). In field coordinates, a receiver station records a weighted mix of the SH-, SV- and P-waves depending on its orientation to the source. Early 9-C 3-D seismic processing took place in field coordinates with processing parameters (velocities, statics, deconvolution operators, etc.) generally estimated independently for the 'main' shear components (SxRx and SyRy) and applied to the cross-term datasets (SxRy and SyRx). Noise attenuation processes are typically applied to each of the four datasets independently. Processing in field coordinates neglects the inherent differences between wave modes (Simmons and Backus, 2001).

The appropriate coordinate system for processing shear wave data (converted and pure) is the radial-transverse system (R-T) (Gaiser, 1999; Simmons and Backus, 2001). The radial direction for any source-receiver pair is the direction along the source-receiver azimuth and the transverse direction for any source-receiver pair is orthogonal and clockwise to the radial direction (Figure 3.14). The R-T system removes the azimuthal dependence of the source-receiver orientation and for shear wave data, the azimuthal dependence of the horizontal point -force sources. For rotation of converted wave data, the azimuth of one of the horizontal receiver components (with the other assumed perpendicular), and the source-receiver azimuth must be known. For rotation of the pure shear wave data, the azimuth of one of the horizontal sources must also be known.

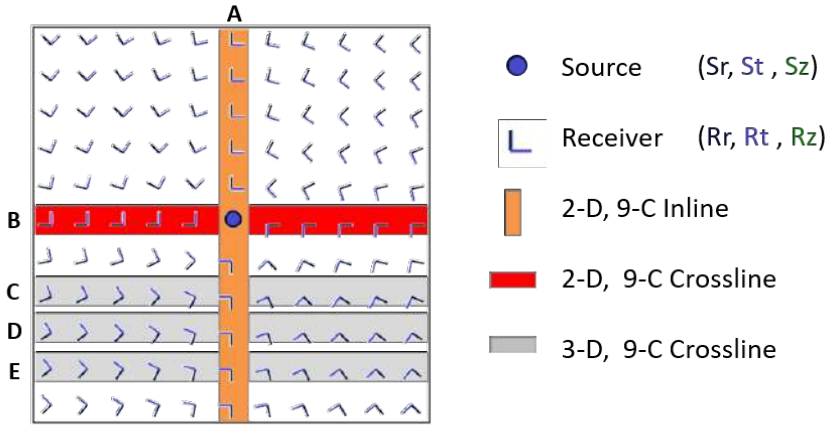

Figure 3.14: Description of the Radial-Transverse coordinate system. The radial direction for any source receiver pair points outward and along the source-receiver azimuth. The transverse direction for any source receiver pair is orthogonal and clockwise from the radial direction. The source location is described as a point, but for the pure shear data, the the horizontal sources and horizontal receivers are rotated for each source-receiver quadruplet.

Figures 3.15 and 3.16 show the nine data components rotated to R-T space for the same model presented previously. In R-T coordinates, the P-wave data remains concentrated onto the SzRz data component at both azimuths, similar to XY space. For converted wave, the vertical source generates a wave propagating along the radial-vertical plane to a radially oriented receiver. In R-T coordinates, the converted wave is always recorded on the SzRr component for both the crossline and inline orientations shown in Figure 3.15 and 3.16.

For shear wave data, a radially-oriented source (Sr) will generate a wave propagating along the radial-vertical plane to the radially-oriented receiver (Rr). The particle motion is parallel to the radial-vertical plane and as such the radial component of the receiver registers the SV-wave regardless of azimuth. For the crossline and inline receivers presented in Figures 3.15 and 3.16, the SrRr components are the same.

The particle motion created by a transverse source (St) is orthogonal to the plane of wave propagation and this particle motion is registered on the transverse component of the receiver (Rt) as an SH-wave. The StRt components for Figures 3.15 and 3.16 are the same.

In a flat layered, isotropic earth, the initial wave generated by the source will be unaltered as it approaches the receiver. As such, in the R-T system, all SV energy will be concentrated onto SrRr, SH energy will be concentrated onto StRt and the cross-term components (SrRt) and (StRr) will not contain any coherent signal.

This remains true for receiver lines offset from the source location, where azimuthal variation of the sources and receivers is introduced (Figure 3.17). In R-T space, the SzRr = P-SV, SrRr = SV and StRt = SH. Figure 3.18 presents a 3-D view of these components which show the consistency of wave mode distribution.

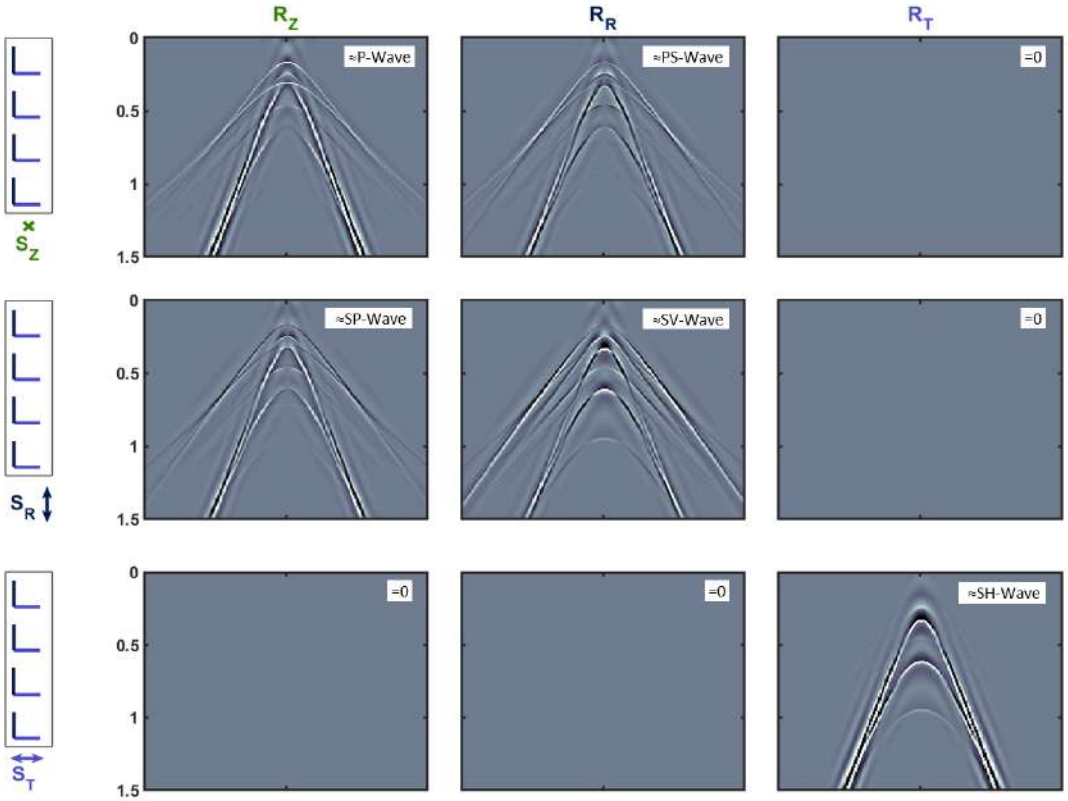

Figure 3.15: Synthetic seismograms in radial-transverse coordinates extracted along receiver line A oriented N-S over the source location as described in Figure 3.14. SzRz=PP, SrRr=SV and StRt=SH and cross-terms contain no signal for this isotropic model.

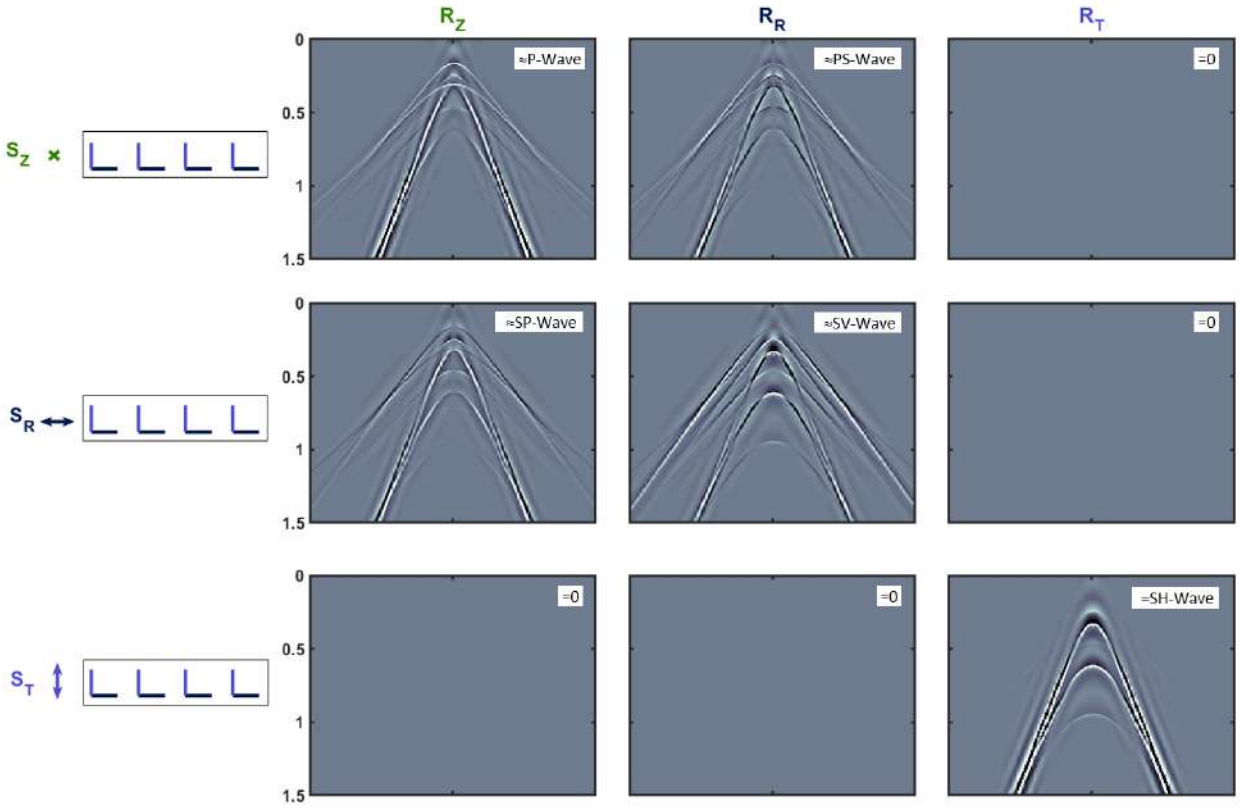

Figure 3.16: Synthetic seismograms, in radial-transverse coordinates, extracted along receiver line B oriented E-W over the source location. The nine components register the same wave modes as Receiver line A in Figure 3.15.

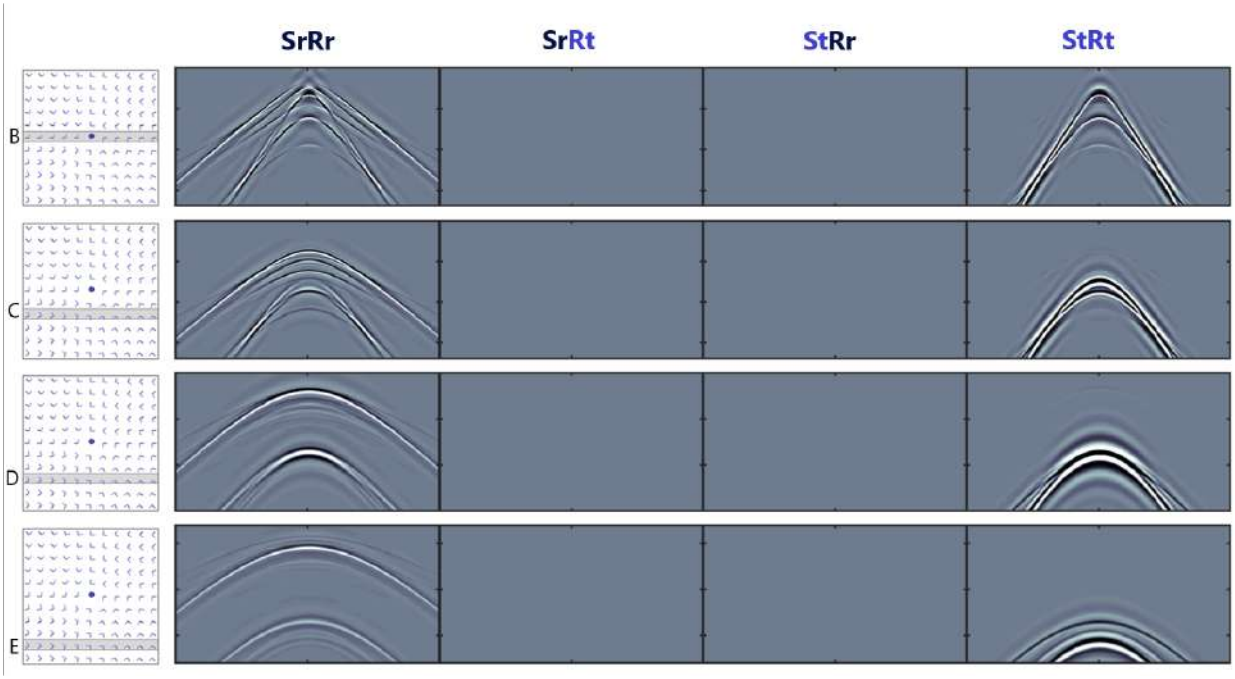

Figure 3.17: Shear components in R-T space for receiver line B and offset receiver lines C, D and E. At all receiver lines, the SrRr=SV, StRt=SH and the cross-terms are zero for the isotropic model.

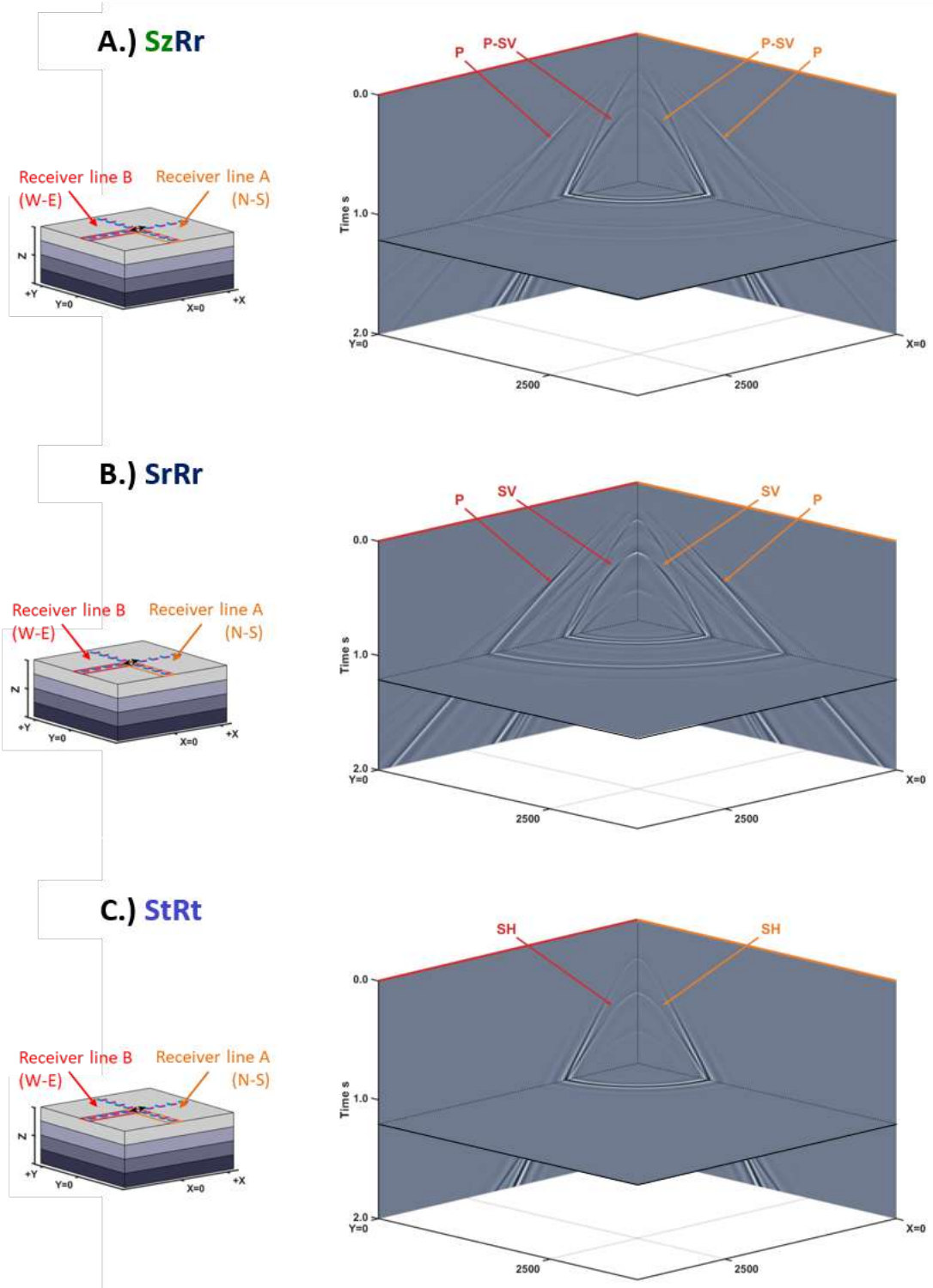

Figure 3.18: 3D view of converted and pure shear data components at varying receiver azimuths in R-T coordinates. Figure A = SzRr component, Figure B = SrRr component and Figure C = StRt component. All wave modes are appropriately separated and independent of source-receiver azimuth

3.6 Conclusions

Processing in acquisition coordinates was standard when the P-wave component was the sole data collected or 2-D seismic lines were used to acquire multicomponent data. Over the source location, 2-D lines appropriately show no cross-term energy in an isotropic model. However, for 2-D lines at orthogonal azimuths, the main horizontal components register opposite shear wave modes (SV and SH) and the response at receiver locations vary.

In early years of acquiring and processing 9-C, 3-D data sets, acquisition coordinates were standard until the impact of varying source-receiver azimuth was recognized. The shear data are azimuthally dependent. Parallel or perpendicular to the source direction, a single shear mode (SV or SH) is recorded, however, between these azimuths, there is a weighted mixing of the modes. The mixing of these modes on acquisition data components causes intrinsic problems in processing. In addition, at oblique azimuths, in an isotropic earth, energy on the cross-terms is observed because of the source-receiver geometry effects.

The coordinate system that allows for separation of SV- and SH-waves onto different components is the radial-transverse (R-T) system. R-T coordinates remove the azimuthal dependence of the horizontal components and is the recommended system for shear-wave processing. For any inline or crossline examined on 3-D seismic surveys, the SV-waves=SrRr (radial component), SH-waves=StRt (transverse component) and in a flat layered, isotropic earth, the cross-terms are zero.

In an anisotropic earth, the horizontal components register unique signals that can be inverted for fracture parameters. In R-T space, a popular observation is the minimization of cross-term energy along source-receiver azimuths parallel or perpendicular to fracture strike. This observation is the basis for prestack shear wave rotation which is a modern technique that aligns the shear wave data into fast and slow components prior to processing. The next chapter introduces shear wave propagation in an anisotropic medium and discusses these two systems for processing: Fast-Slow versus Radial-Transverse (SV-SH).

CHAPTER 4

SHEAR WAVES IN HTI MEDIA: FAST-SLOW AND RADIAL-TRANSVERSE COORDINATES

Many studies on shear wave interpretation use data sets that have been processed in the field coordinate system (X-Y) or a fast-slow (F-S) coordinate system (DeVault et al., 2002; Grechka and Vasconcelos, 2007; Mueller, 1991; Shuck, 1993; Terrell, 2004). Shear waves split on propagation through a fractured medium and the F-S system attempts to separate the fast and slow waves onto different data components. Prestack data are rotated to a coordinate system that is parallel (fast) and perpendicular (slow) to a predetermined maximum horizontal stress direction (DeVault et al., 2002; Lewis et al., 1991). This fast-azimuth is typically determined from auxiliary datasets (regional stress maps or VSP data) or estimated from prestack rotation analysis. This first approach assumes that the regional stress direction is correct, laterally invariant, and that the shear wave data are implicitly sensitive to the presumed stress field.

In F-S coordinates, similar to acquisition coordinates, the two shear wave modes (SV and SH) are mixed and the prestack gathers are asymmetric. Previous RCP studies on the Wattenberg Field have used shear data that are interpreted in these coordinates. A brief comparison of fracture interpretation in F-S space versus R-T space is presented in Motamedi and Davis (2015), and an impedance inversion in F-S space is presented in Mueller (2016). For this research, the prestack shear data sets are properly rotated into the radial-transverse (R-T) system as recommended by Gaiser (1999) and Simmons and Backus (2001).

This chapter compares the prestack shear wave data components in F-S and R-T coordinates through anisotropic modeling. The third layer of the four layer earth model used in Chapter 2 is fractured using Hudson's fracture parameters to produce a single layer with horizontal transverse isotropy (HTI).

4.1 Shear Waves in HTI Media

An isotropic medium with a single set of parallel, vertical cracks is described as having horizontal transverse isotropy (HTI). In an HTI model, there exists two mutually orthogonal, vertical planes of symmetry (principal azimuths) as depicted in Figure 4.1. The symmetry-axis plane is perpendicular to the fracture strike and the isotropy plane is parallel to the fracture strike (Figure 4.1). For this research, the HTI model will be the primary descriptor of the fractured Niobrara-Codell interval.

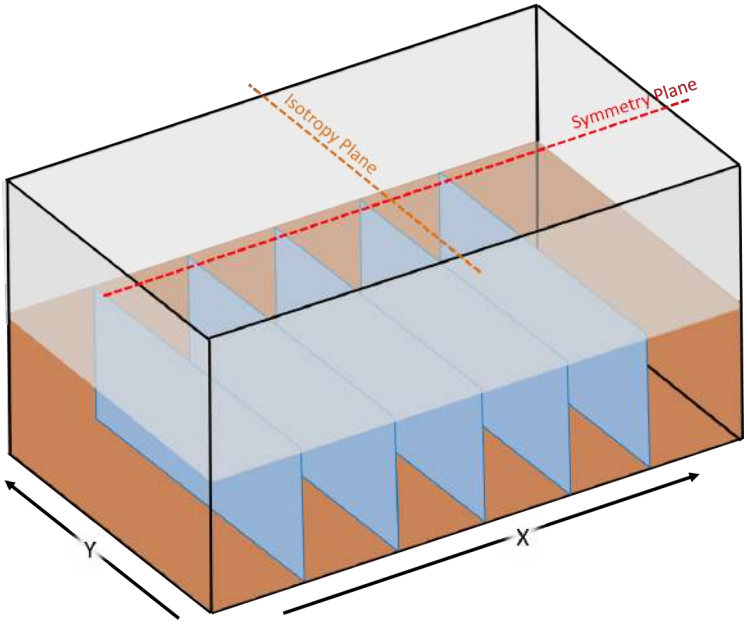

Figure 4.1: Description of an HTI medium created by a system of parallel vertical cracks in an isotropic background (Modified from Tsvankin (2012)).

Shear waves split on transmission through an HTI medium due to its particle motion in the horizontal plane. This phenomena of the shear wave splitting (SWS) is explained by Tsvankin (2012) as the shear waves polarizing into fast and slow directions. Fast shear waves are those that exhibit particle motion in the direction of fracture strike. They maintain fast velocities i.e. isotropic velocities as the particle motion is parallel to the vertical fractures. Slow shear waves are those that exhibit particle motion perpendicular to fracture strike and interfere with the vertical fracture plane.

It is easiest to break down the shear wave reflectivies in an HTI media with respect to the principal azimuths identified in Figure 4.1.

4.2 The Isotropy Plane

An SV-wave has particle motion in the vertical and horizontal plane. For a source-receiver azimuth parallel to fracture strike, SV-wave particle motion is also parallel to the fracture strike. As a result, SV-waves generated from this source-receiver azimuth propagate at the fast, isotropic SV-wave velocity and have isotropic SV-wave amplitude variations with angle (AVA) as described in Equation 4.1. This equation is based on the linearized approximation of the Zoeppritz equations (Aki and Richards, 1980) for the two principal azimuths (Ruger, 2002).

SH-waves propagating at this azimuth have particle motion perpendicular to the vertical fractures and propagate with a slow velocity. The reflection coefficient of the SH-wave traveling in the isotropy plane is shown in Equation 4.2 where $\gamma^{(V)}$ denotes the fractional difference between the vertical and horizontal shear wave velocity and j is the angle of incidence.

$$R_{SV}^{isotropy} = R_{SV}^{iso} \qquad \text{(Fast SV)} \qquad (4.1)$$

$$R_{SH}^{isotropy} = R_{SH}^{iso} + \frac{1}{2}\Delta\gamma^{(V)} tan^2(j) \qquad \text{(Slow SH)} \qquad (4.2)$$

4.3 The Symmetry Plane

An SV-wave propagating parallel to the symmetry plane has particle motion perpendicular to fracture strike. The velocity of this wave is slowed and its AVA is described in Equation 4.3 where $\epsilon^{(V)}$ denotes the fractional difference between the vertical and horizontal P-wave velocity, $\delta^{(V)}$ denotes the change in P-wave velocity with phase angle at near incidence and α and β are the P-wave and shear wave velocities respectively. An SH-wave traveling parallel to the symmetry plane exhibits particle motion parallel to fracture strike and has an isotropic shear wave velocity. This SH-wave AVAz is described in Equation 4.4.

$$R_{SV}^{sym} = R_{SV}^{iso} + \frac{1}{2}\left(\frac{\bar{\alpha}}{\bar{\beta}^{\perp}}\right)^2 (\Delta\epsilon^{(V)} - \Delta\delta^{(V)}) sin^2(j) \qquad \text{(Slow SV)} \qquad (4.3)$$

$$R_{SH}^{sym} = R_{SH}^{iso} \qquad \text{(Fast SH)} \qquad (4.4)$$

From this evaluation of wave mode reflectivities by Ruger (2002), sorting the shear data into fast and slow components will result in data sets that contain a mix of SV- and SH-waves. These wave modes can be separated along the principal fracture azimuths as explicitly defined by Ruger (2002) however, this means that although we acquire, process and image, shear waves in 3-D, F-S coordinates limit examination to these two azimuths.

Shear wave data can also be sorted such that the SV and SH components are separated using the R-T system. This results in a mix of fast and slow shear waves on each data component which can be used to solve for the principal fracture directions based on velocity variations with azimuth (VVAz).

There are advantages to both coordinate systems (F-S and R-T) for interpretation however, in the next section I evaluate which system is most appropriate for preprocessing and imaging using anisotropic modeling.

4.4 Shear Wave Processing in HTI Media: Fast-Slow Coordinates versus R-T Coordinates

The goal of pre-processing rotation is to facilitate shear-wave splitting studies for fracture characterization. To compare the fast-slow and radial-transverse systems, I present comparative synthetics for several anisotropic earth models.

4.4.1 N-S Fractured Layer with Isotropic Overburden

The simplest anisotropic model is a single HTI layer with the principal azimuths aligned with the X-Y acquisition coordinate axes. For this model, the data are acquired in F-S space i.e. no rotation is necessary. The base maps in Figure 4.2 describe the F-S and R-T coordinate systems for this model with fractures oriented N-S in the third layer.

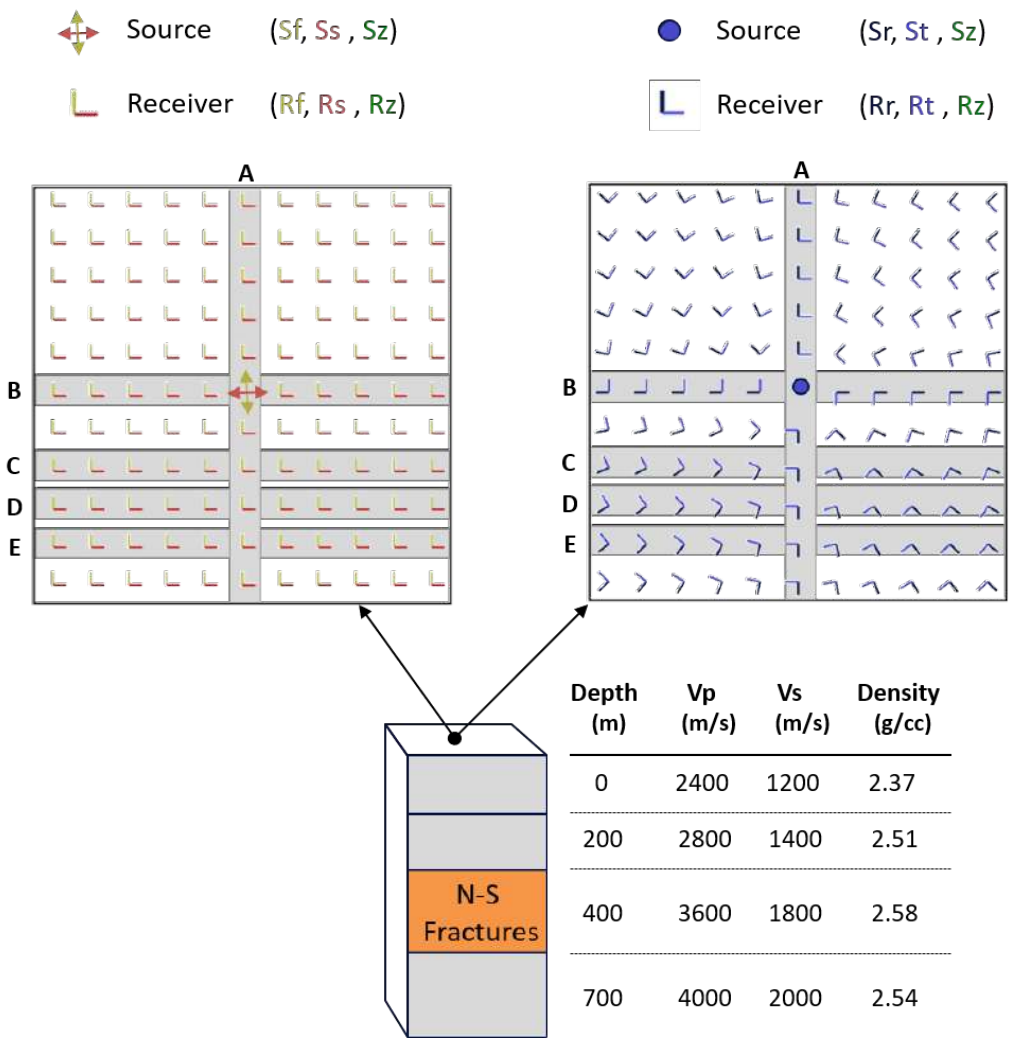

Depth (m)	Vp (m/s)	Vs (m/s)	Density (g/cc)
0	2400	1200	2.37
200	2800	1400	2.51
400	3600	1800	2.58
700	4000	2000	2.54

Figure 4.2: Base map for the Fast-Slow and R-T coordinate systems and description of the 4 layer model with N-S fractures in layer 3. Receiver lines are labeled A through E. In this model, the acquisition coordinate system is naturally aligned in F-S coordinates.

Figure 4.3 compares the F-S and R-T space for receiver line A i.e. the azimuth parallel to fracture orientation (isotropy plane). Along this receiver line, SfRf = fast SV-waves since the SV-waves generated in the Y-direction exhibit particle motion parallel to fracture strike and maintain a fast velocity. The SH-waves propagating in the Y-direction are slow since their particle motion is perpendicular to fracture strike. In the R-T coordinate system, SrRr = fast SV-wave and StRt = slow SH-waves. The red line across the upper and lower panels is drawn at the top of the fourth layer at the fast shear arrival time.

Figure 4.4 compares the F-S and R-T space for receiver line B which is along the symmetry plane (perpendicular to fracture strike). In F-S space, SfRf = fast SH-waves and SsRs = slow SV-waves. In R-T space, the shear wave modes remain separated onto the different components with SrRr = slow SV-waves and StRt = fast SH-waves.

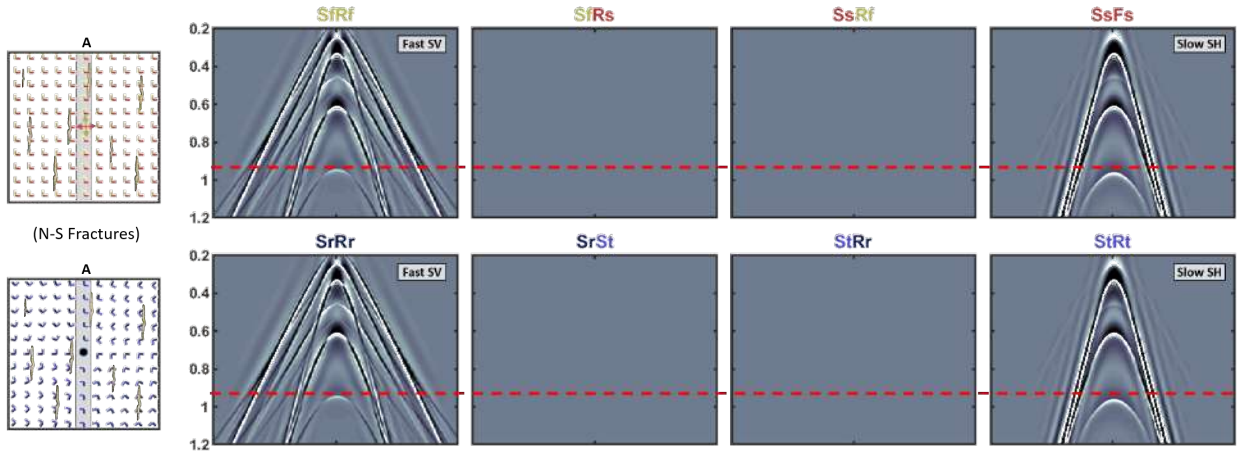

Figure 4.3: Comparison of F-S and R-T space for receiver line A. The four-layer model contains one HTI layer with the fractures oriented N-S. The horizontal dashed lines are datumed at the fast shear arrival at the top of the fourth layer.

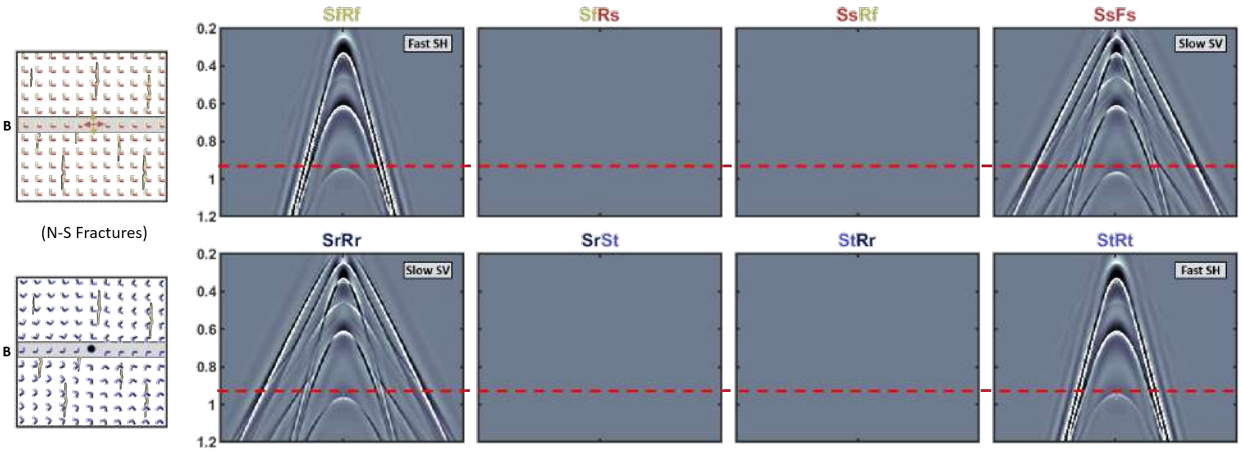

Figure 4.4: Comparison of F-S and R-T space for receiver line B. The four-layer model contains one HTI layer with the fractures oriented N-S. The horizontal dashed lines are datumed at the fast shear arrival at the top of the fourth layer.

The cross terms for both receiver lines in both coordinate systems, are zero as expected. This same interpretation was observed in X-Y space in Figures 3.2 and 3.3 since for this model, F-S = X-Y.

The F-S gathers are complicated when azimuthal variations are introduced by shifting the receiver lines away from the source location in the Y direction (Figure 4.5). Over the source location, the cross-term components are zero. For the offset receiver lines (C-E), the cross-terms show significant amounts of coherent energy. The system is in fast-slow coordinates and the expectation is that the cross-term components are indicative of split shear waves, however, this is not the case. The cross-terms for receiver lines C-E contain signal similar to that on the main components. All F-S components contain a mix of SV- and SH-wave modes once source-receiver azimuthal variation is introduced. In F-S coordinates, the cross-term energy is dominated by the geometry effect rather than evidence of shear wave splitting.

Figure 4.6 shows a similar display of varying offset receiver lines for R-T components. This display looks similar to the isotropic case (Figure 3.17) except for the split shear waves on the cross-terms. For all receiver lines, SrRr = SV-waves and StRt = SH-waves. Over the source location at receiver line B, the cross-terms are zero as the propagating shear waves are not influenced by the fracture set. At offset receiver lines, the source-receiver azimuths are oblique to the fracture strikes oriented N-S. For these lines, the cross-term components show coherent energy indicative of shear wave splitting.

The azimuthal dependence of the fast-slow data components confuses processing and interpretation techniques which are spatially and azimuthally dependent. In the next model, I present a more complicated model with fractures oriented NE-SW and we observe additional complications of the fast-slow coordinates.

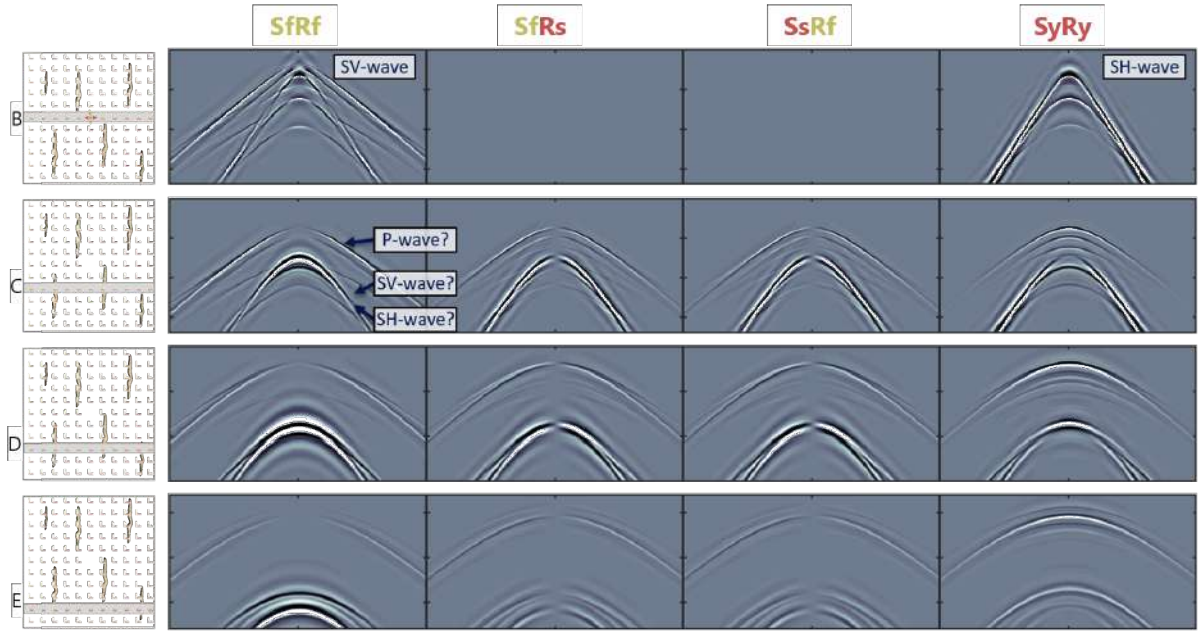

Figure 4.5: Gathers in F-S space for receiver lines offset from the source location. The four-layer model contains one HTI layer with a fracture set oriented N-S.

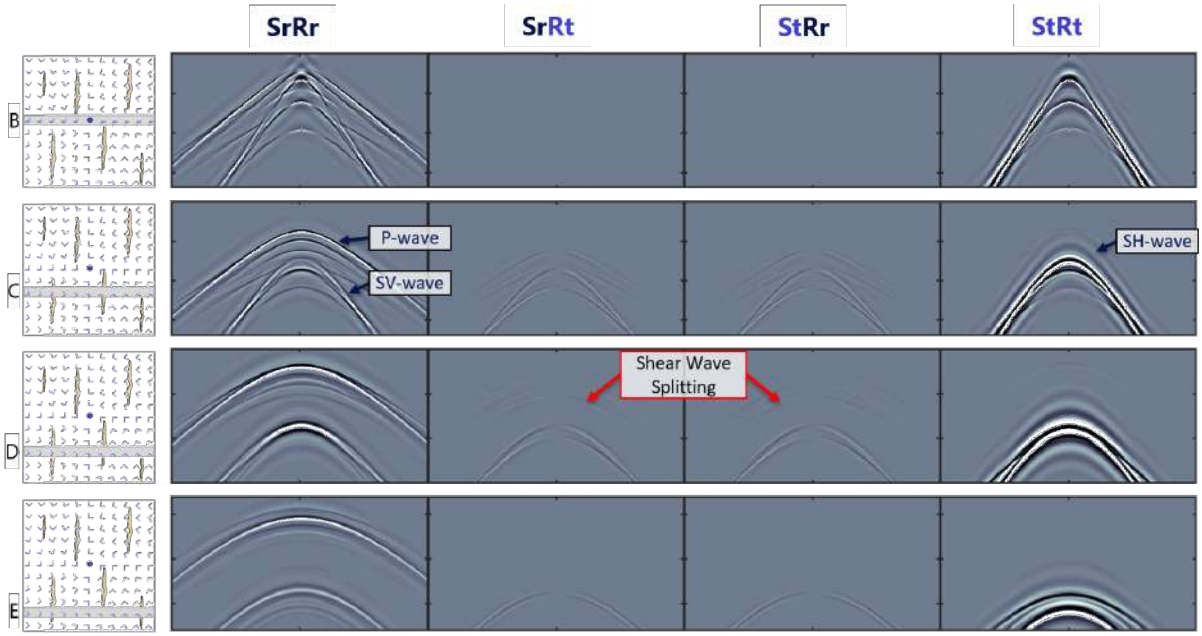

Figure 4.6: Gathers in R-T space for receiver lines offset from the source location. The four-layer model contains one HTI layer with a fracture set oriented N-S.

4.4.2 NE-SW Fractured Layer with Isotropic Overburden

In an anisotropic subsurface where the fractures are not aligned to the acquisition coordinates, the processing of F-S shear data is further complicated. To demonstrate, the fractures in the simple HTI model were rotated to a 45 degrees azimuth (NE-SW). The model was shot in the acquisition coordinate system and then rotated 45 degrees to F-S space (Figure 4.7). The R-T rotation was conducted similar to the previous model.

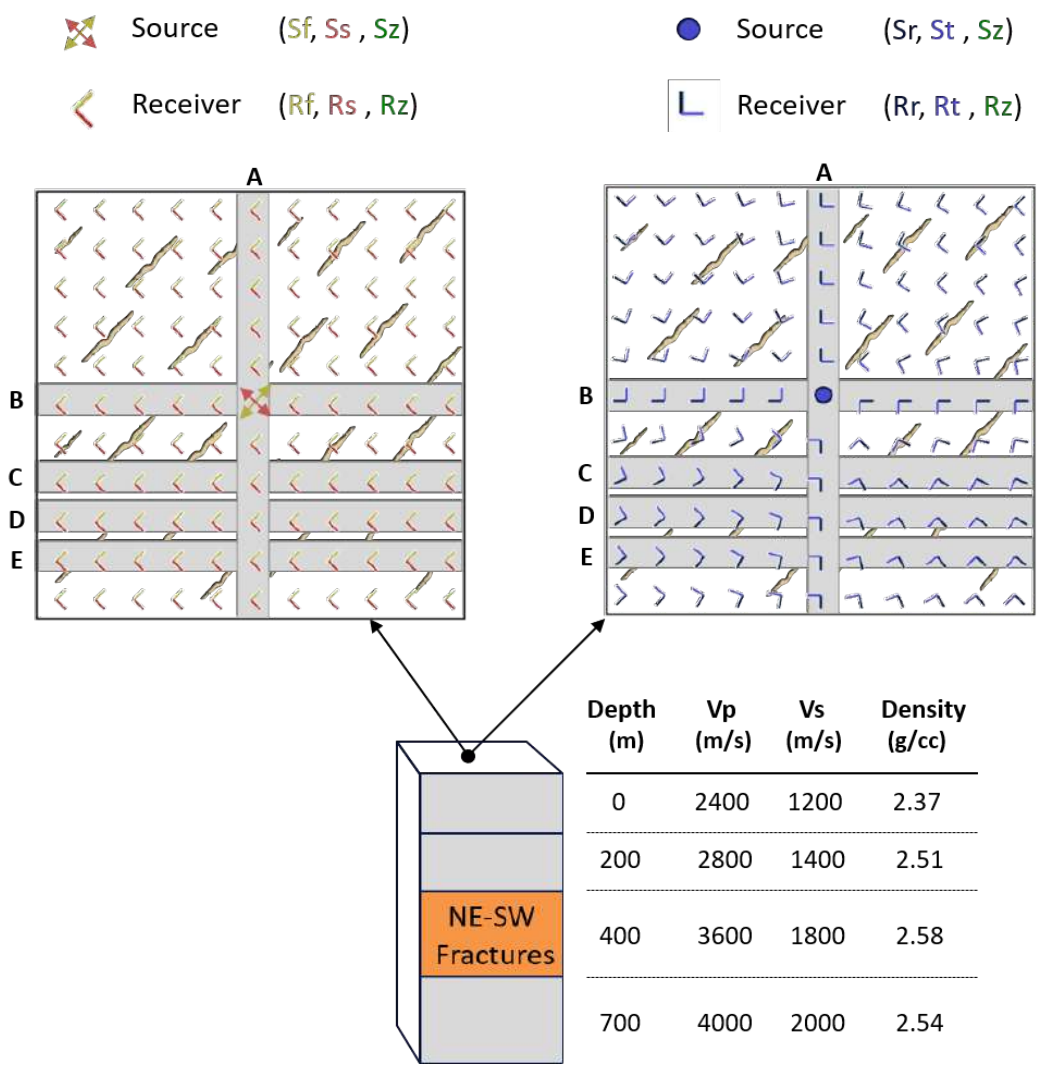

Depth (m)	Vp (m/s)	Vs (m/s)	Density (g/cc)
0	2400	1200	2.37
200	2800	1400	2.51
400	3600	1800	2.58
700	4000	2000	2.54

Figure 4.7: Base map for the Fast-Slow and R-T coordinate systems and description of the 4 layer model with NE-SW fractures in layer 3. Receiver lines are labeled A through E.

Figures 4.8 and 4.9 show the shear wave shot gathers for receiver lines B to E. In F-S space, at all receiver lines, the cross-term energy (SfRs and SsRf) is again dominated by geometry effects and look similar to the main components (SfRf and SsRs). The main shear components register asymmetrical shot gathers for receiver lines C, D and E. That is, an SV-wave and coupled P-wave shows a strong response on half the gather and the other half shows a dominant SH-wave.

In Figure 4.9, the R-T components separate the SV and SH data into different datasets. The SV-data remains concentrated on SrRr, the SH-data is recorded on StRt and the cross-term components are minimized at all offsets. For receiver lines B - E, the source-receiver azimuths are obliquely oriented to fracture strike and the cross-term components expose shear wave splitting.

Looking at receivers along a constant azimuth, we can better observe the systematic mixing of shear modes with azimuth in F-S space. Figure 4.10 shows shot gathers for different source-receiver azimuths from -45 degrees (perpendicular to fracture strike) to 45 degrees (aligned with fracture strike). Panels A - J show the SfRf component and panels K - T show the SsRs component. In the gather displays labeled A. on Figure 4.10, we observe P-waves on the fast (panel J) and slow (panel K) SV components at -45 and 45 degree azimuths. Between these azimuths, the P-wave coupled with the SV-wave varies in amplitude. On the fast (panel A) and slow (panel T) SH components, no P-wave energy is observed.

The mixing of the amplitude versus offset (AVO) effects between SV- and SH- wave modes is also evident between the principal azimuths. This is better observed in the NMO corrected display (lower display labeled B. in Figure 4.10), where panel A shows the fast SH-wave AVO with no polarity reversal and panel K shows the polarity reversal associated with the fast SV-wave. Between these principal azimuths, the polarity reversal is weak due to the mixing of the shear wave modes.

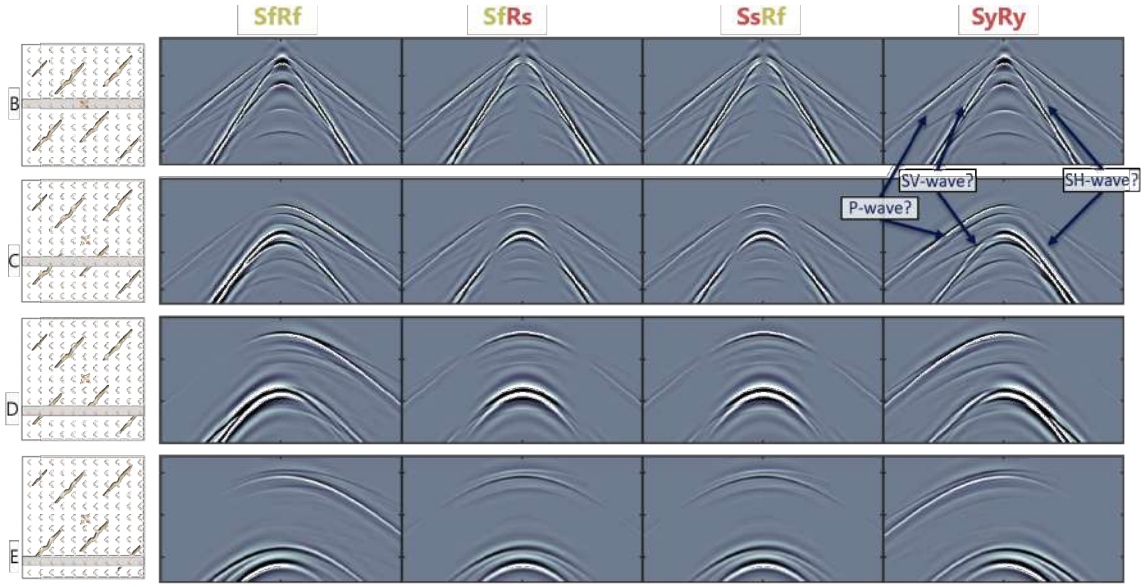

Figure 4.8: F-S synthetic gathers generated from the HTI model described in Figure 4.7 for receiver lines offset from the source location. SfRf = fast shear waves with coupled P-waves, SsRs = slow shear waves with coupled P-waves and cross-term energy is dominated by effects of variable source-receiver azimuth.

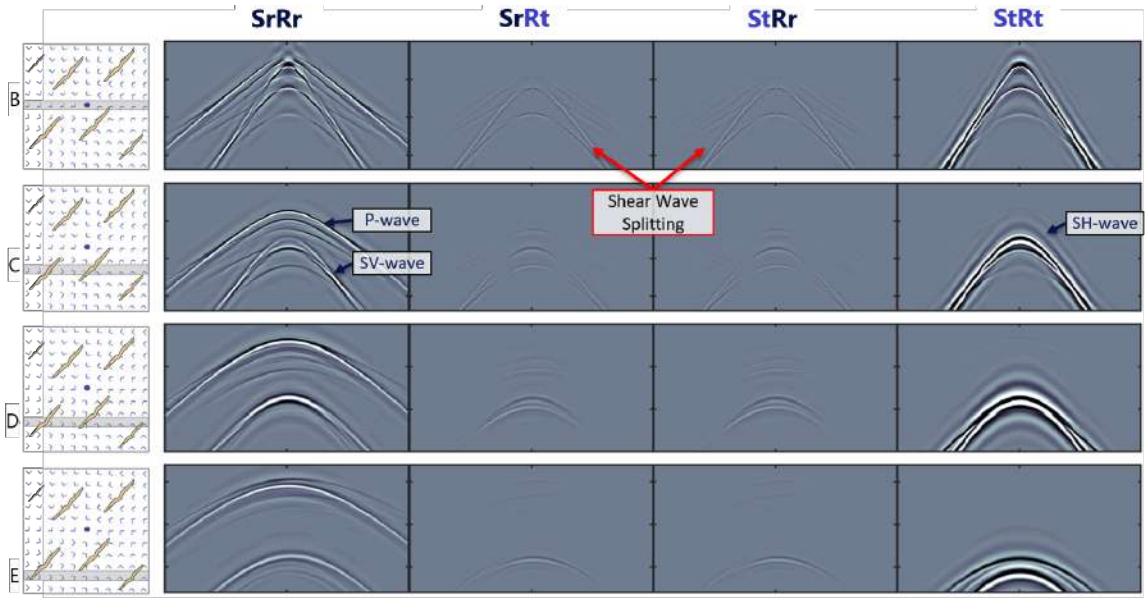

Figure 4.9: F-S synthetic gathers generated from the HTI model described in Figure 4.7 for receiver lines offset from the source location. SrRr = SV- and coupled P-waves, StRt = SH-waves and the cross-terms, SrRt and StRt are equal and expose shear wave splitting.

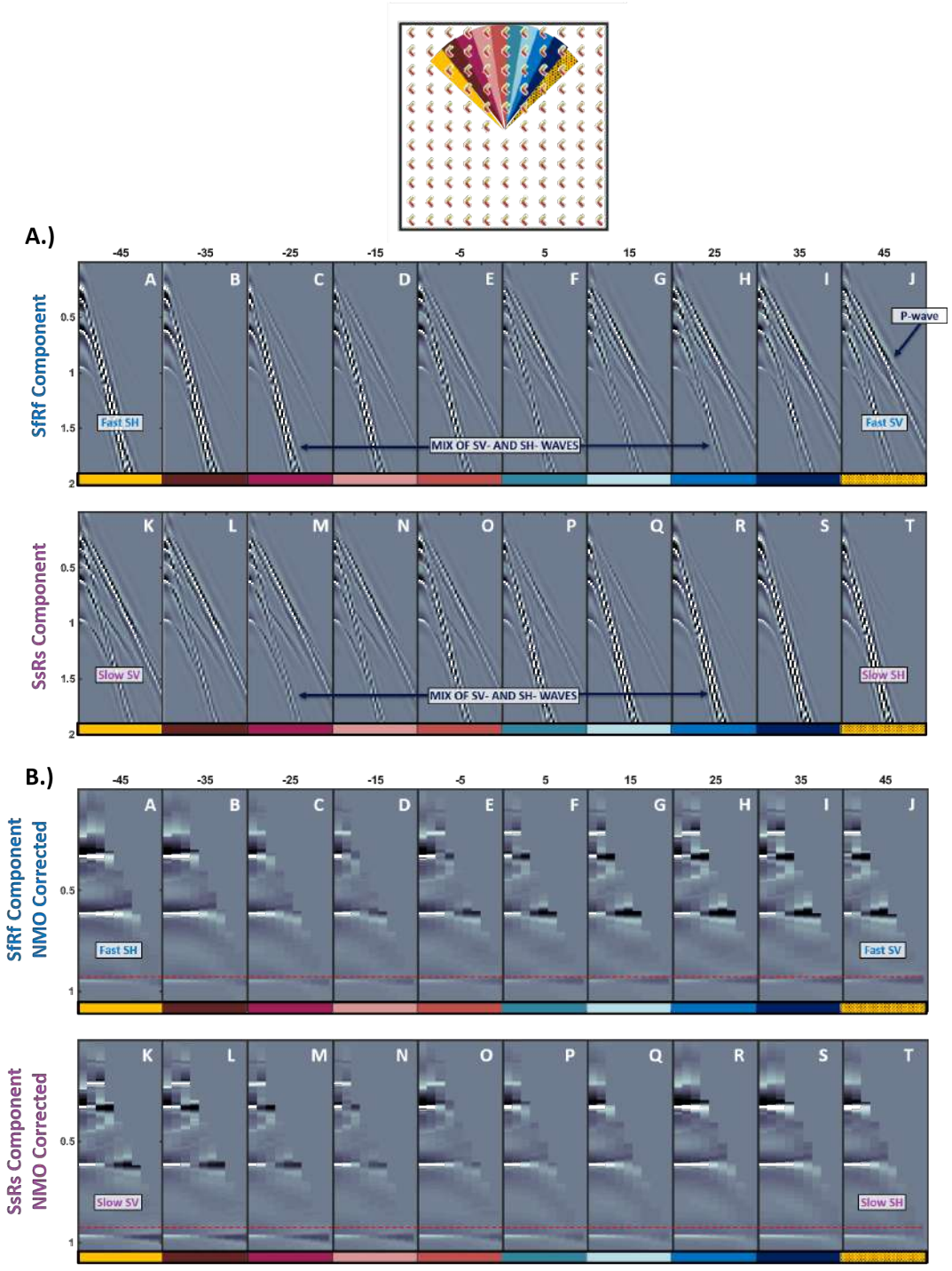

Figure 4.10: Comparison of F-S main components for source-receiver azimuths between -45 degrees (orthogonal to fracture strike) and 45 degrees (fracture strike). Azimuthal bins are colored coded in accordance with the basemap shown at the top. The principal azimuths (-45 and 45 degrees) are colored yellow. A.) Shot gathers and B.) Move out corrected shot gathers for the SfRf and SsRs components. SfRf component = fast shear waves and SsRs component = slow shear waves. Between the principal azimuths, a mix of SV- and SH-waves are recorded on both components.

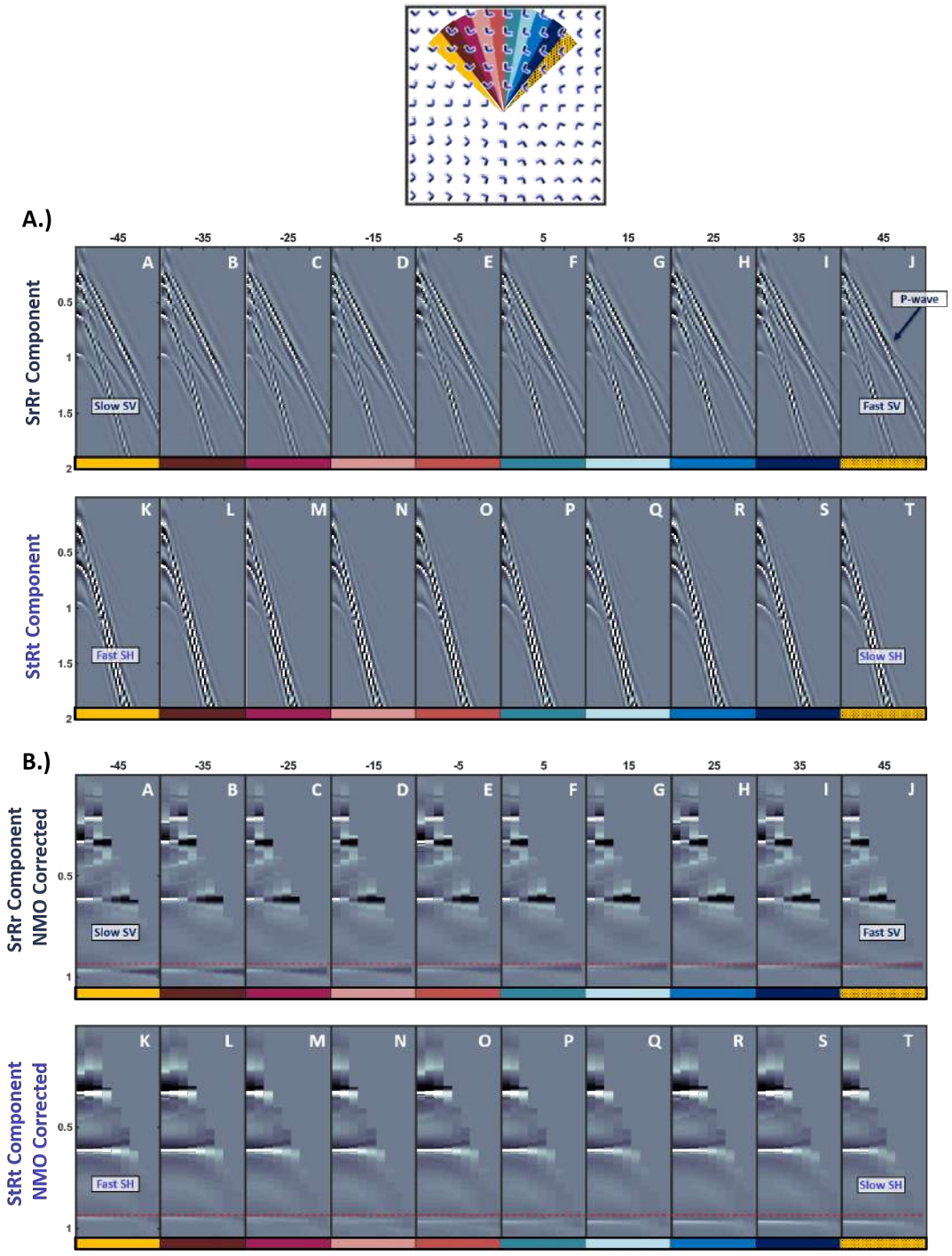

Figure 4.11: Comparison of R-T shot gathers for different source-receiver azimuths between -45 degrees (orthogonal to fracture strike) and 45 degrees (fracture strike). Azimuthal bins are colored coded in accordance with the basemap shown at the top. The principal azimuths (-45 and 45 degrees) are colored yellow. A.) Shot gathers and B.) Move out corrected shot gathers for the SrRr and StRt components. SrRr component = SV-waves and StRt components = SH-waves.

This mixing of shear wave modes has implications on both processing and interpretation. First, processing panels B-I and L-S in this F-S coordinate system is not meaningful. The SV- and SH-wave modes have different coupling and amplitude response that cannot be uniformly processed. In terms of interpretation, equations of linearized reflectivity (Ruger, 2002) are only applicable at the two principal azimuths where the fast and slow SV- and SH-wave modes are separated. There is no documented formula for the reflectivity at oblique azimuths and the information is neglected in amplitude interpretation.

Figure 4.11 shows shot gathers for different source-receiver azimuths in the R-T space. Panels A - J show the SrRr component which contains SV-waves for all azimuths. Panels K - T display the StRt component with SH-waves for all azimuths. Between the principal azimuths, the arrival times of the waves vary such that along fracture strike (45 degrees) the fast SV-wave is recorded on SrRr and the slow SH-wave is registered on StRt. Unlike the F-S coordinate system, the AVO responses in the R-T system are consistent for all azimuths.

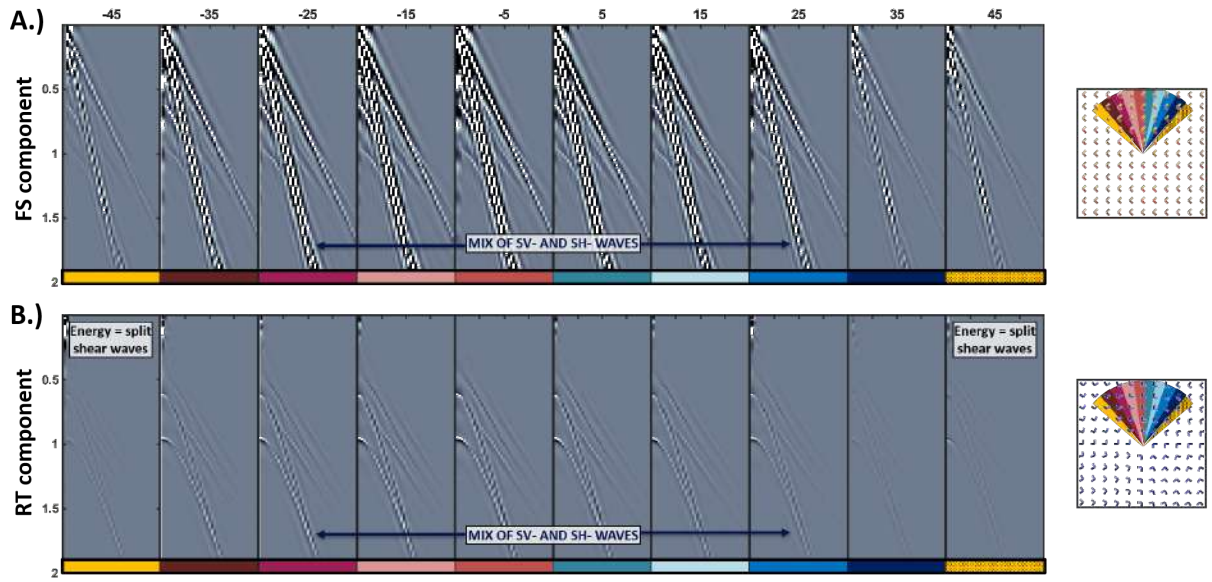

Figure 4.12: Comparison of cross-term shot gathers in F-S and R-T space. A.) FS cross-term and B.) RT cross-term. Energy exposed on the RT component at principal azimuths are indicative of shear wave splitting. Energy on the FS component is dominated by effects of variable source-receiver azimuth.

The comparison of FS and RT cross-terms for all source-receiver azimuths is shown in Figure 4.12. Cross-term energy in the F-S coordinate system is dominated by variable source-receiver azimuth whereas in the R-T coordinate system, the energy is indicative of split shear waves. This energy is minimized at the principal azimuths (yellow bins) and maximized at +/- 45 degrees from these azimuths (North azimuth on Figure 4.12)

4.4.3 Complex Fracture Model with Overburden Anisotropy

In the presence of overburden anisotropy, the radial-transverse system continues to separate the SV and SH modes whereas the modes in the F-S system remain azimuthally dependent. The four layer model with 45^o fractures in the third layer is extended to seven layers with the sixth layer having fractures oriented 105^o (Figure 4.13).

Figures 4.14 and 4.15 show the comparative shot gathers for a complex model with HTI overburden in F-S and R-T space. To obtain an F-S coordinate system (Figure 4.14), the data is rotated to the fast direction of the overburden anisotropy. Similar to observations made on the four layer model with one HTI layer, the F-S space produces a mix of SV- and SH-wave modes with asymmetric shot gathers on each component. The cross-terms in F-S space are dominated by energy related to the varying source-receiver azimuth for all receiver lines, including the 2-D line. In R-T space (Figure 4.15), the cross-terms expose split shear waves and the main components, SrRr and StRt, still separate the SV-waves and the SH-waves.

Overburden anisotropy does not limit the effectiveness of the R-T coordinate system in removing the source-receiver azimuthal effects and the system improves identification of shear wave splitting related to an HTI subsurface.

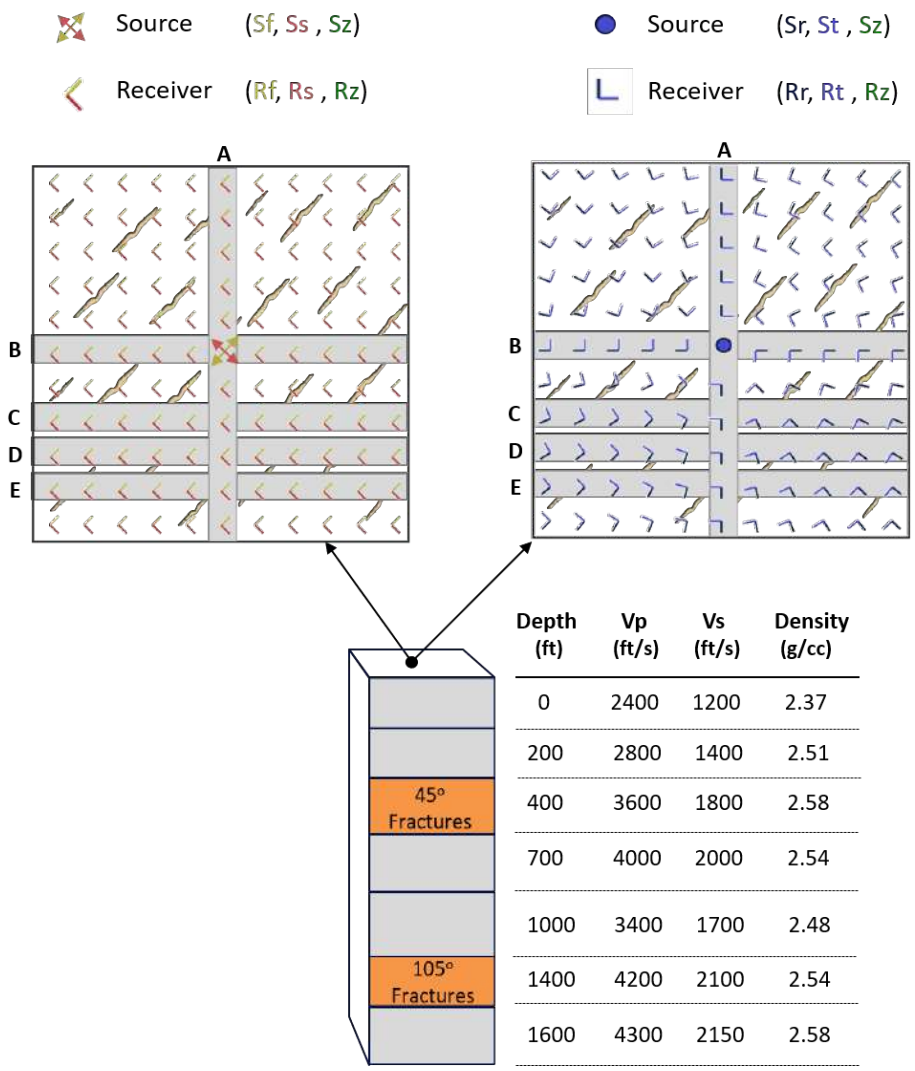

Depth (ft)	Vp (ft/s)	Vs (ft/s)	Density (g/cc)
0	2400	1200	2.37
200	2800	1400	2.51
400	3600	1800	2.58
700	4000	2000	2.54
1000	3400	1700	2.48
1400	4200	2100	2.54
1600	4300	2150	2.58

Figure 4.13: Description of the seven-layer model with the third layer containing 45^o-oriented fractures and the sixth layer containing 105^o-oriented fractures.

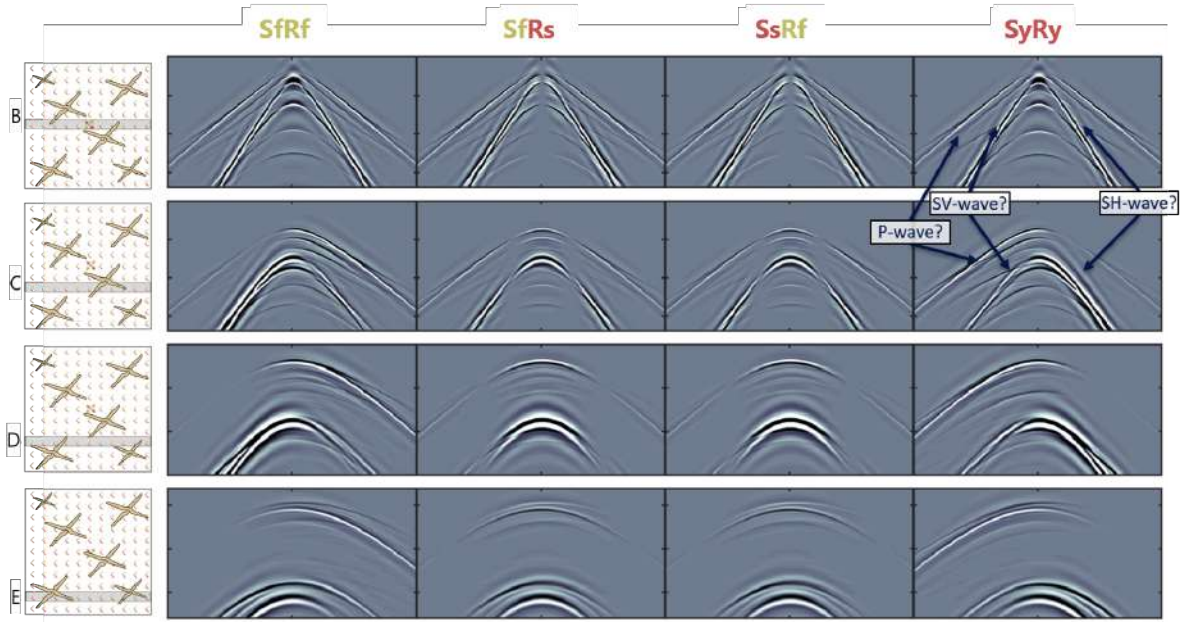

Figure 4.14: Gathers in F-S space (fast orientation 45 degrees) for inlines offset from the source location. The four-layer model contains one HTI layer with a fracture set oriented 45 degrees and a second fractured lower layer with 110 degree oriented vertical cracks.

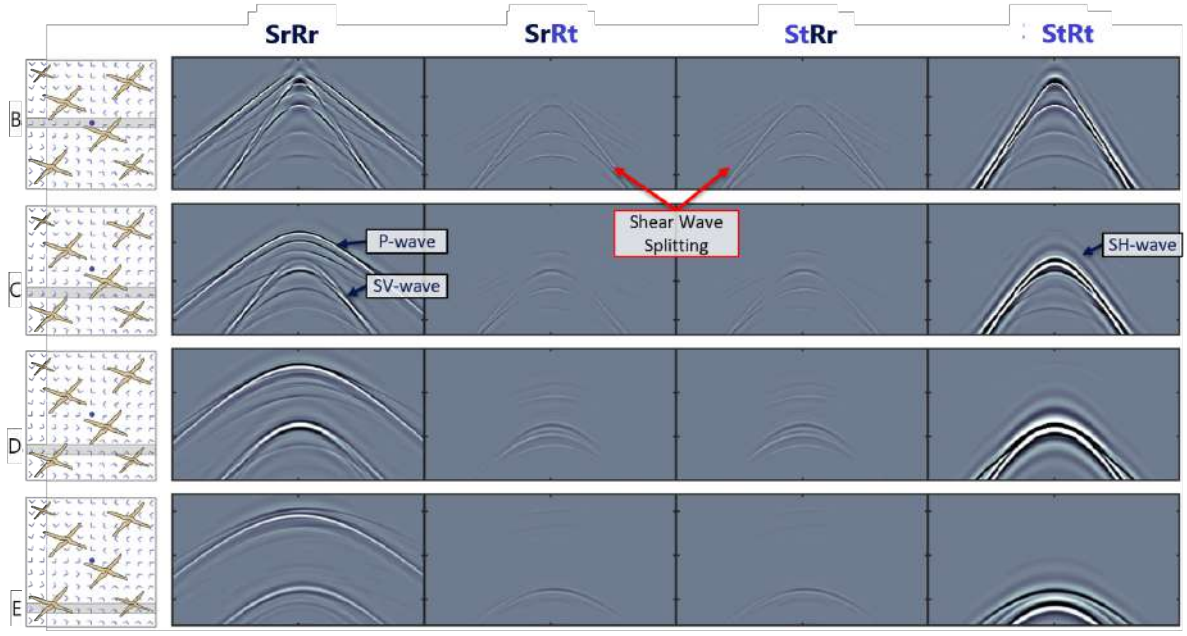

Figure 4.15: Gathers in R-T space for inlines offset from the source location. The four-layer model contains one HTI layer with a fracture set oriented 45 degrees and a second fractured lower layer with 110 degree oriented vertical cracks.

4.5 Conclusions

Acquisition coordinates record a mixture of SH-, SV- and P-waves which are irregularly recorded on different receiver stations. In the presence of anisotropy, the shear waves are more complicated as they split into fast (along fracture strike) and slow azimuths. A well-known industry solution is to rotate the data to fast-slow coordinates which separates the fast and slow arrivals and attempts to minimize cross-term components, but as shown in the HTI modeling with isotropic and anisotropic overburdens, this is not the case.

This system complicates interpretation as it mixes the shear wave modes which have unique kinematic and amplitude character. Although energy resolved on the cross-terms is considered a primary indicator of shear wave splitting and fracture presence, modeling reveals that the cross-term energy in F-S space is dominated by the varying source-receiver orientations. Azimuthal anisotropy is masked by geometry effects and interpretation for fracture presence is not easily obtained.

A fundamental problem associated with this technique is finding the fast-slow coordinates. A common method is to rotate the data to a regional stress orientation under the assumption that the seismic is sensitive to this subsurface stress state. This is a high risk and incorrect assumption in most cases. Another method is to use interpreted azimuthal information from the seismic data to define a fast orientation. To get to this interpretative space, the data may have been preprocessed in X-Y coordinates which is incorrect. Ideally, the data should be pre-processed in R-T coordinates which removes the signal dependence on source-receiver azimuth and separates the wave modes (SV and SH) onto different receiver components.

Azimuthal stacking in the R-T system allows us to examine azimuthal variations of the seismic data and identify a fast orientation (if any) to which the seismic responds. The next chapter introduces this R-T azimuthal stacking for interpretation of HTI anisotropy on multicomponent data. Using a simplified Niobrara model, a resolution study is presented with a focus on the added value of shear components to interpretation of thin anisotropic layers.

CHAPTER 5

9-C SYNTHETIC STUDY OF THE NIOBRARA-CODELL VVAZ

Increased production in the unconventional Niobrara reservoir of the Wattenberg Field is correlated to higher fracture conductivity (Alfataierge, 2017). 3-D seismic methods are thus essential for mapping fracture networks with the ultimate focus being to update and validate reservoir simulations. I define a fractured medium as being horizontally transverse isotropic (HTI) and present a velocity approach for fracture detection.

The azimuthal variation of shear waves produced by shear wave splitting in HTI media is complementary to the P-wave VVAz response. The P-wave response, whether analyzed as limited-azimuth stacks (LAS) or common-offset, common-azimuth bins (COCA) may not uniquely identify fractures and loses sensitivity as the thickness of the fractured interval decreases (Williams and Jenner, 2002).

I examine converted and shear wave data in the R-T domain and study their response to HTI media. I demonstrate the complementary HTI-related interpretations on LAS and COCA displays of all wave modes using the same model implemented by Simmons (2009) with only the shallow HTI layer. To determine the expected VVAz response of the Niobrara-Codell reservoir on field data, I build a simplified Niobrara model and discuss the interpretation in LAS and COCA displays for changing thicknesses of the HTI intervals.

To simplify notation from this point forward, the following terminology will be used to identify the components in R-T space.

For the P-waves: $S_zR_z \equiv ZZ$

For the converted P-waves: $S_rR_z \equiv RZ$ and $S_tR_z \equiv TZ$

For converted waves: $S_zR_r \equiv ZR$ and $S_zR_t \equiv ZT$

For the pure shear waves, $S_rR_r \equiv RR$, $S_rR_t \equiv RT$, $S_tR_r \equiv TR$ and $S_tR_t \equiv TT$.

5.1 Azimuthal Stacking for Anisotropic Interpretation

Velocity variation with azimuth (VVAz) is the difference in arrival time with azimuth of a single reflection. It occurs because the particle motion of waves relative to the isotropy (parallel to fractures) and symmetry planes (perpendicular to fractures) determine whether the reflected wave is fast or slow (Tsvankin, 2012). Azimuths that are oblique to the principal fracture orientations of the HTI media show a changing travel time variation with azimuth. VVAz effects are observed at reflections below the fractured medium since waves must propagate through the fractures for travel time variations to occur.

At most, industry uses only seven of the nine components to assess VVAz and shear wave splitting. The two other components, RZ and TZ, contain the S-P converted waves generated from horizontal point forces (Chapter 3, Section 3.3). Since this mode is obtained from the shear waves sources, it is of lower temporal frequency as horizontal vibes typically do not shake to frequencies as has high as the vertical vibe. In this section, I show these components but do not interpret them for VVAz effects.

5.1.1 Limited Azimuth Stacks

Binning rotated prestack data (which have been NMO corrected) by azimuth and then stacking over offset allow us to observe the reflection of a layer at all azimuths and identify VVAz effects. This binning arrangement is referred to as limited azimuth stacks (LAS) where each trace represents the full offset stack for that azimuthal bin (Figure 5.1).

Conventional LAS displays (Figure 5.2) are generated using an outer mute typically at the angle of the SV-wave (RR) polarity reversal since stacking over the polarity reversal will cancel the signal. At near incidence, vertically propagating P-waves are not affected by vertical fractures and no VVAz effect is observed. Unlike P-waves, converted and shear waves are sensitive to fractures at near offsets since their particle motion is horizontal and is affected by the vertical fracture planes.

For the main converted and shear wave components (ZR, ZT, RR and TT) at near offsets, a reflection below the HTI layer will exhibit sinusoidal character associated with travel time variation as a function of azimuth. For a source-receiver azimuth parallel to fracture strike, the SV-waves are fast since particle motion is uninhibited by the fractures. For these SV data components (ZR and RR as shown in Figure 5.2), the fast arrivals of the sinusoidal reflection in LAS displays are the fast SV-waves traveling parallel to fracture strike. Conversely, the TT component (Figure 5.2), which registers SH-waves, exhibits sinusoidal character that is 90-degrees shifted to the RR component. For a source-receiver azimuth parallel to fracture strike, the SH-wave particle motion is perpendicular to the fractures and the velocities are slowed due to interaction with the fracture plane. These slow SH-waves are observed as slow arrivals on the sinusoidal reflections of the TT LAS displays.

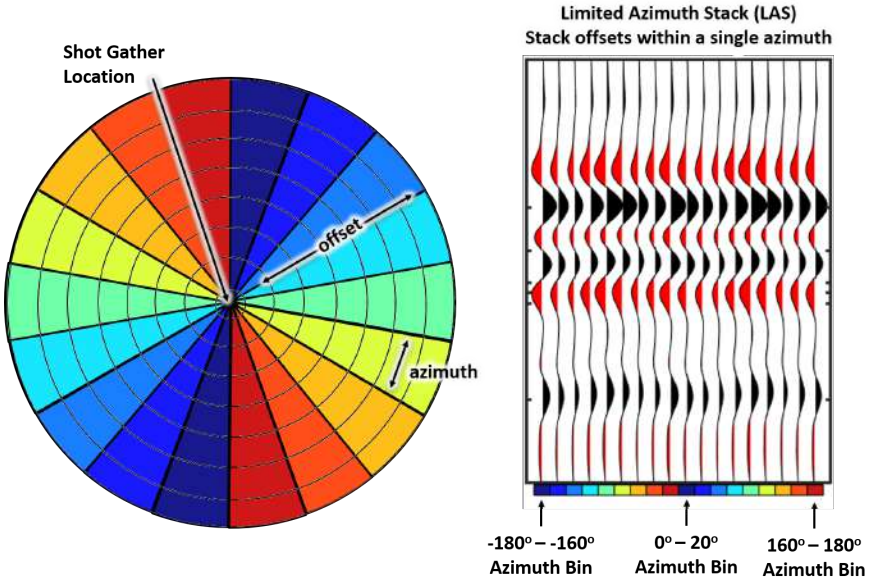

Figure 5.1: Description of Limited Azimuth Stack. Each trace represents an offset stack for a single azimuth bin. The northern direction is plotted in the center of the LAS display.

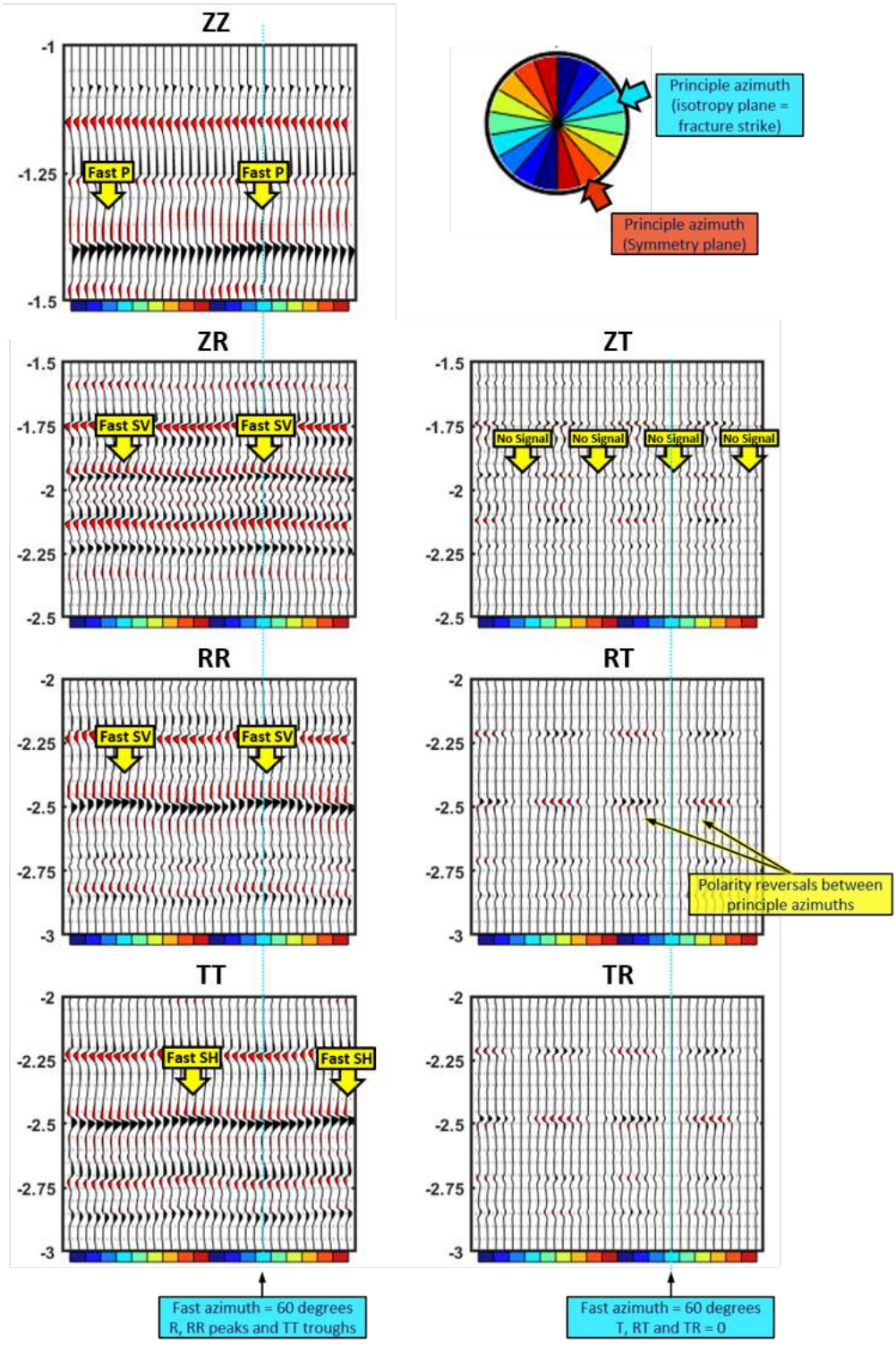

Figure 5.2: Limited Azimuth Stacks for seven data components in R-T space (RT=TR) at the same gain. Vertical red bars indicate the interval of the fractured layer and the color bar at the base of each panel shows the azimuthal binning. The yellow bin indicates the 110 degree azimuth parallel to fracture strike. Note the different time scales for the P-wave, converted wave and shear waves components.

The model demonstrated in Figure 5.2 is that implemented by Simmons (2009) with only the shallow HTI layer. The fracture strike in this layer is oriented along the 60 degree azimuth and the fractured interval is 150m thick. For this example, the converted waves approximate a travel time variation of 9.8ms between the fast and slow arrivals and the shear waves approximate a 16ms travel time variation. In this model, the cross-term amplitudes are relatively weak with the converted wave R/T ratio being approximately 2 and the shear wave RR/RT ratio approximating to 1.8. For the Niobrara reservoir which is considerably thinner, the travel time variation is expected to be smaller and the cross-term amplitudes significantly weaker.

Converted and shear wave cross-terms (ZT, RT and TR) are also sensitive to vertical fractures at near offsets. Along the isotropic or symmetry planes (principal azimuths), no energy will be observed on the LAS (Figure 5.2). That is, no split shear waves occur at these azimuths and all shear wave energy is concentrated onto the main data components (ZR, RR and TT). At all other source-receiver azimuths oblique to the principal azimuths, the vertical fractures causes shear-wave splitting which is observed as energy polarized onto the ZT, RT and TR terms where RT=TR. The polarity of the cross-term components reverse between the principal azimuths due to the source-receiver azimuth relative to the principal fracture directions. The cross-terms have maximum amplitude at azimuths +/- 45 degrees relative to the principal directions.

Limited azimuths stacks can be interpreted for the two principal azimuths by first identifying the azimuths with no energy on the cross-terms. Within a 0-360 degree azimuthal range, there are four azimuthal degrees that should align with the principal azimuthal planes and show 'null' traces (ZT=0, RT=0 and TR=0). For these principal azimuths, we can identify which principal azimuth is parallel or perpendicular to fracture strike by analyzing the ZR, RR and TT components. The principal azimuth that correlates to fast arrivals on the ZZ, ZR and RR components and slow arrivals on the TT component is the fracture strike orientation. Sinusoidal character on an LAS that are indicative of HTI layer should thus

show two fast azimuths and two slow azimuths within a 0 to 360-degree range.

Wave kinematics control the VVAz character on LAS displays for all wave modes. P-wave interpretation of limited azimuth stacks may not resolve a fractured medium if the applied mute is severe as shown in Figure 5.2 however, as offset increases, the P-wave particle motion rotates in the radial-vertical plane and the particle motion begins to interact with the vertical cracks.

If shear data is acquired (3-C or 9-C), several components are produced (ZR and ZT or RR,TT,RT and TR) and all components can be uniquely interpreted for the principal azimuths. Shear-wave interpretation, where all components conclude with the same 'story', provides a better constrained solution that complements the single P-wave interpretation.

Whether we have only P-wave data or multicomponent data, it benefits and constrains the interpretation to not only examine the VVAz changes on all components but at all offsets. Overburden anisotropy, lateral velocity variations, tilted cracks or multiple fractures can change the VVAz signature with respect to offset on all data components. For this modeling, we have assumed a flat-layered earth with isotropic overburden and HTI reservoir. As such, we expect a VVAz response for all offsets on the converted and shear wave components and an onset VVAz response starting at mid offsets for the P-wave component.

5.1.2 Common-Offset, Common-Azimuth Gathers

Common-offset, common azimuth gathers (COCA) preserve azimuth and offset information by sectoring NMO corrected, prestack data by offset and then stacking over azimuth within each offset plane (Cheadle et al., 2000) (Figure 5.3). The COCA display extends the offset stack by adding the third dimension of azimuth (Gray, 2007) and can be used as quality control for NMO and visualization of azimuthal anisotropy. The stacking over azimuth also improves the signal to noise ratio and we can now visualize the changes in VVAz character for all offsets as shown in Figure 5.4.

In COCA displays, the P-wave (ZZ) shows the onset of VVAz signature at mid to far offsets while the converted and shear components show SV and SH VVAz at all offsets (Figure

5.4). The converted and shear cross-term components expose anisotropy at all offsets in the form of polarity reversals.

Within each offset plane, the principal azimuth interpretation is similar to that described in the limited azimuth stack analysis. The location of the ZT, RT and TR polarity reversals within each offset plane are aligned with the principal azimuths. Additionally, RT=TR as observed on the LAS displays. ZZ, ZR and RR fast arrivals on the sinusoidal VVAz character are aligned with fracture strike and the TT fast arrivals occur at azimuths perpendicular to fracture strike (Figure 5.4). The RR COCA gather preserves the polarity reversal on the SV-data associated with the P-wave coupling described in Chapter 3, Section 3.3. SV-wave VVAz character strengthens beyond this critical angle.

In general, azimuthal velocity analysis requires dense sampling of azimuths and offsets (Gray, 2007) as opposed to amplitude analysis (Amplitude Variation with Azimuth, AVAZ) that provide higher resolution interpretations. Shear wave VVAz analysis, however, should not be discounted based on lack of VVAz exposure on P-wave data. The next section presents the added value of shear VVAz analysis to fracture interpretation by modeling thin Niobrara HTI layers which are still detected on the shear components as opposed to the P-wave data.

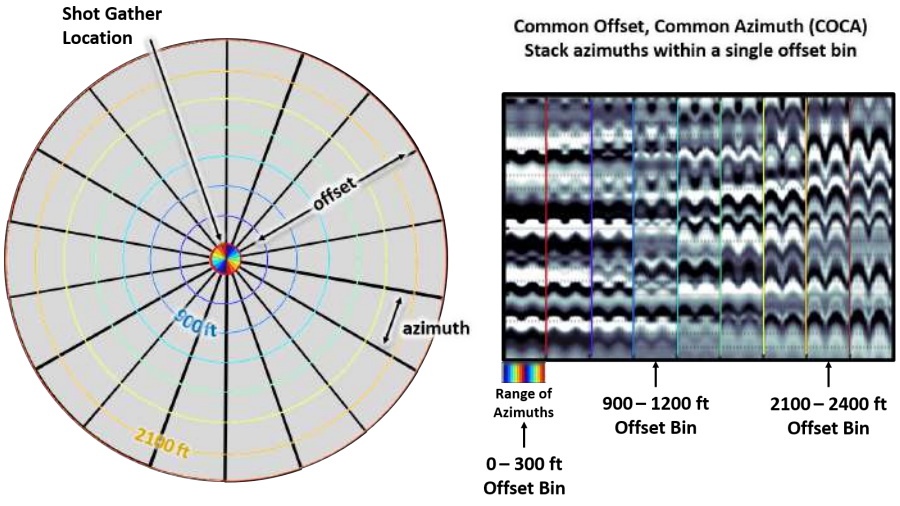

Figure 5.3: Description of COCA gather for the SV-wave or RR component. Azimuths are colored at the center of the pie chart and are shown below the data of the 0-300ft offset bin.

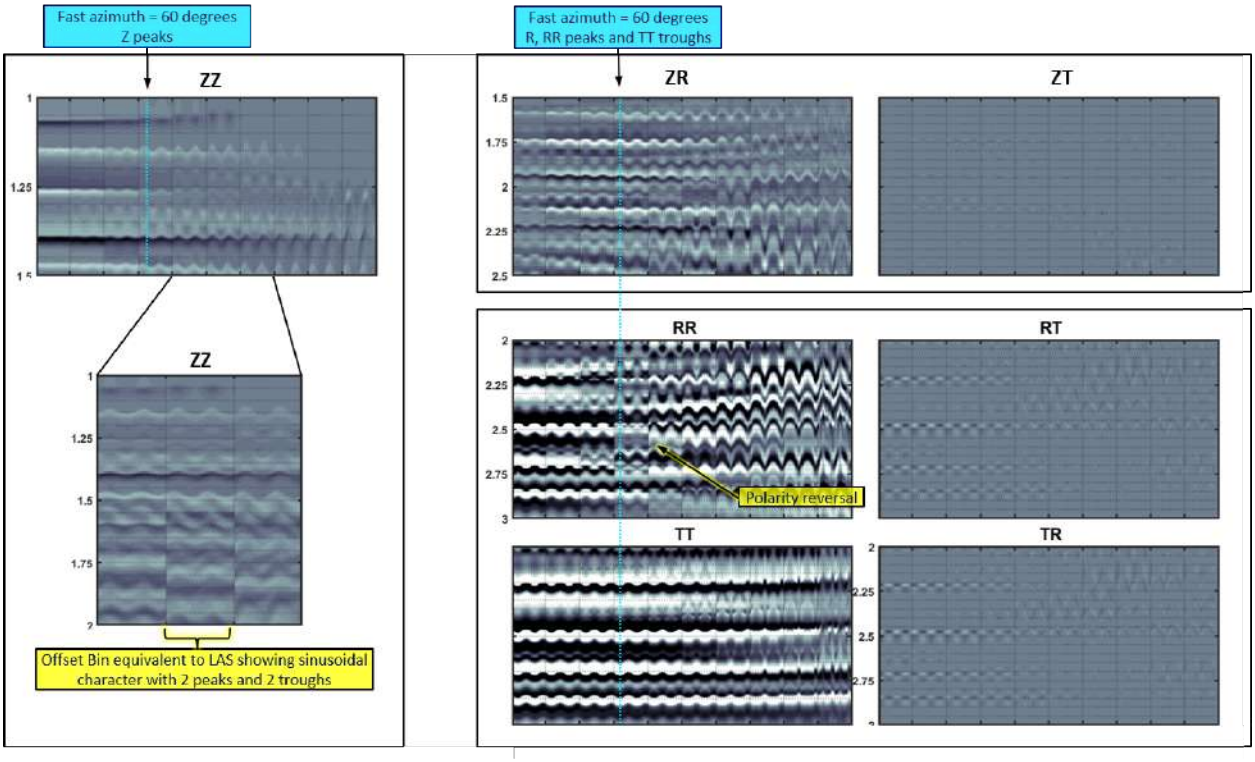

Figure 5.4: Common-Offset, common-azimuth gathers for seven data components in R-T space (RT=TR) at the same gain. Vertical red bars indicate the interval of the fractured layer and the color bar at the base of each panel shows the azimuthal binning. The yellow bin indicates the 110 degree azimuth parallel to fracture strike. Note the different time scales for the P-wave, converted wave and shear waves components.

5.2 Simplified Niobrara Earth Model

An eleven layer model representative of the Niobrara-Codell stratigraphy in the Wattenberg Field is used to assess velocity variations with azimuth (VVAz) due to fracturing in the reservoir. The 1D model consists of an isotropic overburden constraining the fractured reservoir interval. All layers of the model are described in Figure 5.5 and Table 5.1, with the fractured Niobrara-Codell layers highlighted in orange.

The modeling algorithm is the reflectivity method used and described in Chapter 3, Section 3.2. A single set of vertical fractures oriented N70W (-70 and 110 degree azimuths) is added to an isotropic Niobrara background. This orientation is aligned with the interpretation of induced fracture strikes in the Niobrara interval (Chapter 2, Section 2.4.1). Hudson's

fracture model was used to populate each Niobrara layer with a crack density of .04, crack aperture of .01, and gas fill. The density may be interpreted as the area occupied by a crack per unit volume and in this case, the value is an upscaled estimate from the Wishbone discrete fracture network model (Grechishnikova, 2017). The fracture aperture and gas fill estimates are used to compute the fracture compliance which is translated to stiffness coefficients for input into the reflectivity modeling.

Prior to interpretation, the isotropic overburden was removed by generating synthetics for the first layer of the model and subtracting these from the synthetics generated using the full model. While this is not an exact method of layer stripping it does eliminate the head waves which are the primary signal masking the shear wave data. The nine component data sets in acquisition coordinates were then rotated to radial-transverse (R-T) coordinates. Each rotated data set was move-out corrected using ray-tracing.

Gain Treatment

The Niobrara reservoir is thin compared to the example models shown previously. The VVAz is very weak and the cross-term components have very weak amplitude responses compared to the main components. To demonstrate this weak VVAz, some figures in this section display all components on the same gain (no amplitude adjustment is made to any component). To best visualize the VVAz character on the cross-term components, in some figures, the gain on these cross-term components are multiplied by five (x5). The gain is described in each figure caption and where the cross-terms are gained x5, there is an added yellow label to the top right corner of the component display.

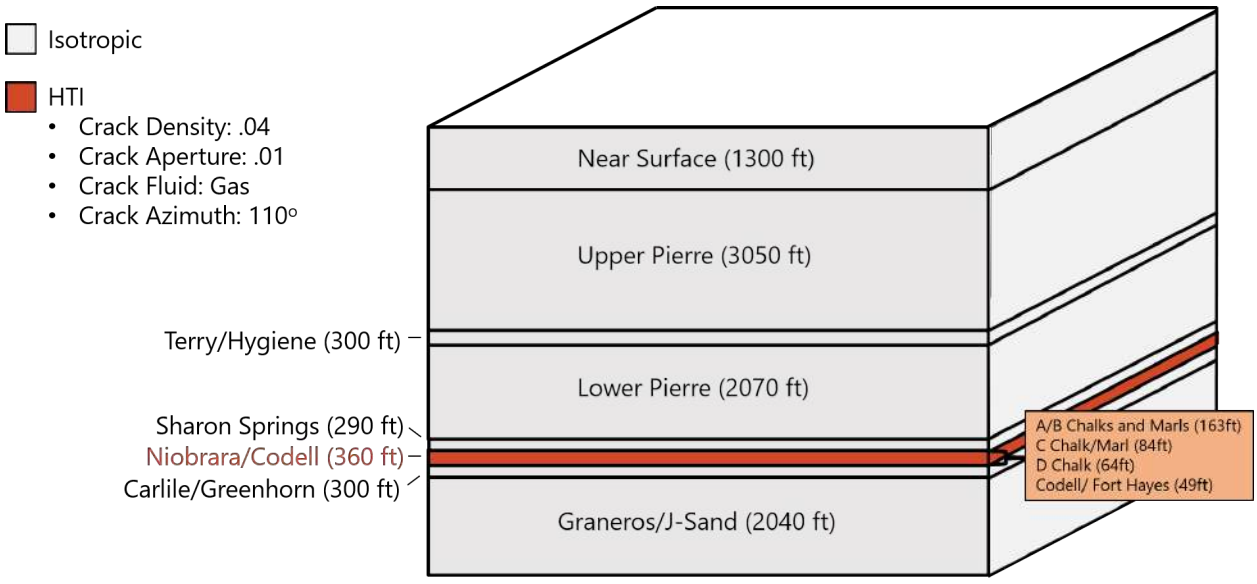

Figure 5.5: Eleven layer Niobrara earth model with a single fracture set oriented 110^o (N70W) from Niobrara Top to Codell base. The layer parameters are extracted and upscaled from a real well located in the Wattenberg Field.

Table 5.1: Interval Properties of the eleven layer Niobrara model. Highest reflectivities within the reservoir are observed at the top of the Niobrara D and Fort Hayes/Codell layers

	Thickness (m)	**Interval Vp (m/s)**	**Interval Vs (m/s)**	**Density (g/cm^3)**
Near Surface	396.42	2634.6	1238.84	2.37
Upper Pierre	928.41	3292.72	1679.38	2.51
Terry/Hygiene	89.95	3540.85	2032.01	2.55
Lower Pierre	629.83	3570.22	1978.57	2.58
Sharron Springs	89.17	3314.24	1864.72	2.57
Niobrara A/B	49.76	4273.37	2428.11	2.51
Niobrara C	25.54	4118.4	2345.62	2.51
Niobrara D	19.43	4718.81	2576.47	2.64
Fort Hayes/ Codell	14.83	3829.81	2229.76	2.54
Carlile	92.19	3797.6	2126.79	2.58
Graneros	621.22	4050.76	2384.93	2.54

Figure 5.6 show the LAS displays for the nine data components generated. In this figure, the cross-terms are gained the same as the main components and the RZ and TZ components are shown but not evaluated for HTI interpretation. The Niobrara and Graneros reflectors are marked on all plots by the blue and orange arrows. The vertical extent of the fully cracked Niobrara-Codell interval (360ft or 110m) is represented by the red bar.

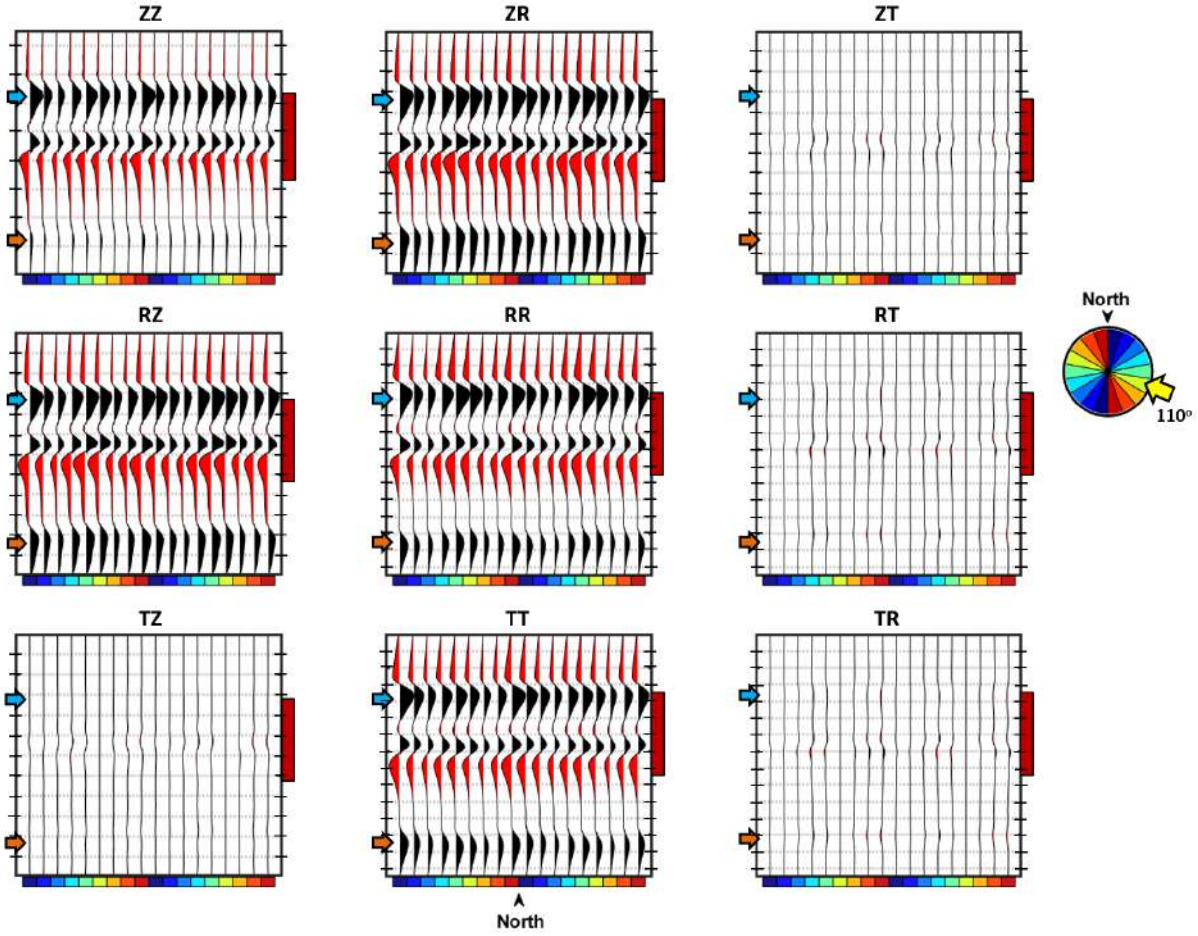

Figure 5.6: Limited Azimuth Stacks for nine data components in R-T space. All panels have the same gain applied such that amplitudes are comparable (cross-term amplitudes are relative to the main component amplitudes). The time interval for each component shows the Niobrara (blue arrow) to Graneros (orange arrow) horizons and timing lines for all panels are 20ms apart. Vertical red bars indicate the interval of fractured Niobrara and the colorbar at the base of each panel shows the azimuthal binning. The yellow bin is the 110 degree azimuth parallel to fracture strike.

The azimuthal variations are more evident once the stacks are zoomed as shown in Figure 5.7. Six of the nine components are shown since the RZ and TZ components are not typically processed in field data and RT = TR. A bandpass filter of 2/4-50/70 is applied to the P-wave, 2/4-30/40 is applied to converted wave components and 2/4-20/30 is applied to the shear wave components. Evidence of anisotropy in the Niobrara interval is exposed at the strong Graneros reflector for the converted and shear waves. P-wave VVAz is most significant at the reflector at the base of the Niobrara-Codell interval.

ZZ, ZR and RR fast azimuths (fast P-waves and SV-waves) occur at the 110 degree azimuth (along fracture strike). TT fast azimuths (fast SH-waves) occur at the 30 degree azimuth (perpendicular to fracture strike). The cross-term components in Figure 5.7 are gained x5 (RT amplitude = 5 x RR amplitude, TR amplitude = 5 x TT amplitude, ZT amplitude = 5 x ZR amplitude) to show the polarity reversals between principal azimuths (30-degree and 110-degree azimuths).

The COCA displays for the nine components are shown in Figure 5.8 and the six components (RT = TR) typically used in industry are zoomed in Figure 5.9 to show VVAz effects. The P-wave VVAz signature is onset around 1200 m offset, however, the decreasing amplitude with offset makes the signature less noticeable. The converted and shear wave amplitudes remain high at all angles and expose consistent VVAz character at all offsets. Within each offset plane, the two fast azimuths on the sinusoidal reflections for the ZZ, ZR and RR components occur at the same 110-degree and 290-degree azimuth (N70W direction). At these azimuths, slow arrivals on the sinusoidal TT reflections are observed for all offset bins.

Both the LAS and COCA observations for the Niobrara model align with the expected VVAz responses for all components. This initial model assumes that the Niobrara is fully cracked however, it is unconfirmed whether this is the case for the Wishbone section. In the next section, I model the VVAz response for changing fractured intervals to assess the minimum thickness below which VVAz is indistinguishable on the various components.

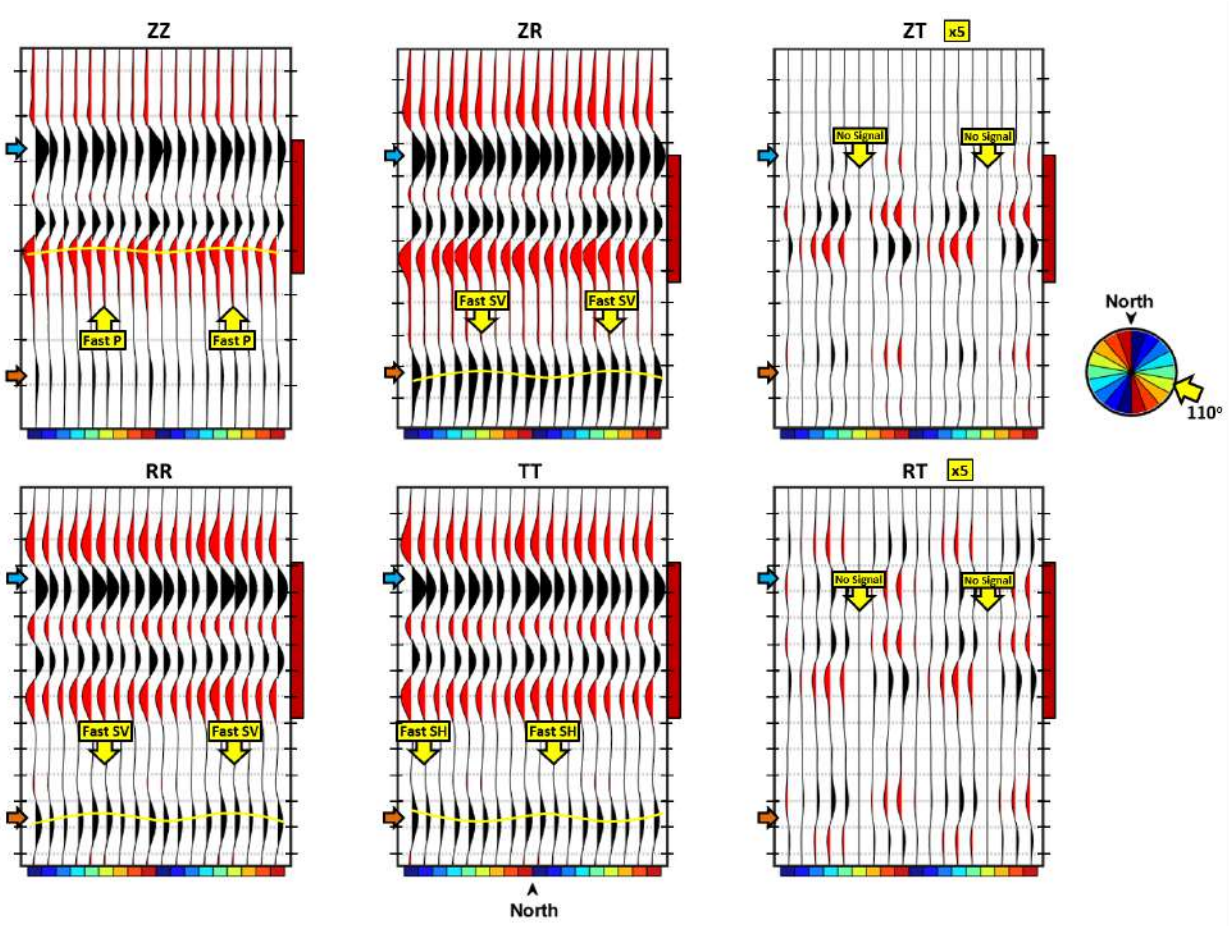

Figure 5.7: Bandpass filtered Limited Azimuth Stacks for six data components in R-T space. The VVAz for the Niobrara is relatively small and the cross-terms (T and RT) are gained x5 to show the VVAz effects. The time interval for each component shows the Niobrara (blue arrow) to Graneros (orange arrow) horizons and timing lines for all panels are 20ms apart. Yellow trendlines along the Graneros horizon highlight sinusoidal VVAz effect.

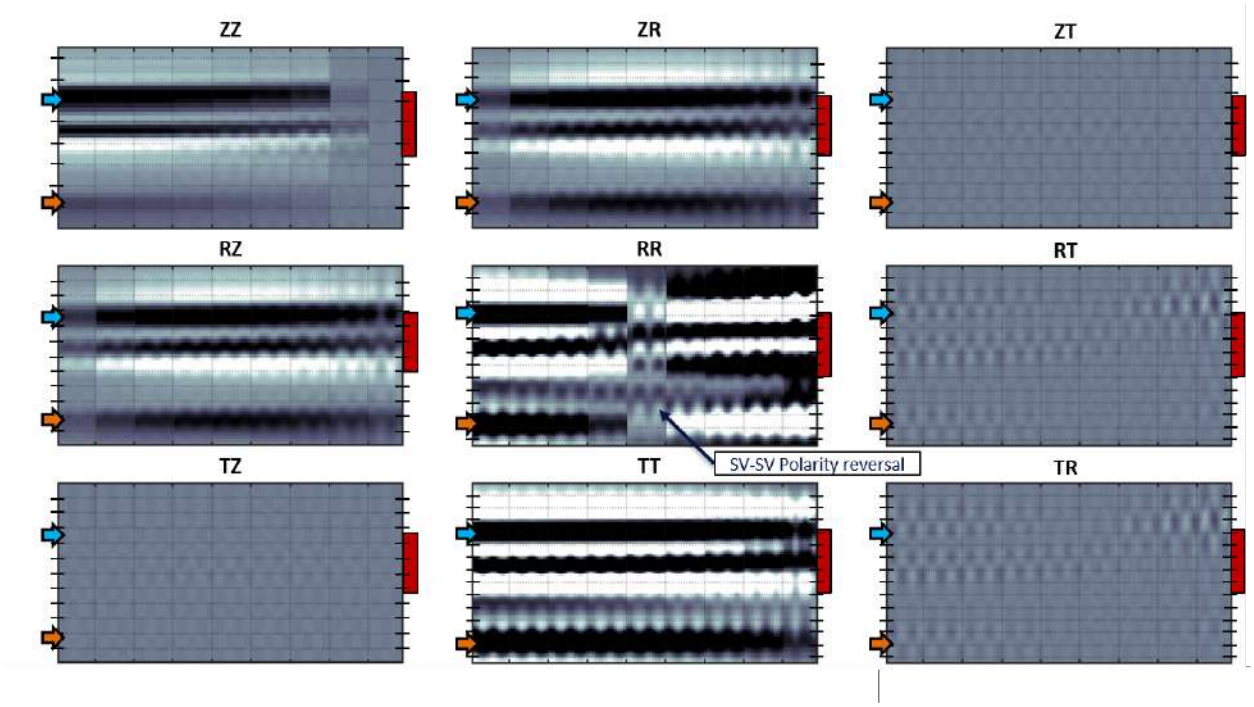

Figure 5.8: Bandpass filtered COCA displays for nine data components in R-T space. All panels have the same gain applied such that amplitudes are comparable (cross-term amplitudes are relative to the main component amplitudes) The time interval for each component shows the Niobrara (blue arrow) to Graneros (orange arrow) horizons. Timing lines for all panels are 20ms apart and offset bins of 300m are defined by light gray vertical lines.

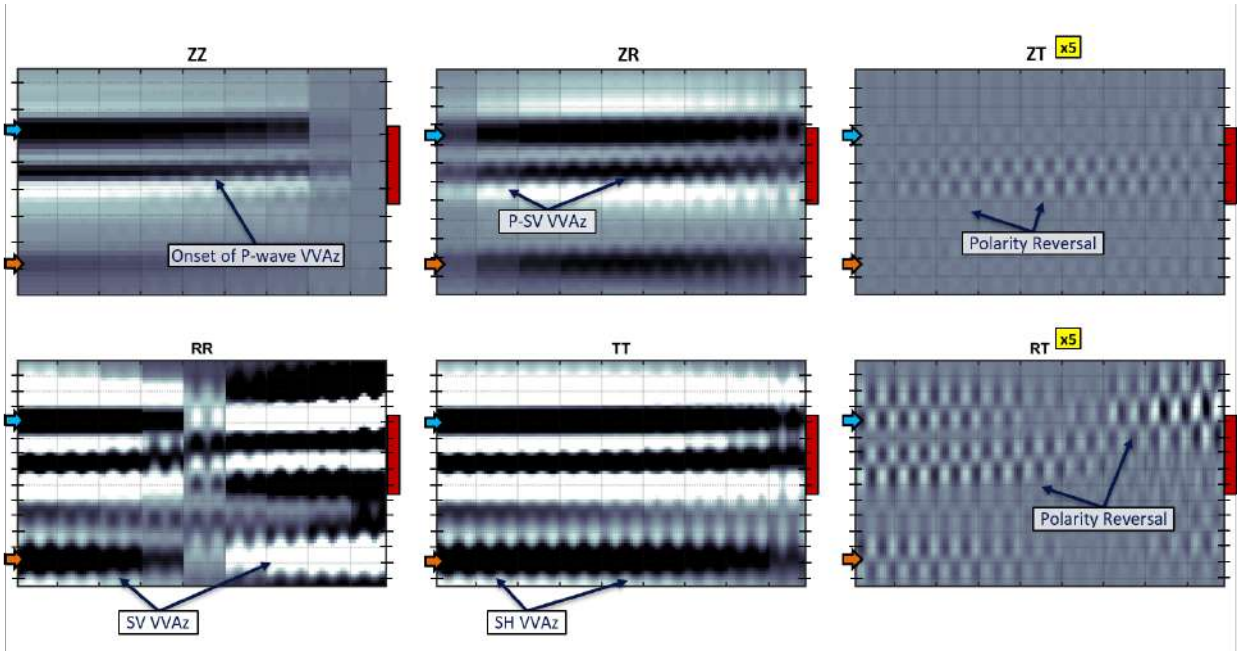

Figure 5.9: Bandpass filtered COCA displays for six data components in R-T space. The VVAz for the Niobrara is relatively small and the cross-terms are gained x5 to show the VVAz effects.

5.3 Thickness Modeling: Value added by Shear Components

It is well documented by Alfataierge (2017) and Ning (2017) that increased production of the Wishbone Niobrara wells is correlated to higher fracture conductivity and mapping natural and induced fracture networks should be prioritized for improved well placement and performance. The results of hydraulic fracturing simulation of three Wishbone Niobrara wells is shown in Figure 5.10 (Alfataierge, 2017). The model used for simulation is structurally and stratigraphically accurate to the Wishbone section with spatially varying elastic parameters and completion parameters input to the simulation are those used in the field for each well. The estimated fracture heights range from 6 meters (20 feet) to 40 meters (130 feet) in unfaulted zones. Based on these results, four variations of the Niobrara model with 110m, 50m, 25m and 12m thicknesses of the fractured reservoir is described in Table 5.2. The synthetics generated from these models illustrate the VVAz sensitivity of the various wave modes as the fractured interval thins.

For all models, the largest VVAz character is observed on the converted and shear wave components (Figure 5.11). The VVAz character on the shear data remains significant when the HTI medium thins to less than 25m unlike the P-data. With a 110m cracked Niobrara (red model), P-wave VVAz is onset at 1200m offset whereas with a 50m cracked interval (purple model), resolvable VVAz effects start at 1500m offset. Below 50m HTI (green and blue models), VVAz effects are indistinguishable on P-wave data at any offset range. It becomes increasingly difficult to identify thin bed anisotropy on the P-wave components, although the shear wave components maintain distinguishable VVAz at all offsets. Beyond the angle of SV-wave polarity reversal on the RR component, the VVAz response remains particularly strong even at thin HTI layers less than 12m thick. This suggests that the large incidence angle shear wave components may potentially contain valuable information that is

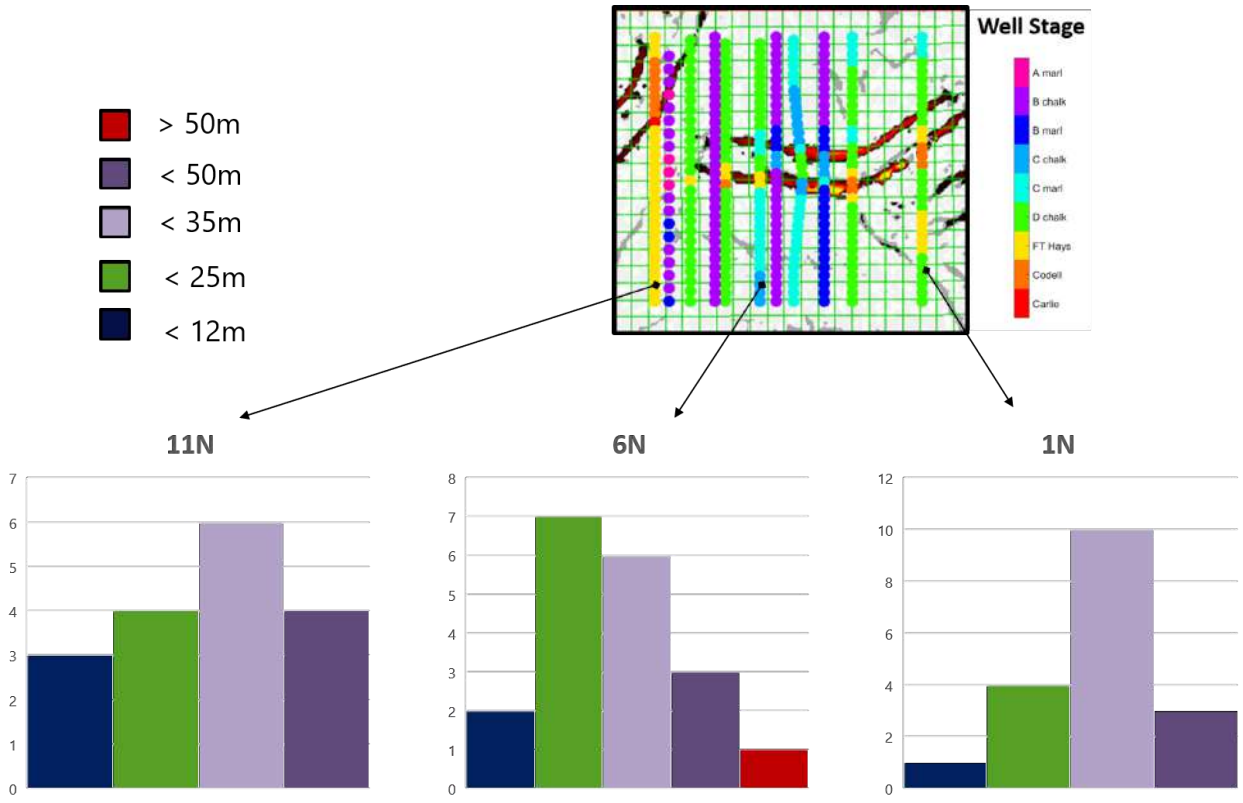

Figure 5.10: Simulated fracture properties including heights from 3 Niobrara wells in the Wishbone Section (Alfataierge, 2017).

Table 5.2: Anisotropic Properties of 3 Variations of Niobrara Model

	Model 1 Anisotropy	**Model 2 Anisotropy**	**Model 3 Anisotropy**	**Model 4 Anisotropy**
Overburden Layers	Isotropic	Isotropic	Isotropic	Isotropic
Niobrara A/B	50m HTI	50m HTI	25m HTI	12m HTI
Niobrara C	25m HTI	Isotropic	Isotropic	Isotropic
Niobrara D	19m HTI	Isotropic	Isotropic	Isotropic
Fort Hayes/ Codell	15m HTI	Isotropic	Isotropic	Isotropic
Lower Layers	Isotropic	Isotropic	Isotropic	Isotropic

typically muted out when creating conventional LAS displays.

The cross-terms of the converted and shear data (ZT, RT and TR) for all models show polarity reversals in the fractured medium. Although the amplitudes of this cross-term response is weaker for thinner fracture intervals, the polarity reversals are still noticeable for the thinnest model (12m HTI) and ZT, RT and TR remain primary indicators of splitting. The cross-term energy is weaker for smaller shear-wave splitting and it may be increasingly difficult to recognize HTI anisotropy on field data due to the smaller signal to noise ratio.

An interesting observation on the shear data sets is the reflection at which VVAz is observed, changes with the thickness of the fractured interval. For the ZR, RR and TT components, the Graneros reflector shows the largest VVAz effect for the 110m HTI model. As the HTI layer thins, the effect is less noticeable on the Graneros and more apparant on shallower reflectors within the Niobrara. With a 12m HTI layer, the VVAz effect is observed at the top of the Niobrara.

I suspect this observation to be a result of the vertical resolution of the shear data and the constructive interference between a weak Niobrara layer containing the VVAz effect and the stronger reflector at the Niobrara top. HTI manifests itself as travel time variations with azimuth which is dependent on both change in velocity and depth. Shear data not only detects anisotropy through velocity variations but can possibly be used to determine the vertical extent of the anisotropy by locating the VVAz signature in depth.

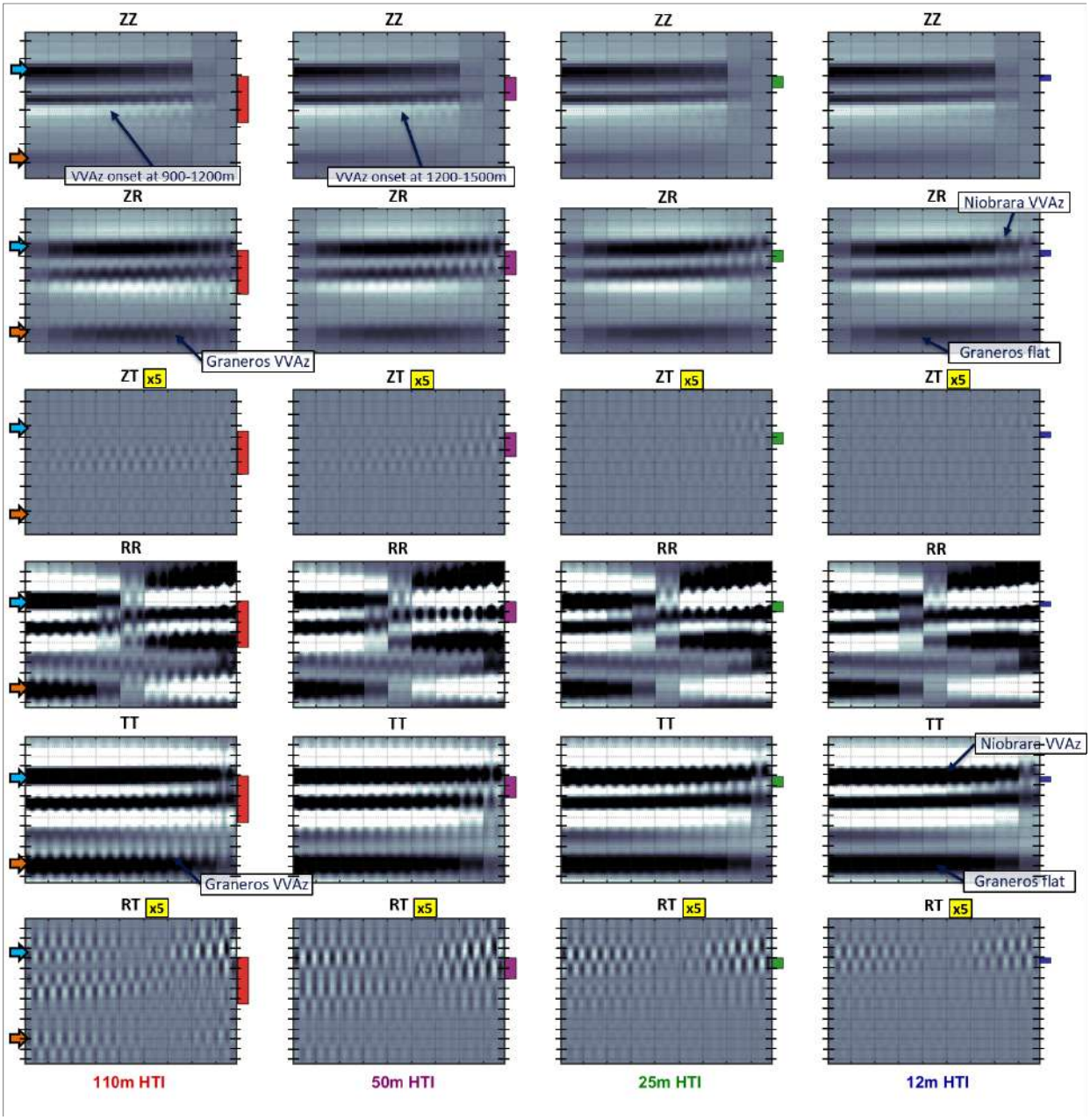

Figure 5.11: Bandpass filtered COCA Volumes comparing the response of the six components for different thicknesses of HTI layers. All panels for a single thickness model are gained the same. That is, for a single thickness model, all components show amplitudes that are comparable. Timing lines are separated by 20ms and the vertical bars indicate the extent of the fractured interval for each model.

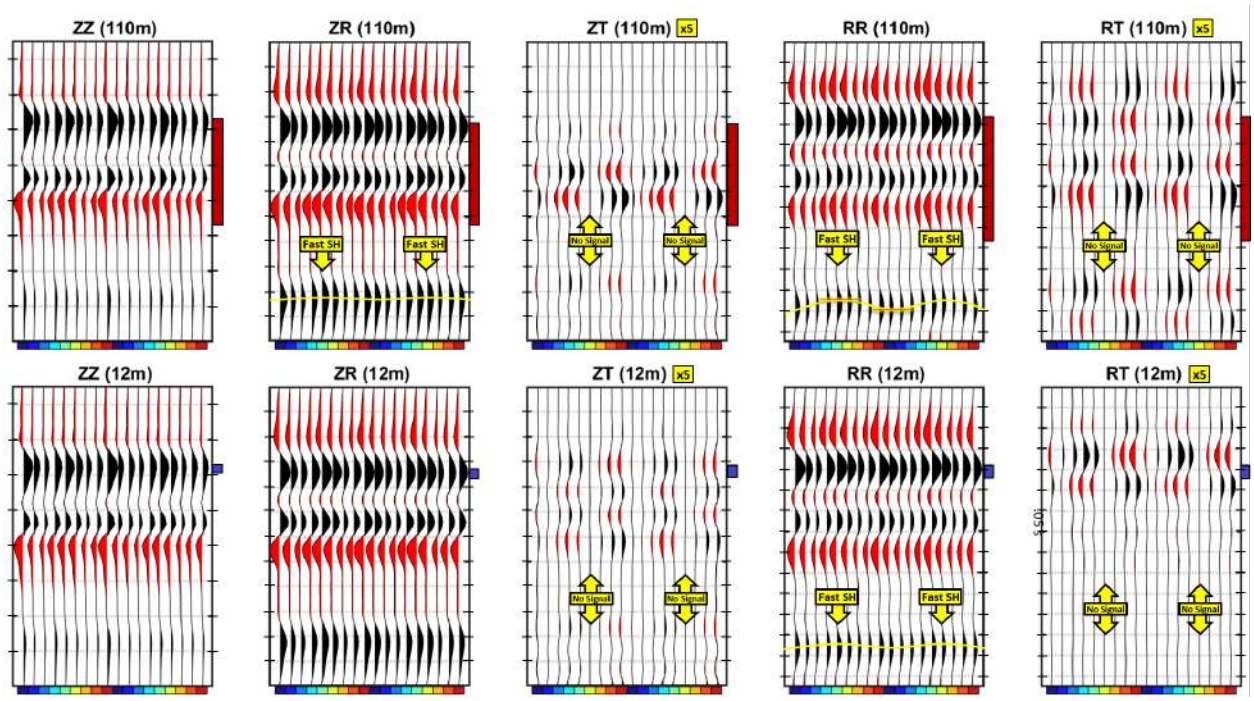

Figure 5.12: Bandpass filtered LAS displays models with different HTI layer thicknesses. The TT and TR components are not shown since the TT is the RR shifted in azimuth by 90 degrees and TR=RT. The cross-term components (ZT, RT) are gained x5 and in both models resolve fracture strike as they show 'null' traces at 110 degrees (yellow azimuthal bin). For the 12m model, the P-wave and converted SV-waves (ZZ and ZR) do not resolve the thin HTI layer and show little to no sinusoidal variation. In both models, the pure SV-wave (RR) show the expected sinusoidal variation associated with VVAz at a reflector below an HTI layer. Timing lines=20ms.

Conventional LAS displays (with outer mute) are generated for the 110m and 12m models (Figure 5.12). The 'null' azimuths on the shear cross-term components (ZT, RT and TR) are consistent at 110 degrees for both models. The main components of the pure shear wave (RR and TT) better maintain the sinusoidal character versus the converted and P-wave data which show relatively flat reflectors. Although the VVAz on the main components is difficult to see without an extreme vertical zoom, the cross-terms, with gain, clearly expose the HTI in the Niobrara-Codell reservoir. The splitting estimated from the 110m model is 1.77ms on the converted wave data and 2.52ms on the shear waves data. For the 12m model, the converted wave splitting is .21ms and the shear wave splitting is .49ms. These results are

based on inversion algorithms presented and discussed in Chapter 7.

5.4 Conclusions

In an effort to conserve cost, P-wave analysis is often the sole component used for fracture interpretation. If 3C or 9C data are available then the additional components should be considered. Time is lost on convoluted P-wave fracture interpretation in order to constrain the result and resolve thinner beds. The manipulation of the P-wave data in this manner reduces the certainty of the interpretation. To this extent, we must first carefully assess the added value of fracture characterization to improved production of a reservoir, and then consider the cost saved and time spent on P-wave interpretation versus the additional cost but saved time and improved accuracy of shear wave interpretation.

Whether one has P-wave or multicomponent data sets, conventional limited azimuth stacks can limit the interpretation as far offset signatures are muted out. These far offsets contain valuable information, hence COCA gathers are effective interpretation tools that preserve offset and azimuth dependence. COCA gathers are common for P-waves but as shown in this chapter, the complementary observations on the converted and shear wave COCAs can reduce the ambiguity and risk of P-wave interpretation.

Part of the reason for this modeling analysis is to provide an expectation as to the VVAz effects that might be observed on the field data. P-wave seismic data interpretation is limited in assessing anisotropy in unconventional shale reservoirs however, shear components can significantly improve the accuracy of the interpretation and provide better resolution for analysis of thinner HTI intervals. Not only are VVAz effects impacted by the difference between fast and slow velocities, but also by the thickness of the fractured interval.

For the Niobrara model, where the fractured interval thins below 25m, the P-wave VVAz is undetectable. The VVAz effect of shear wave data however, is observed even at 25m thick fractured reservoirs. Additionally, the difference between VVAz effects on the shear wave data show measurable differences depending on the thickness of the cracked medium. As a result, shear components may be used to determine the extent of the fractured medium.

CHAPTER 6

9-C FIELD DATA INTERPRETATION OF THE NIOBRARA-CODELL VVAZ

Prestack modeling of the Niobrara-Codell in Chapter 5 has demonstrated that VVAz is observed on all components when the entire reservoir is fractured. For this 110m HTI model, the VVAz is exposed at the strongest reflectors below the top of the Niobrara. At 12m HTI thickness, there is no significant P-wave and converted wave VVAz, whereas the pure shear wave response continues to show VVAz effects but at the Niobrara top.

In this chapter, I examine the Turkey Shoot multicomponent data for evidence of HTI anisotropy using the azimuthal stacking and model learnings of Chapter 5.

6.1 Data Availability and Conditioning

The Turkey Shoot survey is a multicomponent (9-C) acquisition spanning 4 square-miles over the Wishbone Section. The survey was shot three times (4-D) over the course of two and a half years. The Baseline survey was shot after eleven horizontal wells were drilled in the Wishbone Section targeting the Niobrara-Codell reservoir. The Monitor 1 and 2 surveys were drilled after hydraulic stimulation and after two years of production, respectively. The acquisition timeline is illustrated in Figure 6.1 with the aid of key maps showing lateral well trajectories, the microseismic response during stimulation, and the simulated gas saturation after stimulation which potentially influences production. Key observations that may affect the seismic anisotropic interpretation include

1. the tortuous well trajectories in and out of target landing zones
2. the N70W orientation of induced fractures
3. the increased stimulation and gas saturation to the west

The upper map in Figure 6.1 (RCP Sponsors Meeting 2015) shows the lateral variability in well landing positions based on gamma-ray geosteering data. The wells vary in and out of the Niobrara and Codell members which can affect the vertical extent of induced fractures and the seismic reflection at which anisotropy may be observed.

The middle map in Figure 6.1 (RCP Sponsors Meeting 2015) shows the microseismic event locations during hydraulic stimulation of the eleven wells. The dominant N70W orientation of induced fractures is 60 degrees rotated from a second fracture set oriented N50E as mentioned in Chapter 2 (monoclinic fracture system). We must consider the implications on the seismic response, if the Wishbone section is equally influenced by both orientations.

The bottom map of Figure 6.1 describes the simulated gas saturation based on a structurally and stratigraphically accurate reservoir model with uniform fractures oriented N70W (Ning, 2017). There is increased gas saturation to the west of the section which is correlated to a higher frac efficiency as a result of the tighter well spacing (Alfataierge, 2017). Seismic time lapse changes are expected to dominate the western half of the Wishbone Section.

The goal of the Turkey shoot acquisition is to map changes in the reservoir with respect to stimulation and production. While geologic and drilling related conditions can affect the seismic data, the acquisition and processing of the seismic can also inadvertently affect seismic interpretation at the Niobrara.

Preprocessing of the 4-D, 9-C Turkey Shoot survey was done commercially and followed a standard 4-D time-processing flow. The usable frequencies for the P-wave, converted wave and shear wave seismic datasets are 10 - 56 Hz, 5 - 26 Hz and 5 - 22 Hz respectively. This analysis uses the preprocessed, unmigrated gathers with 1-D NMO correction applied and header statics applied to shift the data to final datum. The processing contractor only delivered the migrated ZR, RR and TT components which ignores the potential value added by the cross-term components (ZT, RT and TR).

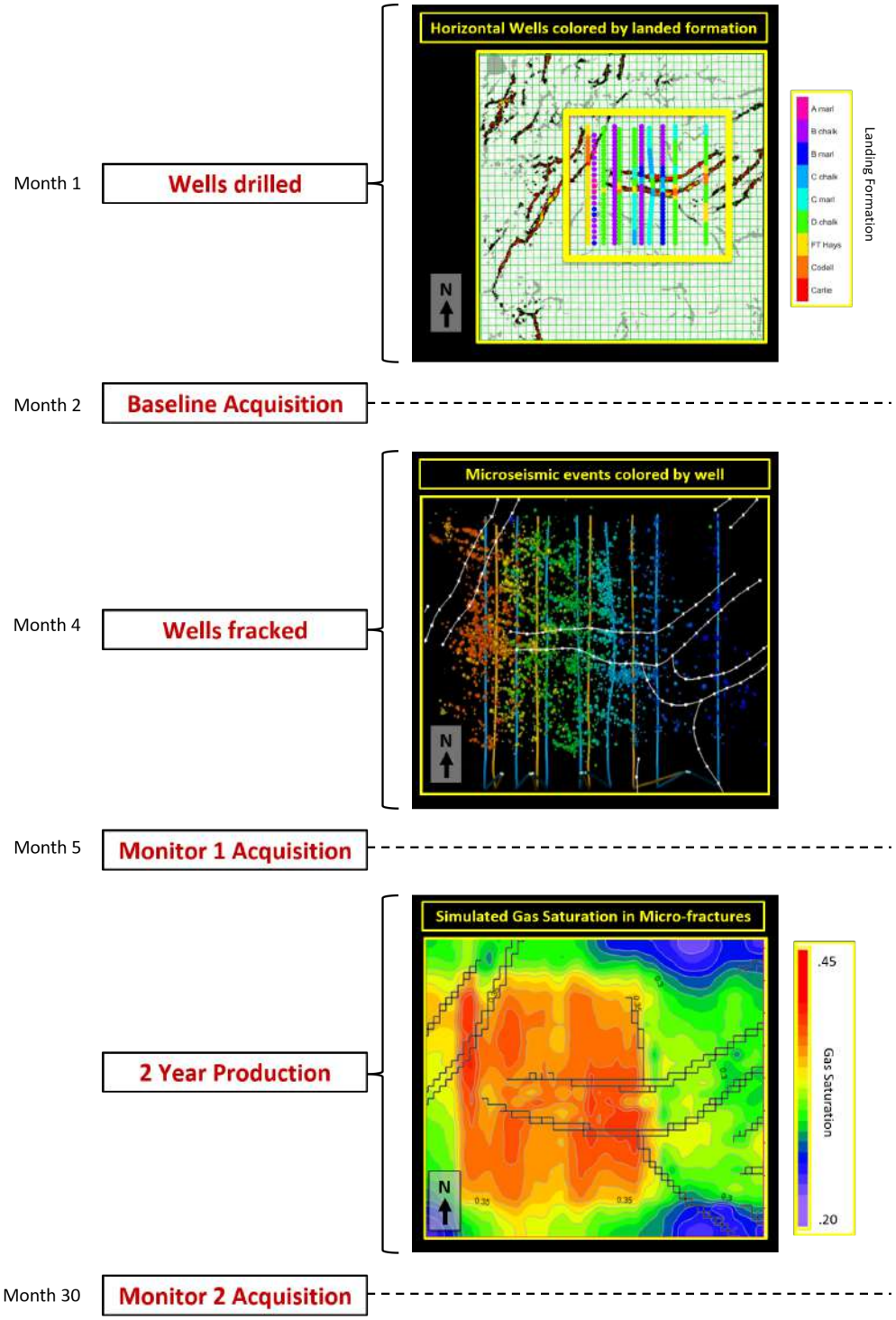

Figure 6.1: Timeline of the Turkey Shoot survey acquisition over the 11 horizontal Niobrara-Codell wells. The three maps highlight the lateral variability of the well landing positions (RCP Sponsors Meeting 2015), the N70W fracture stimulation based on microseismic (RCP Sponsors Meeting 2015) and the simulated gas saturation prior to well production (Ning, 2017).

Improper rotations to R-T coordinates can significantly alter the amplitude and travel time response of the data sets. The processing contractor rotated to R-T space under an incorrect assumption that H1 receiver components (inline receiver components) were due North (H1=0^o) and H2 components (crossline receiver components), by definition, were perpendicular and due east (H2=90^o). The converted and shear data required a precursory receiver orientation analysis to adjust H1 azimuth orientations prior to rotation to R-T coordinates (Daves and Simmons, 2018). This correction was applied to all three Turkey Shoot surveys.

Pre-processing on the source side for the pure shear wave data involved averaging the azimuth headings for the three vibes used for acquisition. While attempts were made in acquisition, to produce orthogonality of $\bar{S}1$ (inline sources) and $\bar{S}2$ (crossline sources) at each shot point location, $\bar{S}1$ and $\bar{S}2$ are averages of the three vibes and are not necessarily orthogonal. Little to no documentation was provided on the source rotations in processing. A rotation of $\bar{S}1$ to 0^o and/or $\bar{S}2$ to 90^o is effectively the same as rotating the receivers only. Proper rotation of shear wave data sets must include both the source and receiver components and the influence of improper rotations become more important when the magnitude of VVAz is small, as is the case here (see Chapter 5 discussion).

6.2 Well Ties and Azimuthal Binning

Vertical wells were tied to the seismic data sets to locate and correlate the reservoir interval on seismic to the well logs (Figure 6.2). Note that in modeling presented in Chapter 5 the Graneros reflector is a peak, whereas the well ties and seismic show the Graneros as a trough. The modeling is based on blocking formations together and the Graneros interval is averaged with large peaks above and below the interval.

COCA gathers of the field data components are generated at gridded locations over the Turkey Shoot survey area (Figure 6.3). While azimuth sectoring and binning provides some signal to noise improvement generating super gathers of 25 IL x 25 XL (55 ft x 55 ft) helped further. Though this 690 ft radius super bin may seem extreme, the VVAz observations of

sinusoidal variations are faint and this constructive binning ensures that even the weakest VVAz signal is observed. The volumes are generated using a 20 degree azimuth bin for a range of 0 to 360 degrees and a 500 ft offset bin for a range of 1000 to 8000 ft.

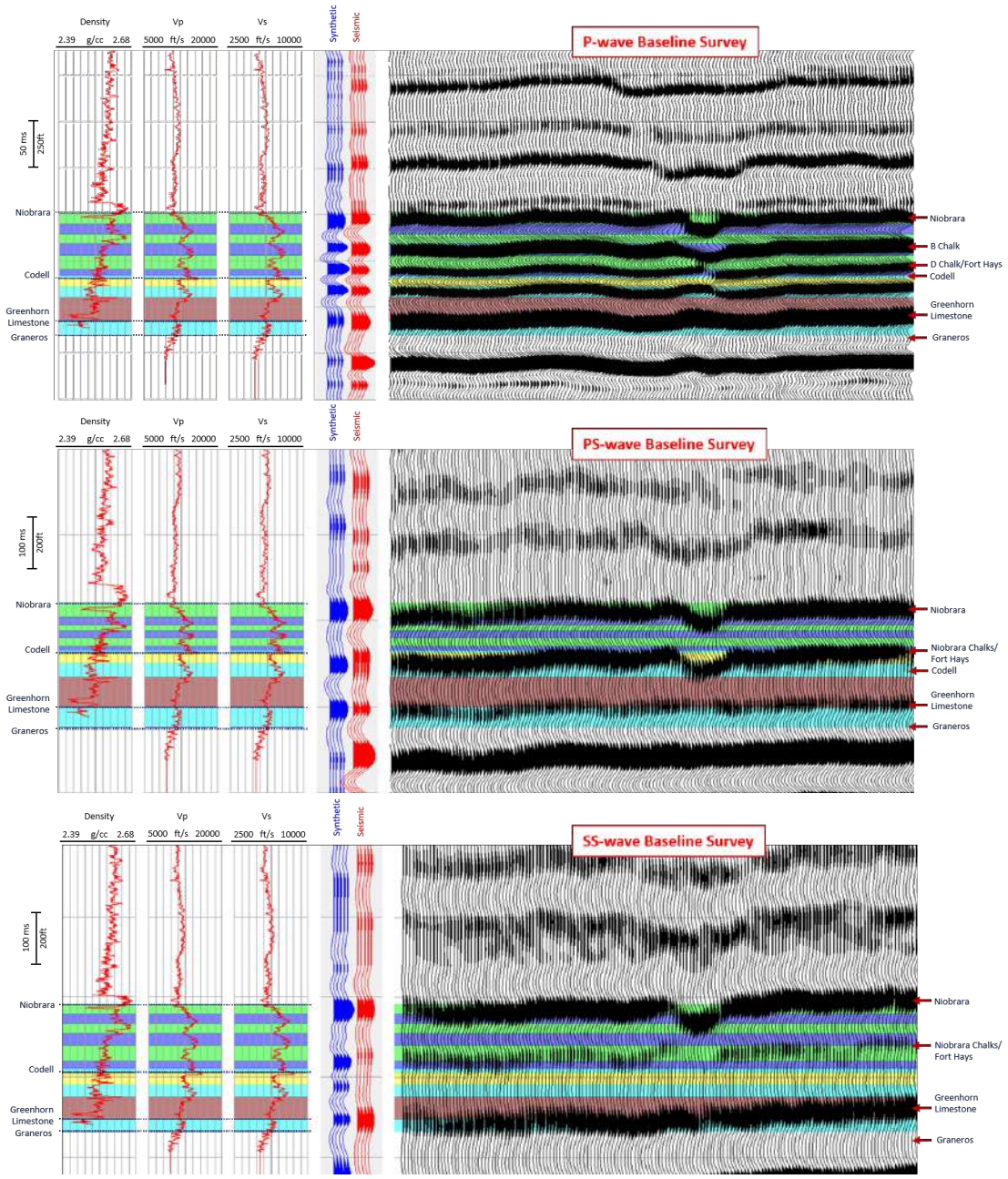

Figure 6.2: Well ties for a vertical well near the Wishbone section for the PP, PS and SS data on the Baseline survey.

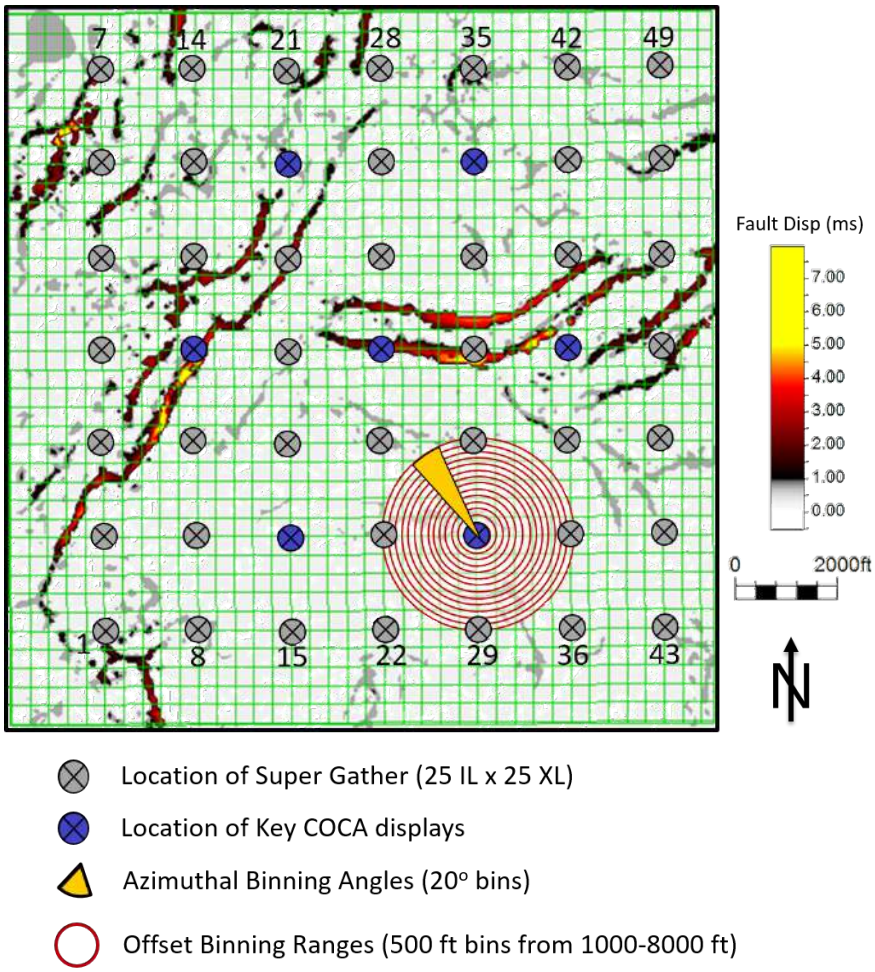

Figure 6.3: Super gather locations at which COCA gathers were generated. The base map is a fault displacement interpretation of the P-wave data at the top of the Niobrara. Azimuthal and offset bin sizes are shown to scale with a 20 degree azimuth bin and 500 ft offset bin. COCA gathers for the locations highlighted in blue are shown in Figures 6.7 to 6.10

6.3 9-C COCA Observations

While the primary evidence of HTI on the main components is sinusoidal character at a reflection below the fractured medium, they must meet certain stipulations in order to be interpreted as HTI. Williams and Jenner (2002) and Jenner (2010), demonstrate sinusoidal character on P-wave data sets as a result of lateral velocity variations. Lateral velocity variations will uniquely affect all other components, for example, energy on the cross-terms may not show systematic polarity reversals and converted wave COCA imaging may be

highly distorted due to the non-reciprocal ray paths. Assuming a flat layered isotropic overburden with an HTI reservoir, Figure 5.4 summarizes the complimentary multicomponent observations indicative of HTI. These include:

1. Energy on the cross-terms (ZT, RT and TR) at all offsets
2. Polarity reversals on the cross-terms with 'null' traces at principal azimuths
3. Sinusoidal character on ZZ starting at mid offsets
4. Sinusoidal character on ZR, RR and TT at all offsets
5. Two fast azimuths within each offset bin
6. Fast azimuths on ZZ, ZR and RR = Slow azimuths on TT
7. No influence of overburden anisotropy

Field data observations are generally noisy and will never retain the resolution of modeled data. Data quality can blur the interpretation at near offsets and mask the faint signal on the cross-term components. If sinusoidal character on the main data components is observed, the last three items listed (items 5 through 7) are critical pieces of evidence that are less influenced by noise and can validate HTI interpretation.

Using this list of HTI evidence, multicomponent observations for the key COCA volumes (blue locations in Figure 6.3) are detailed in Figures 6.7 through 6.10. The P-wave, converted wave and shear wave components are independently scaled in amplitude and time to highlight reflectivity at the Niobrara interval. The cross-term ZT is gained relative to ZR and RT/TR are gained relative to RR/TT. The average locations of the Niobrara and Graneros reflectors are indicated by the blue and orange arrows respectively. In these figures, a checklist of observations related to an HTI subsurface are listed to the right of each survey. I visually analyze each survey for HTI-related observations and in the following section I summarize these observations.

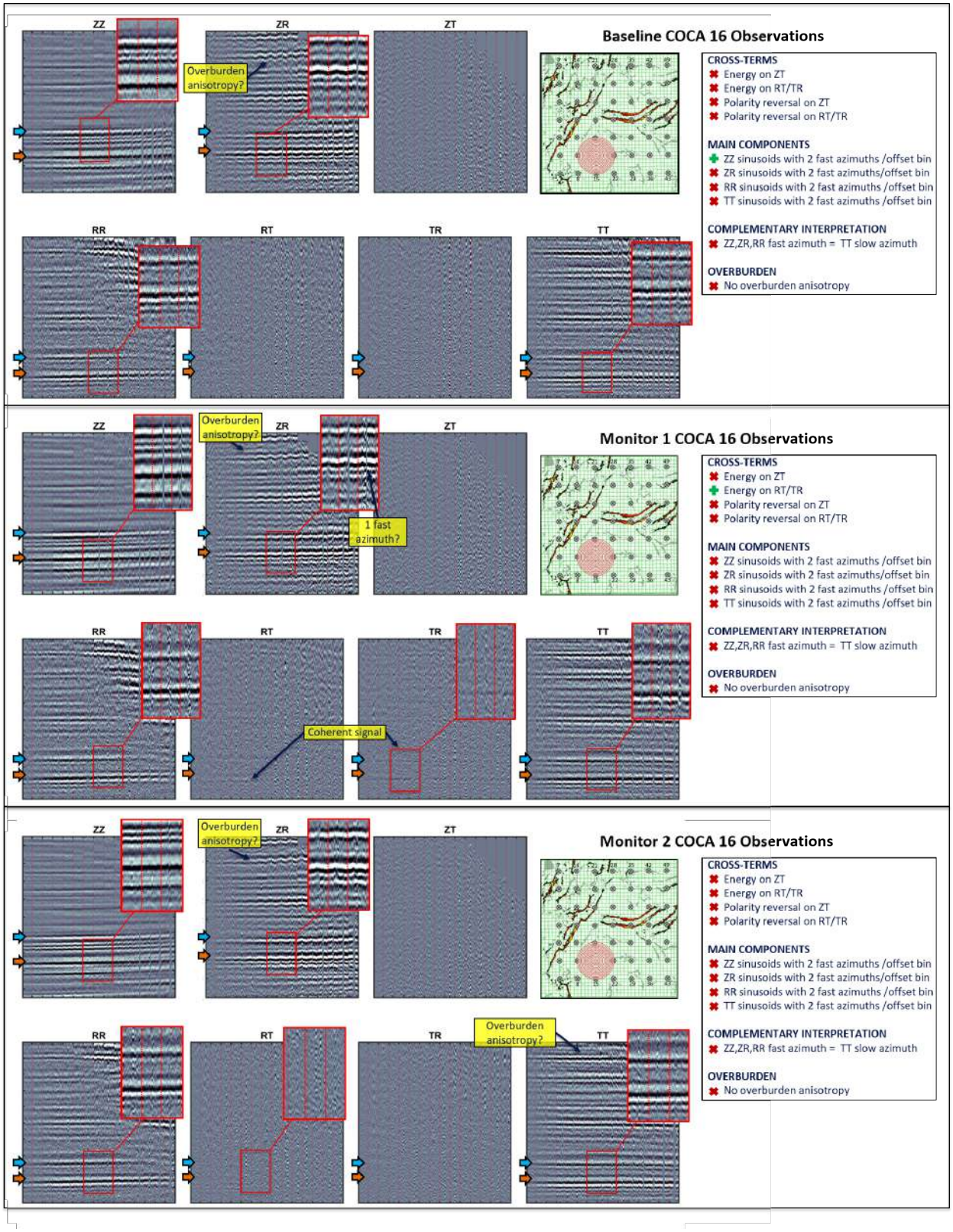

Figure 6.4: COCA gathers for 4-D, 9-C Turkey Shoot Survey at Location 16

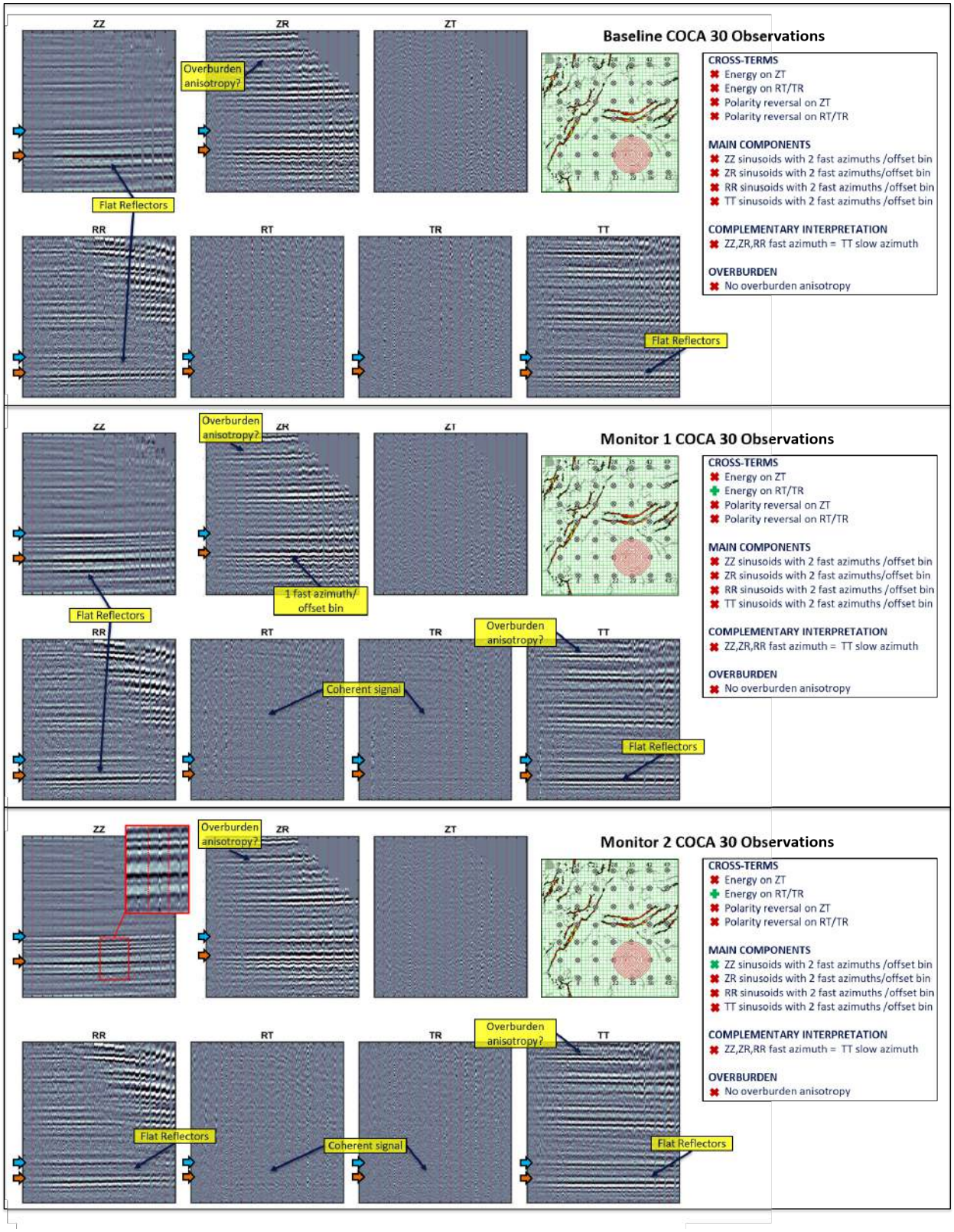

Figure 6.5: COCA gathers for 4-D, 9-C Turkey Shoot Survey at Location 30

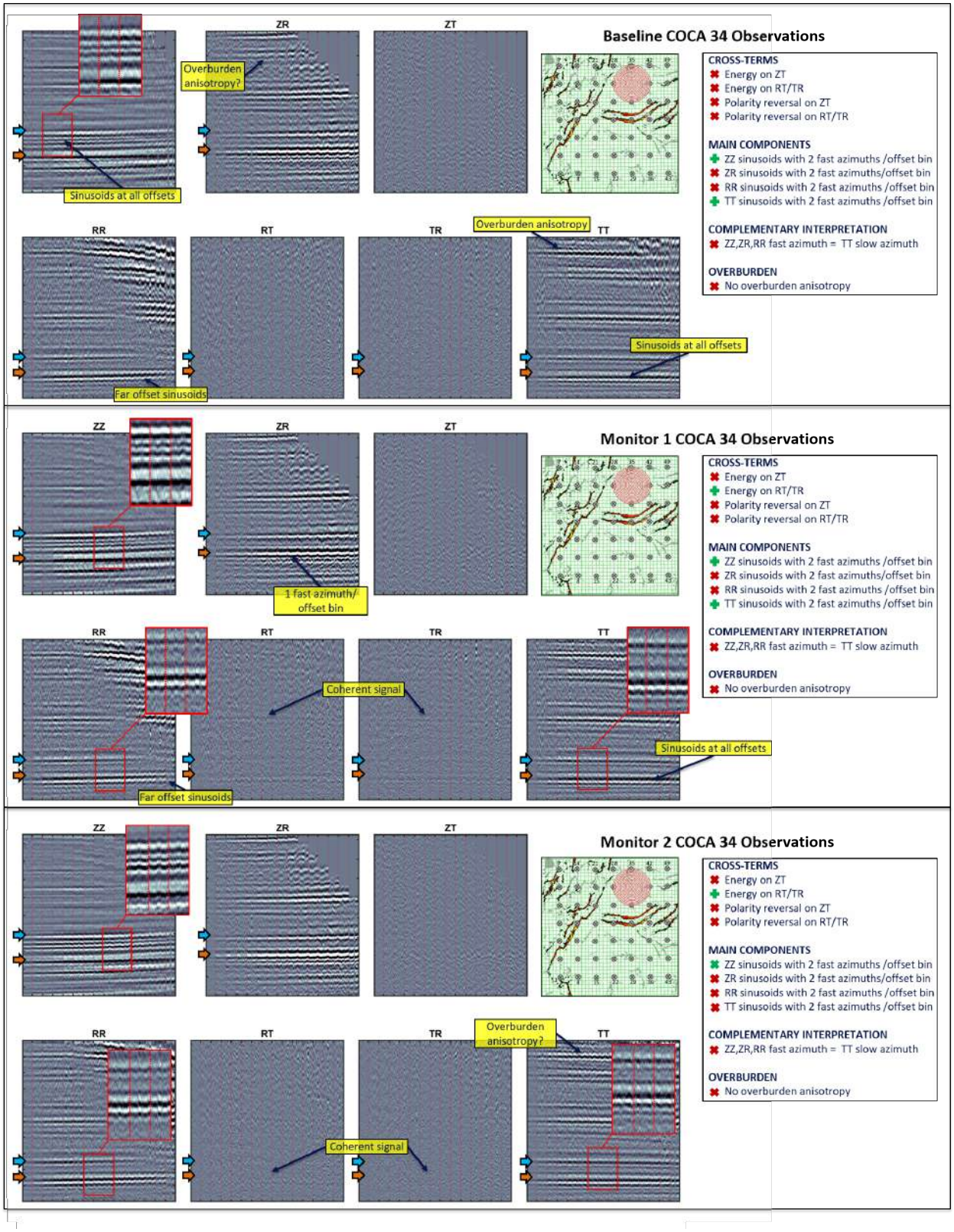

Figure 6.6: COCA gathers for 4-D, 9-C Turkey Shoot Survey at Location 34

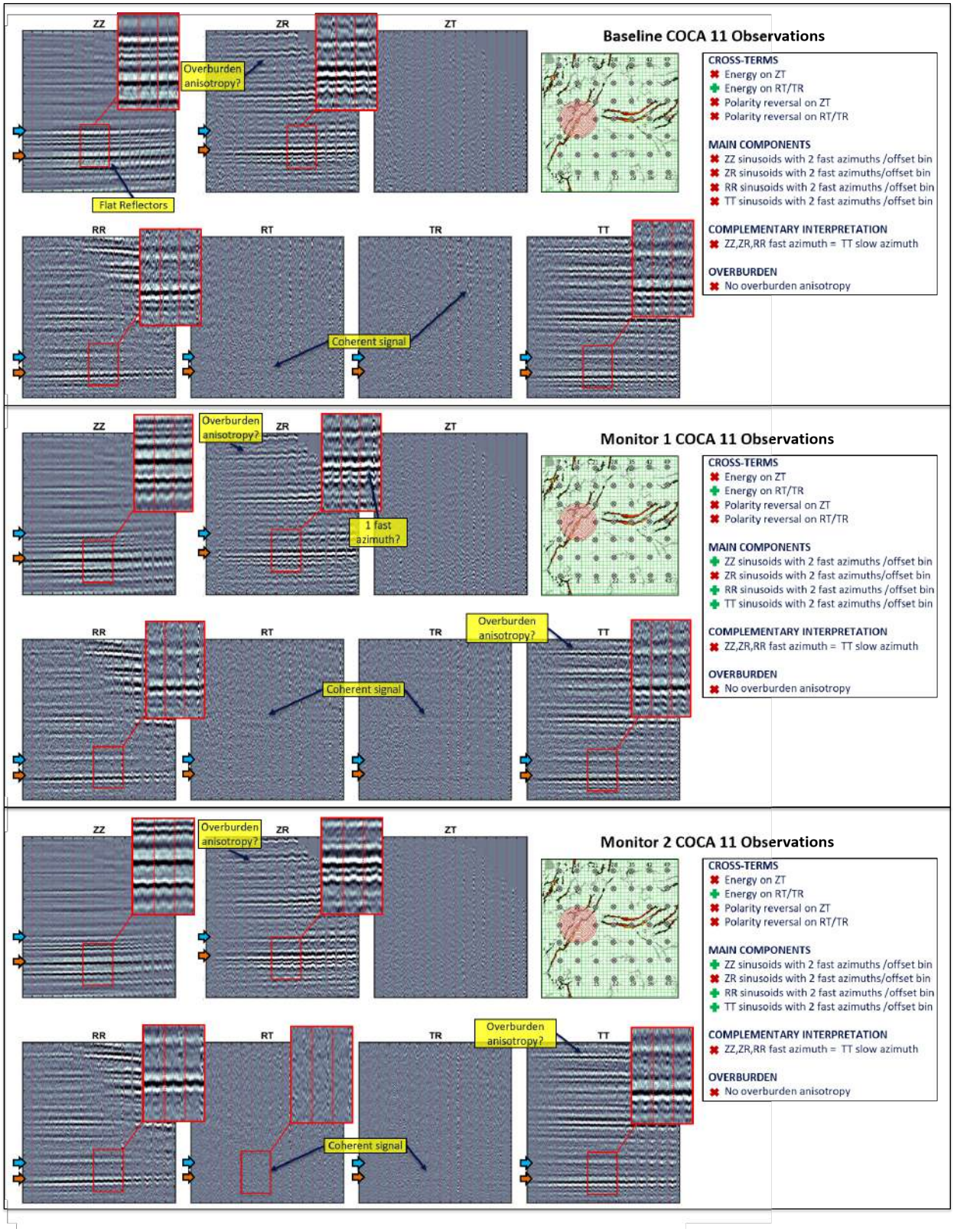

Figure 6.7: COCA gathers for 4-D, 9-C Turkey Shoot Survey at Location 11

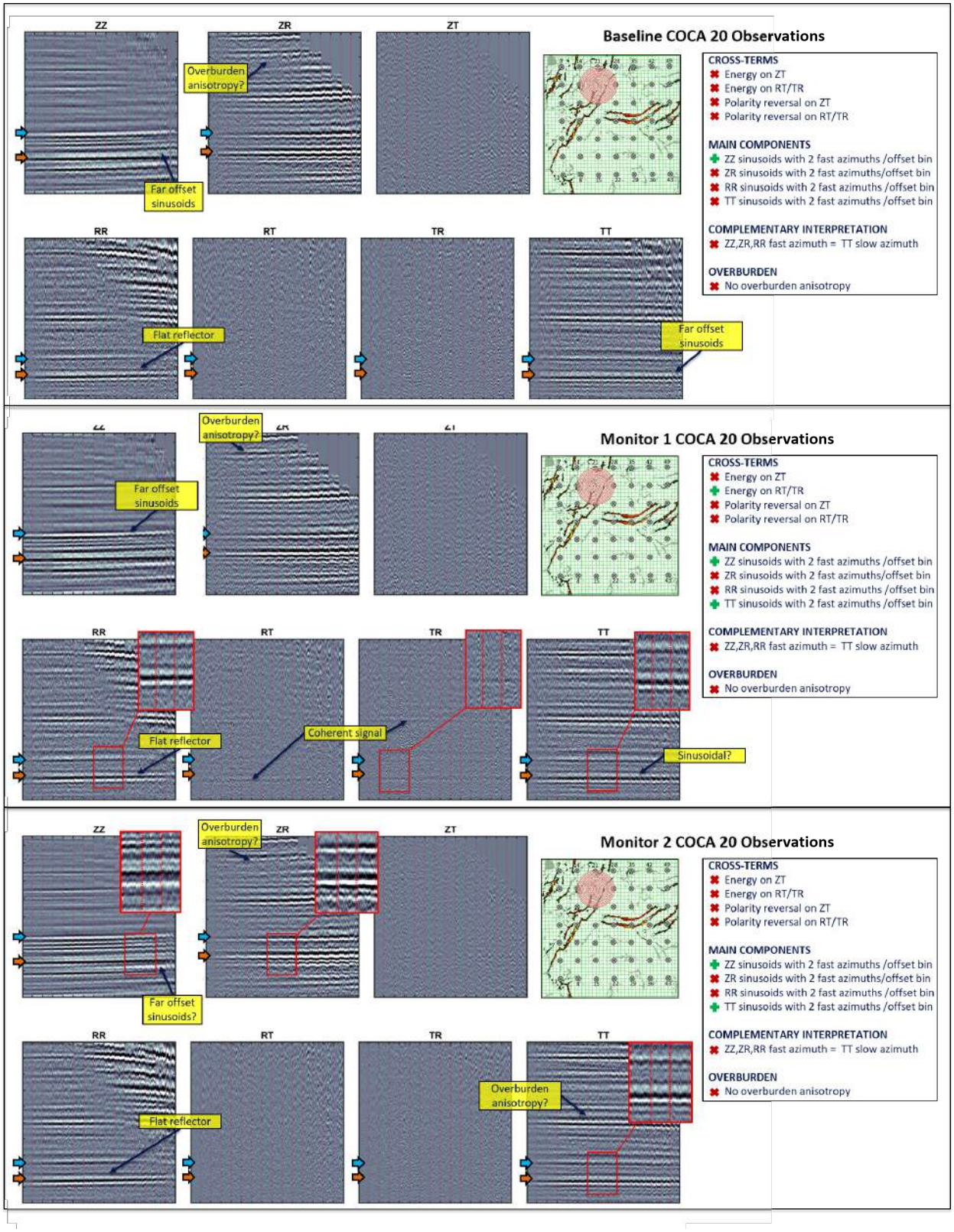

Figure 6.8: COCA gathers for 4-D, 9-C Turkey Shoot Survey at Location 20

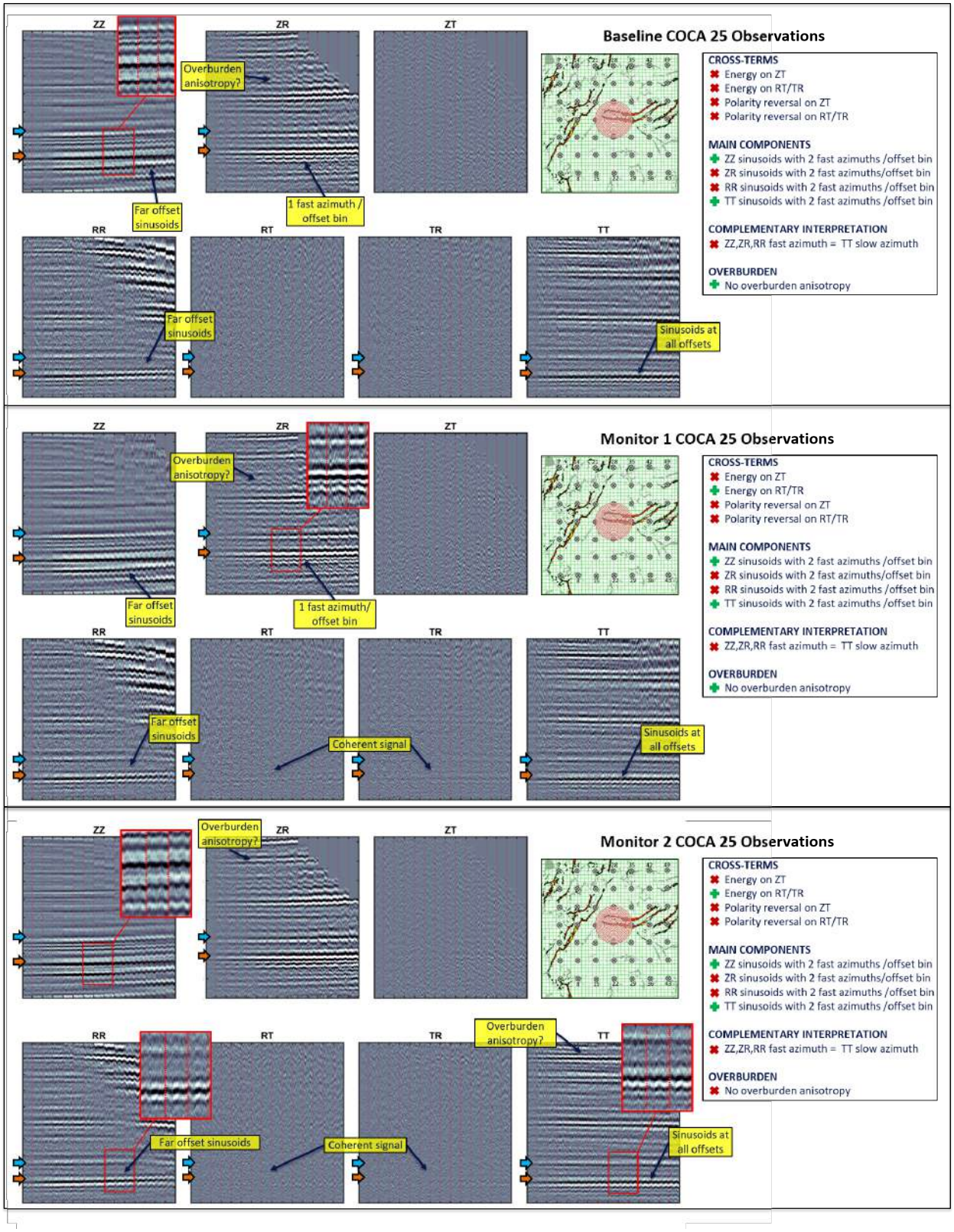

Figure 6.9: COCA gathers for 4-D, 9-C Turkey Shoot Survey at Location 25

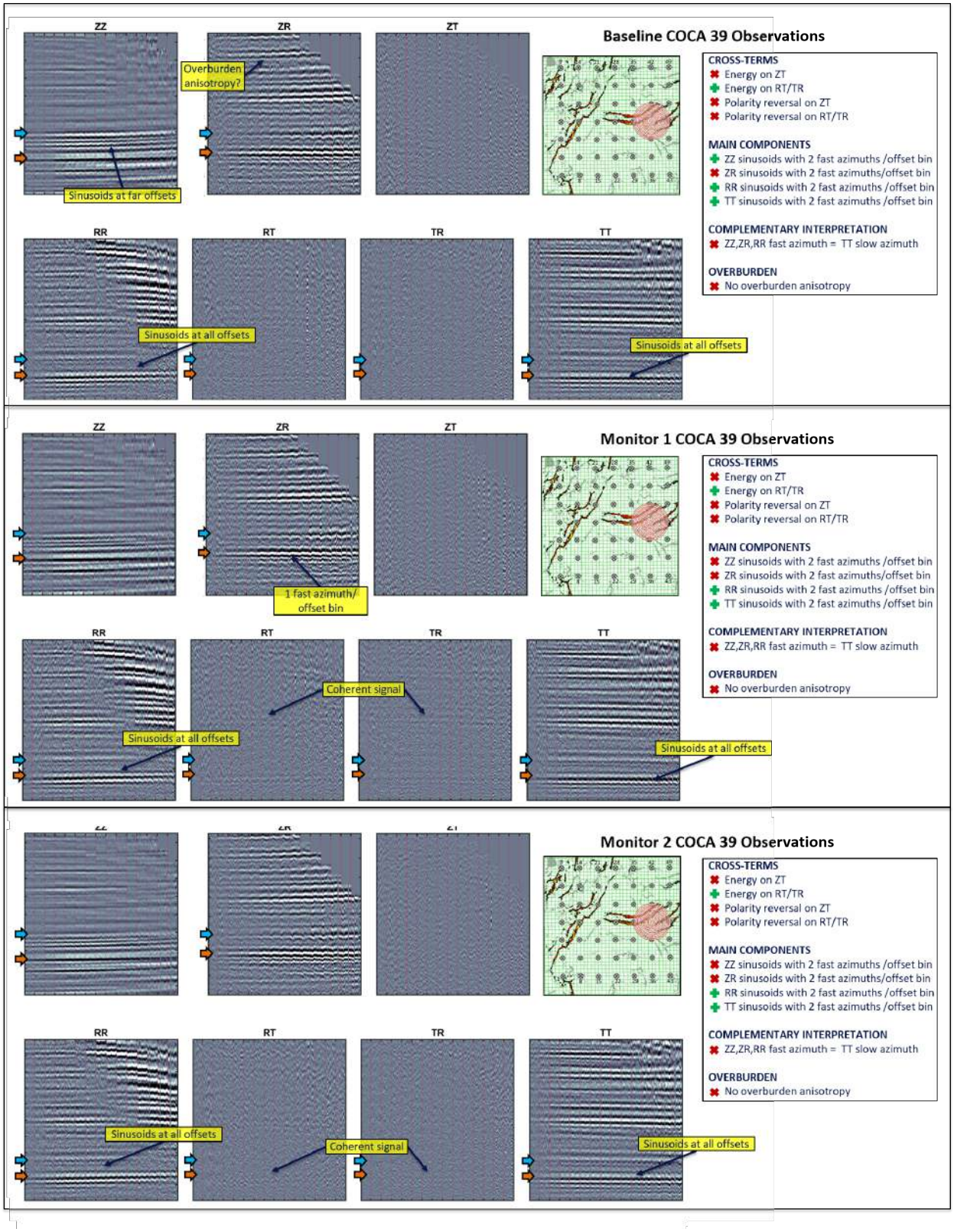

Figure 6.10: COCA gathers for 4-D, 9-C Turkey Shoot Survey at Location 39

To prelude my observations, it is important to recognize that any interpretation is subject to interpreter's bias. The modeling in Chapter 5 suggests that the VVAz signature, if any, will be relatively small which increases the uncertainty of interpretations made. However, in addition to evaluating several locations across the survey, analysis of the nine data components help strengthen my final conclusions.

COCAs 16, 30 and 34 are located in unfaulted Niobrara areas of the Wishbone section. At COCA 16 (Figure 6.4, a sole P-wave (ZZ) interpretation of the Baseline survey would suggest HTI in the subsurface based on the sinusoidal character with two fast azimuths within an offset bin. For Monitors 1 and 2, the P-wave reflectors in the Niobrara interval are flat. The converted shear for all three surveys show sinusoidal variation, however, this character is observed throughout the vertical section and there is one fast azimuth per offset bin (single period sinusoid per offset bin). The pure shear components (RR and TT) are flat in all three surveys. Although noise masks interpretation of the cross-term energy, in Monitor 1, there is a coherent signal on the RT and TR components.

Interpretation at COCA 30 (Figure 6.5), just east of location 16, also suggests no HTI with all main components, inclusive of the P-wave data, showing flat reflectors for all three surveys. The converted wave sinusoids are consistent in all three surveys for these COCA locations and the anomalous coherent signal in Monitor 1 RT and TR are also observed in Monitor 2. These two COCA interpretations shown in Figures 6.4 and 6.5 are representative of other COCA interpretations south of the east-west trending Wishbone graben.

At COCA 34 (Figure 6.6), the sinusoids on the ZZ, RR and TT components seem, at first, to be evidence of Niobrara HTI however, the TT component shows sinusoidal variation in the overburden and the fast azimuth on RR is equal to the fast azimuth on TT. Recall, from Chapter 5, due to the orthogonality of radial vs transverse orientations and fast vs slow, fast azimuths on the RR component should correlate to slow azimuths on the TT component. Similar to COCA 16 and 30 interpretation, no significant time lapse VVAz changes are observed.

COCAs 11, 20, 25 and 39 are super binned at locations over Niobrara faulting. In COCA 11 (Figre 6.7), the P-wave reflectors are flat in the Baseline survey and show some VVAz in Monitors 1 and 2. The converted shear continues to show the single period sinusoidal character throughout the vertical section for all surveys. The pure shear components show sinusoidal character as well, however, they are not fitting of HTI-related VVAz effects. First, the fast azimuths on the RR component is equal to the fast azimuth on the TT component for all three surveys.

At all four locations, a trend observed in some surveys is the presence of VVAz at all offsets on the TT component, but only on the far offsets of the RR component. In COCA 20, there is no HTI related VVAz on the RR component and the TT which shows VVAz throughout the vertical section and at all offsets. COCAs 25 and 39 also follow suit with inconsistent HTI interpretation.

6.4 Discussion of Field COCA Observations

The interpretation of all nine components of the Turkey Shoot survey do not tell a cohesive story that is indicative of HTI in the Niobrara-Codell interval. Modeling in Chapter 5 suggests that for a 12m fractured layer in the Niobrara, the shear wave data should still resolve the anisotropy at the top of the Niobrara. However, regardless of resolution, where VVAz character is observed, it does not fit the stipulations of HTI interpretation as listed earlier in this chapter.

6.4.1 Time-Lapse Observations

The P-wave data has a very low S/N ratio even with the super binning and there is no obvious evidence of HTI at the Niobrara-Codell reservoir that is correlated with observations on other components for any survey. The shear wave cross-term data show appreciable energy but no polarity reversals, nor do the main shear components (RR and TT) show VVAz character on any survey.

6.4.2 Implications of Mis-rotation

The observed energy on the shear wave cross-terms may be a result of non-orthogonal source orientations. The energy does not show polarity flips in accordance with HTI presence, but the RT resembles a scaled version of RR and TR is a scaled version of TT. While this is observed on most all COCA gathers, it is most significant in the Monitor 1 surveys of Figures 6.5 and 6.10.

A similar observation was made during the preliminary analysis of the data which included ZT being a scaled down version of ZR (RCP Sponsors, Fall 2017). This phenomena is attributed to receiver orientations offset from North-East azimuths and rotated to radial-transverse coordinates under the assumption of nominal orientation (N-E). This is demonstrated by Daves and Simmons (2018) using isotropic modeling.

I model this effect for the anisotropic Niobrara model by changing the X-Y receivers orientation to 10 degrees prior to rotation to R-T space. The upper synthetics described in Figure 6.11 and labeled in green represent the expected cross-term response when rotations are done appropriately. The lower synthetics labeled in red represent the cross-term components produced if the rotation is done with an incorrect assumption. Note the ZT and RT cross-term responses in this case are equal to the reciprocal of the main components (ZR and RR) multiplied by some scalar. The TR cross-term is equal to the main TT component multiplied by some scalar.

The cross-term data are 'scaled down' versions of the main components for both converted and pure shear data on isotropic and anisotropic reflectors. Prior to interpretation, this receiver correction was made and associated energy on the ZT component was completely resolved. We still, however, observe energy on the RT and TR cross-terms but appreciably lessened.

Shear waves are not only dependent on horizontal receiver orthogonality but also horizontal source orthogonality. Commercial processing prior to data delivery, attempted to remedy shot rotation errors, however, there is no detail on what exactly was done. There

is no documentation on the minimum error allowance for corrections made (if any). Analysis of the baseline vibrator orientations by RCP student, Matthew Bray suggests that at least 17 source locations had horizontal shots with a minimum of 10 degree deviation from orthogonal azimuths. Resolving rotation errors should better expose HTI character on the COCA volumes, provided that the signal to noise ratio is high.

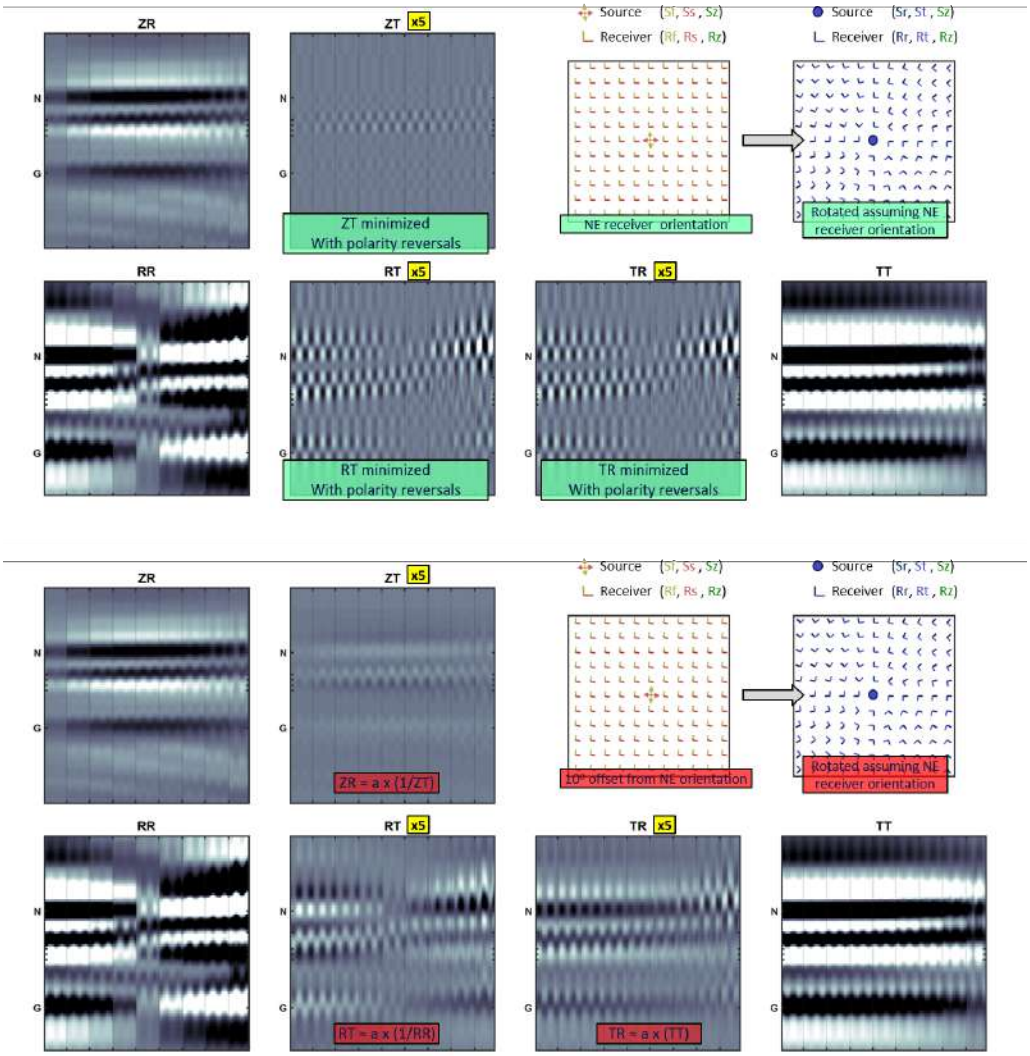

Figure 6.11: Modeling of converted and pure shear wave COCA volumes for receiver components oriented 10 degrees NE and rotated to R-T space under the assumption of N-E oriented components. The cross-terms are gained x5. Cross-term components labeled in green are the result of proper rotation. Cross-term components labeled in red are the result of poor rotation and represent a 'scaled down' version of the main component.

6.4.3 Spatial Observations

It is difficult to identify changes in the VVAz response across the survey area and COCA gathers near the faults, or in unfaulted locations, do not convey an intuitive story about faulting influence. This does not mean however, that shallow lateral velocity variations (from faulting and compartmentalization or velocity anomalies) are not impacting the COCA gather observations.

The sinusoidal variation with a single fast azimuth per offset bin observed on the converted wave data is consistent for most COCA gather locations shown for Baseline, Monitor 1 and Monitor 2 surveys. I hypothesize that this is a result of the non-reciprocal ray paths associated with the converted shear data. In a laterally variable subsurface, converted wave arrival times and velocities between a single source-receiver pair will vary under an interchange of source and receiver position (Thomsen, 1998). This phenomenon is coined 'diodic velocity' based on an electronic diode operating differently in forward and reverse. Figure 6.12 illustrates that for a laterally varying subsurface (note the zone of slow P-wave velocity to the right), a converted wave traveling from A to B arrives sooner than the converted wave traveling from B to A. This occurs because the converted wave is only affected by the velocity anomaly when traveling from B to A and the incident P-wave traverse the zone.

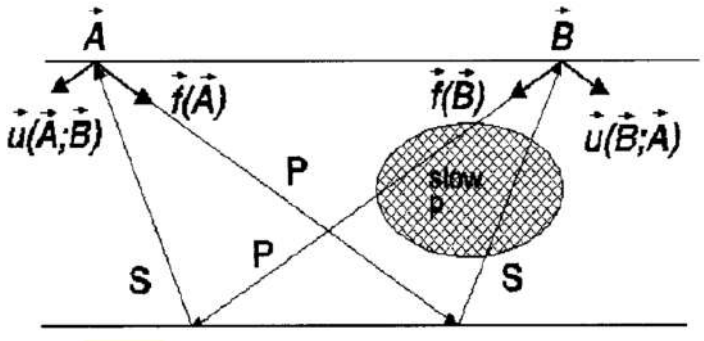

Figure 6.12: Description of the converted wave 'diodic effect' in subsurface conditions with lateral variation in velocities (Modified from Thomsen (1998)).

Limited azimuth stacks that are tightly muted could potentially reduce the 'diodic effect' since the near vertical ray-paths of the P-wave leg and shear wave legs should ideally interact with the same shallow velocity anomalies whether down-going or up-going.

6.5 9-C LAS Observations

Figures 6.13 and 6.14 show the limited azimuthal stacks at locations 16 and 39 over the survey area. The binning for the LAS displays are smaller (500ft) than the COCA gathers and can better potentially show lateral variations in HTI anisotropy.

There is no obvious sinusoidal character observed on any component in LAS displays and similar to the COCA gathers, interpretation of small VVAz signature are subjective to the interpreters bias. In Figures 6.13 and 6.14, I have highlighted a few of my observations.

Recall that HTI related VVAz is exposed as sinusoidal character on the ZZ, ZR, RR and TT components with ZZ, ZR and RR fast azimuths = TT slow azimuths. A potentially observed fast azimuth on the Baseline ZZ and ZR components of Figure 6.13 does not correlate with the flat reflections on the shear wave components. Arguments can be made in favor of and against the ZZ sinusoidal character being observed on Monitors 1 and 2. On the cross-term components, it is difficult to identify polarity reversals or 'null' azimuths due to noise in the data.

At location 39 (Figure 6.14), the LAS is centered over Niobrara faulting. The apparent slow azimuth on ZZ is possibly observed as fast azimuths on ZR and RR. This slow ZZ azimuth on Baseline is also observed as the fast azimuth on the Monitor surveys. As observed on the COCA gathers, no definite HTI-related VVAz or time-lapse change is observed.

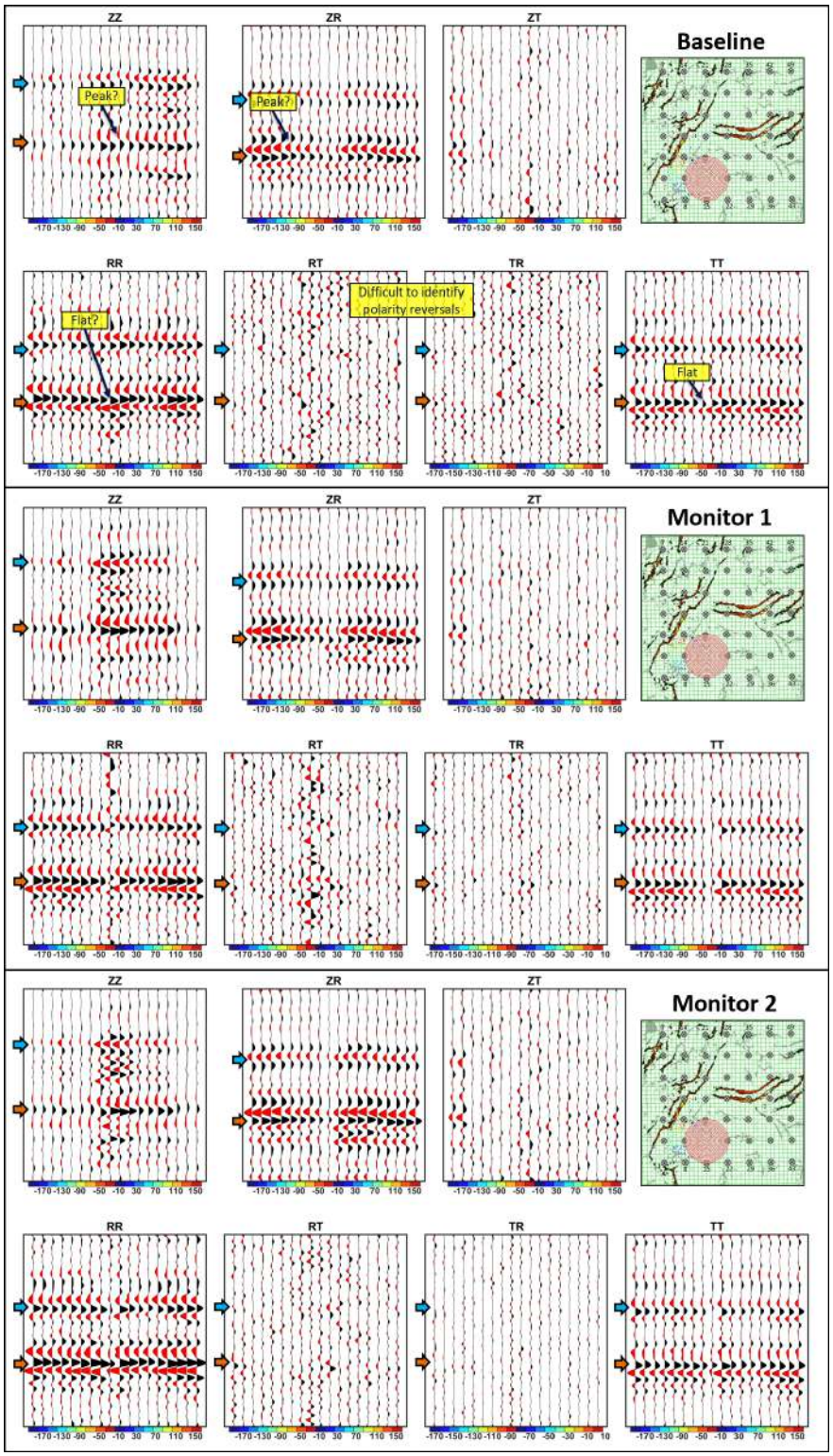

Figure 6.13: LAS for 4-D, 9-C Turkey Shoot Survey at Location 16

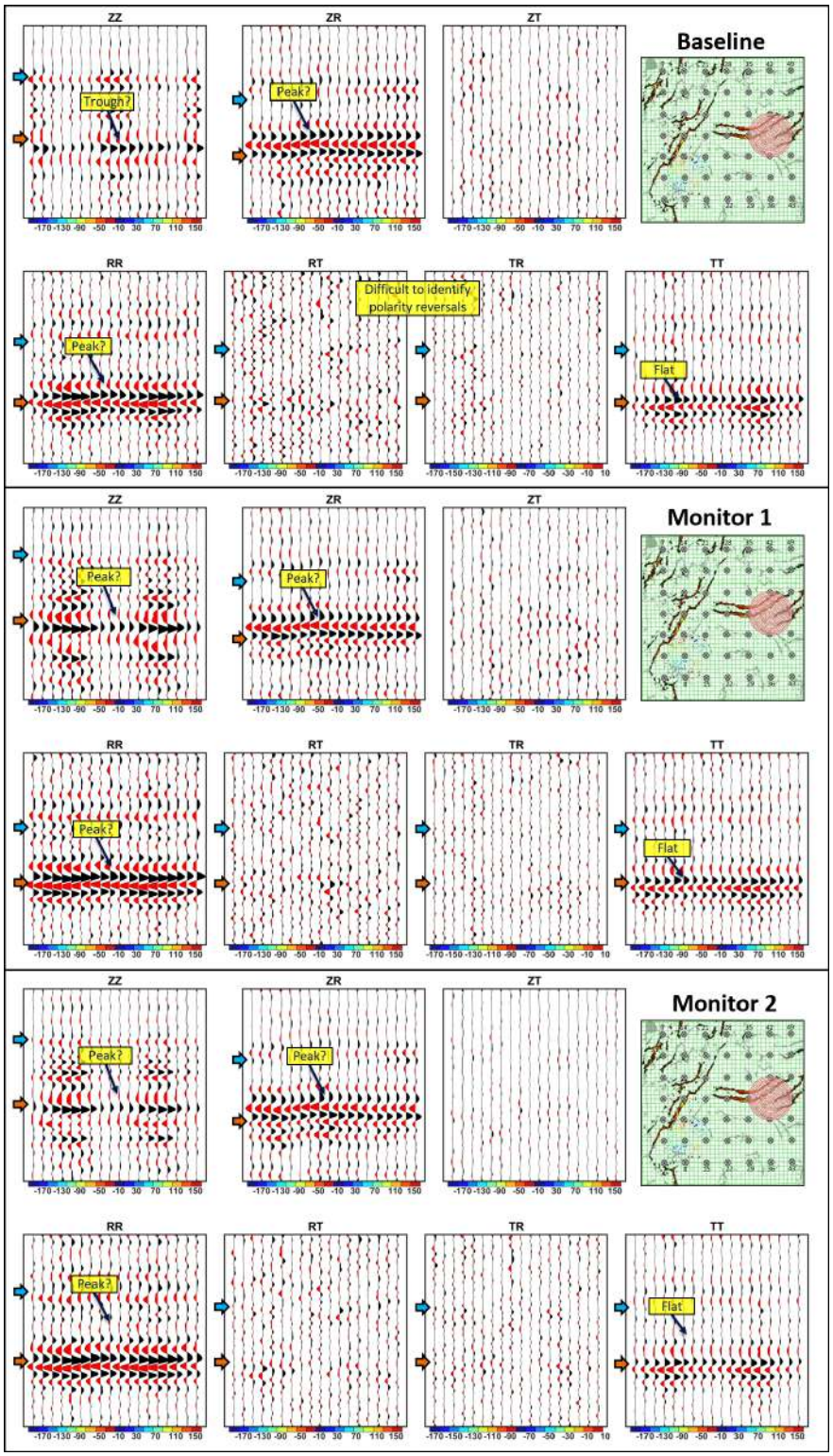

Figure 6.14: LAS for 4-D, 9-C Turkey Shoot Survey at Location 39

6.6 Geologic Assumptions and Implications on the Field Interpretation of the Wishbone Section

There are several reasons as to why the seismic is unable to resolve the natural or induced fracture sets mapped by core, FMI log and microseismic studies summarized in Chapter 2. Possible explanations can be attributed to data constraints or geologic conditions. In section 6.4, I discuss two such data constraints being the shear wave source rotation and converted wave non-reciprocity. The converted wave 'diodic effect' is particularly tied to subsurface conditions and introduces a possible flaw in the geologic assumptions made.

The modeling of the Niobrara presented in Chapter 5 assumes lateral homogeneous geology; that is, no shallow lateral velocity variations, no overburden anisotropy and a reservoir with a single vertical fracture set throughout the section.

6.6.1 Consideration of Monoclinic Reservoir

Recall that two primary fracture orientations are observed in the Wishbone section based on the fracture network study by Grechishnikova (2017) (Figure 2.9). The first, which is oriented N70W and the second is oriented N50E. Assuming that both fracture sets are present and have similar fracture aperture and density values, the reservoir is now monoclinic (with an approximate 60 degree separation between fracture sets) and the interpretation of fracture strike is complicated. A monoclinic Niobrara model was shot and the COCA volume displays are shown in Figure 6.15. The cross-terms show polarity reversals in the fractured medium at the same azimuths that fast arrivals occur on ZZ, ZR and RR and slow arrivals occur on TT. These azimuths occur at 80 degrees, half way between the two fracture sets as detailed in the LAS displays of Figure 6.16. This does not explain the field data observations since the two period sinusoids on the main components and complimentary signatures between components are not met. A monoclinic reservoir is not necessarily the explanation for the field data interpretation.

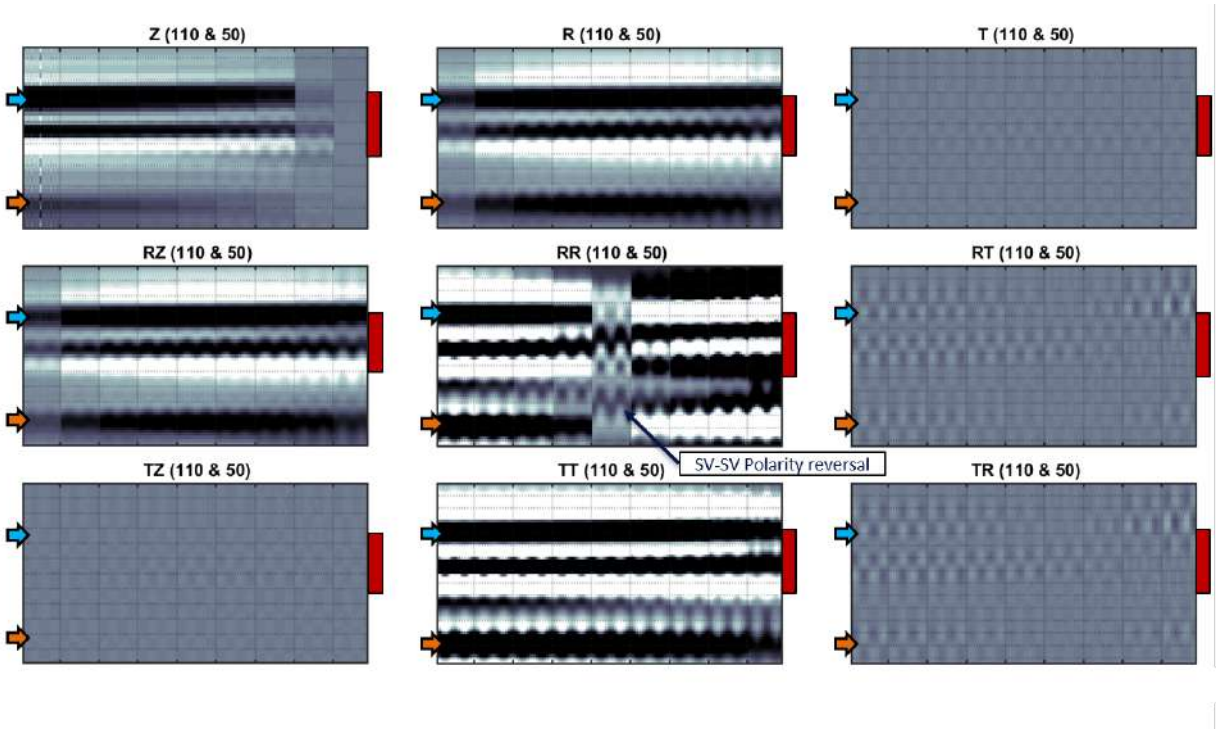

Figure 6.15: Filtered COCA displays for nine data components in R-T space for the monoclinic Niobrara model. The two fracture sets are oriented 50 degrees (N50E) and 110 degrees (N70W) and distributed evenly across the entire Niobrara interval (same density and aperture) . Timing lines for all panels are separated by 20ms and show the Niobrara (N) to Graneros (G) horizons. All components have the same gain. Offset bins are defined by light gray vertical lines. Vertical red boxes indicate interval of cracked Niobrara.

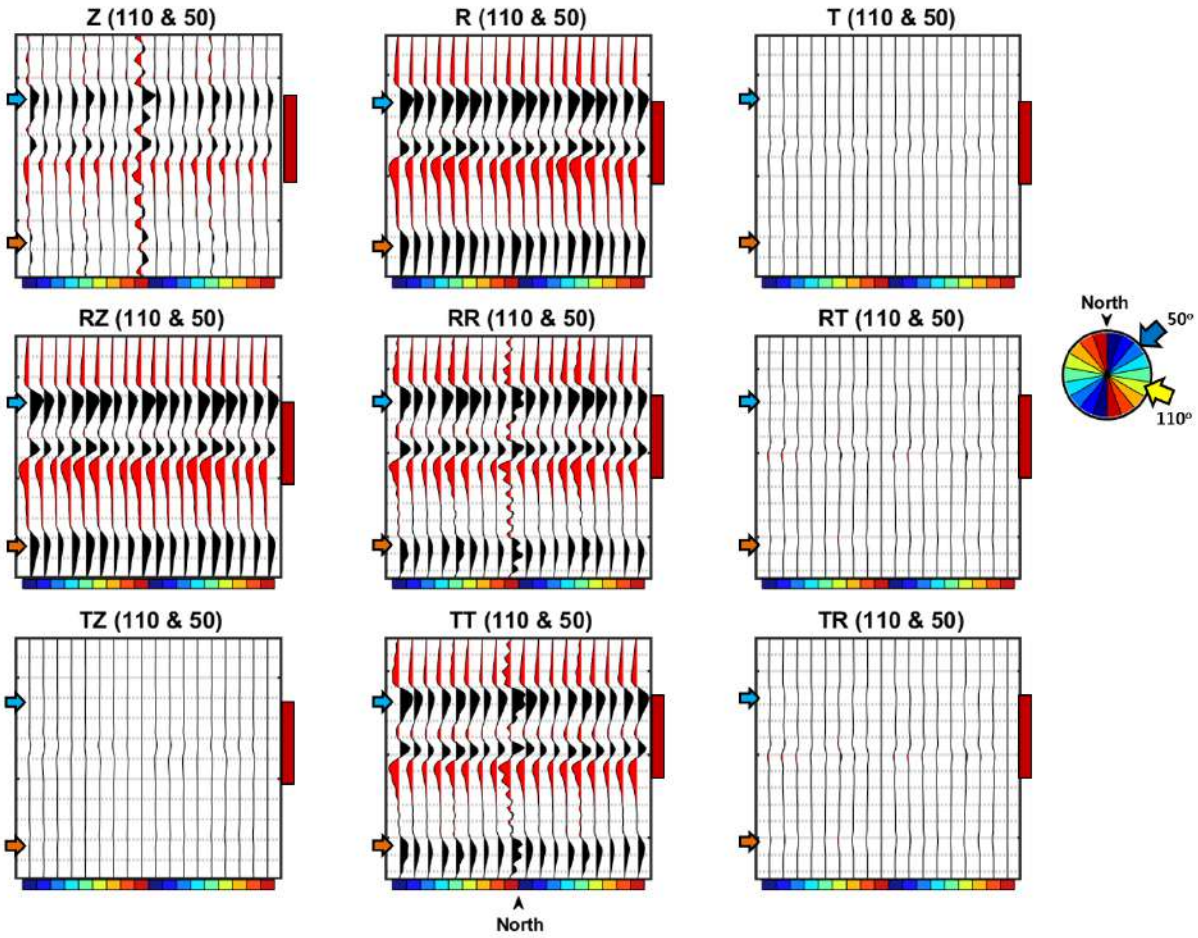

Figure 6.16: Filtered LAS displays for nine data components in R-T space for the monoclinic Niobrara model. The two fracture sets are oriented 50 degrees (N50E) and 110 degrees (N70W) and distributed evenly across the entire Niobrara interval (same density and aperture). Timing lines for all panels are separated by 20ms and show the Niobrara (N) to Graneros (G) horizons. All components have the same gain such that the amplitudes are comparable. RR fast azimuth, TT slow azimuth and polarity reversals on the cross-term are at 80 degrees azimuth.

6.6.2 Consideration of Lateral Velocity Variations

The Niobrara surface is heavily faulted with an E-W trending graben dominating the Wishbone section and NE-SW trending faults in the surrounding sections. Moving up section, Figure 6.17 shows the changing fault regimes at the Lower Pierre 2 and the Terry-Hygiene intervals. The faulting can cause lateral velocity variations that complicate the

multicomponent interpretation for VVAz signature.

Jenner (2010) attempts to map the P-wave response of shallow lateral velocity variations however, there is no attempt to understand the shear and converted wave response. Time constraints have not allowed me to elaborate on the hypothesis that lateral velocity variations are dominating the field data response, however, the observations made on the converted wave data (Section 6.4) with respect to the diodic theories of Thomsen (1998) support this theory.

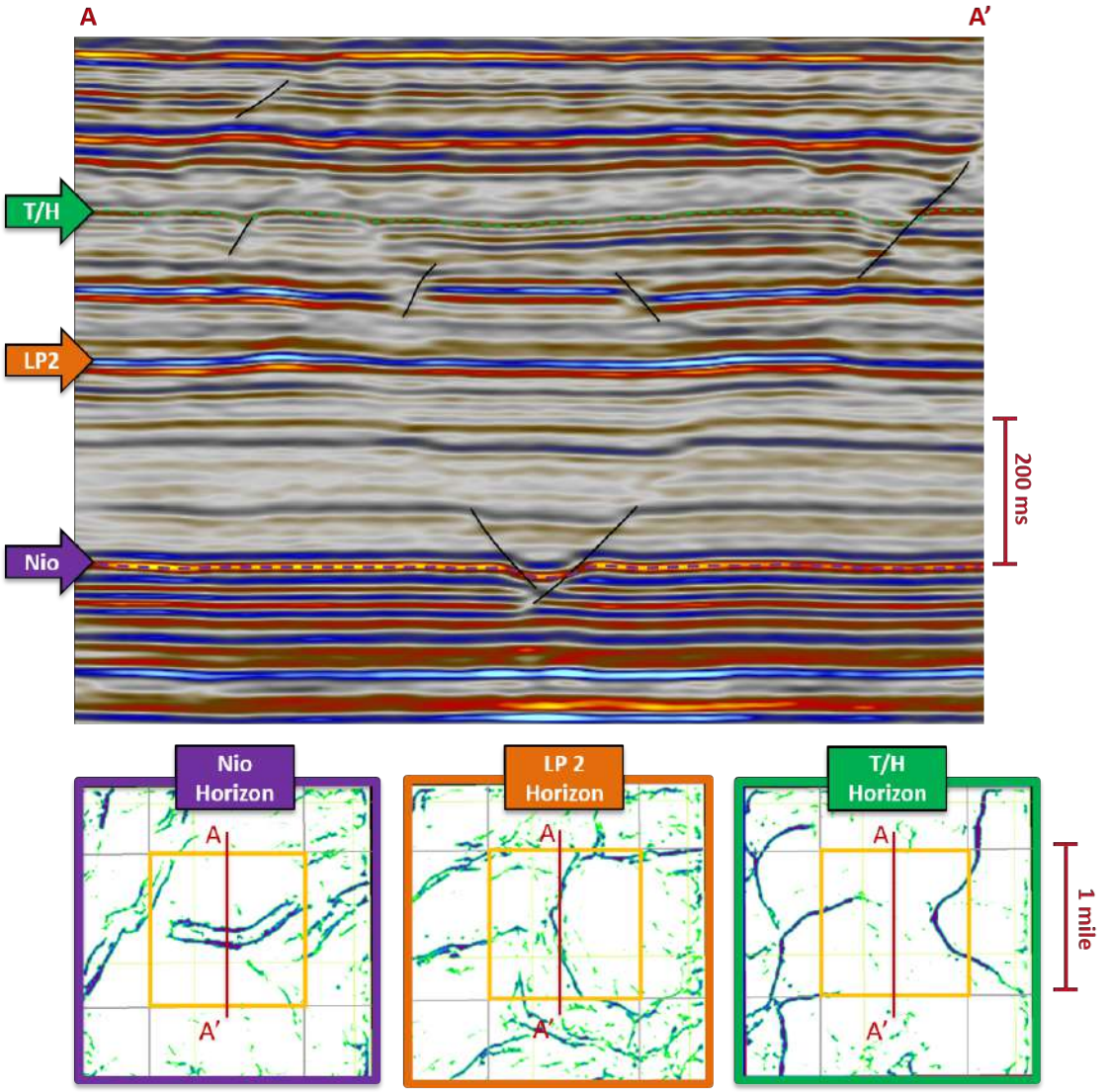

Figure 6.17: Changing fault regimes throughout vertical profile of the Wishbone section that potentially masks HTI signature at the Niobrara-Codell reservoir.

6.7 Conclusions

The 9-C, 4-D Turkey Shoot survey does not suggest that the Niobrara-Codell interval is a simple HTI reservoir. Modeling and ancillary studies, however, have helped with understanding the implications of the data and geologic constraints on interpretation of HTI conditions. The resolved hypothesis is that anisotropy at the Niobrara-Codell reservoir is not only influenced by a single vertical fracture set as observed by microseimic and FMI logs, but one consideration is possible lateral velocity variations in the overburden.

Unfortunately, a detriment to validating this hypothesis is the limited survey area over the Wishbone section and the changing fault regimes throughout the overburden. This small spatial coverage makes it difficult to interpret the influence of lateral velocity variations on the seismic response since faulting influences most of the Wishbone area.

Provided more time, modeling the influence of different overburden anisotropy on an HTI reservoir could help better assess the Wishbone seismic response. If this hypothesis is validated, we also need to acknowledge that conventional P-wave layer stripping algorithms assume HTI overburden anisotropy. To appropriately apply layer stripping to the Wishbone Section would require reformulation of layer stripping techniques to account for shallow lateral velocity variations.

In the next chapter, I take interpretation of multicomponent data sets one step further by discussing converted and shear wave inversion techniques for fracture identification. Although, I have acknowledged the Wishbone section to be more complex, the models input to the inversion are simple HTI reservoirs with no anisotropic overburden. To move multicomponent research forward to the point where we can interpret fractured intervals with anisotropic overburden, we must first formulate techniques for inverting simple HTI reservoirs using all available data components.

CHAPTER 7

SPLITTING ANALYSIS AND COMPENSATION: JOINT INVERSION OF PS AND SS

7.1 Shear Wave Splitting Estimation using Alford Rotation

Applications of shear-wave splitting in exploration began with the pioneering work of Alford (1986). On transmission through a fractured medium, the shear waves polarize parallel (fast) and perpendicular (slow) to the fracture strike. Alford's inverse problem solves for fracture orientation by rotating the reflected energy into post-stack fast and slow data components by minimizing energy on the cross-terms whether in radial-transverse coordinates (RT and TR) or acquisition coordinates (XY and YX).

The inverse problem for finding the fast-slow orientations is broken down in Equation 7.1 and summarized in Figure 7.1. The R-T input data sets are move-out corrected, muted, azimuthally sectored and stacked over offset i.e. each trace represents an azimuthal bin (θ_{data}). The algorithm rotates the RR, RT, TR and TT data sets by $\theta_{trial} - \theta_{data}$ where θ_{trial} is a vector of trial azimuths. Each iteration of a trial azimuth produces 'pseudo-fast' and 'pseudo-slow' data components (FF', FS', SF' and SS'). From those, the azimuths at which energy on the cross-term components (SF' and FS') is minimized is identified as the principle azimuths. One such minimization technique involves measuring the polarization quality which is the ratio of principal component energy (FF' and SS') to cross-term energy (FS' and SF') as defined by Shuck (1993). The trial azimuth which produces the best polarization quality is interpreted as the fast azimuth (θ_{fast}). A final rotation of the RR, RT, TR and TT components by $\theta_{fast} - \theta_{data}$, will produce true fast-slow data components (FF and SS).

$$\begin{bmatrix} FF' & FS' \\ SF' & SS' \end{bmatrix} = \begin{bmatrix} \cos(\phi) & \sin(\phi) \\ -\sin(\phi) & \cos(\phi) \end{bmatrix} \begin{bmatrix} RR_{\theta_{data}} & RT_{\theta_{data}} \\ TR_{\theta_{data}} & TT_{\theta_{data}} \end{bmatrix} \begin{bmatrix} \cos(\phi) & -\sin(\phi) \\ \sin(\phi) & \cos(\phi) \end{bmatrix} \tag{7.1}$$

$$\phi = \theta_{trial} - \theta_{data} \tag{7.2}$$

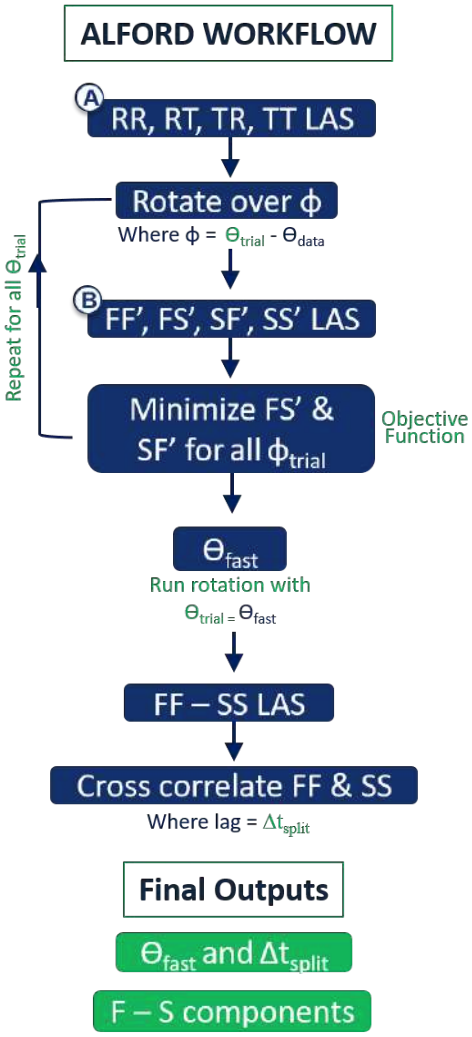

Figure 7.1: Description of Alford rotation workflow for pure shear wave data (Alford, 1986).

Figures 7.2 and 7.3 demonstrate the Alford rotation algorithm for an input model containing a simple HTI layer with no overburden anisotropy and vertical fractures oriented at a 60 degree azimuth. The model is the same as that used by Simmons (2009) with only the shallow HTI layer included. In these figures, the upper panels labeled 'A' are the input LAS in R-T coordinates and correlate to the step labeled 'A' in the Alford workflow (Figure 7.1).

In Figure 7.2, an iteration with θ_{trial} not equaling θ_{fast} is shown. In this case, there is significant energy on the FS and SF cross-terms and there is no clear travel time difference between the reflections in FF and SS. In Figure 7.3, $\theta_{trial} = \theta_{fast}$ and the energy on the

shear wave cross-terms is minimized. There is also an obvious travel time difference between reflections in the FF component and the SS component.

Figure 7.4 shows the 1-D objective function on which the cross-term energy is minimized. The range of trial azimuths for this inversion was 0 to 90 degrees and for a trial azimuth of 60 degrees, the energy on the cross-term components is minimized.

The second step in Alford's technique is to determine the degree of shear-wave splitting (SWS) at the fractured interval. This is done by calculating the time shifts (Δt_{split}) between the fast and slow data sets using a cross-correlation approach. The lag associated with the maxima of the cross-correlation gives an estimate of the time shift. It is important to note that large amplitudes may bias cross-correlation results and as such the time window over which Alford rotation is applied must be carefully chosen.

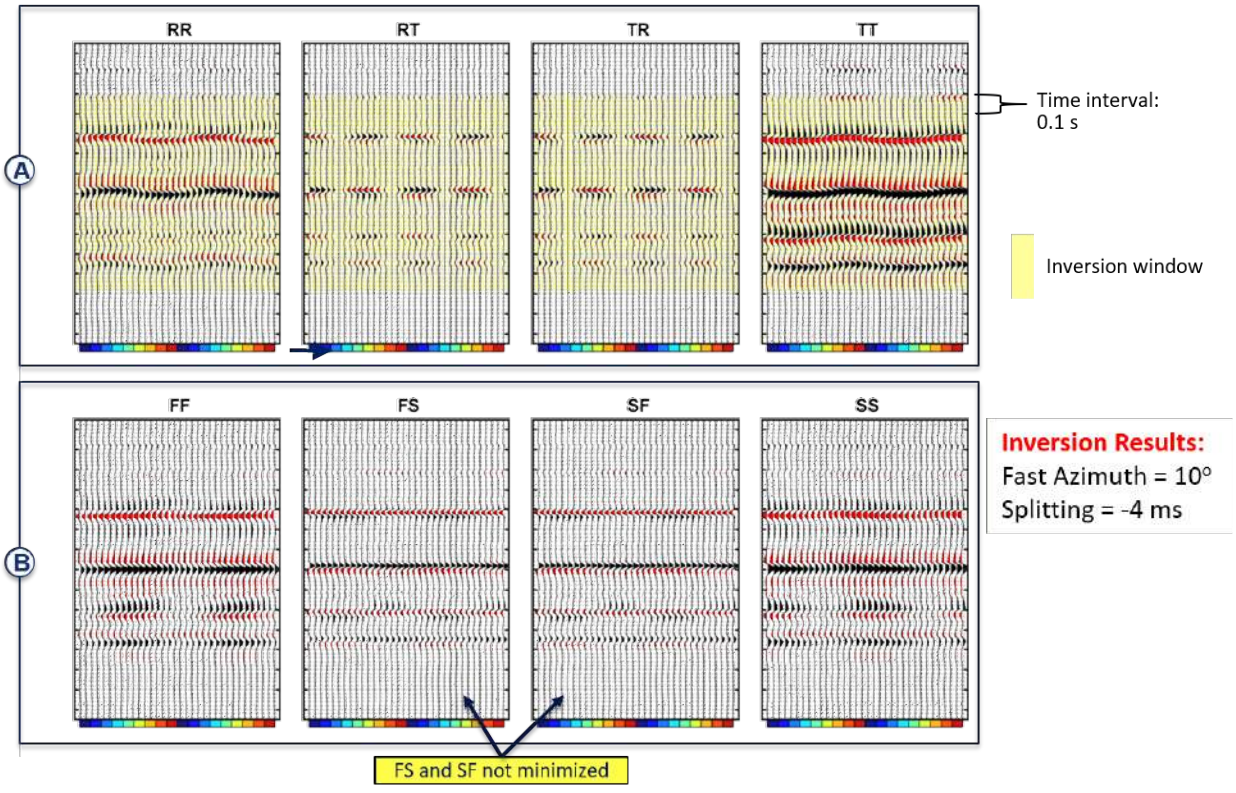

Figure 7.2: Iteration of Aflord rotation algorithm for θ_{trial} **not** equal to θ_{fast}. For this iteration, shear wave crossterms, FS and SF, are not minimized and the FF and SS components both contain a mix of fast and slow shear waves.

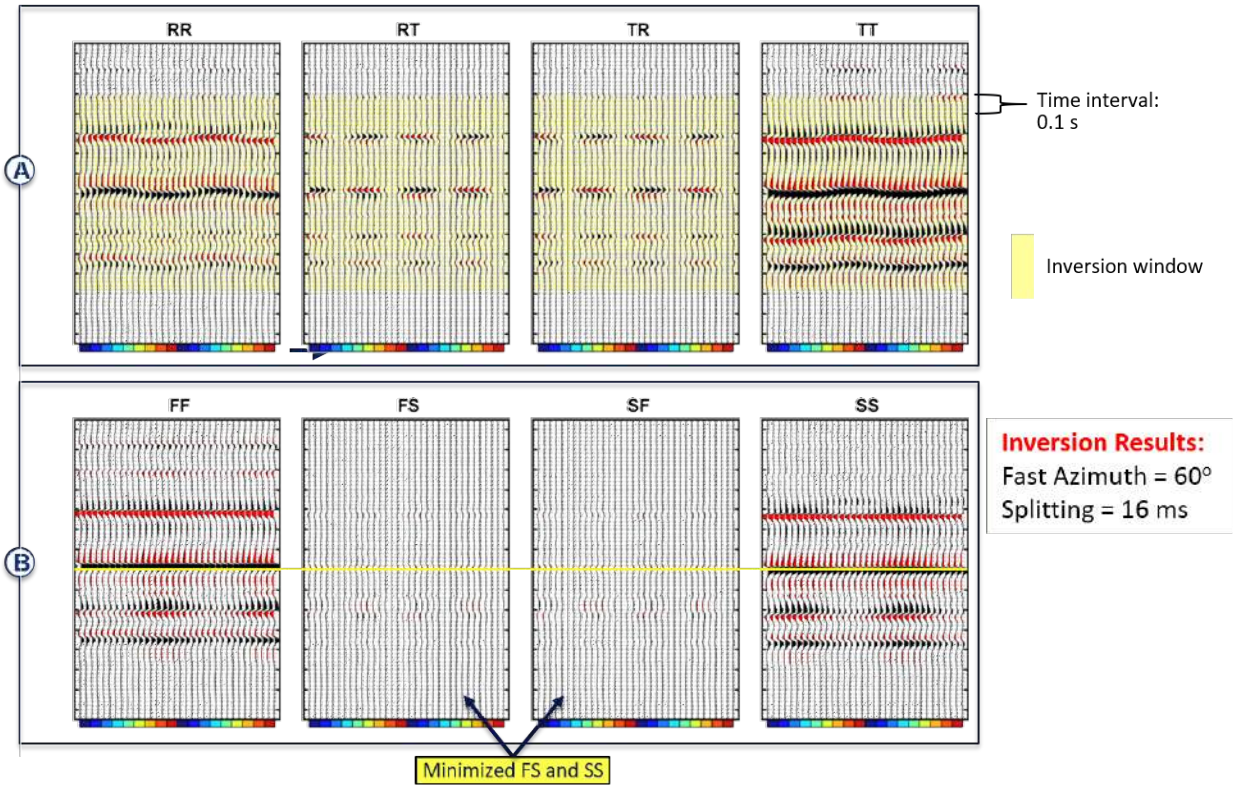

Figure 7.3: Iteration of Aflord rotation algorithm for $\theta_{trial} = \theta_{fast}$ where FS and SF are minimized and the FF and SS components contain the separated fast and slow shear waves. A travel time difference is observed between FF reflections and SS reflections. The dashed yellow line is datum at a FF reflection and helps identify the amount of splitting.

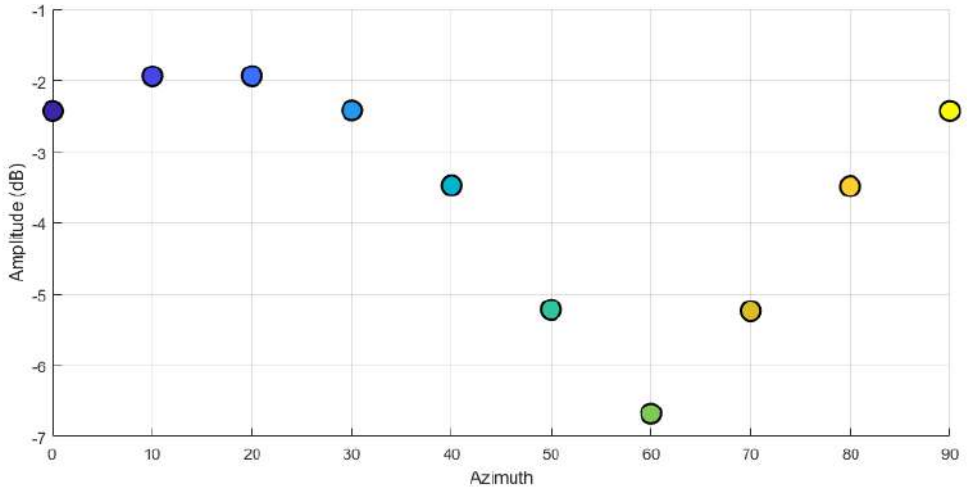

Figure 7.4: 1-D objective function of Alford Rotation for model with 60 degree fast azimuth.

7.2 Discussion of Alford Rotation Assumptions and Application using simple Niobrara Modeling

There are a few assumptions that Alford Rotation makes prior to application. The input LAS data is expected to be normal incidence reflections and the inversion window needs to be carefully and appropriately selected. In this section, I demonstrate the impact of these assumptions on the 110m and 12m thick HTI Niobrara models described in Chapter 5. The input limited azimuth stacks for this section were built by sectoring the Niobrara models into 20^o azimuth bins from -170^o to 170^o.

7.2.1 Normal Incidence Assumption

Alford rotation theory is strictly valid at normal incidence (Thomsen, 1988) where there are only orthogonally polarized SH-waves, and no SV-waves. A common industry technique is to apply Alford rotation on pre-stack data sets that have been rotated to F-S based on a regional stress direction (DeVault et al., 2002; Shuck, 1993). Once offset is introduced in F-S pre-stack data, both SV- and SH-waves are recorded on the pure shear wave components and the strict assumptions of Alford rotation are void. Recall that energy on the cross-terms are not solely related to shear-wave splitting and geometry effects dominate the pre-stack signal in F-S space. Figure 4.5 of Chapter 4 shows this pre-stack F-S cross-term energy dependence on source-receiver azimuth.

Another typical industry practice is to apply a mute on the pure shear wave components at the angle of the polarity reversal on RR. This polarity reversal is discussed in Chapter 3 and Figure 7.5 shows the COCA gathers for the converted and shear wave components with two mute angles outlined. Figures 7.6 and 7.7 show the outputs of Alford rotation for the fully cracked Niobrara model described in Chapter 5 using both mutes. Recall, that the VVAz effects for the Niobrara models are very small. As such, for all displays presented in this chapter, the RT, TR, FS and SF cross-terms are gained by a defined factor as documented in the figure captions.

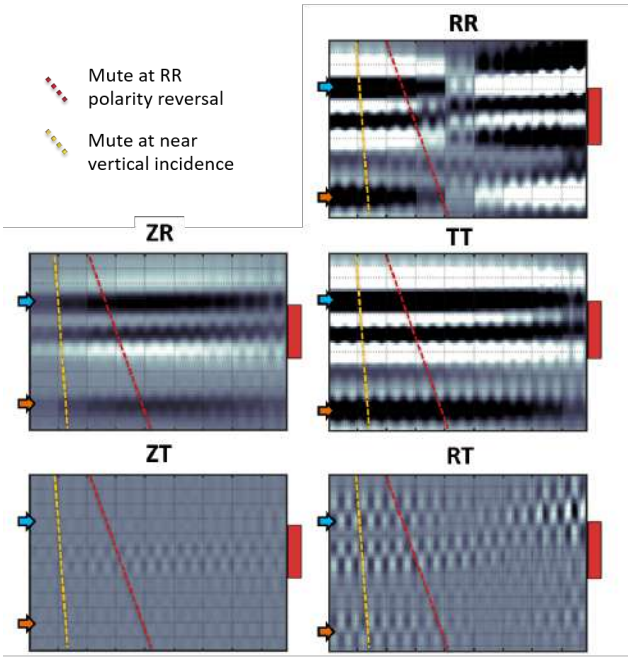

Figure 7.5: Description of mutes applied to shear wave synthetics generated from the fully cracked (110m) Niobrara model described in Chapter 5, Table 5.2. Two sets of limited azimuths stacks were generated for input into Alford rotation using the two different mutes. Timing lines = 20ms

In Figure 7.6, an outer mute is applied at the angle of polarity reversal on the RR data and in Figure 7.7, the mute is tightened such that only near-vertical incidence angles are considered. Ideally, this would imply that RR=TT. Figures 7.6 and 7.7 are at the same relative gain. With the far mute on the 110m HTI model, the algorithm is still able to solve for the correct azimuth, however, the cross-terms FS and SF are not minimized and the solution for Δt_{split} cannot be trusted. With the tight mute, the cross-terms are significantly minimized and the algorithm identifies the fast azimuth and a plausible Δt_{split}. Note that the Δt_{split} calculated at the reflector marked by the green arror will not have the same amount of Δt_{split} at the reflector marked by the orange arrow. I discuss this in detail in the next section.

The importance of the normal incidence assumption becomes increasingly obvious for thinner HTI models. Figures 7.8 and 7.9 describe the solutions for the model with 12m of HTI in the Niobrara (Chapter 5, Table 5.2). The solution based on limited azimuth stacks

with far offset mutes (Figure 7.8) incorrectly identifies the fast azimuth as 100 degrees. The solution based on limited azimuth stacks with a tight mute correctly identify the fast azimuth at 110 degrees.

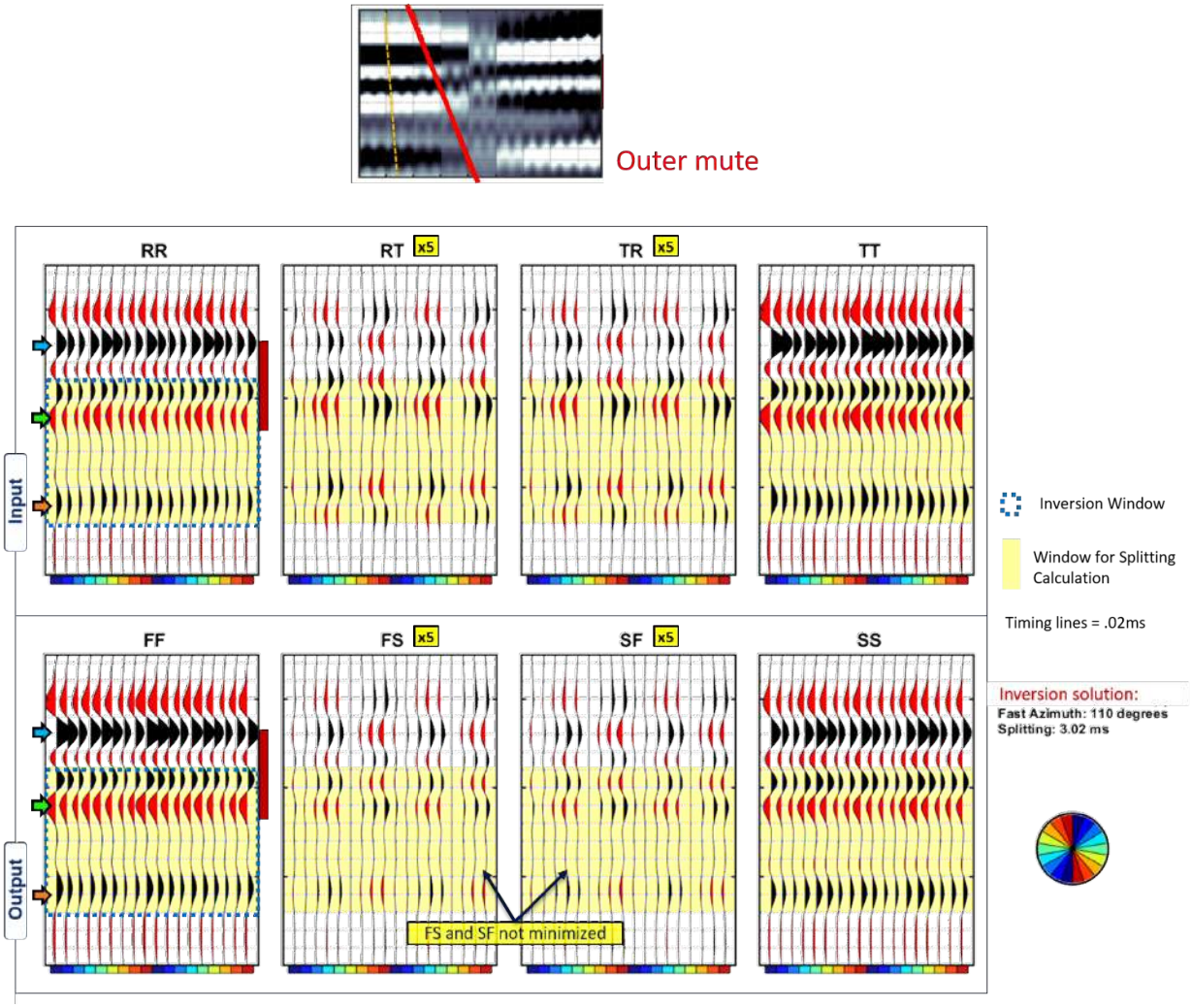

Figure 7.6: Solution of fast azimuth and shear wave splitting for radial-transverse LAS generated using a mute at the polarity reversal on the RR component (RR $\neq$ TT). The input LAS are built from the fully cracked Niobrara model (110m). The solution is based on the Alford Rotation technique described in Figure 7.1. The Niobrara, Carlile and Graneros reflectors are highlighted by the blue, green and orange arrows respectively and the red bar indicates the extent of the HTI interval. The cross-terms RT, TR, FS and SF are gained x5 to show the weak VVAz response.

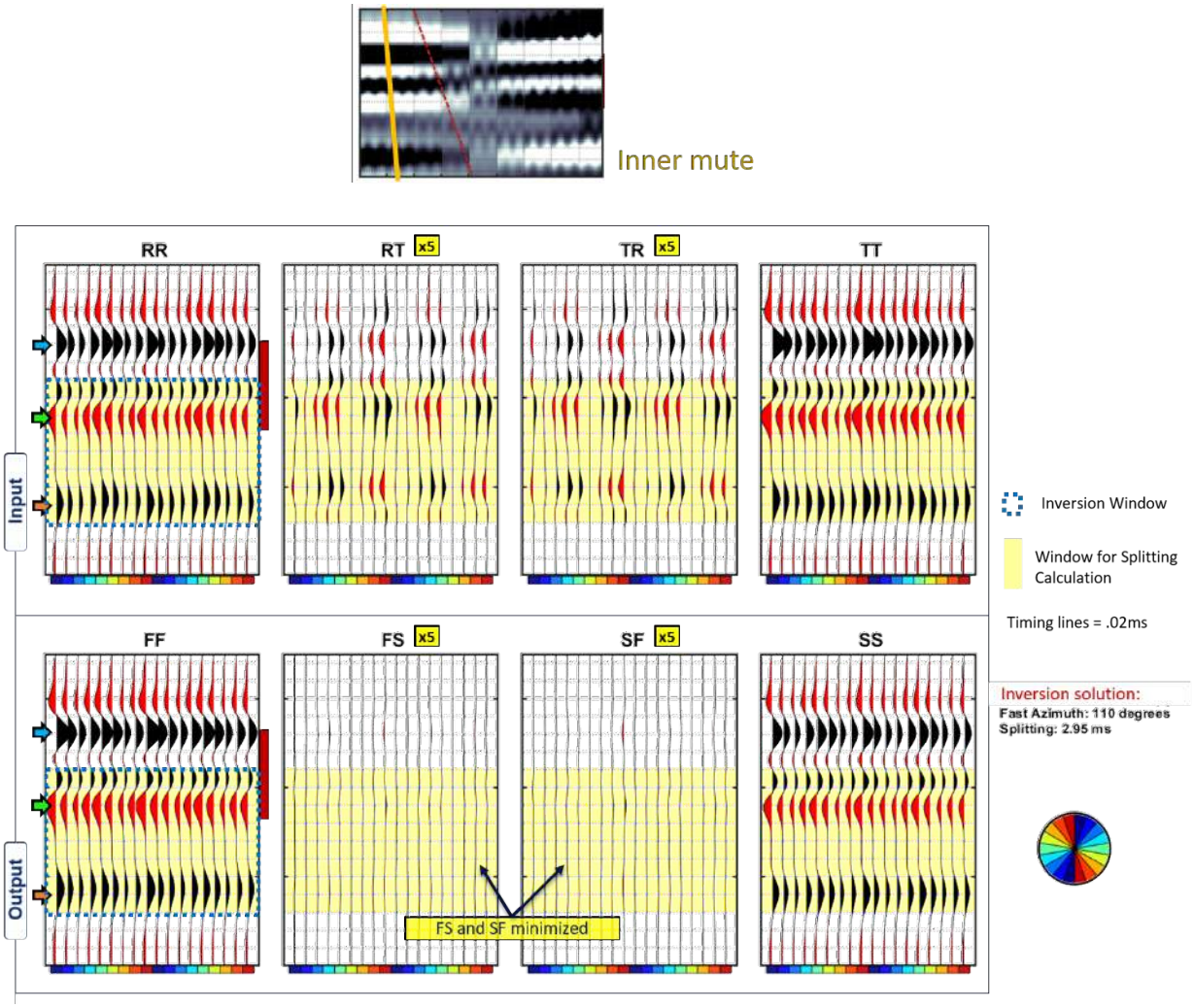

Figure 7.7: Solution of fast azimuth and shear wave splitting for radial-transverse LAS generated using a tight mute at near-vertical angles of incidence (RR = TT). The input LAS are the same 110m HTI model used in Figure 7.6 and the gain treatment is also the same. The fast azimuth solution is the same, however, with the tight mute, the cross-terms are appropriately minimized. The Δt_{split} calculation is slightly different.

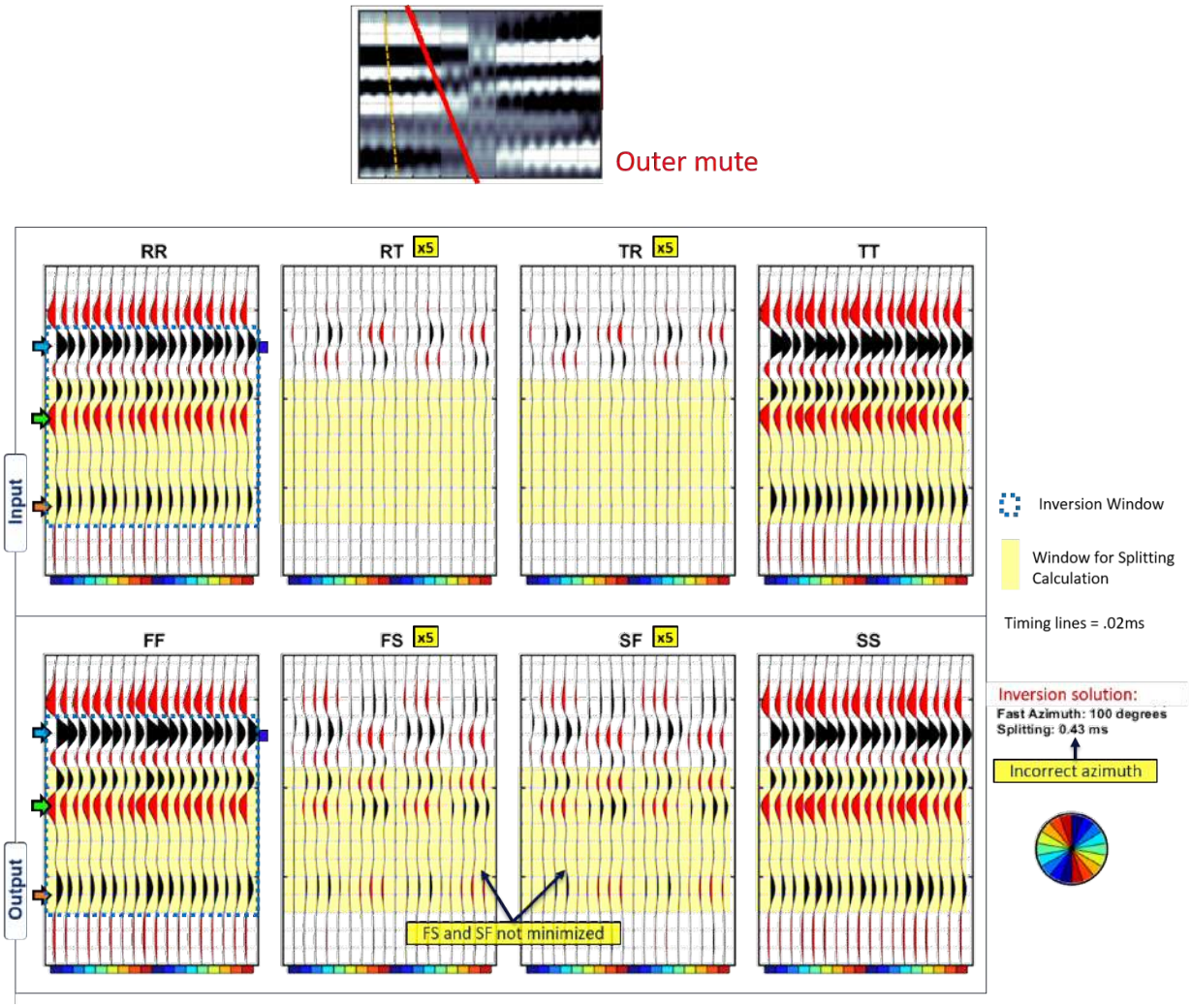

Figure 7.8: Solution of fast azimuth and shear wave splitting for radial-transverse LAS generated using a mute at the polarity reversal on the RR component (RR $\neq$ TT). The input LAS are built from the Niobrara model with cracks in the upper 12m.The Niobrara, Carlile and Graneros reflectors are highlighted by the blue, green and orange arrows respectively. The purple bar indicates the extent of the HTI interval and the cross-terms RT, TR, FS and SF are gained x5 to show the weak VVAz response. For this thin model with a far offset mute, the cross-terms are not minimized and the fast azimuth calculation is incorrect.

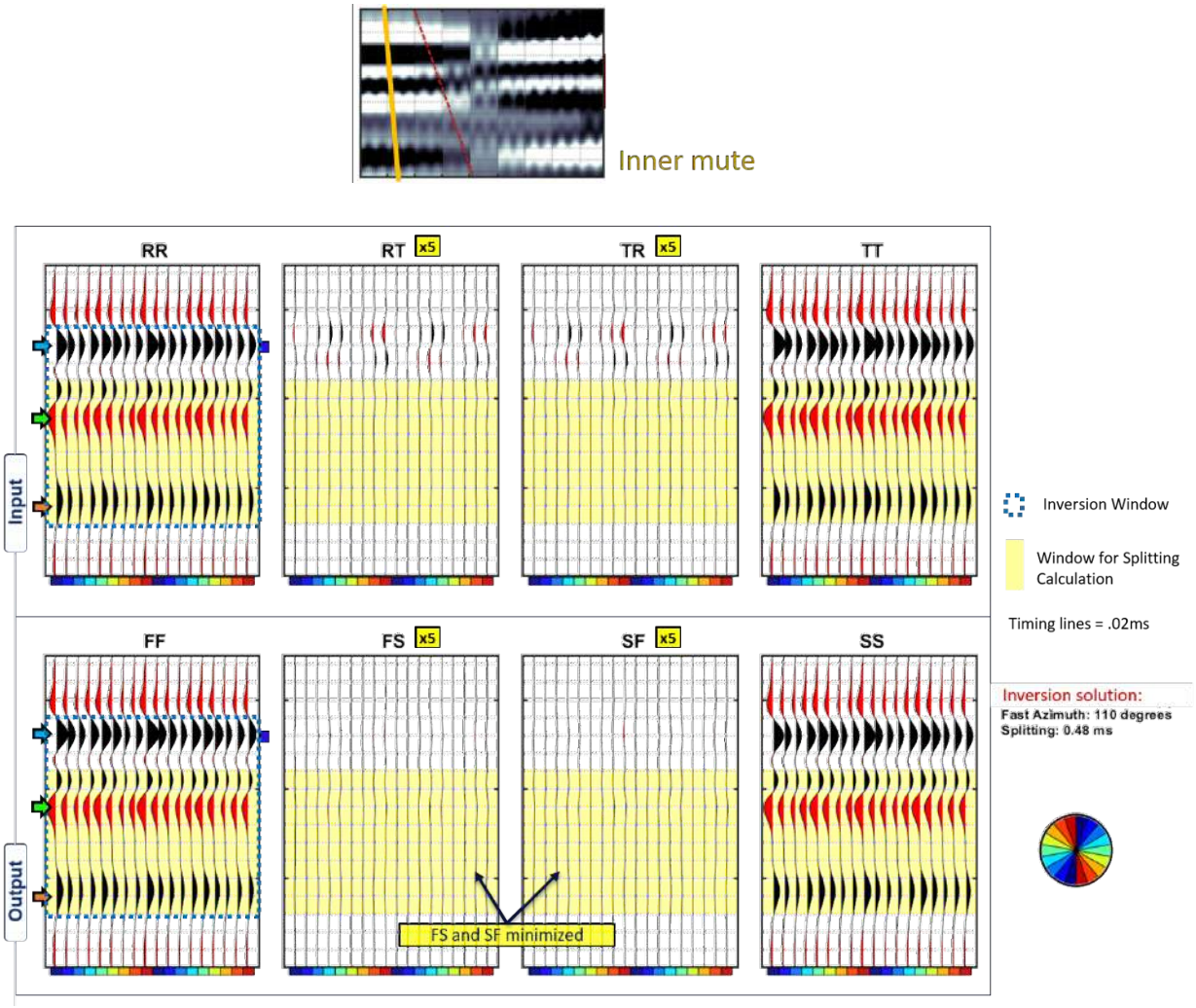

Figure 7.9: Solution of fast azimuth and shear wave splitting for radial-transverse LAS generated using a tight mute at near-vertical angles of incidence (RR = TT). The input LAS are the same 12m HTI model used in Figure 7.8 and the gain treatment is also the same. The fast azimuth solution is correctly calculated with this mute and the FS and SF cross-terms are minimized.

7.2.2 Selecting the Inversion and Cross-correlation Window

Note that for the Niobrara model with a 12m HTI interval, the inversion window for the fast azimuth was extended vertically (blue outline on Figures 7.8 and 7.9). Analysis of the limited azimuth stacks for different HTI thicknesses (Chapter 5), showed that the VVAz effects for thinner HTI medium are observed at the strongest reflector nearer the top of the HTI layer. If the Niobrara top is not included in the inversion, the fast azimuth is incorrectly calculated. The Δt_{split} solutions for the examples above are based on the same correlation window highlighted in yellow which are not necessarily optimal.

Not only, should the azimuthal inversion window be adjusted according to R-T cross-term energy, but the window for calculating the splitting between the FF and SS components should also be carefully selected. While the original Alford rotation technique uses cross-correlation to find Δt_{split}, correlation solutions are biased to high amplitude values. Figures 7.10 and 7.11 show the calculated Δt_{split} for the fully cracked Niobrara model (110m HTI) using different windows highlighted in yellow. Over the deep interval, the estimated splitting is 4.07 ms and for a shallower interval the estimated splitting is 2.52 ms. The shallow interval has not seen the full effect of the splitting as opposed to the deep reflector.

Travel time is cumulative with depth (Gaiser, 1999) and validating the Δt_{split} solution is difficult given that it varies with the selected window. However, as reiterated in this thesis, all components must tell the same story and where 9-C is available, analysis of shear wave splitting on both the converted and shear wave data can constrain the Δt_{split} solution.

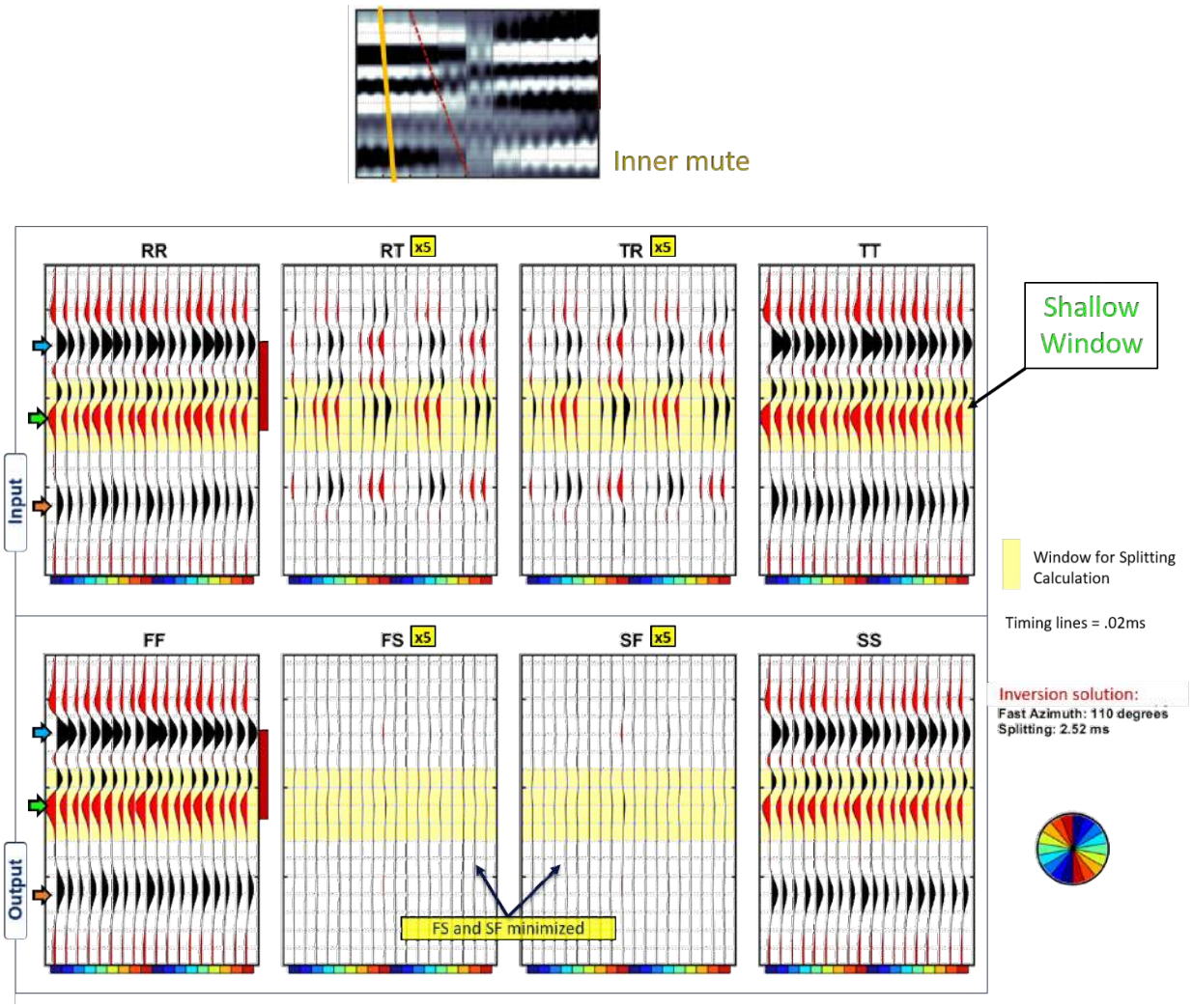

Figure 7.10: Alford rotation solution using a shallow cross-correlation window for the fully cracked Niobrara model (110m). For this shallow window: fast azimuth solution = 110 degrees and travel time split solution = 2.52ms. The Niobrara, Carlile and Graneros reflectors are highlighted by the blue, green and orange arrows respectively and the red bar indicates the extent of the HTI interval. The cross-terms RT, TR, FS and SF are gained x5 to show the weak VVAz response.

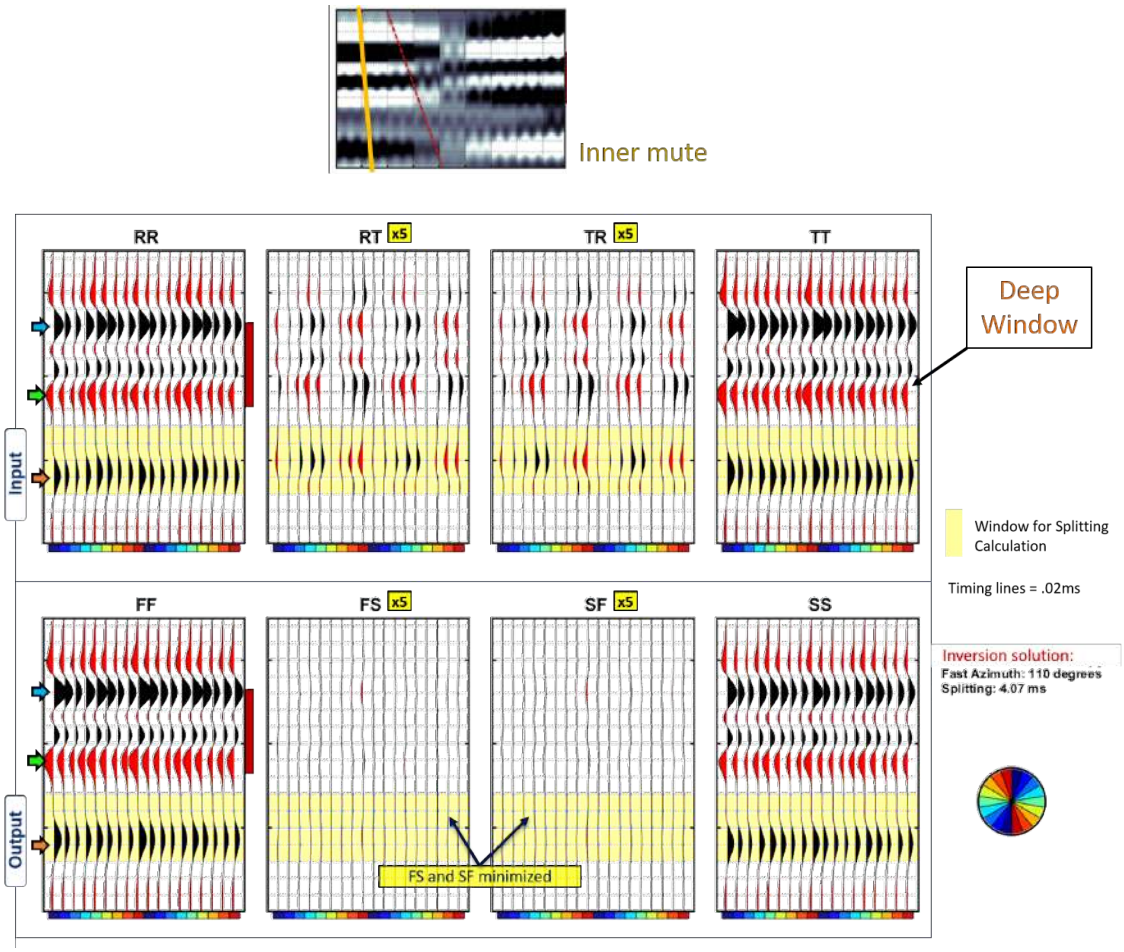

Figure 7.11: Alford rotation solution using a deep cross-correlation window for the fully cracked Niobrara model (110m). For this deep window: fast azimuth solution = 110 degrees and travel time split solution = 4.07ms. The Niobrara, Carlile and Graneros reflectors are highlighted by the blue, green and orange arrows respectively and the purple bar indicates the extent of the HTI interval. The cross-terms RT, TR, FS and SF are gained x5 to show the weak VVAz response.

7.3 Converted Wave: Splitting Estimation and Compensation (SEAC)

Gaiser (1999) adapted the pure shear-wave rotation analysis of Alford to converted SV-waves with an added layer stripping approach. The Δt_{split} is calculated at a shallow time interval and applied to the slow shear wave component produced after Alford rotation. This travel time estimation is done for the overburden layers from shallow to deep since Δt_{split} is cumulative in depth. The result is a layer-stripped converted shear wave volume that allows for interpretation of shear-wave splitting and amplitudes in F-S space at the reservoir level.

Simmons (2009) optimizes the converted wave splitting estimation by simultaneously finding the θ_{fast} and Δt_{split} from azimuthally sectored R-T offset stacks and produces compensated R-T gathers with the splitting removed. The splitting estimation and compensation (SEAC) algorithm (Figure 7.12) attempts to remove the splitting effects at the reservoir interval which improves the radial component data set (SV-wave data) and produces a data misfit volume that potentially better exposes reservoir splitting.

This splitting compensation is achieved by shifting the slow data component (after rotation by θ_{trial}) by $-\Delta t_{trial}$ (processes A through C on Figure 7.12). This effectively removes the time delay between the fast and slow shear wave and rotating back to R-T space (process D on Figure 7.12) concentrates all converted SV-wave energy onto Rc (compensated radial component) and misfit energy, associated with shear wave splitting, onto T-misfit. The θ_{trial} and Δt_{trial} for which the T-misfit component is minimized are the fast azimuth aligned with fracture strike and the associated shear wave splitting (Simmons, 2009).

In Figures 7.13 and 7.14, I run the simple model, with an HTI layer containing 60-degree oriented fractures, through the SEAC algorithm and show the by-products of each step described in Figure 7.12. Figure 7.13 describes an iteration of the inversion that tests a θ_{trial} that is not equal to the fast azimuth. For this trial, the 2-D objective function (energy on T-misfit for a range of θ_{trial} and Δt_{trial}) plotted to the right of Figure 7.13 is not minimized. The objective function is minimized when $\theta_{trial} = \theta_{fast}$ (Figure 7.14) and the solution for $\Delta_{t_{split}}$ is correct.

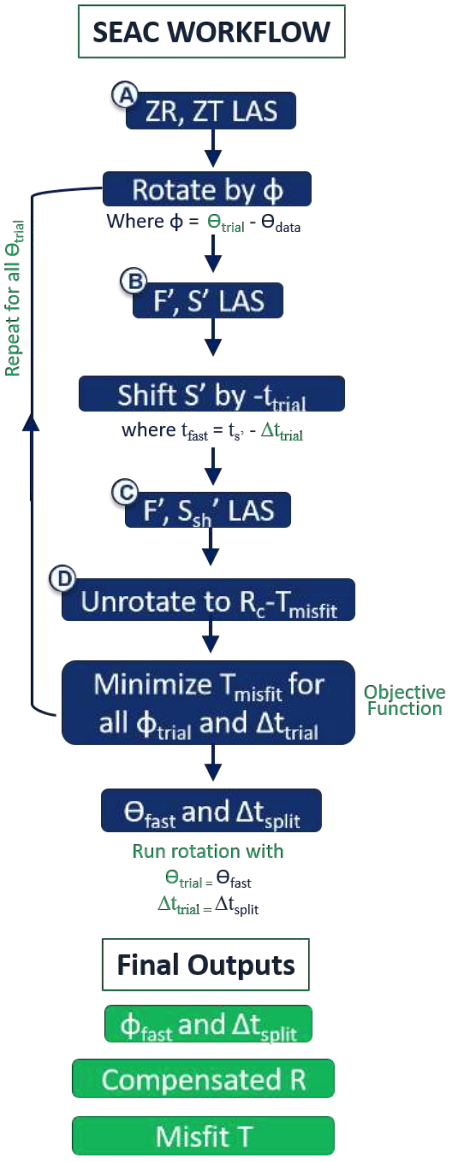

Figure 7.12: Description of SEAC (splitting estimation and compensation) workflow for converted wave data developed by Simmons (2009).

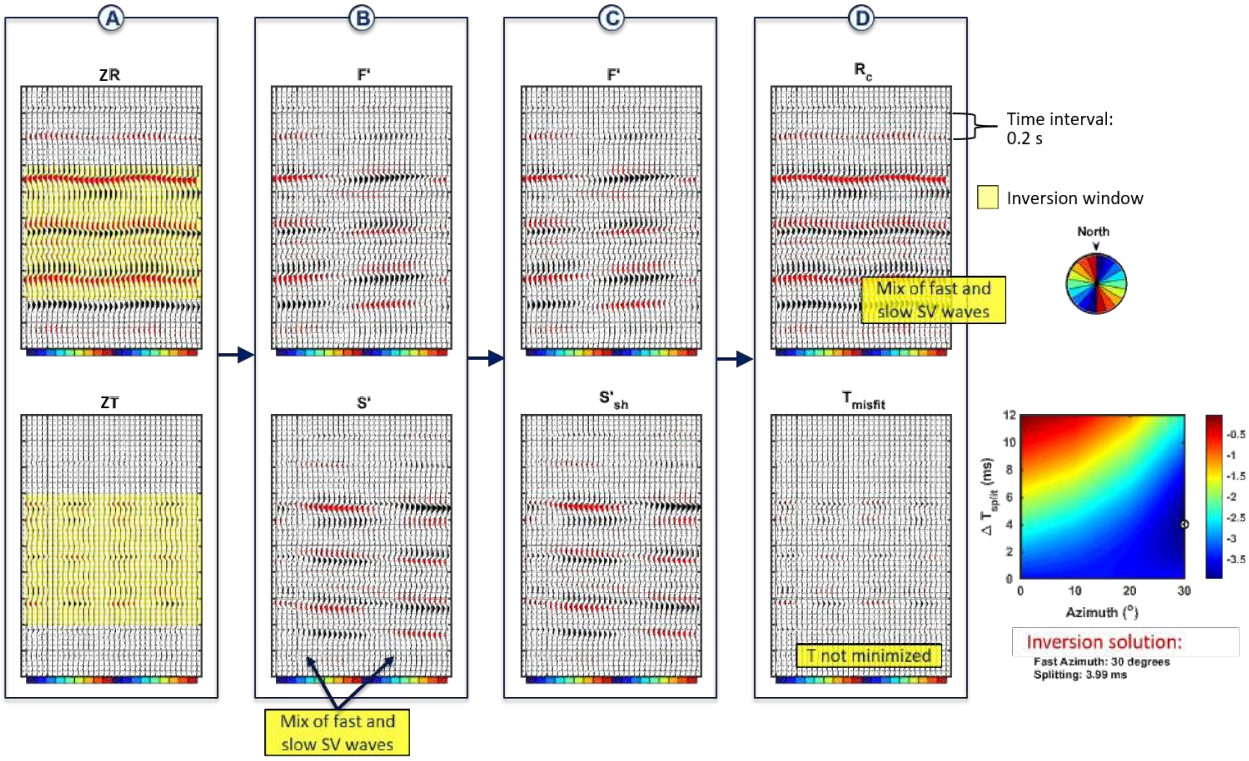

Figure 7.13: Iteration of SEAC inversion code for θ_{trial} not equal to θ_{fast}. The solution is based on the SEAC algorithm (Simmons, 2009) as described in Figure 7.12. The inversion QC is minimizing the objective function (plotted in decibels to the bottom right) for a given azimuth and travel time split. For this iteration, the objective function is not minimized and the F and S components contain a mixed response of fast and slow shear waves.

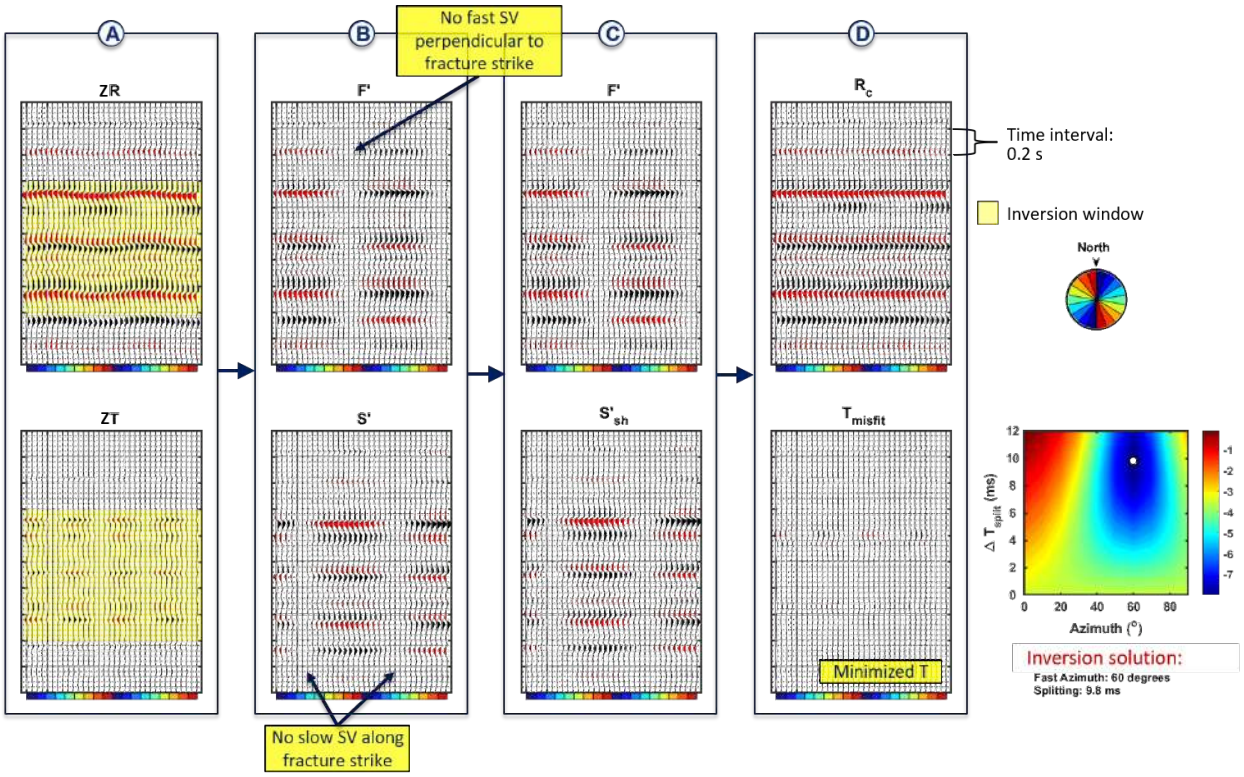

Figure 7.14: Iteration of SEAC inversion code for $\theta_{trial} = \theta_{fast}$. For this 60 degree azimuth and travel time split of 9.8 ms, the objective function (plotted in decibels to the bottom right) is minimized i.e. little energy is left on the T-misfit component and all converted wave energy is mapped onto the compensated R component.

7.4 Application of SEAC on Niobrara Models

Similar to Alford rotation on pure shear wave data, SEAC is sensitive to the time window used for analysis. The SEAC rotation is based on minimizing the energy on the T-misfit component which exposes split shear waves unresolved by the time-shift. Similar to pure shear wave data, this Δt_{split} varies in depth. One advantage to SEAC in the calculation of Δt_{split} is that the algorithm uses a grid search technique similar to the azimuth calculation. This eliminates complications associated with cross-correlation which affect the Alford technique.

A broad window (top Carlile to Graneros) for the thin HTI model (12m cracks in the Upper Niobrara) with far offset mute resolves the correct fast azimuth using SEAC (Figures

7.15 and 7.16) as opposed to the Alford rotation method (Figure 7.9). Recall that for this thin model, it is difficult to visualize the energy on the crossterms since the converted wave shear wave splitting is small. In Figure 7.15, the ZT and T-misfit components are gained by a factor of 5 and in Figure 7.16, these components are gained by a factor of 15. In Figure 7.16, the minimization of the T-misfit compared to the input ZT is observed. The results of the SEAC inversion for the 110m HTI is shown in Figures 7.17 where the cross-terms are gained by a factor of 5.

7.4.1 Validating SWS Solution

The travel time splitting calculated from SEAC will vary with the inversion window used (similar to Alford). We can however, validate the estimated shear wave splitting from SEAC by comparing the result to the splitting estimated from Alford. The pure shear wave data contains a downgoing and upgoing shear wave while the converted wave data has only an upgoing shear wave. The downgoing P-wave of the converted wave data will show VVAz effects on transmission through a fractured medium, however, it will be much smaller compared to the response of the shear wave as demonstrated on the LAS shown in Chapter 5.

A reasonable expectation is that the splitting estimated from the pure shear wave data will be double that of the converted wave provided that both solutions are based on the same time window. The estimated Δt_{split} using the SEAC and Alford techniques were calculated for the 110m model using three different inversion windows. These windows and results are noted in Figure 7.18. The ratio between the Δt_{split} estimation from the pure shear wave data and the converted wave data is approximately 2 for all windows. This confirms that the converted wave and shear wave data are telling the same story and the inversion results from both Alford and SEAC are valid.

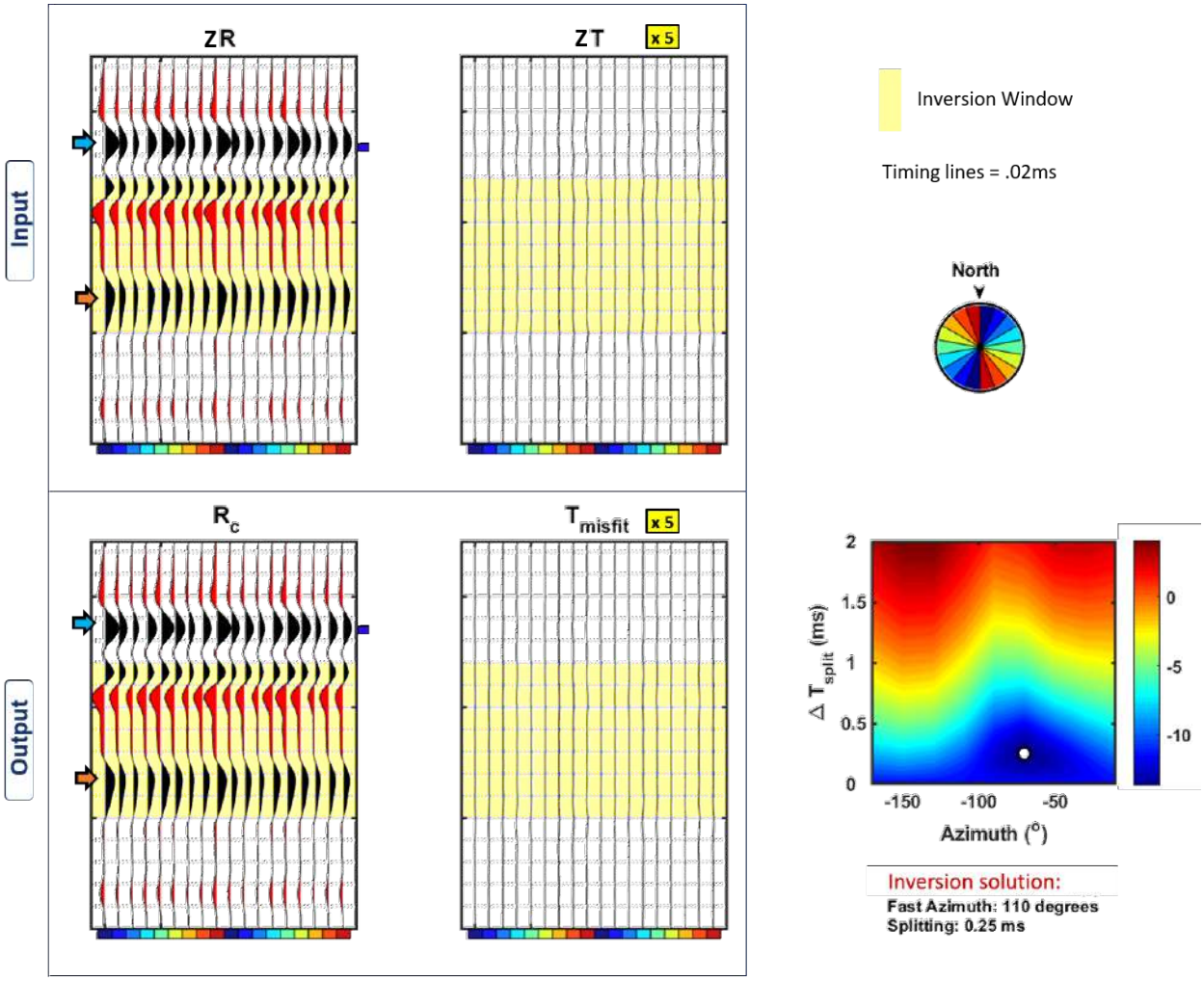

Figure 7.15: Solution of fast azimuth and shear wave splitting for radial-transverse LAS generated from the Niobrara model with cracks in the upper 12m. The Niobrara and Graneros reflectors are highlighted by the blue and orange arrows respectively and the purple bar indicates the extent of the HTI interval. T and T-misfit components are gained x5, however, regardless of the difficulty in visualizing this energy the SEAC algorithm still solves for the correct fast azimuth of 110 degrees. The objective function displays the T-misfit amplitudes in decibel scale.

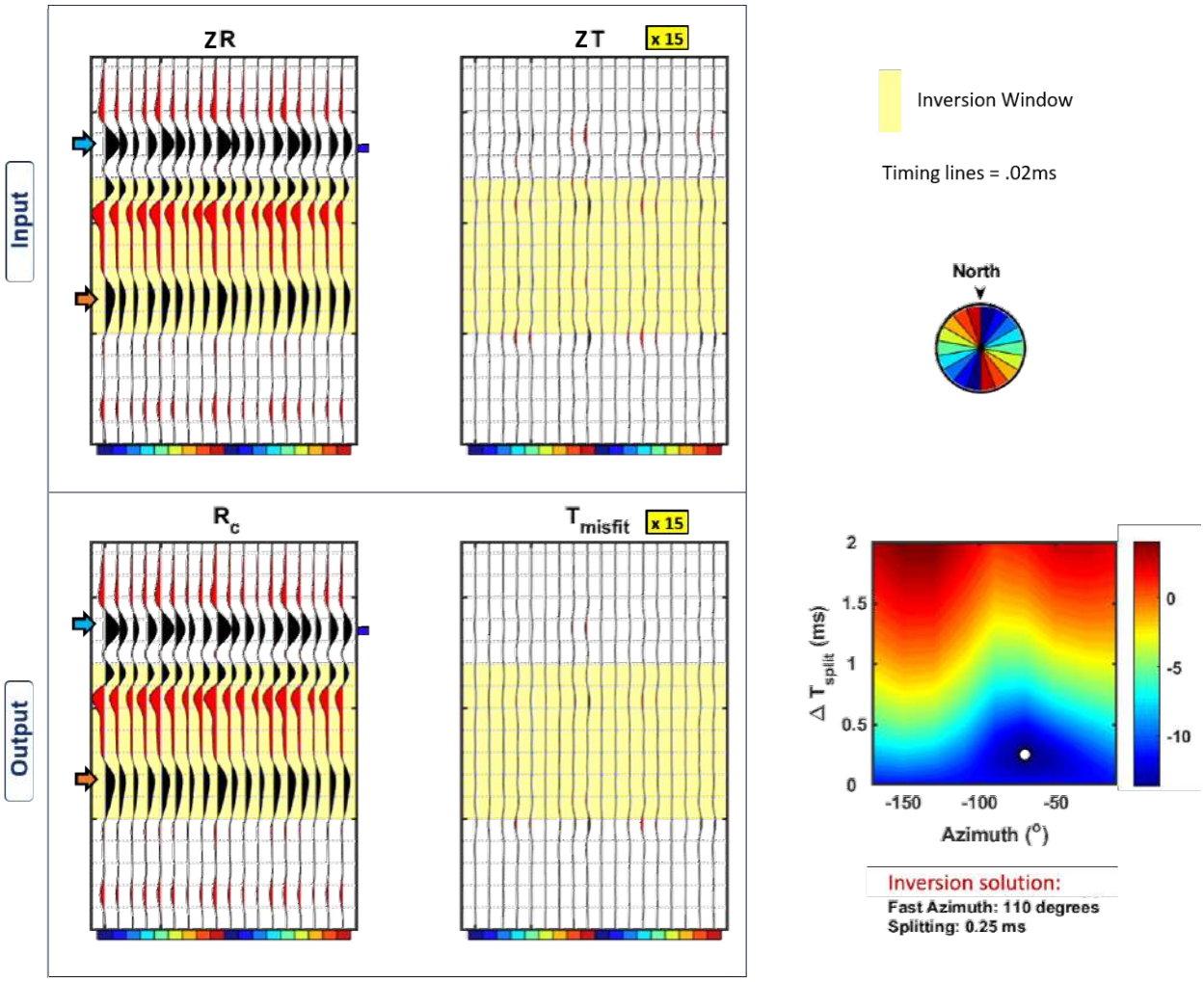

Figure 7.16: Solution shown in Figure 7.15 with T and T-misfit components gained x15 to show the energy minimization effectively accomplished by the SEAC algorithm. The objective function displays the T-misfit amplitudes in decibel scale.

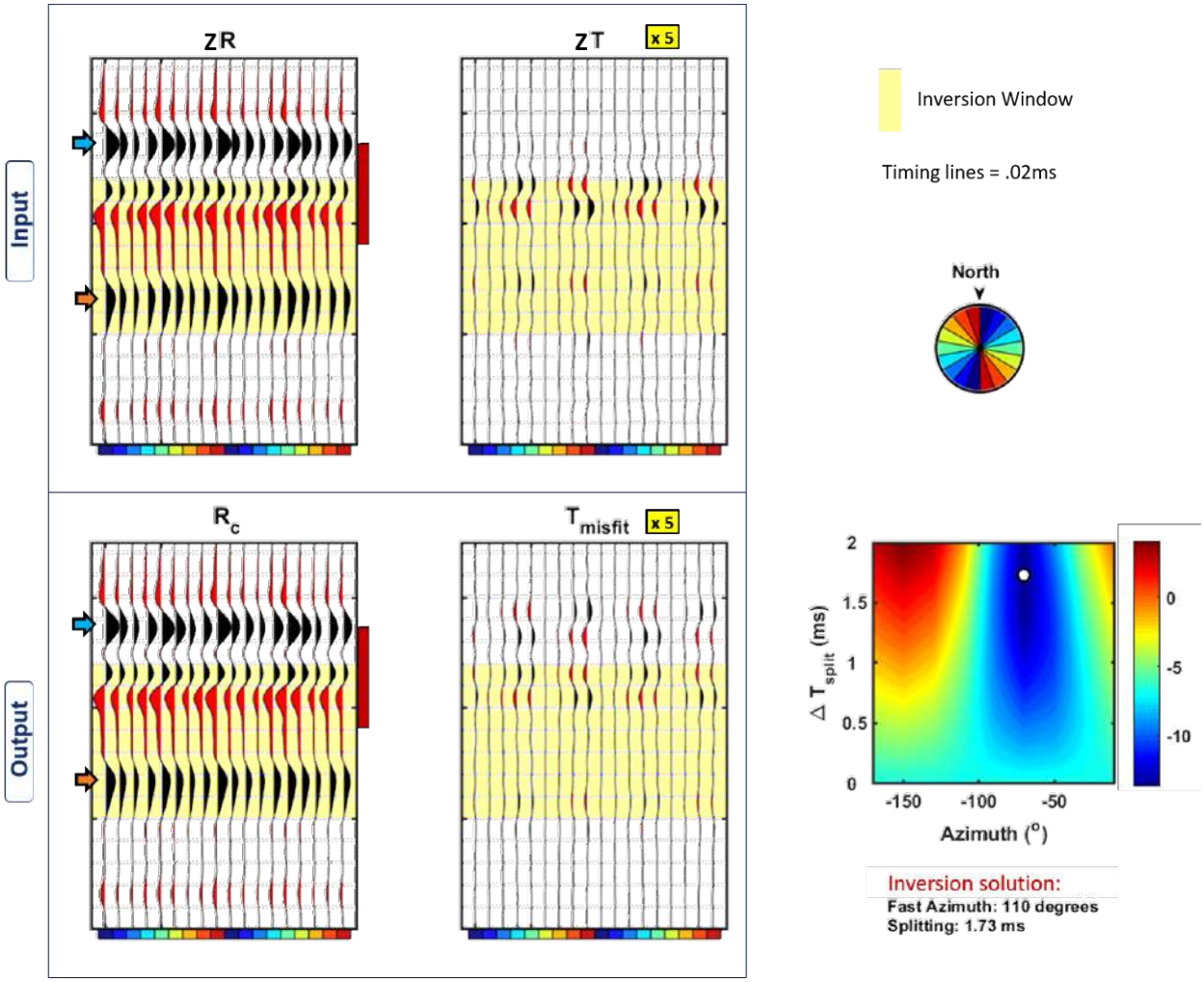

Figure 7.17: Solution of fast azimuth and shear wave splitting for radial-transverse LAS generated from the fully cracked Niobrara model (110m). The Niobrara and Graneros reflectors are highlighted by the blue and orange arrows respectively and the red bar indicates the extent of the HTI interval. T and T-misfit are gained by a factor of 5 to show comparable energies but not relative to the main components. The objective function displays the T-misfit amplitudes in decibel scale.

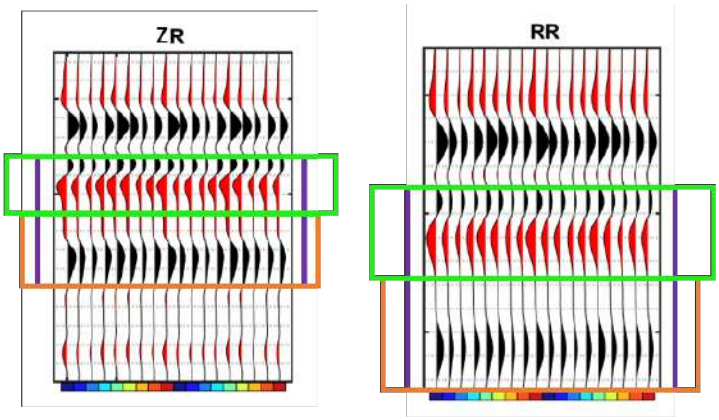

	SEAC Tsplit	ALFORD Tsplit	RATIO	
110m Model	1.73	2.95	1.7	Full window
	1.77	2.52	1.4	Shallow window
	1.64	4.07	2.5	Deep window

Figure 7.18: Comparison of Δt_{split} estimations from Alford and SEAC for different inversion windows for the 110m Niobrara model. The inversion windows span the same layers for the converted and pure shear LAS components.

7.5 Application of Alford Rotation and SEAC on Field Data

There are intrinsic complications with the Turkey Shoot data based on the acquisition and processing steps applied (Chapter 6). A primary concern is that there is little documentation on the processing steps and while receiver rotation analysis was completed within RCP, there is no record of source rotation analysis to validate that the rotations were done correctly. Additionally, a look at the LAS displays in Chapter 6 has revealed little to no HTI-related VVAz effects that are exposed on all components for the same location. Despite these known complications, the field data were input into the SEAC and Alford rotation algorithms.

SEAC was run on the converted wave components over a time interval spanning the Niobrara to Graneros interval. The input LAS were generated with a 20 degree azimuth bin and 500 ft offset bins and a tight outer mute was applied to the field data. Figure 6.5, discusses the LAS observations and shows the stacks for two locations, 16 and 39 on Figure

6.3. The SEAC solution for these two locations on the Baseline survey are shown in Figures 7.19 and 7.20. The ZT and T-misfit components are gained by a factor of 3 relative to the main ZR and Rc components. The pure shear wave LAS were generated with a similar tight mute and input into the Alford rotation code. The solutions at locations 16 and 39 are shown in Figures 7.21 and 7.22.

The 2D SEAC objective function and 1D Alford rotation objective function are plotted for each display. Both algorithms were run for trial azimuths ranging from -170^o to 0^o.

7.5.1 Discussion of Field Data Inversion

For location 16 in Figure 7.19, SEAC solves for a 110 degree (N70W) fast azimuth. While this an appealing solution given that the Turkey Shoot microseismic data indicate that induced fractures propagate along this direction, it is not necessarily accurate. There is little change between the Rc and input ZR component and no significant minimization of energy on the T-misfit component. At location 39 in Figure 7.20, the fast azimuth solution from SEAC is 70 degrees however, we also do not see the appropriate minimization of the T-misfit that would validate this solution. For both locations, the Alford rotation (Figures 7.21 and 7.22) produces FS and SF terms that are not minimized and these solutions are also questionable.

It is important to consider that the input LAS data do not show coherent energy on ZT, RT or TR components that is indicative of HTI-related VVAz. These inversion techniques are simply moving the energy around and not necessarily minimizing the cross-terms.

The inversion outputs are only shown for these two locations however Figure 7.23 shows the calculated fast azimuth for the key locations highlighted in Figure 6.3. The Alford rotation produces either a 90-degree or 180-degree solution and SEAC produces either a 70-degree or 110-degree solution. While the input LAS are binned by 20 degree azimuths, which would limit the solution to 20 degree intervals, the consistency of the solutions are still questionable. Inversions based on the Monitor 1 and 2 datasets show similar biases and a time-lapse interpretation is currently unachievable.

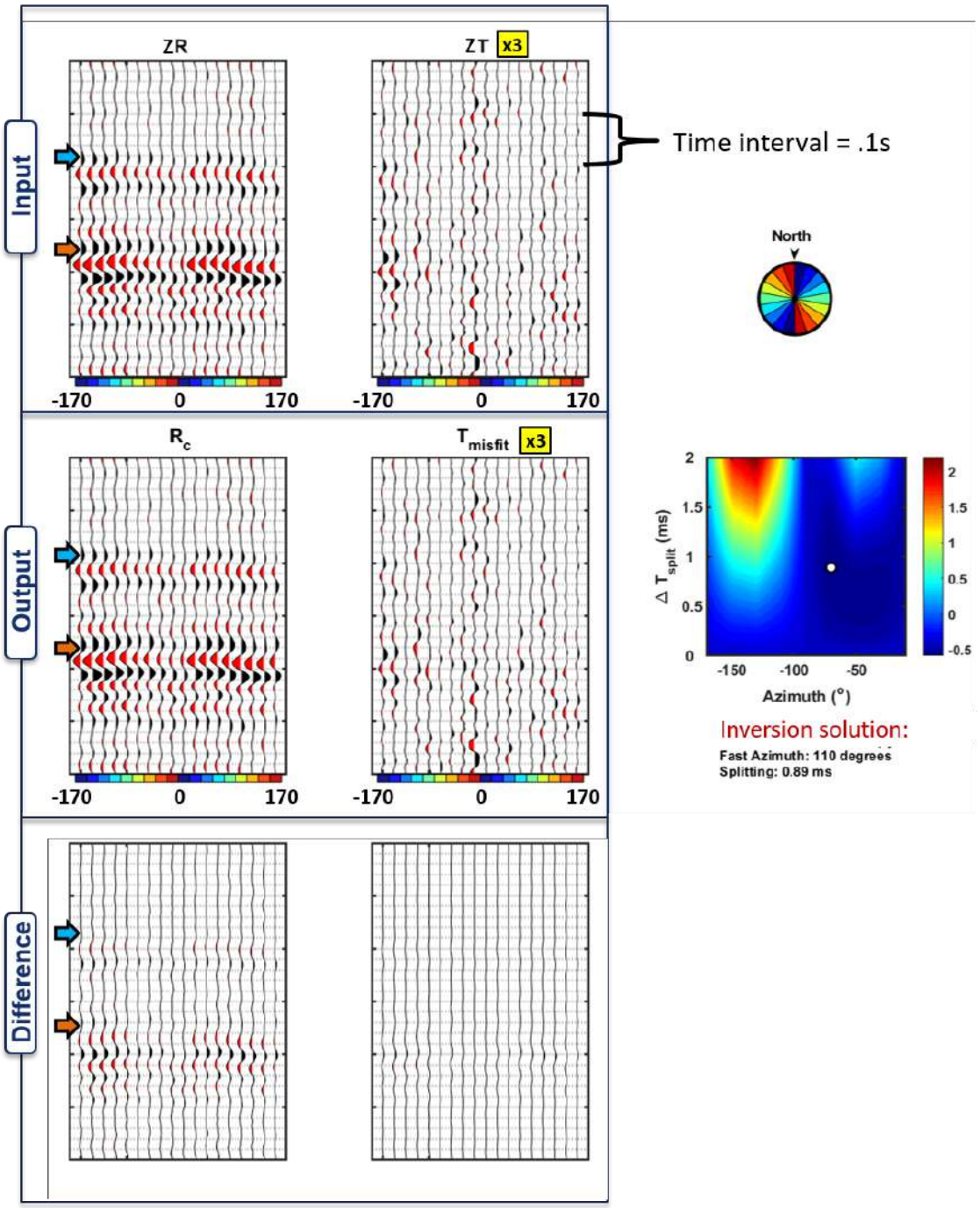

Figure 7.19: Inversion for fast azimuth and shear-wave splitting using Turkey Shoot Baseline converted-wave data at location 16 (Figure 6.3). The solution is based on the SEAC algorithm (Simmons, 2009) described in Figure 7.12. The input ZR and ZT LAS do not show HTI-related VVAz character and the result of the SEAC inversion is not correct. The objective function is not exactly minimized for this field data input.

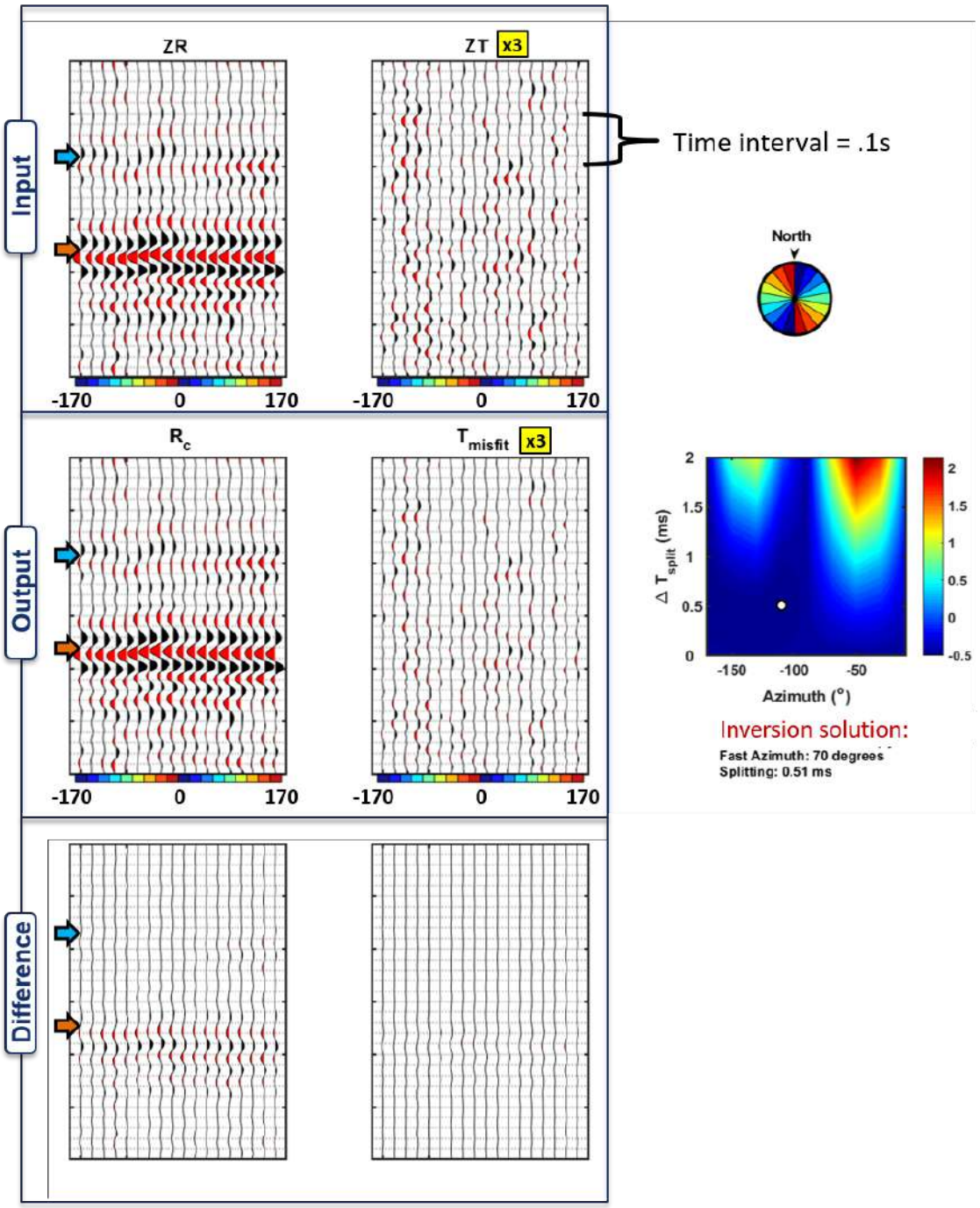

Figure 7.20: Inversion for fast azimuth and shear-wave splitting using Turkey Shoot Baseline converted-wave data at location 39 (Figure 6.3). Similar to location 16 shown in Figure 7.19, the input ZR and ZT LAS do not show HTI-related VVAz character and the result of the SEAC inversion is not correct.

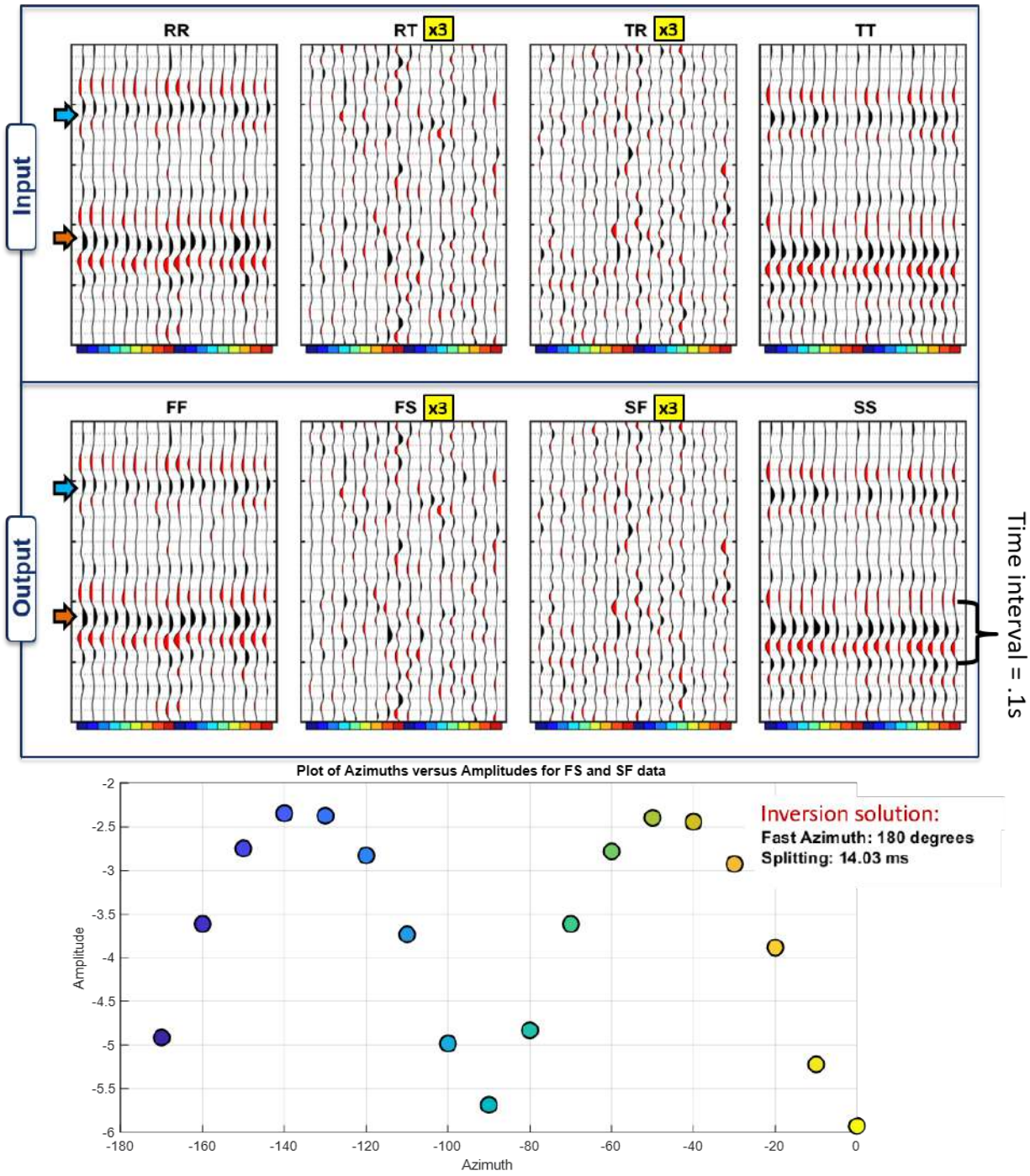

Figure 7.21: Alford rotation for fast azimuth and shear-wave splitting using Turkey Shoot Baseline pure shear-wave data at location 16 (Figure 6.3). The 1-D objective function for Alford rotation is plotted at the base of the LAS plots. The input LAS components do not show HTI-related VVAz and the result of the Alford Rotation does not minimize the FS and SF cross-terms. The estimated fast azimuth cannot be trusted and the estimated splitting is not accurate.

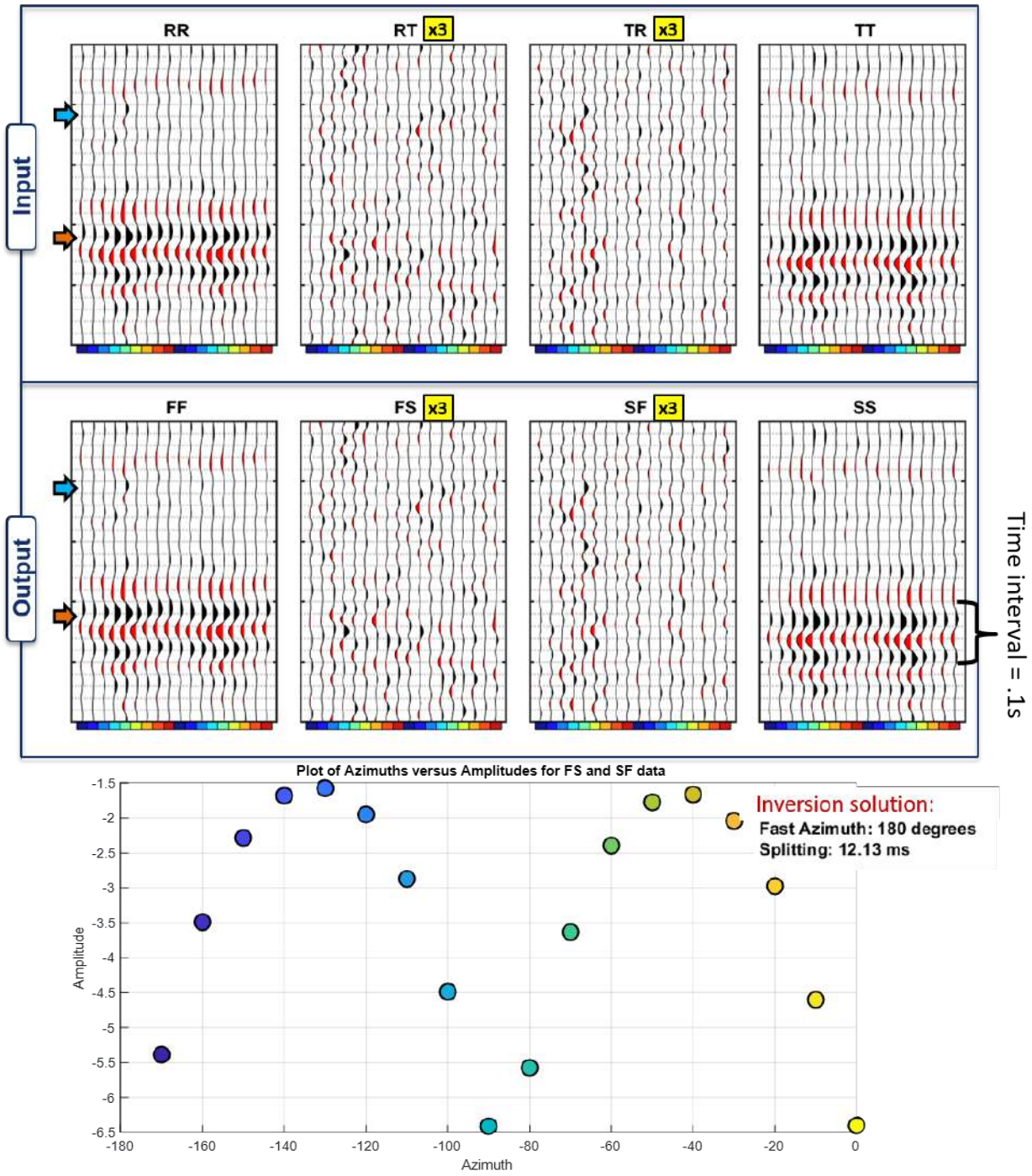

Figure 7.22: Alford rotation for fast azimuth and shear-wave splitting using Turkey Shoot Baseline pure shear-wave data at location 39 (Figure 6.3). The 1-D objective function for Alford rotation is plotted at the base of the LAS plots. Similar to location 16 in Figure 7.21, the input LAS components do not show HTI-related VVAz and the result of the Alford Rotation does not minimize the FS and SF cross-terms. The estimated fast azimuth cannot be trusted and the estimated splitting is not accurate.

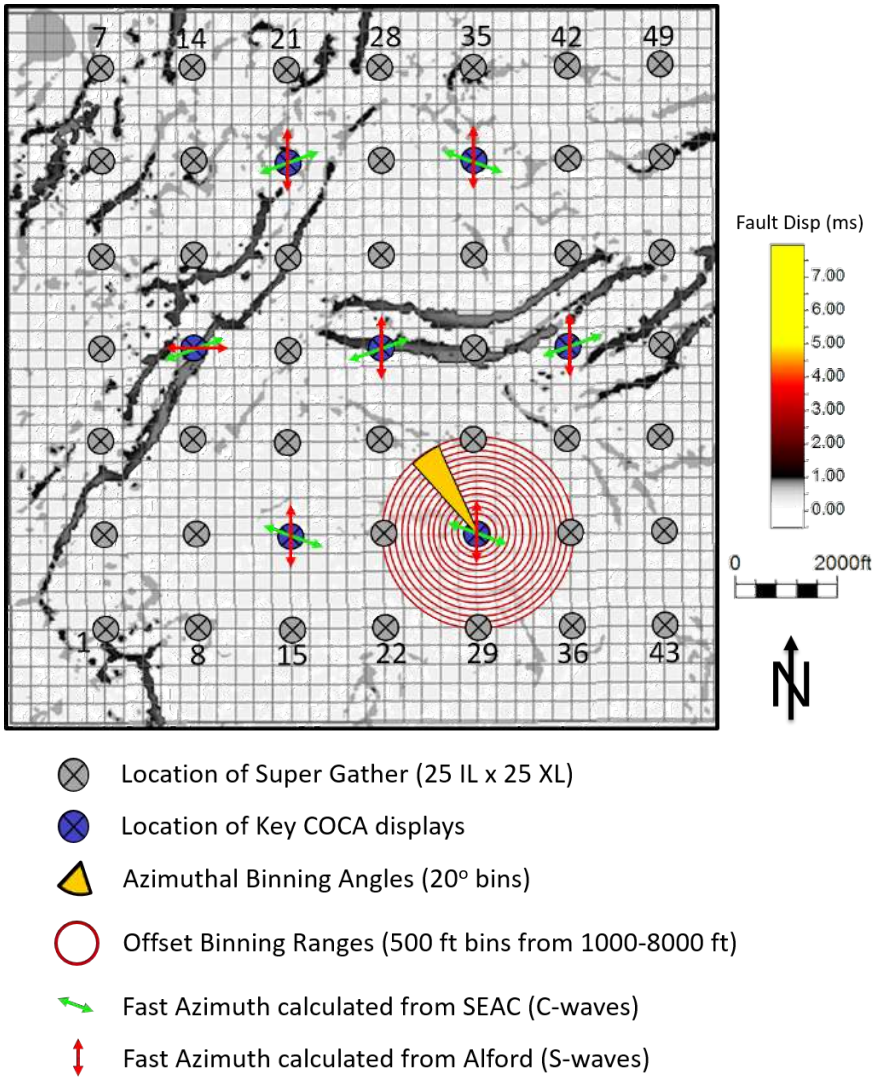

Figure 7.23: Map describing the orientations of the fast azimuth calculated from the Turkey Shoot converted and pure shear wave data. The green arrows represent the solutions based on SEAC and the red arrows are solutions based on Alford rotation.

7.6 Shear and Converted Wave: Joint Inversion for Fast Azimuth and Splitting Estimation

SEAC uses a 2D objective function that minimizes T-misfit for a range of Δt_{split} and θ_{trial}. Alford uses a 1D objective function which minimizes the cross term energy based on a range of θ_{trial}. As mentioned, a QC for the shear wave splitting calculation is to compare the Δt_{split} estimate from SEAC with that produced from the Alford rotation. The converted wave and shear wave inversions should tell the same story and should thus be inverted together.

An objective function for a joint splitting inversion using the converted and pure shear wave data was designed (Figure 7.24) such that the SEAC and Alford objective functions over the range of θ_{trials} are weighted and summed. The weighting factor, γ, allows the interpreter to identify which data component should be most trusted on input to the inversion for θ_{fast}.

The simple model with a single HTI layer used to demonstrate the Alford and SEAC algorithms (Figures 7.3 and 7.14) is run through the joint inversion code. The converted wave and shear wave data are weighted equally in the inversion and Figure 7.25 shows the results which include the converted and pure shear wave components rotated to F-S space and the compensated ZR and T-misfit components for the converted wave data.

The objective function is plotted in Figure 7.26. This function, which represents the weighted and summed energy of the SF, FS and T-misfit components is minimized for $\theta_{trial} =$ 60 degrees and converted wave $\Delta t_{split} = 9.8ms$. Comparing the objective function result to Figure 7.14, the is stronger confidence in the azimuthal solution given that the pure shear wave components are now taken into consideration. The converted wave Δt_{split} is the same as that calculated using only the SEAC inversion (Figure 7.14). Calculating the shear wave Δt_{split} from the FF and SS products of this joint inversion gives 16ms which is the same as that calculated using only Alford rotation (Figure 7.3).

Recall that when the LAS synthetics from the 12m cracked, Niobrara model was muted at a far offset and using a broad window for the inversion (top of Carlile to Graneros), the Alford rotation produced a fast azimuth of 100 degrees (Figure 7.8). The SEAC algorithm

produced an accurate calculation for the fast azimuth at 110 degrees (Figure 7.15) using the same broad window. Running the joint inversion for this 12m cracked, Niobrara model, a single fast azimuth is calculated to be 110 degrees. Figure 7.27 shows the inversion results and Figure 7.28 shows the objective function plot. The objective function is minimized for $\theta_{trial} = -70$ degrees $= 110$ degrees and converted wave $\Delta t_{split} = 0.25ms$. The converted wave Δt_{split} estimation is the same as that calculated using only the SEAC inversion. Calculating the shear wave Δt_{split} from the FF and SS products of this joint inversion gives 0.46ms.

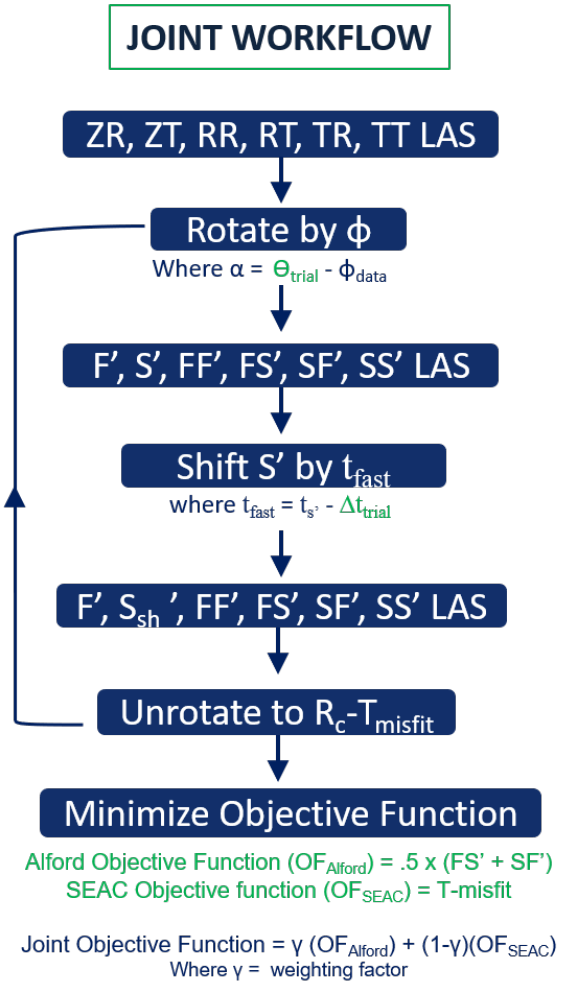

Figure 7.24: Description of joint inversion workflow for calculating the fast azimuth using converted and pure shear wave data.

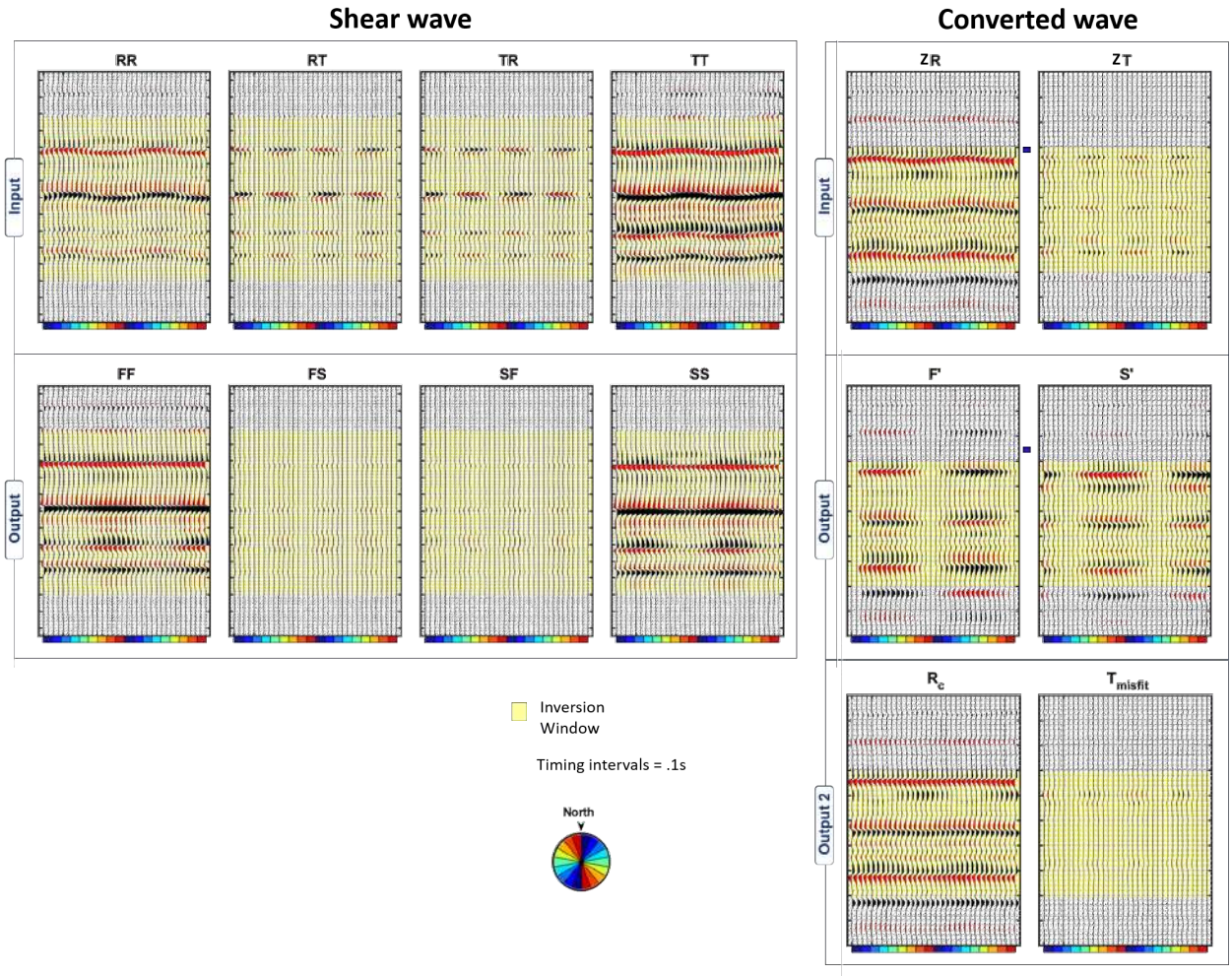

Figure 7.25: Solution of joint VVAz inversion for a simple model with a single HTI layer and isotropic overburden. The outputs include the F-S components for the pure shear wave and converted shear wave as well as the compensated R and minimized T-misfit. All components are gained on the same relative scale and amplitudes are thus comparable.

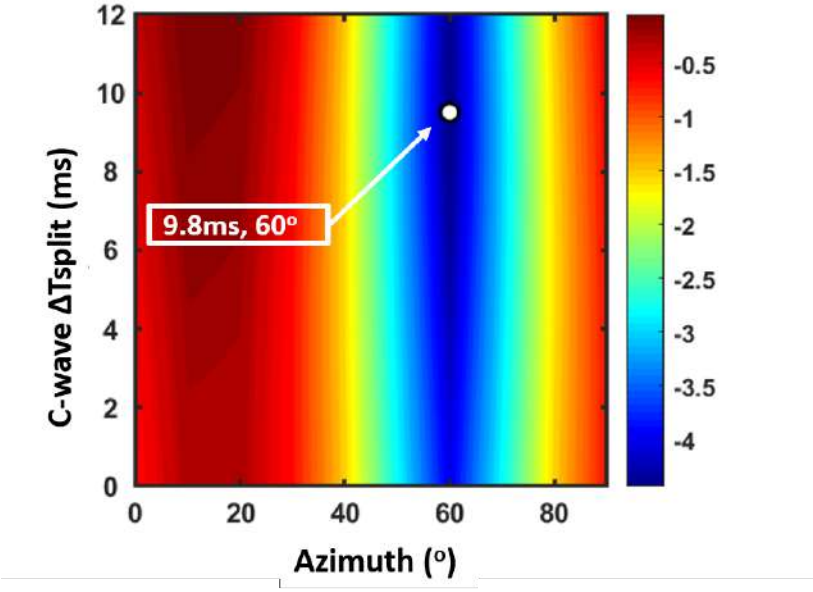

Figure 7.26: Objective function for the joint inversion on the simpled HTI model which represents the summed energy of SF, FS and T-misfit for a calculated fast azimuth and converted wave travel time splitting estimation. The objective function is minimized for $\theta_{trial} = 60$ degrees and converted wave $\Delta t_{split} = 9.8ms$. The calculated shear wave Δt_{split} using cross-correlation over the same window of inversion shown in Figure 7.25 is 16ms

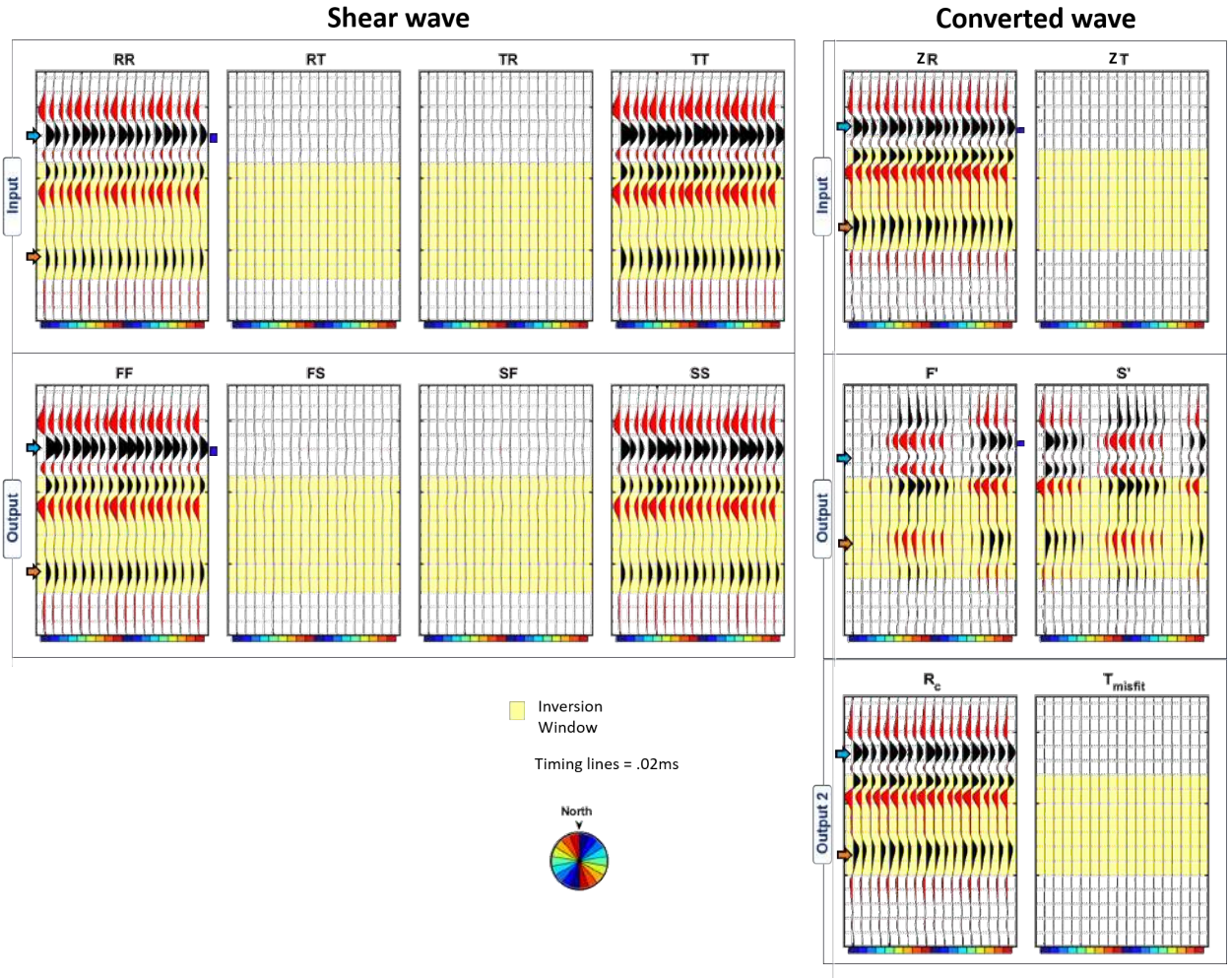

Figure 7.27: Solution of joint VVAz inversion for fast azimuth and converted wave splitting estimation for the 12m cracked, Niobrara model. The outputs include the F-S components for the pure shear wave and converted shear wave as well as the compensated R and T-misfit components.

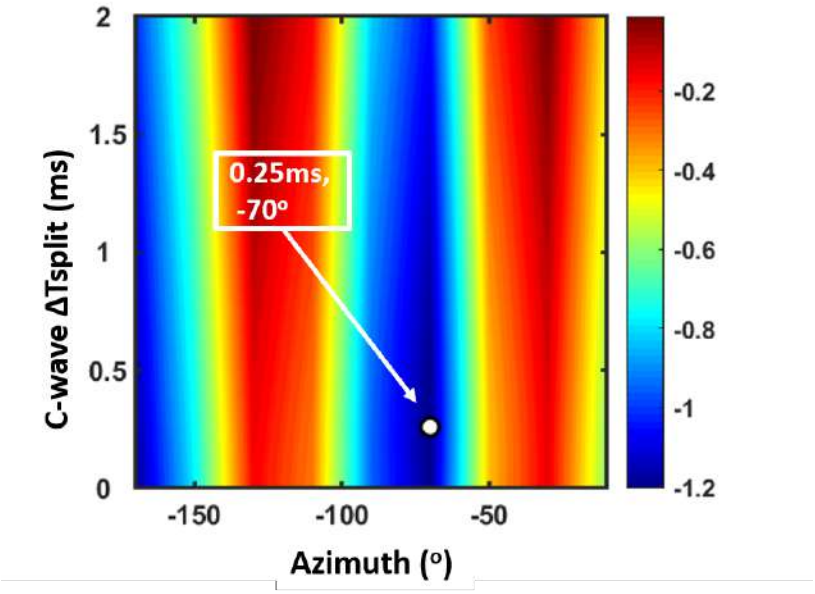

Figure 7.28: Objective function for the joint inversion on the simpled HTI model which represents the summed energy of SF, FS and T-misfit for a calculated fast azimuth and converted wave travel time splitting estimation. The objective function is minimized for $\theta_{trial} = -70$ degrees $= 110$ degrees and converted wave $\Delta t_{split} = 0.25ms$. The calculated shear wave Δt_{split} using cross-correlation over the same window of inversion shown in Figure 7.27 is .46ms

The joint inversion constrains the solution for the fast azimuth as the solution now depends on the FS', SF' and T-misfit components. I have demonstrated the complexities of Alford rotation to be a necessary tight mute to fit the normal incidence assumption as well as a careful selection of the inversion window. The joint inversion provides a unique solution based on both the shear wave and converted wave components.

7.7 Conclusion

Δt_{split} is a function of both depth and offset as demonstrated in the Alford and SEAC inversions for different time windows and mutes. There is no Δt_{split} at the top of the HTI layer and the depth at which it is largest, varies for different HTI thicknesses. θ_{fast} does not vary with depth or offset for this HTI modeling with no overburden anisotropy. However, the fast azimuth solution based on a single inversion of the shear wave or converted wave

data can be affected by the time windows used for the inversion and muting parameters.

With the necessary conditions met for the input limited azimuth stacks, Alford rotation and SEAC are valid techniques for estimating fast azimuth on pure shear wave and converted wave data respectively. However, running such inversions on the separate components does not facilitate the idea that all seismic components tell the same story. A joint inversion potentially constrains the solution such that all components of the converted and pure shear wave data are used to interpret a single fast azimuth. This improve the accuracy of inversion for the fast azimuth especially when the selection of a mute and an inversion window add uncertainty.

CHAPTER 8

SUMMARY, CONCLUSIONS AND RECOMMENDATIONS

8.1 Research Summary

If 3-C or 9-C data is available in oil and gas exploration, then the components additional to the P-wave data should be analyzed as they add constraint to the interpretation. In this research, the added value of multicomponent interpretation has been evidenced by reflectivity modeling. The importance of coordinate systems in analyzing the wave modes and preservation of azimuthal and offset effects have been demonstrated, and observations made on field data support the need for multicomponent feasibility studies prior to acquisition.

8.1.1 Rotation of Horizontal Components

Typical 3-D seismic acquisition orients sources and receivers along inlines and crosslines such that energy recorded on the horizontal receiver components, varies with source-receiver azimuth. In the presence of anisotropy, converted and pure shear waves propagate with fast velocities along fracture strike and slow velocities perpendicular to fracture strike. A typical practice is to rotate the data to fast-slow coordinates which separates the fast and slow arrivals. The fast-slow components contain a mix of shear wave modes and, like acquisition coordinates, can complicated data for processing.

Multicomponent data should be rotated to the radial-transverse coordinate system which separates the P-SV, SV- and SH-waves onto different components. The radial direction for any source-receiver pair is along the source-receiver azimuth and contains only SV-wave information for a horizontal source and the P-SV information for a vertical source. The transverse direction for any source-receiver pair is orthogonal to the radial direction and contains only SH-wave information for a horizontal source. The cross-term components for the converted and pure shear wave data are minimized compared to the main components and residual energy is indicative of shear wave splitting. This coordinate system removes

the azimuthal dependence of the horizontal components and is the recommended system for shear-wave processing and interpretation.

8.1.2 Multicomponent Interpretation of Fracture Characteristics

To get to an interpretive space, the data should be preprocessed in R-T coordinates. From this point, the data can be rotated to fast-slow coordinates for interpretation of shear wave splitting. It can be dangerous to define a fast azimuth as the regional stress direction since this assumes that the seismic is sensitive to this stress condition. The fast azimuth should be interpreted from the seismic data in the R-T coordinate system.

Azimuthal binning of the R-T components exposes velocity variation with azimuth (VVAz) for all components and a fast azimuth can be identified. Limited azimuth stacks, stack over offset and bin the data into azimuthal sectors. Each trace of an LAS is representative of a single azimuth bin and the arrival times of the reflector will vary depending on the fracture azimuth and amount of shear wave splitting. Limited azimuths stacks are conventionally built using an outer mute at the angle of the SV-wave polarity reversal. The conventional P-wave limited azimuth stack may show VVAz effects, however the largest effects are observed at the far offsets. Converted and pure shear wave data LAS appropriately expose VVAz effects at reflections below the fractured medium.

For P-wave data (ZZ) at far offsets:

- V_{P-fast} = along fracture strike
- V_{P-slow} = perpendicular to fracture strike

For converted SV-wave (ZR) and pure SV-wave data (RR) at all offsets:

- $V_{SV-fast} = V_{PSV-fast}$ along fracture strike
- $V_{SV-slow} = V_{PSV-slow}$ perpendicular to fracture strike

For pure SH-wave data (TT) at all offsets:

- $V_{SH-slow} = V_{PSH-slow}$ along fracture strike
- $V_{SH-fast} = V_{PSH-fast}$ perpendicular to fracture strike

Energy on the cross-term components (ZT, RT and TR) exposes HTI related shear wave splitting. The principal fracture directions (isotropy/symmetry planes) on cross-term components are identified as those LAS azimuths with no energy. The far offset data for all components contain valuable information that is preserved in common-offset, common-azimuth gathers (COCA) gathers. Where an LAS does not expose P-wave VVAz, the COCA gather will show VVAz variation with offset. The VVAz response for an HTI layer is onset at mid-offsets for the P-wave data and is observed at all offsets for the shear wave data sets.

The converted and shear wave interpretations can significantly reduce the ambiguity and risk of a single P-wave interpretation. Additionally, VVAz effects are better resolved on the horizontal components for thinner HTI intervals. For models with a thick HTI interval, the VVAz effects on the horizontal components are observed at deep reflectors. For models with a thin HTI interval, these VVAz effects are observed at shallower reflectors within the fractured interval.

The observations on all components are complementary and should convey the same conclusions regarding subsurface conditions. Alford rotation for pure shear wave data and SEAC for converted wave data invert for the fast azimuth and shear wave splitting from limited azimuth stacks. Alford rotation involves many assumptions and splitting estimates from both inversions are dependent on the inversion window selected. A joint inversion potentially best constrains the solution for a single fast azimuth which satisfies both the converted and shear wave modes.

8.1.3 Qualitative Interpretation of HTI in the Niobrara

Where the Niobrara fractured interval thins below 25m, P-wave VVAz is visually undetectable. The pure shear wave data resolves a VVAz response for a fractured Niobrara layer as thin as 12m. The difference between VVAz effects on the shear wave data for the

Niobrara model with 12m of HTI versus 110m of HTI is measurable such that the pure shear components may be used to determine the extent of the fractured medium.

The 9-C, 4-D Turkey Shoot field data, however, does not suggest that the anisotropy of the Niobrara-Codell interval is a simple HTI model. The VVAz splitting is expected to be relatively small (1.7 ms for converted wave and 4 ms for shear wave) based on the fully cracked Niobrara model (110 degrees). The noise of field data in addition to unoptimized acquisition and processing steps mask any potential VVAz effects on the Turkey Shoot surveys. Additionally, anisotropy at the Niobrara-Codell reservoir is not only influenced by a single vertical fracture but also possible lateral velocity variations in the overburden and this requires more complex modeling to understand the expected VVAz response.

8.2 Conclusions

There is underutilized value in multicomponent data sets that maybe lost due to mishandling of the horizontal components in acquisition and processing. These components should be rotated to a radial-transverse coordinate system such that the wave modes, which contain unique kinematic and amplitude signatures, are separated. While the nine components respond differently to subsurface conditions and are individually informative, the relationships between the components are an important element to consider. Multicomponent processing and interpretation is derisked by operating on and inverting all components simultaneously and using their relationships as constraints to solutions.

8.3 Recommendations

8.3.1 Modeling Implications of Lateral Velocity Variations on VVAz Effects

The Niobrara-Codell reservoir is not only influenced by a single vertical fracture set but possible lateral velocity variations in the overburden. The changing fault regimes both vertically and laterally in the Wishbone section make it difficult to evaluate their effect on the seismic wave velocities. Modeling the influence of different overburden anisotropy on an HTI reservoir would help lay out expectations for the field data observations.

Modeling lateral velocity variations or faulting influence is not feasible using the reflectivity model since it is based on a flat-layered earth. Additionally, current layer stripping techniques are only valid for HTI overburden. A reformulation of layer stripping techniques would be required before application to shallow lateral velocity variations.

8.3.2 Exploring AVAz Techniques for Improved Anisotropic Characterization of the Niobrara

Reflection coefficients vary in amplitude with both offset (AVO) and azimuth (AVAz) which contains information about the medium on both sides of an interface. These amplitude characteristics are determined by elastic rock properties and as such, have higher resolution than the VVAz methods. Amplitude variations with azimuth are observed at the interface between layers and Figure 8.1 shows the pre-stack amplitude slices at the Niobrara top for the models presented in this research. The slices are extracted on the move-out corrected shot gather for each component. The P-wave (ZZ), converted wave (ZR and ZT) and shear wave (RR, RT and TT) components are gained independently.

Little AVAz is observed on the P-wave at near incidence angles for all thicknesses. The changes between models are also relatively small except for the monoclinic model where the P-wave far offset amplitudes have a very unique signature. The converted wave data shows distinguishable AVAz changes at the far offsets for all models but the pure shear wave components show the largest AVAz changes for models with different HTI thicknesses.

There is potential for multicomponent AVO and AVAz modeling to map HTI anisotropy. Learnings from this modeling can assist in the evaluation of AVAz trends in the Wishbone field data.

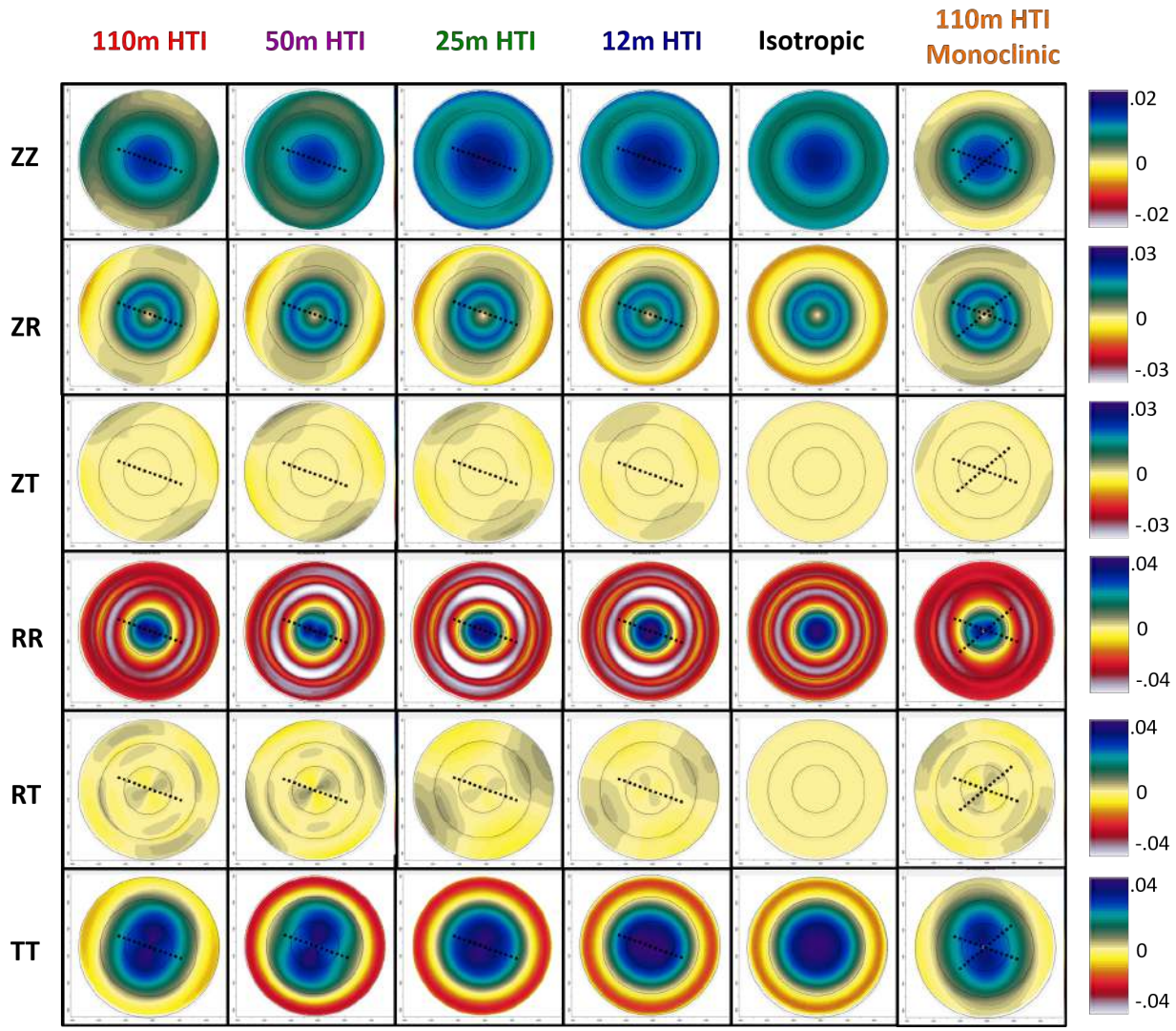

Figure 8.1: Amplitude versus azimuth responses at the top of the Niobrara reflector for different models with fractures in the Niobrara interval. The offset rings are 700m apart and provide an estimate of the offset range required to see azimuthal variations on the different components. Note that the amplitudes of the pure shear waves and converted waves are larger than the P-wave response.

8.3.3 Multicomponent Feasibility Studies and Anisotropic Modeling

Time-lapse feasibility studies are a well-practiced technique in industry used to determine the added value (if any) of using seismic data to monitor changes in a reservoir over time. Such a study helps evaluate whether the seismic can resolve changes in reservoir conditions based on known reservoir properties and expected responses to well completion and production.

Similarly, multicomponent seismic feasibility studies should be completed prior to 9-C acquisition. This study primarily answers the question of whether or not multicomponent data can better resolve the subsurface conditions and how much added information is obtained versus a simple P-wave acquisition. Additionally, it helps identify what anisotropic signal one should expect to see given what one knows about the reservoir properties (for example, thickness). If a shear wave splitting estimate of $\Delta t_{split} = 2$ms is significant to a reservoirs productivity, then, this feasibility study can help determine what acquisition, processing and migration techniques are needed to best preserve, expose and interpret (invert for) a small VVAz.

REFERENCES CITED

Aki, K. and Richards, P. G. (1980). Quantative seismology: Theory and methods. *New York*, 801.

Alfataierge, A. (2017). *3D Modeling and Characterization of Hydraulice Fracture Efficiency Integrated with 4D/9C Time-Lapse Seismic Interpretations in the Niobrara Formation, Wattenberg Field, Denver Basin*. M.sc., Colorado School of Mines.

Alford, R. A. P. C. (1986). Shear Data in the Presence of Azimuthal Anisotropy: Dilley, Texas. In *SEG 1986 Annual Meeting*. Society of Exploration Geophysicists.

Castagna, J. and Backus, M. (1993). *Offset-Dependent Reflectivity: Theory and Practice of AVO Analysis*. Society of Exploration Geophysicists.

Cheadle, S., Miao, X., Gray, D., Dgc, V., Goodway, B., Li, G., and Gallop, J. (2000). Mapping Azimuthal Variations in Amplitude and Velocity in Wide-Patch Land 3D Data. In *SEG 2000 Annual Meeting*, number October. Society of Exploration Geophysicists.

Daves, J. and Simmons, J. (2018). Shear-wave Reflection Signal Recovery Through Horizontal -Geophone Azimith Estimation. In *EAGE 2018 Annual Meeting*, Copenhagen.

Davis, T. (1985). Seismic Evidence of Tectonic Influence on Development of Cretaceous Listric Normal Faults, Boulder Wattenberg Greeley Area, Denver Basin, Colorado. *The Mountain Geologist*, 22(2):47–54.

DeVault, B., Davis, T. L., Tsvankin, I., Verm, R., and Hilterman, F. (2002). Multicomponent AVO analysis, Vacuum field, New Mexico. *Geophysics*, 67(3):701–710.

Dudley, C. (2015). *Integrating Horizontal Borehole Imagery and Cluster Analysis*. PhD thesis, Colorado School of Mines.

Fryer, G. J. and Frazer, L. N. (1984). Seismic waves in stratified anisotropic media. *Geophysical Journal of the Royal Astronomical Society*, 78:691–719.

Fryer, G. J. and Frazer, L. N. (1987). Seismic waves in stratified anisotropic media II. Elastodynamic eigensolutions for some anisotropic systems. *Geophysical Journal of the Royal Astronomical Society*, 91(1):73–101.

Gaiser, J. E. (1999). Applications for vector coordinate systems of 3-D converted-wave data. *The Leading Edge*, 18:1290.

Gaiser, J. E. (2016). *3C Seismic and VSP: Converted Waves and Vector Wavefield Applications*. Society of Exploration Geophysicists.

Garotta, R. and Granger, P. Y. (1988). Acquisition and processing of 3C x 3D data using converted waves. In *SEG 1988 Annual Meeting*. Society of Exploration Geophysicists.

Gray, D. (2007). Observations of Seismic Anisotropy in Prestack Seismic Data. In *SEG 2007 Annual Meeting*, pages 119–123, San Antonio.

Grechishnikova, A. (2017). *Niobrara Discrete Fracture Networks: From Outcrop Surveys to Subsurface Reservoir Models*. PhD thesis, Colorado School of Mines.

Grechka, V. and Vasconcelos, I. (2007). Characterization of multiple fracture sets at Rulison Field, Colorado, USA. *EAGE/SEG 2007 Research Workshop on Fractured Reservoirs: Integrating Geosciences for Fractured Reservoirs Description*, 72(2).

Hardage, B. A., DeAngelo, M. V., Murray, P. E., and Sava, D. (2011). *Multicomponent Seismic Technology*. Society of Exploration Geophysicists.

Higley, D. K. and Cox, D. O. (2007). Oil and Gas Exploration and Development along the Front Range in the Denver Basin of Colorado , Nebraska , and Wyoming. *US Geological Survey Digital Data Series*, pages 1–40.

Jenner, E. (2010). Modeling Azimuthal NMO in Laterally Heterogeneous HTI Media. *First Break*, 28.

Kennett, B. (1983). *Seismic wave propagation in stratified media*, volume 34. ANU E Press, new ed. edition.

Lachance, L. E. R. and Robinson, M. C. (2012). Sequence Stratigraphy of the Upper Cretaceous Niobrara Formation, A Bench, Wattenberg Field, Denver Julesburg Basin, Colorado. *AAPG Annual Convention and Exhibition*, 20176:1–35.

Lewis, C., Davis, T., and Vuillermozd, C. (1991). Three-dimensional multicomponent imaging of reservoir heterogeneity, Silo Field, Wyoming. *Geophysics*, 56(12):2048–2056.

Lynn, H. B. and Thomsen, L. A. (1990). Reflection shear-wave data collected near the principal axes of azimuthal anisotropy. *Geophysics*, 55(2):147.

Martin, M. A. and Davis, T. L. (1987). Shear-wave birefringence: A new tool for evaluating fractured reservoirs. *The Leading Edge*, 6(10):22.

Matuszczak, R. A. (1973). Wattenberg Field, Denver Basin, Colorado. *The Mountain Geologist*, 10(3):99–105.

Miller, G. and Pursey, H. (1954). The field and radiation impedance of mechanical radiators on the free surface of a semi-infinite isotropic solid. *Proceedings of the Royal Society of London A: Mathematical, Physical and Engineering Sciences*, 223(1155).

Motamedi, T. and Davis, T. (2015). Time-Lapse Characterization of The Niobrara Reservoir From Multicomponent Seismic Data, Wattenberg Field, Colorado. *First Break*, 33(July):1–96.

Mueller, M. C. (1991). Prediction of lateral variability in fracture intensity using multicomponent shear wave surface seismic as a precursor to horizontal drilling in the Austin Chalk. *Geophysical Journal International*, 107(3):409–415.

Mueller, S. (2016). *Application of Time-Lapse Seismic Shear Wave Inversion to Characterize the Stimulated Rock Volume in the Niobrara and Codell Reservoirs, Wattenberg Field, CO*. PhD thesis.

Ning, Y. (2017). *Production Potential of Niobrara and Codell: Integrating Reservoir Simulation with 4D Seismic and Microseismic Interpretation*. PhD thesis, Coloraod School of Mines.

Philip, N. and Santus, S. (2011). Gas, Oil, and Water Production from Wattenberg Field in the Denver Basin, Colorado. *United States Geological Survey*, pages 1–23.

Ruger, A. (2002). *Reflection Coefficients and Azimuthal AVO Analysis in Anisotropic Media*. Society of Exploration Geophysicists.

Shuck, E. L. (1993). *Seismic Characterization of a Fractured Coalbed Methane Reservoir Cedar Hill Field , San Juan County*. PhD thesis, Colorado School of Mines.

Simmons, J. (2004). Multicomponent Prestack Modeling in Isotropic/Anisotropic Media. In *2004 CSEG National Convention*, page S083. Canadian Society of Exploration Geophysicists.

Simmons, J. (2009). Converted-wave splitting estimation and compensation. *Geophysics*, 74(1).

Simmons, J. and Backus, M. (2001). Shear waves from 3-D 9-C seismic reflection data: Have we been looking for signal in all the wrong places? *The Leading Edge*, 20(6):604.

Sonnenberg, S. (2011). The Niobrara Petroleum System: A New Resource Play in the Rocky Mountain Region. *Search and Discovery*, 80206:107–112.

Sonnenberg, S. (2012). The Niobrara Petroleum System, Rocky Mountain Region. *Search and Discovery*, 80206:107–112.

Sonnenberg, S. A. and Weimer, R. J. (1993). Oil Production from Niobrara Formation, Silo Field , Wyoming: Fracturing Associated With a Possible Wrench Fault System (?). *The Mountain Geologist*, 30(2):39–53.

Sonnenberg, S. A. and Weimer, R. J. (2003). A Near Miss & Lessons Learned After 35 Years of Development History. pages 1–38.

Stamer, J. (2016). *Geologic Reservoir Characterization of the Codell Sandstone: Central Wattenberg Field, Colorado*. PhD thesis, Colorado School of Mines.

Terrell, M. J. (2004). *Fracture Permeability Characterization at Weyburn field: from Shear Wave Anisotropy Through Flow Simulation*. PhD thesis, Colorado School of Mines.

Thomsen, L. (1988). Reflection seismology over azimuthally anisotropic media. *Geophysics*, 53(3):304–313.

Thomsen, L. (1998). Converted-wave reflection seismology over anisotropic, inhomogenous media. *SEG 1999 Annual Meeting*, 64(3):2048–2051.

Tsvankin, I. (2012). *Seismic Signatures and Analysis of Reflection Data in Anisotropic Media*, volume 19. Soceity of Exploration Geophysicists, third edition.

Weimer, R., Sonnenberg, S. A., and Young, G. (1986). Wattenberg Field, Denver Basin, Colorado. *Geology of Tight Gas Reservoirs*, pages 143–164.

Weimer, R. J. (1996). Guide to the Petroleum Geology and laramide Orogeny, Denver Basin and Front Range, Colorado. Technical report, Colorado Geological Survey, Department of Natural Resources, Denver.

White, M. D. (2015). *Time-Lapse Interpretation of P-Wave Data for a Hydraulically Fractured Reservoir, Wattenberg Field, Colorado*. PhD thesis.

Williams, M. and Jenner, E. (2002). Interpreting seismic data in the presence of azimuthal anisotropy. *The Leading Edge*, 21(8):771–774.